Jetology:
A precision understanding of jet substructure and the dead-cone effect

Jacob Henry Rawling

School of Physics and Astronomy

A thesis submitted to the University of Manchester for the degree of Doctor of Philosophy
in the Faculty of Science and Engineering

2019

Contents

Total Word Count: 47552

Abstract

A measurement of the relative differential cross-section of $t\bar{t}$ production in proton-proton collisions at $\sqrt{s} = 13\,\text{TeV}$ of a novel observable, A_θ, is presented. The measurement was performed in the lepton+jets final state with data recorded by the ATLAS detector. The integrated luminosity of the dataset used was $L = 138.2\,\text{fb}^{-1}$. The effects of the detector were removed using a statistical procedure. The A_θ observable was designed to be sensitive to dead-cone effect, a suppression of radiation in the collinear region around a massive radiator. The A_θ observable was found to be sensitive to the radiative properties of the $t\bar{t}$ system, evaluated by comparison with several NLO predictions. The observed suppression strength of the dead-cone effect was parameterised by the f_{DC} observable, such that $f_{\text{DC}} = 1.0$ corresponds to the SM prediction of the dead-cone effect and $f_{DC} \in [0, 1]$. The dead-cone suppression strength was measured to be $f_{\text{DC}} = 0.527 \pm 0.041(\text{stat}) \pm 0.295(\text{syst})$. The measured f_{DC} lies 1.77σ from the case where the top quark radiates as if it were massless, $f_{\text{DC}} = 0.0$.

Furthermore, a novel analytic approach top tagging was explored. Two top tagging algorithms were proposed: `TopSplitter` and Y_m splitter. The action of these taggers on top jets and quark-initiated jets were studied using all ordered analytic calculation. The calculation was compared to Monte Carlo prediction, and found that the parton shower used within traditional Monte Carlo captures the all order behaviour of jets after the application top tagging algorithms.

Declaration and Copyright

I declare that no portion of the work referred to in the thesis has been submitted in support of an application for another degree or qualification of this or any other university or other institute of learning.

i The author of this thesis (including any appendices and/or schedules to this thesis) owns certain copyright or related rights in it (the Copyright) and he has given The University of Manchester certain rights to use such Copyright, including for administrative purposes.

ii Copies of this thesis, either in full or in extracts and whether in hard or electronic copy, may be made only in accordance with the Copyright, Designs and Patents Act 1988 (as amended) and regulations issued under it or, where appropriate, in accordance with licensing agreements which the University has from time to time. This page must form part of any such copies made.

iii The ownership of certain Copyright, patents, designs, trade marks and other intellectual property (the Intellectual Property) and any reproductions of copyright works in the thesis, for example graphs and tables (Reproductions), which may be described in this thesis, may not be owned by the author and may be owned by third parties. Such Intellectual Property and Reproductions cannot and must not be made available for use without the prior written permission of the owner(s) of the relevant Intellectual Property and/or Reproductions.

iv Further information on the conditions under which disclosure, publication and commercialisation of this thesis, the Copyright and any Intellectual Property University IP Policy,[1] in any relevant Thesis restriction declarations deposited in the University Library, The University Library's regulations[2] and in The University's policy on Presentation of Theses.

---

[1] http://documents.manchester.ac.uk/display.aspx?DocID=24420
[2] http://www.library.manchester.ac.uk/about/regulations/

Acknowledgements

This thesis would not have been possible without the kindness and support of many people

Firstly, I would like thank my supervisor Yvonne for all her guidance over the past four and a half years. She has provided me with the direction and support I needed. Yvonne has also encouraged me to grow as researcher and explore my own crazy ideas, from outreach apps to machine learning. I have thoroughly enjoyed working with Yvonne and appreciate all she has taught me. I would also like to thank Andy Pilkington for his support and guidance throughout my PhD.

I am also grateful to everyone I have worked with, both at Manchester, CERN and further afield. Thanks in particular to Ian Connelly and Jay Howarth. I cannot thank you both enough for your help, support and patience. You have both taught me so much, and I had a lot of fun measuring top quarks with you. Thank you to Michaela Queitsch-Maitland, who provided invaluable guidance and help during my qualification task. To all my friends, the past few years have been fantastic. Thank you for the cheeky pints, D&D sessions, five-aside football, concerts and pub quizzes. You are brilliant.

Finally and most importantly, I would like to thank my fiancée Melissa. Melissa, you have brought love, support, and laughter to the strange and difficult adventure that is a PhD. I would not have made it without you. Thank you.

Preface

All measured data studied within this thesis was collected by the ATLAS experiment. This was made possible by the combined efforts of the members of the ATLAS collaboration, and the members of CERN who operate the LHC. Measured and simulated data were processed using the ATLAS reconstruction software. The work presented here relies on the software and computing infrastructure provided by CERN. The author contributed to the Top Working group of the ATLAS collaboration in the elected role of JetEtMiss Liaison for the Top working group. As part of this role, the author provided expert support on the usage of jet and missing transverse energy related uncertainties, as well as maintaining the reconstruction software implementation of those uncertainties within the ATLAS top reconstruction framework.

For a researcher to become a full member of the ATLAS collaboration, they must complete a qualification task. The qualification task completed by the author was the dijet η inter-calibration presented in Chapter 5. The measurement of the dijet η inter-calibration was performed in close collaboration with Andrew Pilkington and Michaela Queitsch Maitland, who acted as advisers and technical support for the project. Combined with other measurements and studies of the jet energy scale, the work presented in Chapter 5 resulted in the publication [1].

The Work presented in Chapter 6 was performed in collaboration with Marco Guzzi and Gregory Soyez and resulted in the publication [2]. The author's primary contributions to this paper were Monte Carlo studies of the Y_m splitter algorithm, validation of jet mass calculation in the triple collinear and strongly ordered limits, and evaluation of the Sudakov form factors for Y_m splitter with fixed α_s.

The work presented in Chapter 7 resulted in a paper that is currently pending review with the journal Physical Review B. The measurement was performed in close collaboration with James Howarth and Ian Connelly, who participated as advisers to the analysis and editors to the paper. The author was responsible for all parts of the analysis. The data driven background parameterisations used for evaluating "fake" leptons were measured by ATLAS members Nello Bruscino and Erich Varnes.

1. Introduction

The Standard model of particle physics is a theoretical description of fundamental particles and the interactions that govern their behaviour. Quantum Chromodynamics (QCD) is the sector of the Standard Model that describes the strong interaction between colour charged particles. Collimated showers of particles are produced by the QCD decay of colour charged particle. These showers are typically clustered in objects called *jets*. The most massive particle in the Standard Model is the top quark. Like all quarks, the top quark is colour charged, and therefore can emit QCD radiation. Precision measurements of top quark properties in the highly boosted regime require the identification of top quarks, known as *top tagging*. Top tagging requires detailed understanding of jets produced by light partons, as well as a detailed understanding of the top quark's QCD radiation structure. This thesis aims to understand the behaviour of QCD radiation in the top sector of the Standard Model, and further the understanding of jet physics in proton-proton collisions at the Large Hadron Collider (LHC).

Understanding QCD radiation from massive radiators is a central aim of this thesis. A new variable sensitive to the *dead-cone* effect, the suppression of emitted radiation from a massive radiator, is proposed. The relative differential cross-section, $\frac{1}{\sigma_0}\frac{d\sigma}{dA_\theta}$, was measured in a fiducial phase-space in $t\bar{t}$ events in the lepton+jets channel using data recorded at the ATLAS detector in the years 2015, 2016, 2017 and 2018 at a centre of mass energy $\sqrt{s} = 13\,\text{TeV}$. A statistical procedure was validated and optimised to remove detector effects for this measurement. A gradient free black box optimisation procedure, typically used in machine learning hyperparameter optimisation, was used for the first time as a method of optimising a physics analysis and found to increase the statistical significance of the measured result.

To further the understanding of jet physics at the LHC, the calibration of jets across the ATLAS detector was also explored. A data driven calibration procedure was performed with data collected by the ATLAS detector in years 2015 and 2016 at a centre of mass energy $\sqrt{s} = 13\,\text{TeV}$. The calibration procedure corrects the jet energy scale to be uniform as a function of jet direction across the detector. A suite of validation procedures was performed on the measured calibration. Limitations in the procedure were identified and understood. A novel extension to the data driven calibration procedure was introduced to overcome the evaluated limitations in the

method.

Top Tagging techniques are extended and jet substructure is understood using a novel analytic resummed calculation of jet mass after the application of top tagging algorithms. A new top tagging algorithm, Y_m splitter, is constructed based explicitly on an analytic understanding of jet physics. Furthermore, the CMS Top Tagger is studied and limitations with this algorithm identified. These limitations were overcome with the `TopSplitter` algorithm, a new top tagging algorithm motivated by an analytic understanding of jet physics. A novel all order calculation of the action of top tagging algorithms upon jets formed from top quarks and from light quarks was performed. To understand whether traditional Monte Carlo (MC) based predictions captures the all order behaviour of top tagging algorithms, the all order analytic prediction was compared systematically to MC prediction.

This thesis is structured in the following manner. Chapter 2 introduces the theoretical framework of the Standard Model. This chapter details methods for calculating predictions using the framework of Quantum Field Theory, provides detail on the strong force, and motivates the study of the radiative properties of the top quark. In Chapter 3 the ATLAS detector and LHC accelerator complex at CERN are described. Chapter 4 details how measured read-outs from the ATLAS detector are reconstructed into physics objects. The following three chapters discuss measurements with ATLAS data, and studies of the top quark. A method of calibrating jets measured with the ATLAS detector is discussed in Chapter 5. The identification of the jets which fully contain decay products of a top quark is discussed using a novel analytic approach in Chapter 6. Finally, the measurement of a variable sensitive to top quark radiation is discussed in Chapter 7.

All units are given using natural units where $\hbar = c = 1$, where $\hbar$ is the reduced Planck constant and c is the speed of light in a vacuum. Electric charges are implicitly given in multiples of the elementary charge $e = 1.6 \times 10^{-19}$C.

2. Theoretical framework

The description of fundamental particles of nature has evolved dramatically over the past sixty years. The culmination of the theoretical description of experimental results is *Quantum field theory* (QFT). QFTs were formalised in the 1960s from an extension of Dirac's relativistic Quantum Mechanics framework and prediction of the positron (the charge conjugate of the electron) [3, 4]. In the QFT formalism, particles are represented by fields and interactions defined through a Largrange density which operates upon those fields.

The quantum field theory known as the *Standard Model* (SM) is the most successful description of the fundamental constituents of matter ever penned by humanity. It has been tested and found to agree with experiment to extremely high precision, for example the electron magnetic moment has been measured and found to agree with the standard model to 0.7 parts per billion [5]. While it is the best description of the fundamental particles of nature, the SM is incomplete. It does not describe the fundamental force of Gravity. Furthermore, there are no particles in the SM that account for observed astronomical data which imply an abundant massive particle that does not interact electromagnetically, so called *Dark Matter*. The SM also has no mechanism to explain the abundance of matter compared to anti-matter within the universe. With precision study of the SM, it is hoped a more complete description of the universe can be achieved.

This chapter shall detail the Standard Model. In Section 2.1 an overview of the particles and interactions described in the SM is given. The interaction of colour-charged particles is formalised in Section 2.2, including an overview of how SM predictions of jet radiation are calculated. Section 2.3 describes the procedure for simulating events used throughout this thesis. A thorough discussion of the heaviest observed elementary particle, the top quark, is then presented in Section 2.4. Finally, the *dead-cone* effect is introduced in Section 2.5. The effect was predicted over forty years ago, but has never been measured experimentally.

2.1 The Standard Model of particle physics

Particles described by the SM are classified by their intrinsic angular momentum, or spin, as one of the following:
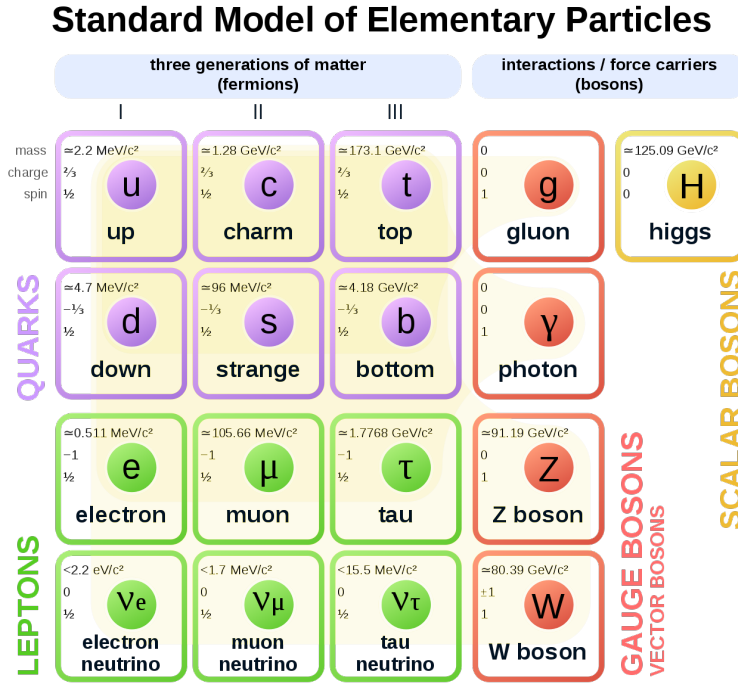
Figure 2.1: The fundamental particles that compose the standard model of particle physics, grouped together by type. The fermions are arranged in three generations by mass [10, 11].

- **Fermions** - particles with half integer spin.

- **Bosons** - particles with integer spin.

The SM describes twelve fermions, three fundamental forces of nature, and the Spin-0 mediator known as the *higgs boson*. The charges, masses and spin of the particles in the SM are shown in Figure 2.1. The three fundamental forces of the SM are the electromagnetic, weak, and strong force described by Quantum Electrodynamics (QED), the Glashow-Salam-Weinberg (GSW) model of electroweak interactions [6–8], and Quantum Chromodynamics (QCD) respectively [9].

The twelve fermion fields of the SM are classified by their couplings to the three fundamental forces of nature into:

- **Leptons:** There are six leptons described by the SM, which can be further classified by their properties. The *charged* leptons carry an electromagnetic charge of $Q = \pm 1$, given in units of the electron charge. The charged leptons can be classified into the following *flavours*, ordered in increasing mass: $e^{\pm}, \mu^{\pm}, \tau^{\pm}$. For each charged lepton, there exists a neutral charged *neutrino* of flavour: ν_e, ν_μ, ν_τ. The SM does not currently encode mass terms into the neutrino sector. However, neutrinos have been observed to oscillate between three flavour states as they travel [12, 13]. Such an oscillation implies that neutrinos have a non-zero masses and measurements of the mass of the neutrino fields have been performed. The sum of the mass of all neutrinos has been measured to be below $\sim 0.2\,\text{eV}$ at 95%

confidence level from cosmological studies [10], orders of magnitude lower than all other standard model particles.

- **Quarks**: There are six types, or *flavours*, of quarks categorised into *up-* and *down-*types. Up-type quarks have an electromagnetic charge of $Q = +2/3$, whereas down type quarks have an electromagnetic charge of $Q = -1/3$. There are three generations of up-down pairs of quarks. In ascending mass these are: (u, d), (c, s) and (t, b). All quarks carry colour charge, and therefore interact via the strong force. This interaction is described by QCD, which is discussed in detail in Section 2.2.

The fundamental forces of nature are mediated by spin-1 vector gauge bosons: the electromagnetic force is mediated by the photon, γ; the weak force is mediated by the W^+, W^- and Z^0 bosons; and the strong force is mediated by the gluon, g. The photon and gluon are massless vector fields, whereas the vector bosons that mediate the weak force have large non-zero mass.

2.1.1   The electro-weak sector of the SM

The interaction between the charged leptons and the photon was first described in a QFT framework by Schwinger and Feynman [14], who pioneered Quantum Electrodynamics (QED). In parallel to the advancement of QED, the weak force was studied and understood. The Fermi interaction is a historic description of the weak interaction, where the weak force was modelled as four-point contact interaction. Heavy vector bosons that mediate the weak interaction were originally introduced to mitigate the high energy divergence of the Fermi interaction. The massive weak bosons couple to left-handed chiral fermion field doublets

$$\begin{pmatrix} u \\ d \end{pmatrix}_{\mathrm{L}} \begin{pmatrix} \nu_\ell \\ \ell \end{pmatrix}_{\mathrm{L}},$$

which transform under the special unitary group SU(2) as doublets. The right handed fermion fields transform as SU(2) singlets and do not interact with the weak massive vector bosons. This difference in transformation of the left and right-handed fermion fields means that the traditionally used Lagrangian mass terms are forbidden [15]. A new mechanism to generate the mass terms for the fermion fields is needed, to replace the now forbidden mass term.

The GSW model unifies the electromagnetic force described by QED with the weak force [16–18] as the *electroweak* force. The GSW model introduces a scalar field that undergoes spontaneous symmetry breaking (SSB), whereby the initial gauge symmetry of the model is reduced. The scalar field generates mass terms for fermions and the weak vector bosons, and the corresponding scalar boson is known as the *higgs* boson. This spontaneous symmetry breaking of a gauge symmetry was postulated by Brout,

Englert and Higgs [19, 20] as a mechanism to generate mass. The Higgs boson was experimentally confirmed in 2012 by the ATLAS and CMS experiments [21, 22].

The weak charged current, mediated by the $W^{\pm}$ boson, provides the Standard Model a mechanism to change the flavour of quarks and leptons. The weak interaction couples to flavour eigenstates, instead of the mass eigenstates of QED and QCD. The mixing of the quark flavours by the weak interaction is governed by the CKM matrix, and given by

$$
\begin{pmatrix} d' \\ s' \\ b' \end{pmatrix} = V_{\mathrm{CKM}} \begin{pmatrix} d \\ s \\ b \end{pmatrix} = \begin{pmatrix} V_{ud} V_{us} V_{ub} \\ V_{cd} V_{cs} V_{cb} \\ V_{td} V_{ts} V_{tb} \end{pmatrix} \begin{pmatrix} d \\ s \\ b \end{pmatrix} ,
\tag{2.1}
$$

where V_{CKM} is the unitary CKM matrix, and (d, s, b) are the mass eigenstates of the down-type quarks [10]. There are four degrees of freedom in the CKM matrix. Three of these degrees of freedom correspond to quark mixing angles, which govern the relative probability of up and down type electroweak quarks decays. The fourth degree of freedom in the CKM matrix corresponds to a complex phase, which generates Charge-Parity (CP) violating processes in the Standard Model [23].

2.2 Perturbative QCD and collider physics

Gell-Mann and Zweig postulated the existence of colour-charged quarks that carry fractional electromagnetic charge [24, 25], after first organising the growing number of new hadrons (particles composed of quarks) that were observed experimentally [9] by their flavour symmetries. The colour charge and its interactions is described by Quantum Chromodynamics (QCD).

The QCD Lagrangian density for quarks and the gluon vector boson can be written as [26]

$$
\mathcal{L}_{\mathrm{QCD}} = \sum_f^{n_f} \bar{q}_f^i (i\gamma^\sigma D_\sigma - m_f)_{ij} q_f^j - \frac{1}{4} F_{\mu\nu}^a F_a^{\mu\nu} ,
\tag{2.2}
$$

where q_f and $\bar{q}_f$ are the quark and anti-quark fields, of which there are n_f flavours with mass m_f. The covariant derivative is defined as

$$
D_\sigma = \mathbb{I}\partial_\sigma - ig_s t^a A_\sigma^a ,
\tag{2.3}
$$

where g_s is the strong gauge coupling constant for QCD interactions and A_σ^a is a component of the gluon field. The generators of the SU(N_C) symmetry group are t^a, where $N_c = 3$ for QCD and a is the colour index for the gluon field. The non-Abelian field strength tensor, $F_{\mu\nu}^a$ in Equation 2.2, is defined by its commutator $[D_\mu, D_\nu] = -ig_s t^a F_{\mu\nu}^a$, giving

$$
F_{\mu\nu}^a = \partial_\mu A_\nu^a - \partial_\nu A^{\mu a} + g_s f^{abc} A_\mu^b A_\nu^c ,
\tag{2.4}
$$

where f^{abc} are the SU(N_c) structure constants. The last term in Equation 2.4 is a direct consequence of the non-Abelian nature of the SU(N_c) symmetry group, and corresponds to gluon self interaction.

The Lagrangian density given in Equation 2.2 must be invariant to gauge transformations of its fermion fields [15]. This requirement on the Lagrangian implies it has additional degrees of freedom, compared to the physics it describes. These additional gauge degrees of freedom are removed with the introduction of an additional gauge fixing term to the Lagrangian, in the form

$$\mathcal{L}_{\text{G.F}} = -\frac{1}{2\lambda}(\partial^\alpha A_\alpha^a)^2 \ , \tag{2.5}$$

where λ is a gauge fixing parameter. To remove all remaining longitudinal degrees of polarisation from the gluon propagator the additional term $\mathcal{L}_{\text{G.F}}$ must be accompanied by a Faddeev-Popov "ghost" term. This introduces a complex-scalar "ghost" field, χ_a, which couples to gluons inside loop diagrams [26]. Beyond this discussion, ghost fields are not considered further in this thesis.

2.2.1   Properties of the SU(N_C) group

The QCD Lagrangian is invariant under SU(N_C) transformations of it fields, where $N_C = 3$. To understand QCD it useful to first understand the properties of this symmetry group. The SU(N_C) symmetry group consists of unitary objects, U, with $\det(U) = \pm 1$ [27]. The number of generators for a generic $SU(N_c)$, symmetry group is $N_C^2 - 1$. Therefore, the elements of this group are spanned by a basis of $N_C^2 - 1$ generators denoted as $\mathbf{T}^a$, where $a \in \{1, ..., N_C^2 - 1\}$. An arbitrary element of the SU(3) group can be expressed generically as

$$U = \exp\left\{i\theta^a \mathbf{T}^a\right\} \approx \mathbb{I} + i\theta^a \mathbf{T}^a + \mathcal{O}((\theta^a \mathbf{T}^a)^2) \ , \tag{2.6}$$

for small θ^a. One can show that the generators $\mathbf{T}^a$ are traceless and hermitian using Equation 2.6 and the unitarity property of $\mathbf{T}^a$.

The generators of the SU(N_C) symmetry group forms a Lie Algebra under the commutator

$$[\mathbf{T}^a, \mathbf{T}^b] = i f^{abc} \mathbf{T}^c \ , \tag{2.7}$$

where f^{abc} are the structure constants of the algebra which is totally asymmetric under exchange of its indices and of unit size. The non-zero structure constants of the algebra shows that SU(N_C) is a non-commutative, or non-Abelian, group.

The generators are normalised according to the convention

$$\text{tr}(\mathbf{T}^a, \mathbf{T}^b) = T_R \delta_{ab} \ , \tag{2.8}$$

where T_R is the normalisation constant for a particular representation.

Group representations

The colour factors, C_F and C_A, determine the relative probability for a quark or a gluon to couple to a soft gluon respectively. The difference in coupling strength between quarks and gluons is a fundamental property of QCD and arises from the transformation properties of the quark and gluon fields. The values of C_F and C_A shall now be evaluated.

The generators of a group have dimension M, and can be represented by matrices of dimensions $N \times L$; the choice of M defines the representation of the group. There are two natural choices:

- $N = L = N_C$: The fundamental representation, with normalization $T_R = \frac{1}{2}$.

- $N = L = N_C^2 - 1$: The adjoint representation, with normalisation $T_R = N_C$.

For an arbitrary representation, R, the *Casimir operator* which takes the quadratic form $T^2 = \mathbf{T}^a \mathbf{T}^a$ can be defined. By Schur's lemma $T^2 = C_R \mathbb{I}_R$ [27, 28]. The proportionality constant C_R can be evaluated by considering the trace of the operator T^2

$$\mathrm{tr}(\mathbf{T}^a \mathbf{T}^a) = \begin{cases} \delta_{ab}\mathrm{tr}(\mathbf{T}^a \mathbf{T}^b) = \delta_{ab} T_R \delta_{ab} = T_R \delta_{aa} = T_R \mathrm{dim}(G) \\ C_R \mathrm{tr}(\mathbb{I}_R) = C_R \mathrm{dim}(R) \ , \end{cases} \tag{2.9}$$

where $\mathrm{dim}(G)$ is the dimension of the group. Therefore,

$$C_R = T_R \frac{\mathrm{dim}(G)}{\mathrm{dim}(R)} \ . \tag{2.10}$$

For the $\mathrm{SU}(N_C)$ group the dimension is simply $N_C^2 - 1$, which is naturally fixed for any representation. Therefore the two representations have Casimir constants given by

$$C_F = \frac{N_C^2 - 1}{2N_C}, \tag{2.11}$$

$$C_A = N_C. \tag{2.12}$$

Taking $N_C = 3$, as shown from measurement, gives the colour factors

$$C_F = \frac{4}{3}, \tag{2.13}$$

$$C_A = 3. \tag{2.14}$$

2.2.2   Scattering amplitudes and the Feynman rules

To make predictions of a generic QFT, defined by its Lagrangian, a scattering amplitude is required. The scattering amplitude connects initial quantum state $|i\rangle$ to the final quantum state $|f\rangle$. The initial state must be evolved in the time domain into the final

state from a point in the distant past $-T$ to a point in the far future T. The time evolution operator for $T \to \infty$ is given by [15]

$$\hat{S} = \mathrm{T} \left\{ \exp \left[i \int d^4 x \mathcal{L}_{\mathrm{int}} \right] \right\} \tag{2.15}$$

$$S_{fi} = \langle f | \hat{S} | i \rangle , \tag{2.16}$$

where $\mathcal{L}_{\mathrm{int}}$ is the interacting Lagrangian density of QFT in position space at position x and T is the time ordering operator, which arranges fields it acts upon chronologically. In general, S_{fi} is not calculable in exponential form. Instead, a perturbative expansion around the non-interacting case is performed. The transition matrix for this expansion is defined as

$$iT_{fi} = \langle f | \hat{S} - \mathbb{I} | i \rangle = (2\pi)^4 \delta^{(4)} (\sum k_i - \sum p_i) i\mathcal{M}_{fi} , \tag{2.17}$$

where the δ function conserves momentum between the initial and final states, k_i and p_i, respectively. The invariant amplitude $\mathcal{M}$ is known as *the matrix element*, and is often represented using graphical analogues known as *Feynman diagrams*. The complete set of Feynman diagrams that span a perturbative expansion are known as the *Feynman rules*. For the QCD Lagrangian these are given in Table 2.1.

The *cross section* for a scattering process, an experimentally measurable quantity, can be defined using the amplitude $\mathcal{M}$ as

$$d\sigma = \frac{|\mathcal{M}|^2}{\mathcal{F}} (2\pi)^2 \delta^{(4)} (\sum k_i - \sum p_f) d\Phi_n , \tag{2.18}$$

where the flux factor, $\mathcal{F}$, is proportional to the number of incoming particles. The quantity $d\Phi_n$ is the differential phase-space of n final state particles. Integration over this phase-space sums over all possible out going final state particle kinematics.

2.2.3   Running of the strong coupling constant

The perturbative expansion of the transition matrix is typically ordered in terms of the coupling constant, α_s. In perturbative QCD calculations which contain one loop or more, typically occurring at order α_s^2 or higher, divergent diagrams occur. Renormalisation is the systematic cancellation of the divergent contributions to a calculation needed to derive a finite prediction. After performing a renormalisation procedure, the coupling constant has a dependence on energy. The renormalized "running" of the coupling constant relates the coupling at scale Q to the coupling at a different scale μ, and at one loop level is given by [26]

$$\alpha_s(Q^2) = \frac{\alpha_s(\mu^2)}{1 + \beta_0 \alpha_s(\mu^2) \ln(Q^2/\mu^2)}. \tag{2.19}$$

The scale dependence of α_s is introduced by loop corrections. The term β_0 is the one loop contribution to the perturbative calculation of the QCD *beta function*, which
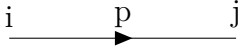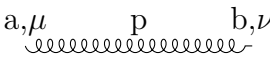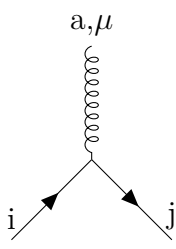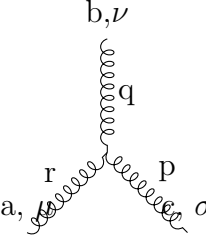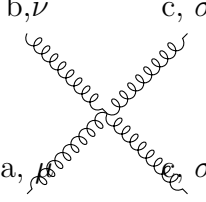
$$\delta_{ij}\frac{i(\not{p}+m)}{p^2-m^2+i\epsilon}$$

$$\delta_{ab}\frac{i}{p^2+i\epsilon}\left[-g_{\mu\nu}+(1-\lambda)\frac{p_\mu p_\nu}{p^2+i\epsilon}\right]$$

$$-g_s\gamma^\mu t_{ij}^a$$

$$-g_s f^{abc}[(p-q)^\sigma g^{\mu\nu}+(q-r)^\mu g^{\nu\sigma}+(r-p)^\nu g^{\sigma\mu}]$$

$$-ig_s^2[f^{xba}f^{xcd}(g_{\mu\kappa}g_{\nu\sigma}-g_{\nu\kappa}g_{\sigma\mu})$$
$$f^{xbd}f^{xca}(g_{\mu\kappa}g_{\nu\sigma}-g_{\nu\mu}g_{\sigma\kappa})+$$
$$f^{xbc}f^{xad}(g_{\mu\mu}g_{\sigma\kappa}-g_{\nu\kappa}g_{\sigma\mu})]$$

Table 2.1: The Feynman rules for propagators and vertices in QCD excluding ghosts. Gluons are represented by curly lines, quarks are represented by solid lines. The momenta in the three gluon vertex is defined as incoming, i.e $p+q+r=0$ [26].

describes how the QCD coupling strength changes with respect to energy scale. It is given by

$$\beta_0 = \frac{1}{4\pi} \left[\frac{1}{3} \left(11 C_A - 4 T_R n_f \right) \right] , \tag{2.20}$$

where n_f is the number of active quark flavours at the energy scale Q^2 with mass $m_f^2 < Q^2$. The number of active quark flavours is always less than $11 C_A / (4 T_R) \sim 17$, therefore β_0 is positive for all energy scales.

The running of α_s at one-loop accuracy in QCD, has two key properties:

- **Asymptotic freedom:** For increasing energy (decreasing length) scale the interaction strength of QCD *decreases* [29]. This property is clear from the positive definiteness of β_0 and the running of α_s at one loop accuracy, given in Equation 2.19. The one loop prediction for the strong coupling constant in the limit $Q^2 \to 0$ is $\alpha_s \to 0$.

- **Confinement:** For decreasing energy (increasing length) scale the interaction scale of QCD *increases*. Colour charges can therefore not be separated by long distances. Furthermore, for low energy QCD becomes non-perturbative as $\alpha_s(Q^2) > 1$. This is known as confinement. Confinement has not been analytically proven in perturbation theory from the QCD Lagrangian, but is strongly supported experimentally [26, 30].

2.2.4   The parton model and factorisation

Due to confinement, colour-charged particles cannot exist in a final state. Hadrons are colour-neutral composite particles of two or more bound quarks. The colour-charged constituents of a hadron are referred to as *partons*, and in perturbation theory are modelled as free particles within the hadron [31, 32]. In addition to the bound, or *valence*, quarks that define the hadron, there are also *sea quarks* arising from virtual gluon splittings to $q\bar{q}$ pairs. Sea quarks are always re-absorbed by the gluon field, such that colour is conserved and the hadron is colour neutral.

The so-called hard scatter interaction between two partons can be factorised from the soft non-perturbative physics of the hadron and the parton dynamics. A hard process has large momentum transfer, whereas a soft process occurs at low energy scales relative the centre of mass energy, $\sqrt{s}$. These two physical regimes correspond to different length scales; the long length scale of the soft dynamics cannot resolve the short length scale of the hard scatter interaction and therefore factorises.

Using the factorisation of long and short range interactions, the *cross section* for some hard process $pp \to X$ is given by [26]

$$d\sigma_{pp \to X} = \int dx_1 f_a(x_1, \mu_F^2) \int dx_2 f_b(x_2, \mu_F^2) d\hat{\sigma}_{ab \to X}, \tag{2.21}$$

where $\hat{\sigma}_{ab} \to X$ is the short range $2 \to N$ scatter between partons a and b and is calculated using Equation 2.18. The function $f_i(x, \mu_F^2)$ describes the likelihood that a parton of flavour i carries a fractional energy x of the colliding parent hadron, and is known as the *parton density function* (PDF). In order to prevent double-counting when calculating first order contributions in α_s, a factorisation scale, μ_F, is introduced that divides initial-state emissions into two classes: those that are part of the hard scatter process and those that are part of the non-perturbative PDF.

2.2.5   The Parton shower

Measurements of QCD processes rely on understanding a collimated shower of particles that are produced by colour-charged partons produced in a hard scatter process. This subsection describes a method to predict and understand these showers.

A generic hard process with two massless quarks in the final state can be used to understand a parton shower. Let the quarks have four-momentum p_1 and p_2, illustrated in Figure 2.2. It can be shown, that the emission of a soft real gluon, with four-momentum k, has a differential cross-section of the form [33]

$$d\sigma_{qqg} = g_s^2 C_F \int \frac{d^3k}{(2\pi)^3 2k_0} \frac{2(p_1 \cdot p_2)}{(p_1 \cdot k)(p_2 \cdot k)} d\sigma_{\mathcal{B}} \ , \tag{2.22}$$

where $d\sigma_{\mathcal{B}}$ is the *Born* cross-section describing the generic hard process which has been left unspecified. The coefficients g_s and C_F correspond to the QCD coupling strength and quark colour factor respectively. The integral in Equation 2.22 has a divergent structure for *soft* ($k_0 \to 0$) or *collinear* ($p_1 \cdot k$ or $p_2 \cdot k \to 0$) radiation. It can be shown, that this divergence is exactly cancelled by the virtual contribution, shown in Figure 2.2b, which has a contribution of the form [33]

$$d\sigma_{qqg} = -g_s^2 C_F \int \frac{d^3k}{(2\pi)^3 2k_0} \frac{2(p_1 \cdot p_2)}{(p_1 \cdot k)(p_2 \cdot k)} d\sigma_{\mathcal{B}}. \tag{2.23}$$

To fully control the divergent structure of collinear and soft radiation in QCD, the virtual contribution *must* be accounted for. As shall be discussed in more detail in later chapters, inexact cancellation between the real and virtual contributions results in large logarithmic structures appearing in the perturbative expansion of an observable. The emissions described in Equations 2.22 and 2.23 factorise from the Born cross-section, therefore the physics of radiation can be described without specifying the hard process.

Now, consider radiation emitted at a wide angle from either of the two hard quarks. Wide angle radiation from either of the final state quarks can only resolve the colour structure of the $q\bar{q}$ pair and *not* the individual particles. In the wide angle limit, the emission probability is proportional to the colour charge of the parent of final state particles 1 and 2, rather than the particles themselves. This is known as *colour coherence*. Due to this colour coherence effect, it can be shown that the radiation pattern from each hard particle 1 and 2 is confined to a cone with angle less than the opening angle of the particles, θ_{12}. This is known as *angular ordering*.
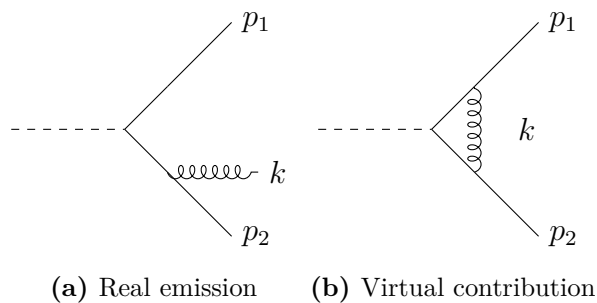
(a) Real emission   **(b)** Virtual contribution

Figure 2.2: An illustration of the diagrams or a generic process with $q\bar{q}g$ in the final state described at order α_s^2.

It can be further shown that collinear radiation factorises from the hard process in the same manner as soft-collinear radiation described above. Using this factorisation and the angular ordering of the radiation, an arbitrary number of emissions from a hard scatter process can be iteratively generated. The differential cross-section for a collinear splitting of a parton $j \to i + k$ is

$$d\sigma_{n+1} = d\sigma_n \frac{\alpha_s}{\pi} \frac{d\xi}{\xi} C_{ij} p_{ij}(z) dz, \tag{2.24}$$

where z is the energy fraction k_0/E_j carried by the daughter parton i. The ordering variable, ξ, is proportional to $(p_j \cdot k_i)/(|p_j||k_i|)$ for emission i. Emissions are ordered such that $\xi_{n+1} > \xi_n$ due to angular ordering. The function $p_{ij}(z)$ is the azimuthally averaged Altarelli-Parisi (AP) splitting functions that describe the probability of splitting for the parton $j \to i + k$, and C_{ij} is the appropriate colour factor for such a splitting. The AP splitting functions describe the splitting probability in the collinear limit. Equation 2.24 can be used to iteratively generate final state radiation from a process with n hard final state particles. This is known as a *parton shower*.

Equation 2.24 contains the collinear and soft QCD divergences discussed in Equations 2.22 and 2.23. These divergences are controlled by introducing a resolution cut-off Q_0 in the integral, such that $z(1-z)\xi > Q_0$, where Q_0 is a small parameter. The cut-off defines the scale at which the parton shower terminates and emissions are no longer considered resolvable. After the parton shower has terminated, the non-perturbative formation of colour neutral hadrons from the products of the shower is evaluated. The formation of hadrons from colour-charged particles is known as *hadronisation*.

2.2.6   Jets

Jets are objects that facilitate the comparison of perturbative QCD predictions to data. Direct prediction of all final state particles measured in a detector is not achievable to high accuracy. Instead, final state particles in a detector are clustered into jets that have a well defined correspondence to a perturbative QCD process of interest. High precision comparisons between data and prediction can then be performed. Jets are defined through a clustering algorithm. Historically, two broad categories of jet algorithms have

been researched: fixed-cone such as SISCone or CellJet [33, 34], and sequential recombination algorithms such as the anti-k_t algorithm. Fixed cone algorithms, in general, can suffer from infra-red and collinear (IRC) unsafety, i.e divergence in perturbative QCD predictions in the soft (infra-red) and collinear regime. There does exist seedless fixed cone algorithms that are IRC safe, such as SISCone [34]. However, due to the computational costs and area properties of seedless fixed cone algorithms they are less well used within experimental collaborations.

Sequential recombination clustering algorithms produce a set of IRC safe jets for a list of initial input entities, $\mathbb{P}$, and a distance metric, d_{iX}. The distance metric defines a distance relation between entities i and X, where $X \in \{j, B\}$ and $j \in \mathbb{P}$. The element B is a special case used to define clustering termination.

The following procedure defines a generic recombination algorithm:

1. Construct a list of the distances d_{ij} between all entities i and j and d_{iB} between i and the beam (B).

2. The smallest element from the distance list is considered, and if the distance is between two four-momenta then they are recombined. Otherwise, i.e if it is a d_{iB} element, then consider entity i a jet and remove it from the list of entities.

3. If there are no elements left in the list stop, otherwise go to step 1.

The definition of the distance metric for a sequential recombination algorithm is the key distinction between several commonly used algorithms. The commonly used set of algorithms known as k_t *clustering algorithms* use the distance metrics

$$d_{ij} = min(k_{ti}^{2p}, k_{tj}^{2p})\frac{\Delta_{ij}^2}{R^2}, \tag{2.25}$$

$$d_{iB} = k_{ti}^{2p}, \tag{2.26}$$

where $\Delta_{ij}^2 = (y_i - y_j)^2 + (\phi_i - \phi_j)^2$ and k_{ti}, y_i and ϕ_i are the transverse momentum, rapidity and azimuthal angle of particle i, respectively. The *radius* parameter, R, controls the extent of the formed jets in (y, ϕ) space. The parameter p defines the following algorithms:

- $p = 0$: The Cambridge/Aachen (CA) algorithm.

- $p = 1$: The k_t algorithm.

- $p = -1$: The anti-k_t algorithm.

The clustering behaviour of these three clustering algorithms differs, because they use different distance metrics. Both CA and k_t clustering algorithms mirror the underlying splitting of QCD. Soft and collinear constituents are preferentially clustered together to form jets. This behaviour makes sense intuitively, however the resultant jets have area properties that are disfavoured by the experimental community.

The area of a jet defines an angular region in (y, ϕ) space around a jet. Soft radiation introduced into an event within a jet's area will be clustered into that jet. Jet area is often used within jet calibration procedures aimed at removing soft contamination [1, 35]. A commonly used definition of the area of a jet is the active ghost associated area. The active ghost associated area is evaluated by filling the input space uniformly with a large number of infinitely soft "ghost" particles. The area of a jet, J, can then be defined for a given ensemble $\{g_i\}$ of ghosts,

$$A(J|\{g_i\}) = \frac{\mathcal{N}_g(J)}{\nu_g}, \tag{2.27}$$

where $N_g(J)$ is the number of ghosts that are clustered into jet J and ν_g is the number density of ghosts introduced to the (y, ϕ) plane.

Introducing infinitely soft ghost particles is a procedure often used within jet physics for *matching* a truth particle to a jet. Therefore, an ideal jet algorithm will have robust behaviour with respect to different ensembles of ghosts. For jets clustered with the CA or k_t algorithms, the active area depends strongly on the exact set of ghosts [36]. This behaviour is a direct result of soft and adjacent constituents clustering before harder constituents. The active area of jets clustered with the anti-k_t algorithm has no dependence on the ensemble of ghosts used, making it ideal for experimental physics. Furthermore, the anti-k_t algorithm preferentially produces conical shaped jets compared to other sequential recombination jet clustering algorithms. Soft contamination from the underlying event in a proton-proton collision, or from nearby proton-proton collisions, are expected to be approximately uniform in the azimuthal plane. Therefore, a jet algorithm with consistently sized and shaped jets, such as anti-k_t, is more amenable to area based soft contamination removal techniques.

2.3 Monte Carlo event generation

The tools to describe a complete proton-proton collision at the LHC have now been established. The physical processes in a proton-proton (pp) collision are factorised, and described in stages by separate simulation tools. Figure 2.3 shows the factorised phases of physics simulation in a typical pp collision. Initially the hard scatter is simulated using a Monte Carlo event generator. For the simulation of a given process, the cross-section defined in Equation 2.18 is integrated over a defined region of phase-space using Monte Carlo methods. Points in phase-space are sampled, which correspond to a set of final state partons. The sampled set of partons are weighted according to their probability of production, allowing a prediction of the full kinematics of the final state to be performed. After that, the parton shower evolves the final state partons of the hard scatter. In Section 2.2.5 the discussion was limited to the showering of colour-charged objects, however QED radiation is also simulated in a generic MC event generator. The generation of QED radiation is often referred to as "dressing" leptons
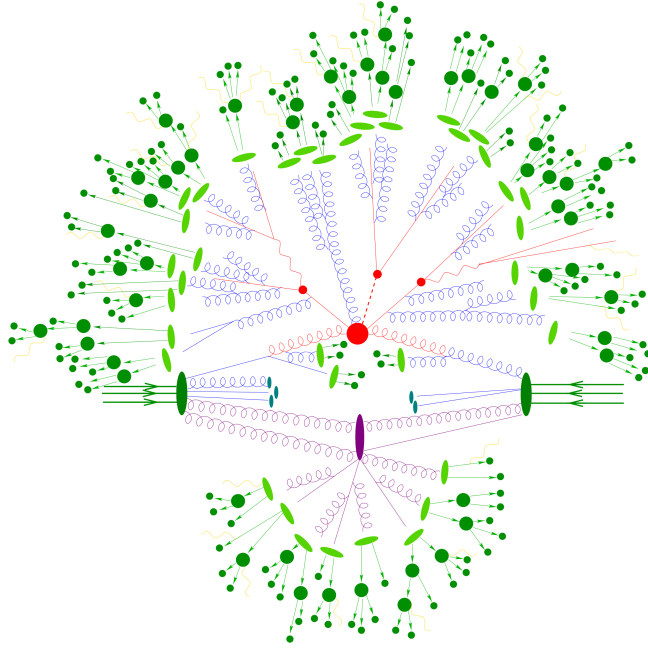
Figure 2.3: A schematic of a typical simulated pp collision. The parts high-lighted in red correspond to the hard scatter matrix element ($pp \rightarrow t\bar{t}H$ in this example). The dark green ellipses correspond to the colliding protons. The purple blob shows a secondary hard scatter event. The dark green circles at the outer edge of the image indicate the final state hadronised products of the interaction [37].

and photons. After the parton shower has terminated, *hadronisation* is simulated and all colour-charged particles are formed into colour neutral hadrons. Finally, the effects of a detector are simulated and the expected read-out from the detector evaluated. Detector simulation is discussed in more detail in Section 3.3. Monte Carlo simulation is used extensively throughout this thesis.

2.4 The Top quark

This thesis aims to understand not only radiation of approximately massless radiators, but also radiation from a system at a non-zero mass scale. The top quark provides a unique avenue to achieve this goal. First discovered in 1995 by the D0 and CDF collaborations at the proton-antiproton ($p\bar{p}$) Tevatron collider [38, 39], the top quark is the most massive particle in the standard model. It's mass is notably at the scale of the electroweak vector boson masses. The most recent measured world average for the top mass is [10]

$$m_{\text{top}} = 173.0 \pm 0.4 \text{ GeV}. \tag{2.28}$$

The large mass of the top quark imparts it with two important properties: it decays to an on shell W boson, the only quark to do so; and it has a very short lifetime. The lifetime of the top is $\mathcal{O}(5 \times 10^{-25})$s, orders of magnitude shorter than that of non-perturbative QCD effects such as a hadronisation, which occurs on time scales $\Lambda_{\text{QCD}} \sim \mathcal{O}(10^{-23})$ s [40].
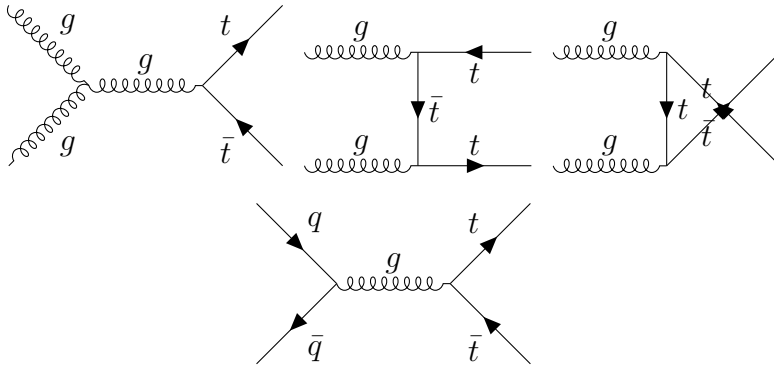
Figure 2.4: The leading order Feynman diagrams for $t\bar{t}$ production in the SM at the LHC. Diagrams with the topologies in the $gg \rightarrow t\bar{t}$ topologies are generically labelled: s, t and u-channel diagrams.

2.4.1   Production

The Large Hadron Collider (LHC) is considered a top factory. On-shell $t\bar{t}$ pairs are produced at rate of $\mathcal{O}(10^7)$ per year at the LHC. Therefore, data recorded at the LHC provides an ideal environment for precision studies of the top quark and its production cross-section. There are two main production modes for top quarks in hadron-collisions: pair production and single top production.

The largest contribution to top quark production is through pair production. The tree level (leading order in perturbative QCD) Feynman diagrams for $t\bar{t}$ production from pp collisions are depicted in Figure 2.4, for both quark-antiquark and gluon-gluon fusion. Gluon-gluon fusion is the dominant production channel at the LHC. It has three production diagrams, known as the $u-$, $s-$, and t-channels. These channels are experimentally indistinguishable, and named after the Mandelstam variables that describe the mass of the virtual particle exchanged in the scattering process [15]. The top quark pair production cross-section has been calculated to next-to-next-to-leading-order (NNLO) in α_s including next-to-next-to-leading-logarithmic soft-gluon contributions (NNLL) as $\sigma_{t\bar{t}} = 832^{+46}_{-51}$ pb at a centre-of-mass energy of $\sqrt{s} = 13$ TeV with an assumed top quark mass of $m_t = 172.5$ GeV [41–46].

Top quarks can be produced in association with either down-type quarks in the s- or the t- channel through vector boson exchange, or with vector boson association (VBA) through a quark exchange. Production of an individual top quark through either of these processes, depicted in Figure 2.5, is known as *single top production*. Single top production in the s- or t- channel has been calculated to next-to-leading order (NLO) in α_s and to NNLO+NNLL for the Wt channel. The cross-sections for these production channels are shown in Table 2.2 for a centre of mass energy of $\sqrt{s} = 13$ TeV. Single top production at the LHC is dominated by the t- channel. VBA has a non-trivial contribution to the single-top production cross-section, whereas s- channel is negligible. The total inclusive single top production cross-section is around 36% of $t\bar{t}$

(a) *s*-channnel   **(b)** *t*-channel   **(c)** Vector-boson association
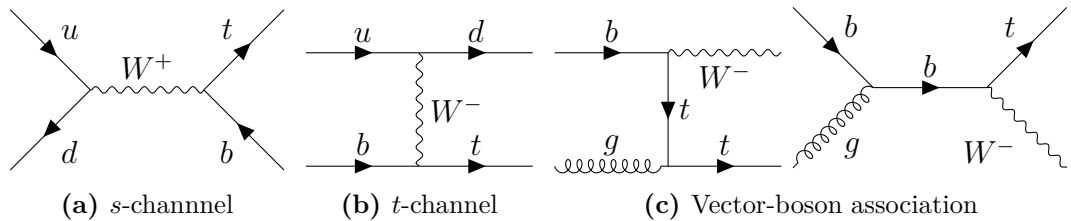
Figure 2.5: The leading order Feynman diagrams for single top production in the SM at the LHC.

Channel	Cross-section σ [pb]
t-channel	$216.99 \pm^{9.04}_{7.71}$
s-channel	$10.32 \pm^{0.4}_{0.36}$
Wt	$71.7 \pm^{3.50}_{3.85}$
Total	$299.01 \pm^{9.83}_{8.63}$

Table 2.2: The production cross-sections for the single top process through the t-channel, s-channel and Wt in *pp* collisions with $\sqrt{s} = 13$ TeV with an assumed top quark mass of $m_t = 172.5$ GeV at next-to-leading order (NLO) in QCD [47–49].

pair production, therefore single top production is an important consideration for any top quark studies performed at the LHC.

2.4.2 Decay

The top quark decays to a W boson and down-type quark. The CKM matrix element V_{tb} governs the strength of flavour changing weak currents between the up-type top quark and down-type bottom quark. The world average measurement of this CKM matrix element is $|V_{\text{tb}}| = 1.019 \pm 0.025$ [10, 50]. Therefore, top quarks decay almost exclusively to a Wb system.

The final-state decay products of a $t\bar{t}$ pair can therefore be understood almost entirely by considering the decay products of the W boson. To a good approximation the decay channels of the W boson can be evaluated by simple counting of the tree level processes. Leptonically, the W decays to an $\ell\nu_\ell$ system, where ℓ denotes the flavour of the lepton. Alternatively, the W can decay to an up-type and down-type quark pair, $q\bar{q}'$. Neglecting Cabibbo-suppressed flavour combinations there are two possible combinations: u, d and c, s.

The W boson is a colour singlet. In order to conserve colour charge, the decay products from a W boson must also be. There are three possible colour singlets that each flavour of $q\bar{q}'$ pair can form. Therefore, quark decays of a given flavour are a factor of 3 times as likely as leptonic decays of a given flavour. The approximate branching ratios are $\mathcal{BR}(W \to \ell\nu_\ell) \sim 3/9$ and $\mathcal{BR}(W \to q\bar{q}') \sim 6/9$. As a top quark almost exclusive decays to a Wb system, the final decay products of the $t\bar{t}$ system can be
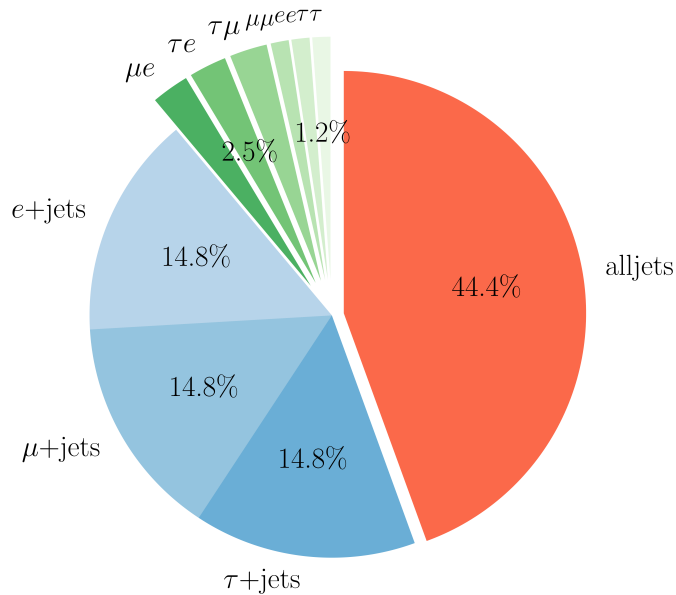
Figure 2.6: The relative branching ratios in percentage points of the final states of a $t\bar{t}$ system for the dilepton (greens), lepton+jets (blues) and all hadronic final state (red).

understood using simple combinatorics.

The decay channels of a $t\bar{t}$ system are typically classified by the number of leptons produced. As the τ lepton decays further via a W boson we take the "experimentalist" definition of leptonic final states, and only consider electrons and muons as leptonic for purposes of top quark decay classification. The branching ratios of the $t\bar{t}$ decay channels are shown in Figure 2.6, and are referred to as: *all hadronic* (or *alljets*) where both W bosons decay as $W \to q\bar{q}'$; *lepton + jets* where one top quark decays leptonically, with a $W \to \ell\nu_\ell$ and the other hadronically, with a $W \to q\bar{q}'$; and finally dileptonic where both top quarks decay leptonically via $W \to \ell\nu_\ell$ decays.

2.5   The Dead-Cone Effect

Radiation of a gauge boson from a massive radiator in any QFT has a characteristic suppression in the collinear region around the radiator. This region is the so-called *dead-cone.* The characteristic angle of suppression, θ_d, is given by

$$\theta_d = \frac{m}{|p|} \sim \frac{m}{E}, \tag{2.29}$$

where m, p, and E are the mass, momentum, and energy of the radiating top quark respectively. The final approximation holds for a radiator with $p_T \gtrsim 2m$. The angle of suppression is typically small for particles produced in collider experiments, as particles are typically produced with a large Lorentz boost. Therefore, the effect has proved challenging to examine experimentally and has never been experimentally observed.

Studying top quarks produced at the LHC provides a unique opportunity to measure a long predicted, but elusive, physical effect of radiation. At a centre-of-mass energy of $\sqrt{s} = 13\,\text{TeV}$ in pp collisions at the LHC, the characteristic angle of suppression for top quarks is almost always larger than the granularity of the detector systems used to measure the final state radiation (FSR) from the final state products of a $t\bar{t}$ system. For example, top quarks are produced with a modal energy of roughly 270 GeV, which corresponds to a dead-cone of size $\theta_d \approx 0.63$. For reference, the relevant granularity scale for detectors at the LHC is 0.1. It is not until the 98th percentile of the top quark energy distribution, where top quarks have an energy $\gtrsim 1500\,\text{GeV}$ that the typical detector systems of experiments at the LHC can no longer resolve the predicted suppression in the radiation of a top quark.

The dead-cone effect can be understood in isolation by considering non-physical stable top quarks produced in e^+e^- collisions. To first-order in the soft and collinear limit, the radiation pattern of a FSR gluon with energy fraction z and opening angle θ is

$$\frac{1}{\sigma}\frac{d^2\sigma}{dzd\theta^2} \cong \frac{\alpha_s}{\pi}C_F\frac{1}{z}\frac{\theta^2}{\theta^2 + \theta_d^2}, \tag{2.30}$$

where α_s is the strong coupling constant, C_F is the colour factor associated with quark to gluon splitting and θ is the angle of radiation between the top and the gluon it emits. The collinear divergence present in massless radiators and discussed extensively in Section 2.2.5 have been removed by the θ_d term. Figure 2.7 shows the relative intensity of radiations from unphyiscal stable top quarks, where the decay of the top quark has not been simulated to provide a clear illustration of the radiation patterns of interest in this thesis. Two radiation patterns are shown: the standard model case, where the mass of the top quark affects the radiation pattern; and the dead-cone "off" case, where top quarks radiate as if they were massless. The top quarks were produced at a centre of mass energy $\sqrt{s} = 2\,\text{TeV}$ in e^+e^- collisions, simulated using the event generator PYTHIA 8.2.24. In the SM "with dead-cone" case, $\Theta = \theta/\theta_d$ is approximately 1. The collinear region of phase-space, $\Theta \lesssim 1$, is suppressed and corresponds to the dead-cone. In the dead-cone off case, radiation from a top quark is most probable in the collinear region of phase-space. The LO prediction Eq. 2.30 has been shown to have good agreement (better than 10%) with NLO fixed-order predictions across a broad range of Θ [51].

2.5.1   Interference effects

As discussed previously, the top quark decays into a Wb system. In order to examine the dead-cone effect, the radiation from a top quark must be distinguished from the FSR radiation of its daughter b-quark. At leading order, two different gluon emission processes can be identified, as shown in Figure 2.8. The signal process which features the dead cone is FSR top quark radiation, corresponding to an excited top emitting a
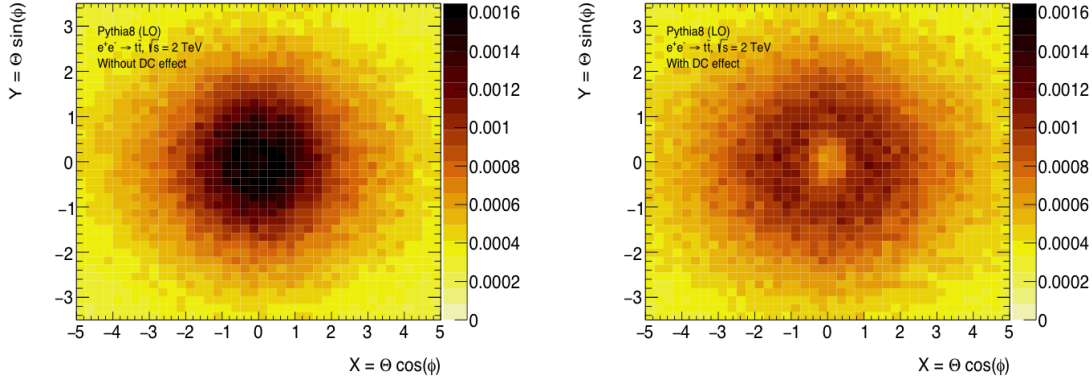
Figure 2.7: The relative intensity of radiation produced by stable top quarks with (left) and without (right) the dead-cone effect produced in e^+e^- collisions at $\sqrt{s} = 2\,\mathrm{TeV}$ where the angle between a radiating gluon and parent top, θ, has been normalized by the characteristic dead-cone angle, θ_d of the radiating top quark for each event.

(a) S   **(b)** B$_1$ **(c)** B$_2$
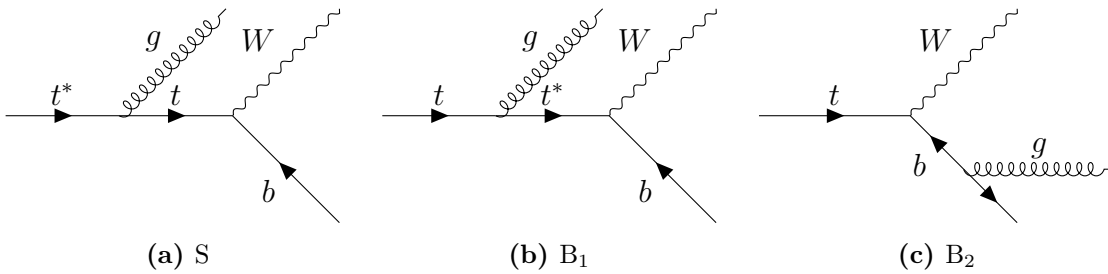
Figure 2.8: Signal (S) and background (B$_{1,2}$) diagrams for top quark decay relevant to this analysis.

gluon and becoming on-shell

$$S : t^* \rightarrow tg. \tag{2.31}$$

This is the process that produces the dead cone distribution in Eq. 2.30. The background process, where the dead cone is absent, is gluon emission during on-shell top decay (see Figure 2.8):

$$B_{1,2} : t \rightarrow bWg. \tag{2.32}$$

Even though diagrams S and B_1 both have an off-shell top propagator, B_1 does not contribute to the dead cone effect. Interference between the signal and background processes is proportional to the top quark width, $\Gamma_t \approx 1.4\,\text{GeV}$. This interference becomes relevant when

$$2p_t \cdot p_g \sim m_t \Gamma_t \tag{2.33}$$

where p_t and p_g are the top and gluon four-momenta respectively. To realise the goal of directly observing the dead-cone the S process must be isolated from both $B_{1,2}$ and the interference of diagrams S and $B_{1,2}$. Furthermore, if the gluon energy is too small, then there is no practical way to distinguish an on-shell top from an off-shell top. In this soft gluon limit the interference between the S diagram and the $B_{1,2}$ diagrams becomes relevant.

The interference effect can be neglected when

$$\frac{E_g}{E_t} \sim \frac{p_{T,g}}{p_{T,t}} \gg \frac{\Gamma_t}{m_t}, \tag{2.34}$$

which for $\Gamma_t/m_t \cong 0.01$ implies $\frac{p_{T,g}}{p_{T,t}} \geq \mathcal{O}(0.1)$. This relation is found using the small angle approximation in the lab frame between the radiative gluon and parent top quark, i.e that $2p_t \cdot p_g \sim E_t E_g \theta_d^2$ for sufficiently small angles.

3. The LHC and the ATLAS experiment

The performance and general design of the Large Hadron Collider and ATLAS detector shall be discussed in this chapter. Section 3.1 details the LHC. The ATLAS detector is then discussed in detail in Section 3.2.

3.1 The Large Hadron Collider

The Large Hadron Collider (LHC) is a 27 km circumference high energy particle collider based at the European Organisation for Nuclear Research (CERN) on the Franco-Swiss border [52]. The LHC accelerates two beams of protons or heavy ions in opposite directions to the highest collision energies ever achieved in a laboratory experiment: $\sqrt{s} = 13$ TeV. This record-breaking centre of mass energy collision was first attained in 2015 with proton-proton collisions.

The LHC tunnel is designed to have eight interaction regions (IR) and eight alternating arcs and straight sections [52]. Four of the IRs are dedicated to instruments to measure beam quality and stability. The other four IRs hold large detectors that collect physics data during LHC operations. The ATLAS (A Toroidal LHC ApparatuS) [53] and LHCf [54] detectors are located at IR1; ALICE (A Large Ion Collision Experiment) [55] is located at IR2; The CMS (Compact Muon Solenoid) [56] and TOTEM (The TOTal, Elastic and diffractive cross-section Measurement) [57] experiments are positioned at IR5 and finally LHCb (LHC beauty) [58] and MoEDAL (Monopole & Exotics Detector At the LHC) [59] are placed at IR8.

The LHC receives protons at an initial energy of 450 GeV from a series of smaller accelerators that serve as the LHC injector chain [60], shown in Figure 3.1. The protons initially originate from a cylinder of hydrogen gas; the hydrogen is ionized by being passed through an electric field. The resultant protons are then accelerated to an energy of 50 MeV in the linear accelerator LINAC2. Afterwards, they are passed through the Proton Synchrotron Booster (PSB) and brought to 1.4 GeV. Protons are then transferred into the Super Proton Synchrotron (SPS). The SPS is the final stage in the injection chain, and accelerates protons to a maximum energy of 450 GeV. After reaching this energy, the protons are injected into the LHC. Radio frequency (RF) cavities accelerate the protons to the beam collision energy: 3.5 TeV in 2011, 4 TeV in 2012, and 6.5 TeV in 2015-2018. The process of beam injection into the LHC takes

approximately 4 seconds; it then takes a further 20 minutes to reach beam collision energy.

Once the beams have reached collision energy they can be brought to collision at the dedicated Interaction Points (IPs) where the detectors are situated. After injection, the beams' relative position is observed; when their relative position is found to be stable and safe, *stable beam* conditions are declared. Once attained, physics data is recorded, typically for 10 hours. Due to beam instability, or reducing the collision rate of circulating beams over time, the beam is periodically extracted from the LHC and safely absorbed into a dedicated beam stop block in a process known as *a beam dump*. The process of injection, acceleration, collision and dumping is referred to collectively as a *fill*.

Within a beam at the LHC, protons are structured into bunches of around 10^{11}. The LHC can be filled with a maximum of 2808 bunches in each ring at the same time. However, due to safety and stability requirements for operational running the maximum achieved is 2556[1]. The bunches are further organised into *bunch trains*, which consist of up to 144 bunches with *bunch spacing* of 25 ns. Trains are separated by between 200 and 1000 ns.

3.1.1 Luminosity and pile-up

A primary parameter of interest to experiments at the LHC is the instantaneous luminosity, $\mathcal{L}$, which is a measure of the rate of collisions. It is given by

$$\mathcal{L} = \frac{n_b f_r n_1 n_2}{2\pi \Sigma_x \Sigma_y}, \tag{3.1}$$

where n_b is the number of colliding bunches, n_1 and n_2 are the number of protons per bunch in beams 1 and 2, respectively, f_r is the LHC bunch revolution frequency, and Σ_x and Σ_y characterise the width of the beam along the x and y axes, respectively. The beam widths Σ_x and Σ_y are measured using Van der Meer (VdM) scans [61], where beams are incrementally separated by a known amount and the interaction rate is measured. The integrated luminosity delivered to each LHC experiment can therefore be written as

$$L = \int dt \mathcal{L}, \tag{3.2}$$

where the integration is over a period of time during which data was recorded.

The LHC delivered proton-proton collisions over the years 2010-2012; this data-taking period is referred to as Run 1 and had a centre of mass energy of $\sqrt{s} = 7$ TeV and $\sqrt{s} = 8$ TeV for years 2010-2011 and 2012 respectively. No further collisions were performed until 2015; this period of time is the first long shut-down (LS1). During

---

[1]This can be seen be examining the 2015, 2016, 2017 and 2018 fill schemes at `https://acc-stats.web.cern.ch/acc-stats/#lhc/super-table`.
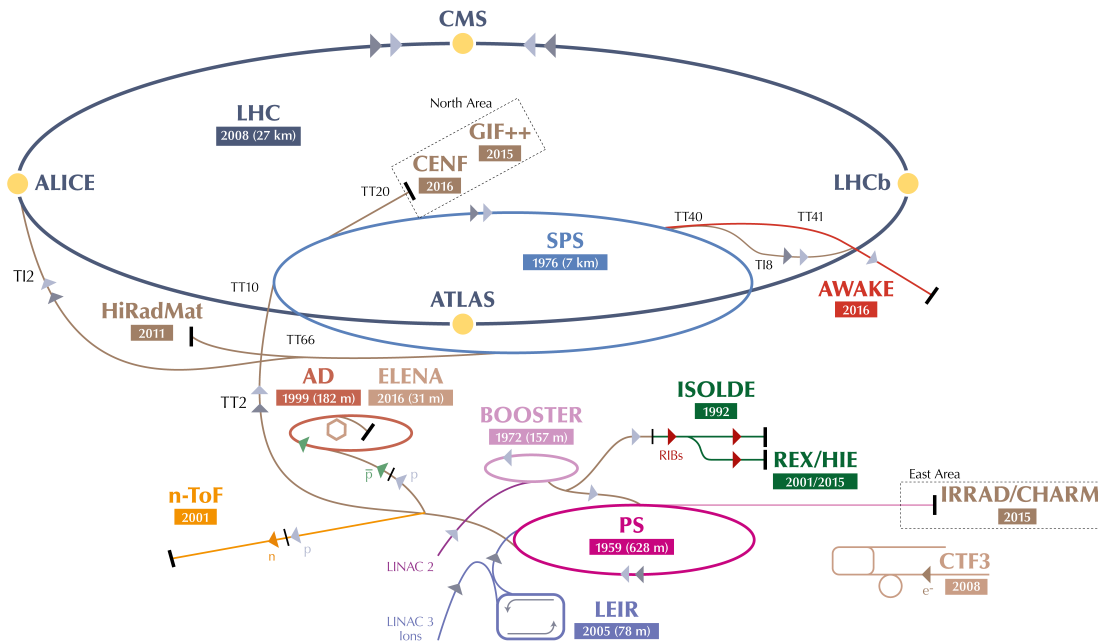
Figure 3.1: Overview of the CERN accelerator complex, including The Large Hadron collider and full LHC injection chain [62].

LS1 the detectors were upgraded and maintained, accounting for the radiation damage taken in their innermost layers. Further to this, the superconducting magnets and their support systems were repaired and consolidated in preparation for high energy running. The LHC delivered proton-proton collisions at a centre of mass energy of $\sqrt{s} = 13$ TeV for the years 2015-2018; this data taking period is referred to as Run 2. The data taken over Run 2 is used for the body of work discussed in this thesis.

As a consequence of the high instantaneous luminosity achieved at the LHC, the rate of additional interactions occurring in a bunch crossing is non-negligible. Additional particles recorded by the detector that originate from *pp* interactions which did not cause the hard-scatter event of interest are known as *pile-up*. There are two cases to consider: *in time pile-up*, where multiple *pp* collisions occur from one bunch crossing; and *out of time pile-up*, where *pp* collisions from multiple bunch crossings cause signals in the detector. The mean number of interactions per bunch-crossing, $\langle\mu\rangle$, quantifies the amount of pile-up for a given run and is a crucial parameter for understanding run conditions. As the instantaneous luminosity was increased throughout Run 2 pile-up became more and more intense, as shown in Figure 3.2. During 2017 running, complications within the LHC machine caused beam stability issues and problematic running conditions. In order to overcome this issue and maintain the planned increase in integrated luminosity for 2017 running, the bunch structure was changed to increase the instantaneous luminosity. This resulted in more pile-up than anticipated and is the source of the peaked structure at $\langle\mu\rangle \sim 55$.
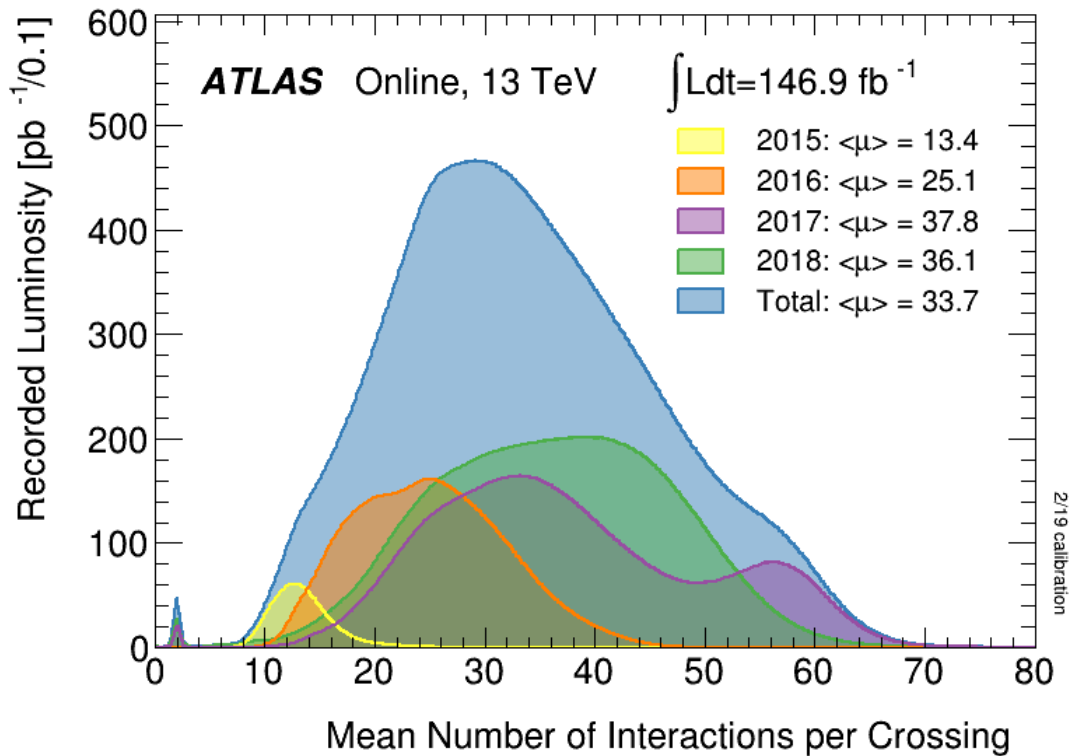
Figure 3.2: The average number of interactions per bunch-crossing, $\langle \mu \rangle$ over the years 2015, 2016, 2017, and 2018 [63].

3.2 The ATLAS Detector

The ATLAS detector is a general purpose detector with forward-backward cylindrical geometry that achieves nearly 4π solid angle coverage around the IP. The stated design goal of the ATLAS detector is an observation of the Higgs boson [64]. However, the generic nature of the detector subsystems allow for a broad range of physics to be studied. The detector is composed of five main subsystems, shown schematically in Figure 3.3: the inner tracking system, the solenoid magnets, the calorimeter system, a set of toroidal magnets, and the muon spectrometer. The near-total solid angular coverage of the detector allows for an accurate measurement of the total energy in an event. From the total recorded transverse energy in an event, the transverse missing energy can be calculated. The transverse missing energy is an important physical quantity, and is discussed further in Section 4.5,

ATLAS uses a right-handed coordinate system with its origin at the nominal IP in the centre of the detector and the z-axis along the beam pipe. The x-axis points from the IP to the centre of the LHC ring, and the y-axis points upwards. Cylindrical polar coordinates (r, ϕ) are used in the transverse plane, where ϕ is the azimuthal angle around the z-axis. The pseudo-rapidity is defined in terms of the polar angle θ as

$$\eta = -\ln \tan(\theta/2). \tag{3.3}$$

Pseudo-rapidity describes the longitudinal boost a massless particle experiences in the
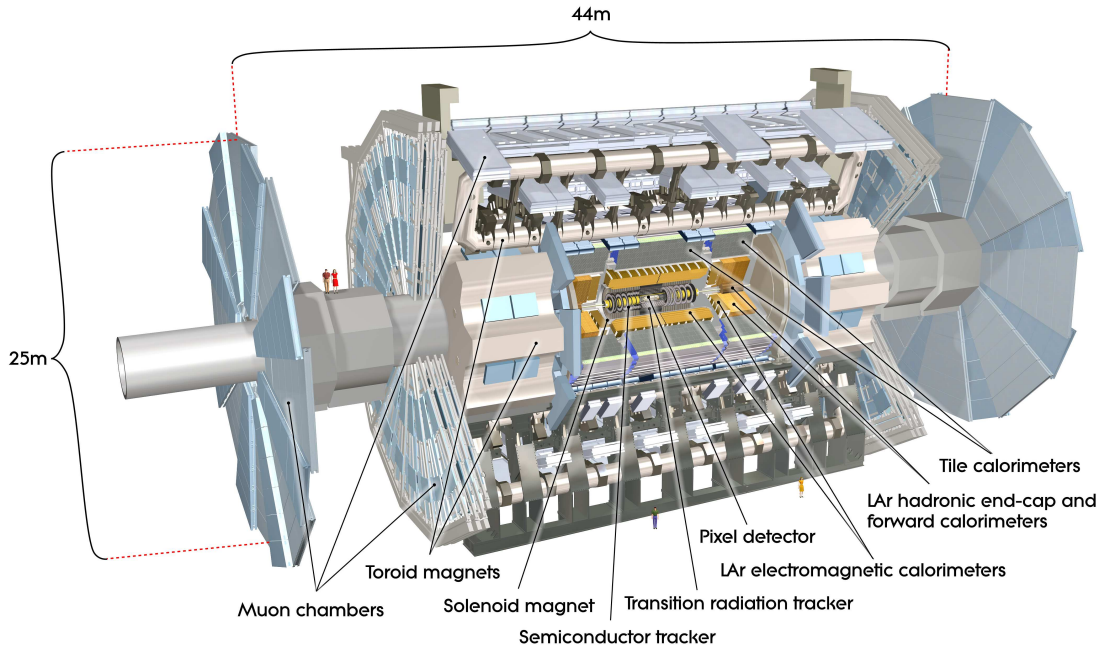
Figure 3.3: Cut-away schematic of the $25\,\mathrm{m} \times 44\,\mathrm{m}$ ATLAS detector [64].

forward direction; in the massless limit it is equivalent to rapidity, $y = \frac{1}{2}\ln\frac{E+p_z}{E-p_z}$, of a particle. Angular distance between two points in the cylindrical (θ, ϕ) plane is measured in units of $\Delta R \equiv \sqrt{(\Delta\eta)^2 + (\Delta\phi)^2}$.

3.2.1 Inner detector

The Inner Detector (ID) measures the trajectory of charged particles within the $|\eta| < 2.5$ region, and provides electron identification within the $|\eta| < 2.0$ region [65]. High precision momentum measurements are achieved through the three complementary and independent detectors that comprise the ID: The Pixel Detector, the Semiconductor Tracker (SCT) [66], and the Transition Radiation Tracker (TRT) [67]. Figure 3.4 shows the trajectory of two particles, without the presence of a magnetic field, as well as the relative layout of the subsystems of the ID, with the exception of the relatively recent additional layer in the pixel detector. Like most subsystems of the ATLAS detector, the subsystems of the ID are a combination of three distinct parts: a barrel in the central region and two endcaps in the forward regions. The momentum resolution of the ID in the central region ($|\eta| < 2.0$) is $p_T \times \sigma(1/p_T) < 0.3$ at $p_T = 500\,\mathrm{GeV}$. In the forward region of the ID ($2.0 \leq |\eta| < 2.5$) the momentum resolution degrades to $p_T \times \sigma(1/p_T) < 0.5$. This difference in performance is a result of the detector material in the central and forward regions of the ID.

The Pixel Detector has a total of four distinct layers in the barrel region ($|\eta| < 1.7$), and three pixel modules in the endcap regions ($1.7 < |\eta| \leq 2.5$). It is constructed of a total of 174444 sensor modules, containing 47232 silicon pixels of size $50 \times 400\,\mu\mathrm{m}^2$ distributed over three outer layers. The innermost layer of the Pixel Detector, known as the Insertable B-Layer (IBL), forms the layer closest to the beam-line at a distance

of 33.25 mm. The IBL was inserted for the start of Run 2 in 2015 to increase vertex reconstruction and tracking performance. As a consequence, the identification of jets formed from the decay of B mesons was improved by the IBL [68].

As a particle passes through a silicon sensor, such as those in the Pixel Detector, it creates electron-hole pairs in the semiconductor material. A bias voltage is applied across the silicon. The voltage induces the electrons and holes in the semi-conductor to flow towards the positively and negatively doped regions of the silicon respectively. This current is read-out by electrons and is registered as a *hit* at the fixed point in space where the sensor is known to be.

The SCT surrounds the Pixel Detector and comprises of four layers of silicon strip modules in the barrel region ($|\eta| < 1.4$) and nine discs in each of the endcaps ($1.4 < |\eta| \leq 2.5$). In total, it is constructed from 15912 sensors across 768 silicon strip modules. Each layer of SCT has double-sided strip modules, where the sides are rotated by 40.0 mrad with respect to each other; the small stereo angle enables a fully three-dimensional measurement. The double-sided design of the strip modules reduces the rate of coincidence hits due to noise faking the expected signal from particles traversing the SCT.

The transition radiation tracker (TRT) comprises of layers of gaseous straw detectors embedded in polymer fibres. The TRT is composed of 73 layers of tubes in the barrel region ($|\eta| < 0.7$) and 160 in the endcap regions ($0.7 < |\eta| \leq 2.5$). The large number of hits per track compensates for the relatively poor resolution compared to the high precision silicon detectors. An aluminium coating of the inner tube surface acts as the cathode and an axially placed tungsten wire acts as the anode. Each straw is filled with a mixture of xenon (70%), carbon dioxide (27%) and oxygen (3%). The polymer fibre that interleaves the straws acts as transition radiation material within the region $|\eta| < 2.0$. As a particle transitions from the polymer to the gaseous tubes it produces high energy transition radiation photons, typically in the X-ray energy regime. These photons are efficiently absorbed by the xenon gas mixture within the tubes, in turn liberating electrons. The transition radiation is detected in addition to the ionised charge carriers liberated from the gas as a particle traverses an individual straw. Since an electron is ultra-relativistic at LHC energy scales, the transition radiation it produces is larger than the less boosted pion. Therefore, the TRT electronics have two thresholds, high and low, to assist in the discrimination between electrons and pions.

The calorimetry system of the ATLAS detector, shown in Figure 3.5, is composed of four sampling calorimeters that provide accurate energy measurements within the $|\eta| < 4.9$ region. The electromagnetic calorimeter (EM) is designed to accurately measure the energy of photons and electrons incident in the detector in the region $|\eta| < 3.9$. The hadronic calorimeter is designed to fully contain collimated showers of charged and neutral particles, known as jets, produced in collisions. Finally, the Forward Calorime-
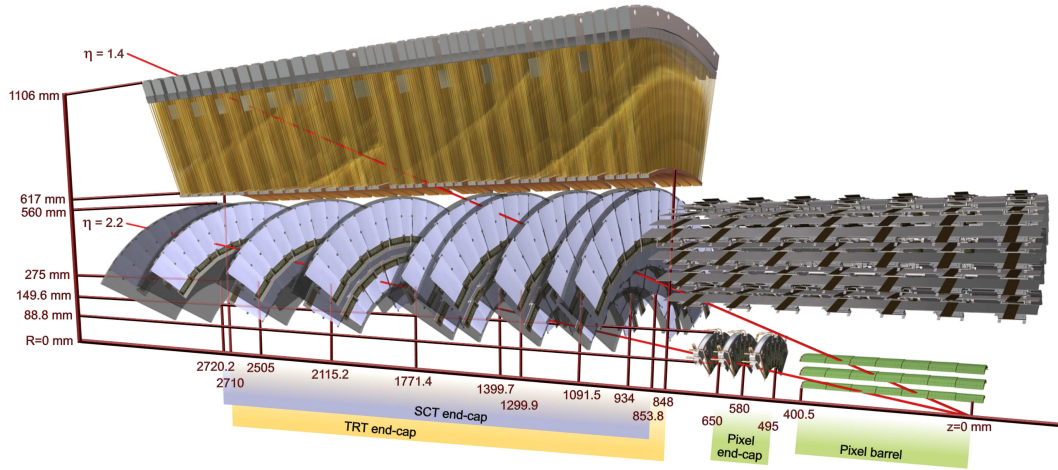
Figure 3.4: Drawing of the Pixel Detector, SCT and TRT subcomponents of the inner detector and their relative placements. The two red lines show the sensors and structural elements traversed by two charged tracks of 10 GeV p_T in the end-cap inner detector ($\eta = 1.4$ and 2.2) in the absence of a magnetic field [64].

ter (FCal) covers the phase-space close to the beampipe in the region $3.2 < |\eta| < 4.9$, providing the near-total hermetic 4π coverage the ATLAS detector requires for calculating the aforementioned missing transverse energy.

Sampling calorimeters consist of layers of active and passive material [69, 70]. The dense passive material induce interactions between an incident particle and the detector, causing a shower of particles. The shower causes either ionisation or scintillation within the active material, which can then be detected and read-out through electronics. ATLAS has both Liquid Argon (LAr) ionisation-based detectors, in particular the FCal and EM calorimeter and parts of the hadronic calorimeter, as well as scintillation-based calorimeters in parts of the hadronic calorimeter.

The EM Calorimeter (ECal) is a LAr-based ionisation calorimeter. The ECal is composed of a barrel calorimeter in the region $|\eta| < 1.475$ and two EM endcap (EMECs) calorimeters covering the regions $1.375 < |\eta| < 3.2$ [71]. The transition region between the barrel and the endcap detectors, $1.37 < |\eta| < 1.52$, is sometimes referred to as the "crack" region as it is not instrumented.

The electromagnetic barrel (EMB) is divided into two identical half-barrels with a 4 mm gap $z = 0$ for the beampipe. The EMB consists of two wheels of 1024 steel clad lead-absorbers, interleaved with the same number of electrodes held in place by a honeycomb structure with a gap size of 2.1 mm. Each EMEC is built out of 256 absorbers for the inner wheel and 768 for the outer wheel. The electrodes are constructed from copper etchings on polyimide and are held a a high voltage compared to the grounded lead absorbers. The ionisation electrons liberated by ionising particles within the LAr have a mean drift time of 450 ns [71].

The EMB and EMEC consist of three layers: the strip, the middle, and the back layer - shown in Figure 3.6. The strip layer consists of strip cells of size $\Delta\eta \times \Delta\phi = 0.003 \times 0.1$. The middle layer consists of cells of size $\Delta\eta \times \Delta\phi = 0.025 \times 0.025$ [64,

Tile barrel

Tile extended barrel

LAr hadronic
end-cap (HEC)

LAr electromagnetic
end-cap (EMEC)

LAr electromagnetic
barrel

LAr forward (FCal)
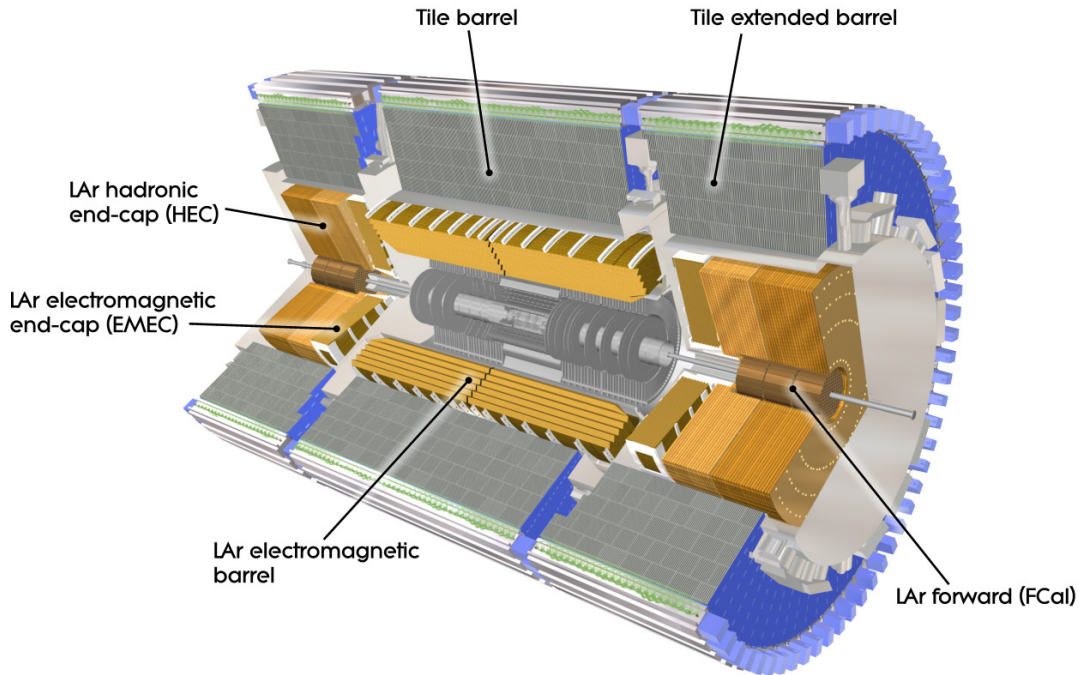
Figure 3.5: Schematic of the calorimeter subsystems of the ATLAS detector [64].

71]. The middle layer is physically the largest layer within the EM calorimeter, corresponding to approximately 16 radiation lengths. The characteristic radiation length, X_0, corresponds to the length after which the number of particles in a shower has doubled. The third layer consists of coarser granularity cells of size $\Delta\eta \times \Delta\phi = 0.05 \times 0.025$, and is intended to provide information about the longitudinal evolution of the shower. In addition to these three layers the EMB has a presampler in the region $|\eta| < 1.8$, which allows for upstream losses in energy of electrons and photons to be measured and corrected for.

Surrounding the EM calorimeter is the hadronic calorimeter. It is a tile sampling calorimeter (TileCal) [72] in the barrel region, $|\eta| < 1.7$, and two identical LAr sampling calorimeters in the range $1.5 < |\eta| < 3.2$ for the hadronic endcap (HEC) calorimetry system. The TileCal uses steel as the absorbing material and scintillating tiles coupled to optical fibers as the active material. Photo-multipliers (PMTs) are attached to the fibers in order to read out the detector activity.

The Forward Calorimeter (FCal) covers the remaining $3.2 < |\eta| < 4.9$ region of phase-space [73]. Its primary design goal is to increase the coverage of the ATLAS detector - affording complete hermetic coverage around the IP. The coverage is necessary for good energy and position resolution of the missing transverse energy signal. A further design requirement of the FCal is a fast response, of order of the beam crossing interval 25 ns [73, 74]. It consists of three modules in each endcap. The first layer consists of copper and LAr and is designed for measuring electromagnetic activity. The last two layers are tungsten and LAr, and designed for measuring hadronic showers. In the first layer absorber rods are situated within copper tubes with a sub-millimeter
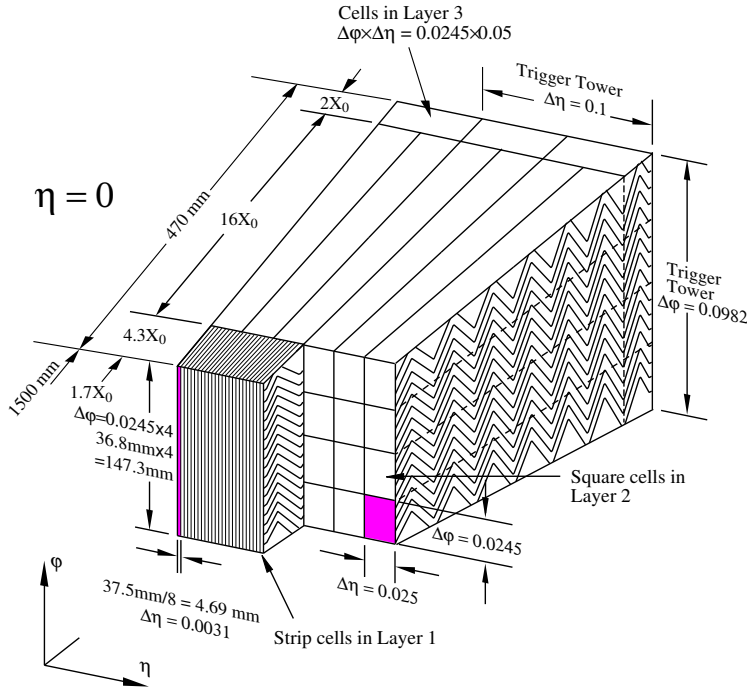
Figure 3.6: A cut-away of the EMB calorimeter showing the three layers that it comprises, as well as the trigger read-out system and presampler. Dimensions of the layers are given in meters as well as characteristic radiation length, X_0, of incident electromagnetically interacting particles [64].

gap. The gap size was chosen to be notably small in order to achieve the design goal of a $\mathcal{O}(25\,\mathrm{ns})$ response; in addition to short response time, the small gap avoids ion build-up caused by the high particle flux in the forward region.

3.2.2 The Magnet Systems

The ATLAS magnet systems, shown in Figure 3.7, are four superconducting magnets, power supply, cryogenics, vacuum system, and the associated control and safety systems needed for these subsystems [75]. The four magnets can be grouped into two categories: solenoid and toroid.

The solenoid magnet is a 5.3 m long cylinder with a bore of 2.5 m placed between the Inner Detector and the Calorimetry systems [76]. It provides a 2 T magnetic field for the central tracking system.

The toroid magnet system is composed of three air core superconducting magnets: the barrel toroid (BT) [77] in the central region, and two endcap toroids (ECTs) [78]. The BT and the ECT all consist of eight flat racetrack coils, each consisting of two double pancake windings housed in a common aluminum alloy casing. Each coil has its own vacuum vessel and each magnet system creates a 4 T magnetic field on the superconductor. The coils are arranged symmetrically around the detector.
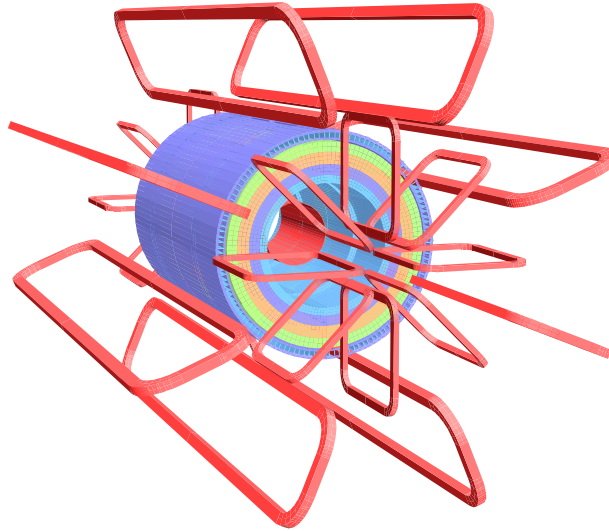
Figure 3.7: The ATLAS magnet system. The toroid system consisting of the BT and ECTS is shown in red. Within the EM calorimeter and TileCal is the solenoid [64].

3.2.3 Muon spectrometer

The Muon Spectrometer (MS) [79], shown in Figure 3.8, comprises of four systems that are used for either high-precision tracking or high-rate triggering (rapid selection of events). Two design goals of the MS were: a total coverage of $|\eta| < 3.0$, and a momentum resolution of 20% or better at a $p_T = 1\,\text{TeV}$. The coverage of MS has a gap at $\eta \sim 0$. The gap is where support systems of the ATLAS detector are located, specifically the support systems for the ID, Calorimeter, and Solenoid Magnet, as well as the feet of the magnet systems.

The two high-precision subsystems are the Monitored Drift Tubes (MDTs) and Cathode Strip Chambers (CSCs). The MDTs are a set of precision chambers in the region $|\eta| < 2.7$. Each chamber is made of a series of $30\,\text{mm}$ diameter tubes of varying lengths from $70\,\text{cm}$ to $630\,\text{cm}$. The active material within the drift tubes is a gaseous mixture of argon (90%), nitrogen (4%) and methane (5%). The large diameter of the tubes results in a maximum drift time of $480\,\text{ns}$, making the MDTs inappropriate for triggering. The tubes are placed transverse to the beam axis to allow for the measurement of coordinates in the bending plane of the toroidal magnets. There are two superlayers of MDTs, each with 3 or 4 layers of tubes. The CSCs comprise the inner layer of the MS in the region $2.0 < |\eta| < 2.7$. They are multi-wire proportional chambers (MWPCs) with an argon, carbon dioxide, and methane mixture as the operating gas, achieving a resolution of approximately $40\,\mu\text{m}$ in the bending plane.

Resistive Plate Chambers (RPCs) in the barrel region of $|\eta| < 1.05$ provide high-rate tracking information used within the trigger system. RPCs are gaseous parallel electrode-plate detectors with an argon (80%) and carbon dioxide (20%) mixture as the active material. The Thin Gap Chambers (TGCs) comprise the endcaps for the high-rate muon tracking systems. These are MWPCs that use carbon dioxide (55%)
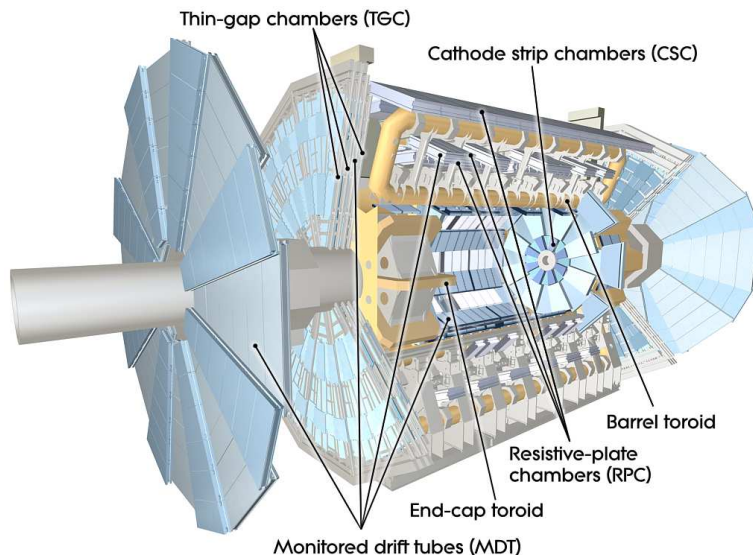
Figure 3.8: Schematic of the muon systems and toroid magnet systems in which the RPCs are embedded [64].

and *n*-pentane (45%) as the active material.

3.2.4 Trigger and data acquisition

The collision rate of protons delivered by the LHC is ~ 40 MHz. In order to read out all detector systems and write the information to disk, the event rate must be reduced to around $1\,$kHz [80, 81]. This limit is imposed by computing and storage constraints [82]. Conveniently, the majority of the *pp* collisions at $13\,$TeV produce soft interactions, which are not the focus of the physics programme within the ATLAS collaboration. These soft interactions do not produce signatures within the detector that mimic signatures of interest.

The ATLAS Trigger and Data Acquisition (TDAQ) systems [83] are designed to efficiently and effectively select and record potentially interesting events for later study. A two-tiered trigger system is used combining hardware and software systems to effectively reduce the event rate to the desired $1\,$kHz.

The Level 1 (L1) Trigger system [84]: The first stage of the TDAQ trigger system reduces the data rate to approximate $100\,$kHz, making decisions within $< 2.5\,\mu$s for Run 2 using custom built hardware with low latency. The L1 system only processes information from a subset of the full ATLAS read-out systems. It uses reduced granularity information from the EM and hadronic calorimeters to search for electrons, photons, taus and jets, as well as large total missing transverse energy. The L1 system also reads activity from the RPCs and TGCs muon system. There are three L1 trigger processors deployed in Run 2: L1Muon, L1Calo, and L1Topo.

The L1Calo trigger is based on dedicated analogue trigger signals from the ATLAS calorimeters. These are independent from the signals utilised by offline reconstruction software. The L1Muon system searches for coincidence hits across multiple layers of

the processed muon trigger system. For each location - or region of interest (RoI) - in a layer there is a pre-calculated window of locations in another layer for which a muon above a certain p_T is expected to produce a coincidence hit.

L1Topo takes the Level-1 trigger objects from the L1Calo and L1Muon triggers. It allows topological selections, combining kinematic information from multiple calorimeter and muon trigger objects, such as angular separation, invariant mass requirements, or global event quantities.

The High Level Trigger (HLT) system [85]: The HLT system refines the L1 selection using the additional information from the full ATLAS detector read-out with the same granularity as offline reconstruction. Object reconstruction is run only in RoIs and therefore reconstruction algorithms differ from the offline algorithms. However, they are constructed as similarly as possible. The final output rate of the HLT system in Run 2 is 1 kHz.

The *trigger menu* is a set of allowed combinations of L1 and HLT trigger selections. There are around 3000 combinations of L1 and HLT triggers that constitute the full trigger menu for Run 2, however, only a subset of these possible combinations are used in any given run.

ATLAS uses a consistent naming convention for all triggers within the trigger menu `<LEVEL>_<OBJECT><`p_T`><EXTRA_INFO>`. `<LEVEL>` specifies the trigger system, either `HLT` or `L1`, `<OBJECT>` specifies the physics object (`e, j` or `mu` for electrons, jets or muons respectively), `<`p_T`>` is the minimum p_T cut in GeV the trigger level object must meet and `<EXTRA_INFO>` describes additional information not fitting this requirement. For example, `HLT_j25` corresponds to an event level requirement of at least one trigger jet with a minimum p_T of 25 GeV. Whereas, `L1_MU20` corresponds to the event level requirement of a L1 muon candidate with at least 20 GeV.

3.3   Detector simulation

The effects of the detector are understood through a detailed simulation procedure. Detector simulation is the final stage in the simulation of events. Two detector simulation procedures are used [86]: GEANT4, known as full simulation (FullSim or FS); and ATLFAST2, known as FastSim or AFII [87]. Detector simulation is performed to high precision with GEANT4. The ATLAS detector and all subcomponents is fully modelled with their true geometry. ATLFAST2 uses full simulation of the Muon Spectrometer combined with ATLAS Fast Calorimeter Simulation (FastCaloSim) for the calorimeter system, and fast ATLAS track simulation (FATRAS) [87]. FastCaloSim is the parameterisation of the calorimeter response, based on the GEANT4 simulation [88]. FATRAS uses simplified reconstruction geometry of the detector to decrease simulation time [89]. As the name suggests, FastSim is computationally less expensive than FullSim detector simulation.

4. Object reconstruction methods

In order to perform physical measurements of particles produced at the LHC, physical objects must be reconstructed from the read-outs of the ATLAS detector. In this Chapter, the primary physics objects used by the ATLAS collaboration are defined and detailed. Charged particle tracks are defined in Section 4.1, followed by the reconstruction of electrons and photons in Section 4.2. The jet reconstruction and calibration procedure is detailed in Section 4.4, and the reconstruction of missing transverse energy in Section 4.5. Finally, a procedure to prevent double counting of recorded energy, known as *overlap removal*, is discussed in Section 4.6.

4.1   Tracks and vertices

Hits in each layer of the Pixel Detector and SCT seed algorithms to reconstruct so-called *tracks* in order to reconstruct the trajectory of particles that have traversed the detector. The track reconstruction algorithm [90] starts at the inner-most layers of the ID and builds tracks radially outward from the beampipe. Track candidates must meet the quality requirements of having at least seven hits across the silicon trackers; no more than one hole in the Pixel Detector; and no more than two holes in the SCT. A hole is defined as a location within a silicon detector where a hit is expected to appear, but is not observed. Track candidates of sufficient quality are projected into the TRT, where the full track is refitted with the hits measured in the TRT.

A vertex is the origin point of a track. After track reconstruction has been performed, the vertices in an event can be reconstructed. Tracks used in vertex reconstruction must pass several additional quality requirements: Tracks must have a minimum transverse momentum of $400\,\mathrm{MeV}$; they must be located within the region $|\eta| < 2.5$; at least one hit in either the IBL or the B-layers of the Pixel Detector; no more than one hole in the SCT; no holes in the Pixel Detector; at least 9 (11) hits in the silicon detectors for $|\eta| \leq 1.65$ ($|\eta| > 1.65$) [91]. The vertex reconstruction algorithm is an iterative procedure. Starting at an initial seed position for a vertex, tracks are used to fit the best vertex position. In each iteration less compatible tracks are down-weighted and the vertex position reconstructed [92]. After the position is fitted, incompatible tracks are removed and used in the determination of another vertex. Vertices are required to have at least two tracks. The algorithm is repeated until there are no unassociated

tracks in the event, or no additional vertices can be found.

The *primary vertex* in an event is defined as the vertex with the largest scalar sum of associated track transverse momentum. The resolution of track reconstruction is understood in terms of the *impact parameters*. The impact parameters, d_0 and z_0, are the closest perpendicular distance between a track to the primary vertex in the transverse and z directions respectively. The impact parameters are often scaled by the inverse uncertainty on their measurement, $\sigma(d_0)$ and $\sigma(z_0)$. Such a scaling results in a dimensionless *significance* of the deviation of a track from the primary vertex, defined as $d_0^{\mathrm{sig}} \equiv d_0/\sigma(d_0)$ and $z_0^{\mathrm{sig}} \equiv z_0/\sigma(z_0)$.

4.2   Electrons and photons

Electrons (and positrons) that traverse the ATLAS detector can leave a track in the ID, and deposit energy in the EM calorimeter. Therefore, the electron reconstruction algorithm must combine the measured energy and momentum from these two separate subsystems in a way that ensures no double counting and maximises resolution. Electrons and positron are collectively referred to as electrons herein.

Energy deposits are clustered together using a *sliding window* algorithm [93]. The EM Calorimeter is divided into a grid in η-ϕ space of size $\Delta\eta \times \Delta\phi = 0.025 \times 0.025$; from this grid *towers* are formed. Towers are sums of energy cells in longitudinal layers of the detector. A fixed window is moved across each element of the tower grid. A *precluster* is formed if the window transverse energy is greater than the threshold value of $2.5\,\mathrm{GeV}$. The window transverse energy is defined as the sum of the deposited transverse energy in all towers in that window. The position of a precluster is computed as the energy-weighted η and ϕ barycentres of all cells within a fixed window around the tower at the centre of the sliding window. Preclusters are used as seeds for EM cluster formation. Cells are assigned to EM clusters by taking all cells within a layer-dependent rectangle around the seeding precluster.

Tracks are then matched to EM clusters. In the cases of multiple candidate tracks matching a cluster, a so-called *primary* track is chosen. The primary track is chosen by evaluating the cluster-track angular distance, R, with differing track momentum hypothesis. The hypothesis with the smallest cluster-track angular distance is chosen [94]. Electron candidates without associated tracks are considered to be photons.

Electron identification algorithms are applied to the candidate electron (track-cluster matches) for all candidates in the region $|\eta_{\mathrm{cluster}}| < 2.47$. Candidate electrons measured in the crack regions between different electromagnetic calorimeter components, $1.37 < |\eta_{\mathrm{cluster}}| < 1.52$, are rejected. The goal of identification algorithms is to distinguish real electron signals from fake electron signals. Fake electron signals arise from hadronic showers that shower strongly in the EM Calorimeter, and from converted (early showering) photons. A multivariate likelihood discriminant is used to distinguish

real electrons from the fake background [94]. The discriminant uses cluster information such as shower shape, information from the TRT, track properties, variables measuring bremsstrahlung effects, and the number of hits in the IBL.

Three levels of identification operating points are provided. Ordered from lowest to highest reconstruction efficiency they are: `Loose`, `Medium` and `Tight` [94]. Lower efficiency identification operating points fully contain higher efficiency operating points, such that all electrons that pass the `Tight` identification requirement also pass the `Loose` and `Medium` requirement. The operating points are defined based on reconstruction efficiency measured in simulated $Z \rightarrow ee$ events. The TIGHT working point is used with an identification efficiency of 78% at $E_\mathrm{T} = 20\,\mathrm{GeV}$ [94].

Two category of electrons are considered: prompt and non-prompt. Prompt electrons originate from heavy resonance decays, such as $W \rightarrow e\nu$, whereas, non-prompt electrons originate from converted photons, heavy flavour decays in hadronic showers and light hadron mis-identification. Electrons originating from a hard scatter process are prompt, therefore prompt electrons are of primary interest in a physics measurement that uses data recorded by the ATLAS detector. *Electron isolation* aims to disentangle prompt electrons from non-prompt.

Isolation variables that characterise the activity of the detector in a cone around the track and EM clusters that constitute an electron are constructed. These variables are measured in $Z \rightarrow ee$ events. From these variables, distinct electron isolation operating points are defined. The isolation efficiency is defined as the number of correctly identified isolated prompt leptons divided by all recorded leptons. The GRADIENT operating point is constructed such that the isolation efficiency has a linear dependence on the transverse energy of the calorimeter and track isolation variables. The GRADIENT isolation working point was used for the work presented in this document. This working point uses a sliding scale isolation which gives an efficiency, $\epsilon(p_\mathrm{T})$, that increases with electron p_T until it reaches a plateau of 100%.

Precise knowledge of the energy scale and resolution of photons and electrons is vital for measurements that use these reconstructed physics objects. Reconstructed electrons and photons are calibrated to mitigate the effect of detector non-uniformity and mis-measurement [95]. A multi-step calibration procedure is used to correct for these effects, and assess the energy scale and resolution of measured photons and electrons. Initially, data-only corrections are applied that equalise the response of the longitudinal layers of the ECal between data and simulation. The uniformity corrections were derived using Run 1 data in 2012, and validated under Run 2 conditions [95].

After detector non-uniformity has been accounted for, the energy scale of measured electrons and photons is corrected. The correction is applied to both data and simulation. A multi-variate regression algorithm calibrates the objects. The regression algorithm corrects for energy deposited in front of the calorimeter and outside of a cluster. Furthermore, the regression algorithm accounts for variations in the measured

energy as a function of the electron direction. Typically, the applied corrections range from a few percent for low-p_{T} electrons, up to $\sim 20\%$ for $100\,\mathrm{GeV}$ electrons. Finally, residual disagreement between data and simulation is measured in $Z \to ee$ events. The residual disagreement is then removed using data-driven correction factors derived from these measurements. The correction factors in the final stage of the calibration chain are applied as energy scale factors to data, and as resolution correction factors to simulation [95].

4.3 Muons

Muon candidates are selected by matching tracks from the Muon Spectrometer (MS) to tracks from the ID [96]. First, hits within an individual MS subsystem's chamber are reconstructed to form a track *segment*. Muon track candidates are then constructed by fitting hits from segments in different layers, starting with segments in the middle layers of the detector, where more trigger hits are available. Segments are matched based on their relative position and angles. The track candidates are extended into the outer and inner layers. Muon track candidates are combined with ID information, typically with an outside-in approach, where MS tracks are reconstructed first and extrapolated inwards to then match with an ID track.

A muon identification procedure is performed to identify prompt muons from non-prompt muons. Non-prompt muons originate from in-flight decays of charged pions or kaons. Non-prompt muon candidates have a distinctive "kink" in their reconstructed track, corresponding to the point in space where the meson decayed. The quality of the fitted track degrades due to the "kink" in the non-prompt muons trajectory. Furthermore, the ratios of measured energy between the ID and MS differs substantially to that of prompt muons. Four muon identification working points are constructed. These use the fit quality and ratio of energy deposited in the ID and MS as input variables. Muon identification efficiencies are studied with a tag-and-probe method in data and simulation $Z \to \mu\mu$ and $J/\Psi \to \mu\mu$ events. An identified muon that satisfies a working point's requirements is used to tag the event, and the other muon is used to measure the efficiency. Efficiency scale factors are calculated that describe deviations of simulation from the real detector behaviour. The calculated scale factors are used to correct for these deviations in simulation, and estimate the uncertainty introduced in a measurement by the muon identification procedure. Of the four calibrated muon identification working points, the MEDIUM muon working point was designed to minimise systematic uncertainties associated with muon calibration and reconstruction. The `Medium` working point was used in the measurements presented in this thesis.

Muon isolation requirements are also imposed on reconstructed muons to discriminate between muons originating from heavy particle decays and those originating from semileptonic decays within a hadronic shower. The detector activity around a muon

candidate is measured and seven isolation working points are provided. The isolation efficiency is measured in data and simulation with the tag-and-probe method, and scale factors are derived to account for deviations. A data- and MC-based calibration is applied to the reconstructed muons to correct the momentum of the measured muons [96]. As with the electron isolation requirements, a so-called GRADIENT operating point is defined such that the isolation efficiency has a linear dependence on the variables used to construct the discriminator. The GRADIENT isolation requirement was used in the measurements presented in this thesis.

4.4   Jets

Jets measured by the ATLAS detector are constructed from three-dimensional *Topological clusters* (TopoClusters) of topologically connected cells within the EM or Hadronic Calorimeter systems [97]. The 4-2-0 scheme is used to construct the TopoClusters [97]. The significance of an observed energy deposit in a cell is considered. The average expected noise of the cell, σ_{cell}, is compared to the energy deposited in a cell, E_{cell}. As the significance is calculated per cell, topological clusters can be composed naturally from cells across different calorimeter systems. TopoClusters are seeded by cells with $E_{\text{cell}} > 4\sigma_{\text{cell}}$. All adjacent cells with $E_{\text{cell}} > 2\sigma_{\text{cell}}$ are added to the TopoCluster iteratively in three-dimensional space until no new cells satisfy the $2\sigma_{\text{cell}}$ requirement. The TopoCluster is completed with a final addition of all adjacent cells satisfying $E_{\text{cell}} > 0\sigma_{\text{cell}}$, removing any negative energy cells that can result from pile-up and electronic noise [98]. The 4-2-0 procedure is repeated for all initial seed cells, forming the complete set of TopoClusters for an event.

TopoCluster directions are constructed from the energy-weighted centroid of the TopoCluster relative to the detector origin. Their energy is taken as the sum of all constituent cell energies, and they are taken to be massless. TopoClusters are measured at the electromagnetic (EM) energy scale, which correctly recovers the energy of an electromagnetic shower. The response of the ATLAS calorimeter system at the EM energy scale has been measured and understood with test beam studies [99–102].

The energy scale of TopoClusters can be refined using the local cluster weight (LCW) scheme [103]. Energy deposits in the calorimeter arise from either hadronic showers or electromagnetic showers. These two categories of particle showers are composed of different particles. Due to the non-compensating nature of ATLAS, the detector response differs between these two categories of particle showers. The LCW energy scale attempts to identify whether a cluster is part of a hadronic or electromagnetic shower, and corrects the energy scale accordingly.

Jets at ATLAS are constructed from TopoClusters using the anti-k_t clustering algorithm with a radius parameter of $R = 0.4$. A multi-step calibration procedure is then applied to each jet, to correct its position, energy and account for non-compensation
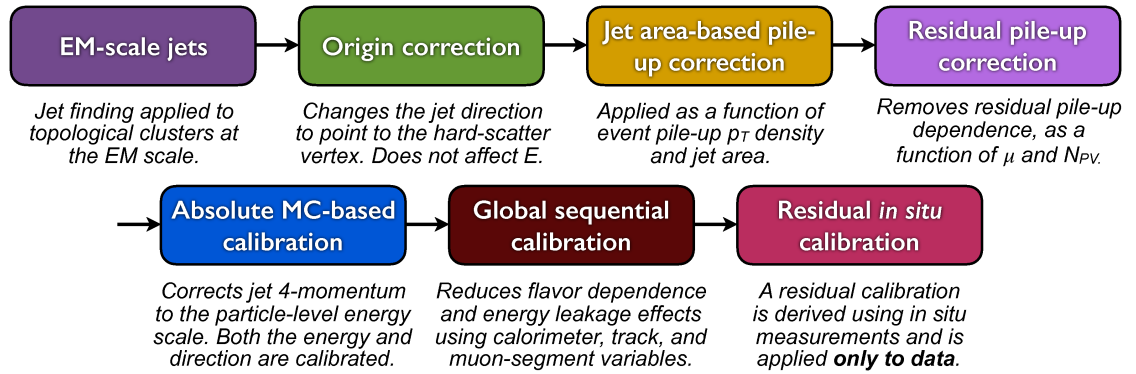
Figure 4.1: The calibration chain applied to $R = 0.4$ jets measured by the ATLAS detector in the years before 2016; after 2016, the origin correction step was performed at the TopoCluster level and not part of the jet calibration sequence [104].

of the detector, shower leakage, dead material in the detector and pile-up.

4.4.1 Jet calibration

The jet calibration chain for $R = 0.4$ jets has the goal of correcting jets to the energy scale of *truth jets*. Truth jets are defined as jets constructed using the anti-k_t algorithm with $R = 0.4$ from detector-stable final-state particles in simulation. Particles are considered stable if their lifetime, τ, satisfies the expression $c\tau > 10\,\mathrm{mm}$, where c is the speed of light. Neutrinos, muons and particles from pile-up activity are excluded from truth jet clustering. Truth jets are considered in the $p_T > 7\,\mathrm{GeV}$ and $|\eta| < 4.5$ region. Detector-level jets, constructed using by applying anti-k_t algorithm to TopoClusters in simulation, are matched to truth jets using the ΔR distance measure. Figure 4.1 shows the calibration chain applied to jets measured in the ATLAS detector. This subsection shall describe in detail the procedures used at each step in the chain.

An *origin correction* procedure is the first stage in the jet calibration chain after TopoCluster formation. The origin of TopoClusters is the geometric centre of the detector. Therefore, initially jets are also reconstructed as originating from the geometric centre of the detector, as used for TopoCluster reconstruction. Origin correction changes the direction of reconstructed jets such that they originate from the primary vertex, as defined in Section 4.1, with the largest scalar sum of constituent track transverse momentum. This increases the η and ϕ resolution of jets, when compared to particle-level truth, but leaves the energy scale unmodified. Origin correction is only necessary for simulation and data processed prior to 2016. The reconstruction software framework within ATLAS was overhauled substantially in the years 2015 and 2016; as part of this overhaul TopoClusters origins were corrected before clustering. This removed the necessity of this state for calibrations derived after 2016.

The next two stages in the calibration chain correct for the effects of pile-up upon jets. First, the pile-up density, ρ, in an event is calculated. The pile-up density in an event is defined as the median p_T^{j}/A^{jet} taken over all jets formed in an event, where

A^{jet} and p_T^{jet} are the area and transverse momentum of a jet in an event respectively. Then ghost associated area, A, of all clustered jets is calculated. The expected amount of pile-up within a jet is given by $\rho \cdot A$, which is used as a subtractive correction factor to the p_T of measured jets. In performing the area-based pile-up subtraction procedure, it is implicitly assumed that the pile-up activity is uniform across the detector. Jets are found to have a residual pile-up dependence after the pile-up subtraction. The dependence is characterised in terms of the average number of interactions per bunch crossing, $\langle \mu \rangle$, and the number of primary vertices in an event, N_{PV}, in bins of η and p_T. The residual dependence is then removed, such that on average $\frac{\partial p_T}{\partial N_{\text{PV}}} = \frac{\partial p_T}{\partial \mu} = 0$.

The fourth procedure applied to reconstructed jets is to correct their absolute energy scale to that of particle level jets. This corresponds to the blue box in Figure 4.1. The energy response is given by

$$\mathcal{R} = \frac{E^{\text{Reco}}}{E^{\text{Truth}}}, \tag{4.1}$$

where E^{Reco} is the energy of a jet at detector level, and E^{truth} is the energy of the ΔR-matched truth jet. The response $\mathcal{R}$ is the inverse of the calibration factor required to correct a jet to the correct truth-level energy scale. The calibration is evaluated in bins of pseudorapidity calculated using the detector centre as the origin, η_{det}, and truth jet energy, E^{truth}. A numerical inversion procedure is applied to the mean of a fitted Gaussian of the binned response distributions, and a calibration derived in terms of η and E^{reco}. At transition regions between detector systems a small bias is observed, as shown in Figure 4.2a. The bias arises from one detector system having a response closer to unity than another, therefore reconstructing part of the jet more completely than the other system. Such a biased reconstruction of energy artificially biases the direction of the jet towards the system with better response, as shown in Figure 4.2b. A second set of calibrations are derived to correct for the difference between η^{reco} and η^{truth}, binned in E^{truth} and η_{det}. The η-calibrations are numerically inverted to provide a calibration in terms of E^{reco} and η_{det}. Jets calibrated with this procedure are often referred to as EM + JES or LCW + JES scale jets depending upon the energy scale of the input TopoClusters.

After the absolute energy scale correction is applied, jets are (on average) calibrated to the appropriate energy scale. However, there remains residual non-closure of gluon-initiated jets compared to quark-initiated jets arising from the differences in energy response between those two jet types. A sequential five step jet-by-jet correction called the *Global Sequential Calibration* (GSC) is applied [35], shown as the brown box in Figure 4.1. The GSC uses the topology of calorimeter energy deposits, properties of the tracks associated with jets, and any associated energy deposits in the muon spectrometer. Jet energy resolution and calibration closure is improved with this correction.

The final stage in the jet calibration chain is a four step data-driven correction procedure called the *in situ* calibration chain. In situ corrections remove residual discrepancies between simulation and recorded data, and are applied to recorded data

(a) The average energy response.

(b) The signed residual bias.
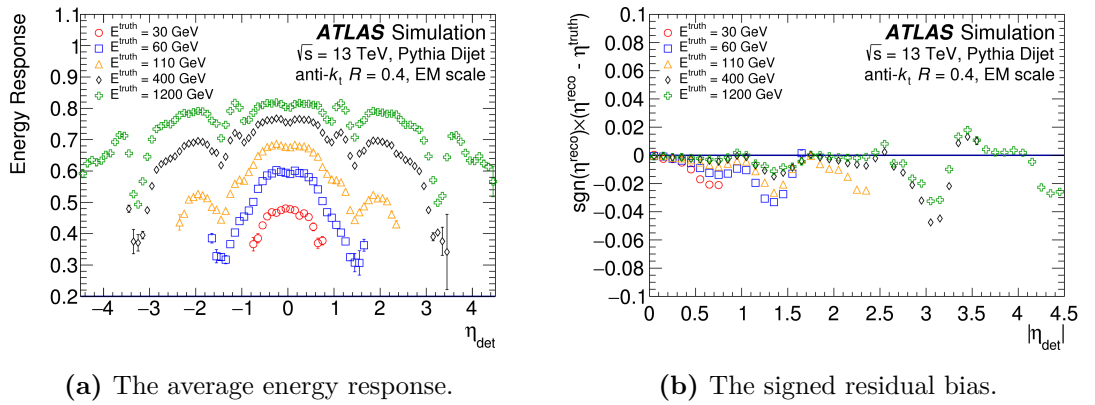
Figure 4.2: The average energy response as a function of η_{det} for truth jets in bins of $E^{truth} \in \{30, 60, 110, 400, 1200\}$ and the the signed residual η_{det} bias of the absolute η JES correction introduces before correction.

only. The p_T response, R_{insitu}, is defined in the same manner as the energy response in Equation 4.1 with the substitution of jet p_T instead of energy. The data-simulation difference is evaluated with the double ratio of a p_T-response as

$$c = \frac{\mathcal{R}_{insitu}^{data}}{\mathcal{R}_{insitu}^{MC}}, \tag{4.2}$$

where c is the correction factor binned in p_T and η_{det}. The p_T-response is evaluated using several different methods, all of which depend on the idea of momentum balance. Due to the conservation of momentum a two body system produced from *pp* collisions at the LHC is expected to have opposite and equal transverse momentum. One of the two objects in a decay is used as *reference*, and measures the expected energy scale of the other object, the *probe*. For instance, a jet is balanced against a photon in the γ+jet event topology. The photon acts as the reference as photons are measured to higher precision than jets by the ATLAS detector.

The first stage of the in situ calibration chain is the dijet in situ η inter-calibration, where a relative calibration factor is applied to jets outside of the central region of the detector, $|\eta| > 0.8$. This stage of calibration aims to calibrate jets such that their response is uniform across the detector. The dijet η inter-calibration is discussed in detail in Section 5.1.1.

After forward jets have their relative response corrected, central jets have a three-stage absolute correction factor applied. Jets in the central region are balanced against Z, γ, or a multi-jet system. The calibration factor c from Equation 4.2 is evaluated in a single bin of $|\eta| < 0.8$. The three different topologies used to derive the absolute in situ calibration of central jets are complementary, each probing a higher p_T regime than the last. They are combined using a global fit and found to have good agreement, as measured by a χ^2 goodness of fit test and depicted in Figure 4.3, for a large range of jet p_T.
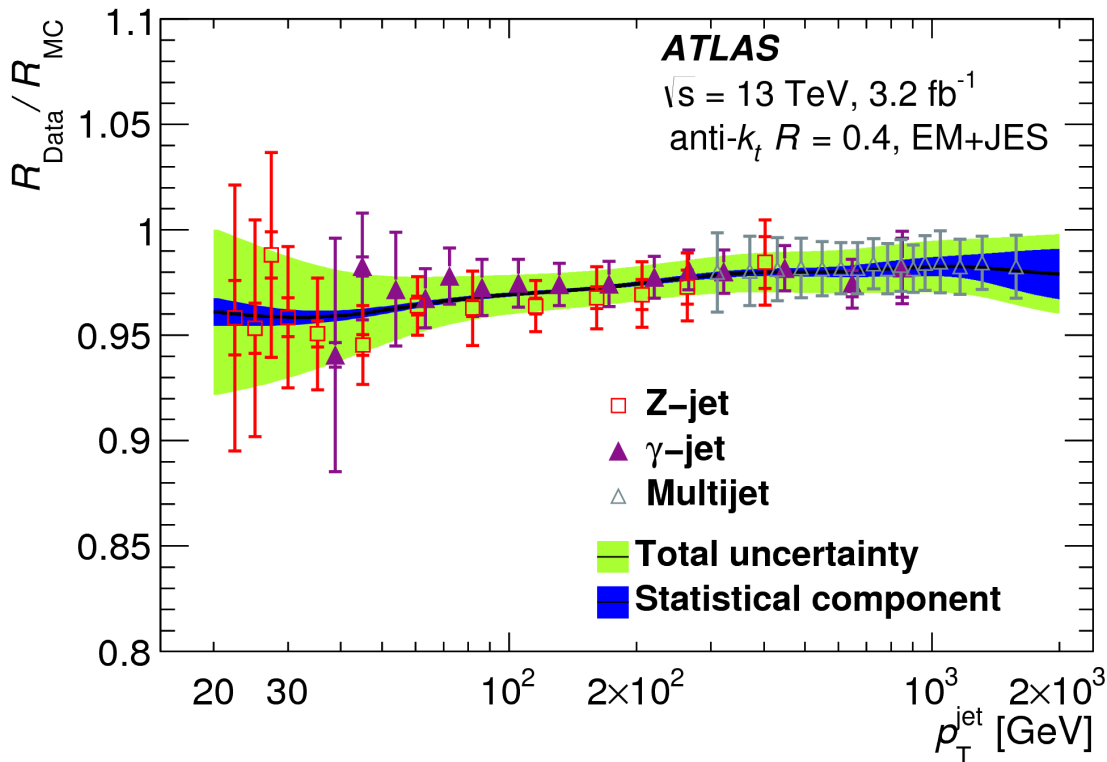
Figure 4.3: The combined absolute in situ calibration factor evaluated from data recorded in 2015 in the Z-jet, γ-jet and multijet topologies [104].

Jet energy scale uncertainties

The uncertainty associated with the energy scale calibration of jets is evaluated primarily through variations in the in situ calibration procedures. The effects of event selection and modelling within the in situ procedures are evaluated. In total there are nearly 100 separate nuisance parameters that arise from these sources of uncertainty; however, for most physics analyses the complete set of nuisance parameters is cumbersome to use and not necessary to accurately describe the uncertainty of the JES. The so-called *category reduction* is used to reduce the total number of nuisance parameters to consider to roughly 30. The eponymous categories in the category reduction scheme are groups of systematics arising from similar sources, such as modelling or a specific detector-related requirement that is a free parameter of an analysis. For each η-p_T bin the correlation between groups of systematics is evaluated. This correlation matrix is diagonalised and the eigenvectors assessed. Leading eigenvectors are retained, and sub-leading ones discarded. In this way, maximal correlation between uncertainties is retained. The reduced set of uncertainties retains a physical meaning, as only related sources of uncertainty are combined.

Jet energy resolution

The quality of the jet energy scale calibration is quantified by the jet energy resolution (JER). This is assessed through studies of dijet simulation and data-simulation comparisons are evaluated in the absolute in situ measurements outlined above [35,

104]. The calibration factor, c from Equation 4.2, is evaluated as the mean of a fitted Gaussian in bins of η and p_T. The width of this Gaussian corresponds to the resolution of the jet energy scale. Uncertainties on the JER measurement are reduced using the eigenvector decomposition technique into 13 nuisance parameters, where the category information is completely lost.

4.4.2 Jet flavour tagging

Jets are identified as originating from b-quarks using a multivariate discriminator called `MV2c10` [105, 106]. B mesons travel a measurable flight distance from the primary vertex before decaying. Therefore, a b-jet is expected to contain tracks that originate from a secondary vertex. The secondary vertex corresponds to the location where the B meson decayed. The `MV2c10` variable exploits this characteristic decay pattern of b-jets to distinguish them from a light and charm jet background. Charm jets are considered separately from light (u-, d-, g-originating) jets due to their experimental properties; The lifetime of the c-quark is sufficient such that a non-negligible fraction of D mesons have a measurable flight distance before subsequent decay. Therefore, charm jets form a source of irreducible background to b-jet identification.

The multivariate discriminator `MV2c10` is constructed from the jet impact parameter, multiplicity, secondary vertex and mass information. The training sample uses a mixture of 7% c-jets and 93% light-jets to provide a balance between charm- and light-jet rejection. In this analysis, the 85% b-tagging efficiency working point is used which has a corresponding rejection rate for light (charm) jets of 28 (2). The procedure of identifying a jet as a b-jet is known as *b tagging.*

4.4.3 Jet cleaning

Jets can be reconstructed from background sources that are unrelated to the *pp* collisions at the centre of the detector. These jets are referred to as pathological. Pathological jets can be reconstructed from: cosmic rays, noise in the detector, or muons produced from decays of proton lost upstream in the beampipe. To reduce jets reconstructed from these background sources, jets are classified as `Good` or `Bad`. Any event containing a `Bad` jet are rejected. The classification is based on a variables based on signal pulse shape in the LAr calorimeters, energy ratio variables between different calorimeter subsystems, and track-based variables. Two working points are constructed: `Tight` and `Loose`.

The efficiency of these working points is measured in dijet data and found to reject the background at 99% and 95% for `Loose` and `Tight` respectively. Events containing a `Bad` jet are rejected; this procedure is referred to as *jet cleaning* [107].

4.4.4   Jet vertex tagging

A multivariate discriminant has been constructed to reduce the impact of pile-up, detector noise, and the underlying event producing jets. This discriminant is known as the *jet vertex tagger* (JVT). By ghost associating tracks to jets, the fraction of jet energy from the primary vertex can be assessed. Jets originating from the hard scatter process are expected to have a large fraction of energy originating from the primary vertex, whereas, jets originating from pile-up, underlying event activity, or noise are expected to have a small fraction of energy originating from the primary vertex. The JVT exploits this difference. The discriminator is constructed from the number of primary vertices in an event and track-based variables. All jets within the region $|\eta| < 2.4$ and $p_T < 50\,\text{GeV}$ have their JVT score - the output of the multivariate discriminator - calculated, and a simple cut is applied based on this score [108].

4.5   Missing transverse momentum

The missing transverse momentum, E_T^{miss}, is reconstructed using calibrated electrons, muons and jets. Electrons and muons are required to satisfy the object selections described above. The missing transverse energy of an event is calculated as the sum of the negative momentum for all calibrated objects measured in that event:

$$E_{x(y)}^{\text{miss}} = E_{x(y)}^{\text{miss},e} + E_{x(y)}^{\text{miss},\gamma} + E_{x(y)}^{\text{miss},\tau} + E_{x(y)}^{\text{miss,jets}} + E_{x(y)}^{\text{miss},\mu} + E_{x(y)}^{\text{miss soft}}, \tag{4.3}$$

The "soft" term is reconstructed from transverse momentum deposited in the detector but not associated with any reconstructed physics object (electron, photon, τ lepton, jet or muon). The soft term is measured using tracks reconstructed in the ID, and known as the Track Soft Term (TST) [109, 110]. Tracks are required to have $p_T > 0.59\,\text{GeV}$ and pass vertex association cuts of $d_0^{\text{sig}} < 2$ and $|z_0|\sin\theta < 3\,\text{mm}$, where d_0^{sig} and z_0^{sig} are impact significance parameters defined in Section [**sec:tracks__and__verts**].

4.6   Overlap removal

An object recorded by the detector may satisfy both the jet and lepton object definitions discussed above. Further to this, in-flight decays of hadrons can produce leptonic signals in the detector that are not removed by lepton isolation requirements. A so-called *overlap removal* procedure is defined such that detector information corresponds uniquely to one physics object hypothesis.

If a selected electron shares a track with a selected muon, the electron is removed. If a jet is within $\Delta R < 0.2$ of a reconstructed electron, the jet is removed. Subsequently, to reduce the impact of non-prompt leptons, if an electron is within $\Delta R < 0.4$ of a jet, then that electron is removed. If a jet has less than three tracks and is within $\Delta R < 0.2$

of a muon, the jet is removed. Finally the muon is removed if it is within $\Delta R < 0.4$ of a jet.

5. Dijet in situ inter-calibration

Jets are calibrated to the truth-jet energy scale using a multi-step procedure known as the *calibration chain*, discussed in Section 4.4.1. The majority of the jet energy scale calibration is derived using Monte Carlo (MC) simulation of various physics processes and the ATLAS detector. The final stage in the jet calibration chain is to correct for residual mis-modelling of the detector, using four data-driven corrections known as the in situ calibrations.

The focus of this chapter is the first in situ correction: the dijet η inter-calibration, in which, forward jets ($0.8 < |\eta| < 4.5$) are calibrated to the energy scale of central jets ($|\eta| < 0.8$). The method aims to produce a uniform jet response as a function of detector position, as well as correcting for residual mis-calibration in the previous steps of the chain. The forward region of phase-space for the dijet event topology is the least well understood region [35], a fact that shall be demonstrated in this Chapter. Calibration based solely on simulation is not sufficient for the goals of the physics programme at ATLAS, and a data driven method is required.

5.1   The η inter-calibration procedure

As with all in situ calibrations, the dijet η inter-calibration is performed by deriving calibration factors from the double ratio of the data to simulation response given in Equation 4.2. Two commonly used methods for deriving the correction factors are: the central reference method, and the matrix method. The calibration factors are derived in bins of the dijet systems kinematics. After the calibration has been measured, a transformation from the dijet kinematics to the kinematics of an individual jet is applied. This transformation allows a measured calibration to be applied to jets measured in different event topologies. Finally, a smoothing is applied to the transformed set of calibrations to reduce the impact of statistical uncertainty.

5.1.1   The central reference method

Due to momentum conservation, the leading order prediction for pair-produced particles at the LHC is for equal and opposite transverse momentum. Imbalances in p_T can arise due to mis-calibrations in one region of the detector relative to another. Next-to-leading order (NLO) effects can also spoil the momentum balance of the system,

however these can be controlled for by event selection criteria that preferentially select a dijet topology. The mis-calibrations ultimately are the result of an imperfect description of the complexities of the ATLAS detector in the MC simulations used earlier in the jet calibration chain.

The *central reference method* exploits the expected p_T-balance of dijet events to calibrate *probe* jets, in any region of the detector, relative to *reference* jets, in the central region ($|\eta| < 0.8$). The central region of the detector is the most heavily instrumented, and also found to have the best p_T response from test beam measurements [99]. Therefore, jets measured in the forward region are calibrated to that of the better measured central region. The relative calorimeter response can be quantified by the balance in transverse momentum between the reference and probe jet. The p_T-balance, or *asymmetry*, is defined as

$$A = \frac{p_T^{\text{probe}} - p_T^{\text{ref}}}{p_T^{\text{avg}}}, \tag{5.1}$$

where $p_T^{\text{avg}} = (p_T^{\text{probe}} + p_T^{\text{ref}})/2$. The asymmetry is evaluated in bins of η_{det}, the probe jet pseudo-rapidity constructed with the geometric center of the detector as the origin, and p_T^{avg}. The η inter-calibration factor, c, and the relative response of the probe jet, R is then taken as

$$R = \frac{1}{c} = \frac{2 + \langle A \rangle}{2 - \langle A \rangle} = \left\langle \frac{p_T^{\text{probe}}}{p_T^{\text{ref}}} \right\rangle, \tag{5.2}$$

where the average asymmetry, $\langle A \rangle$, is evaluated in a fixed region of η_{det} and p_T^{avg} by performing a binned Gaussian fit[1] of the asymmetry distribution in that region. If both jets are within the reference region each jet is used to probe the other. The average asymmetry in the reference region is therefore zero by construction. The fit was required to have passed the quality requirement $\chi^2/N_{DoF} < 15$, where N_{DoF} is the number of bins in the asymmetry distribution. The Pearson χ^2 test statistic corresponds to

$$\chi^2 = \sum_{i \in N} (O_i - E_i)^2 / \sigma_{O,i}^2, \tag{5.3}$$

where O_i and E_i are the observed and expected values of the fitted histogram for the i-th bin of the fitted asymmetry histogram, respectively, and $\sigma_{O,i}$ is the statistical uncertainty on the observed value O_i. The mean of asymmetry distributions was used for asymmetry bins that failed the quality requirement.

5.1.2 Matrix method

The central reference method discards dijet events where both jets lie outside of the central region. The dijet forward cross-section drops steeply as the rapidity interval between the jets increases. In order to probe the response of the forward region with

---

[1]The TMINUIT software package's implementation of the MIGRAD algorithm was used [111].

greater statistical precision, the method is extended by replacing "probe" and "reference" jets by "left" and "right" jets defined as $\eta^{\text{left}} < \eta^{\text{right}}$. Equations 5.1 and 5.2 are correspondingly replaced with

$$A = \frac{p_T^{\text{left}} - p_T^{\text{right}}}{p_T^{\text{avg}}}, \tag{5.4}$$

$$R = \frac{p_T^{\text{left}}}{p_T^{\text{right}}} = \frac{c^{\text{right}}}{c^{\text{left}}} = \frac{2 + \langle A \rangle}{2 - \langle A \rangle}. \tag{5.5}$$

The response R is calculated from the ratio of η inter-calibration factors, c^{left} and c^{right}, for the left and right jets respectively. The average response, $\langle R_{ijk} \rangle$, is evaluated using the Gaussian fitting procedure outlined previously for each η^{left} bin, i, η^{right} bin, j, and p_T^{avg} bin, k. The relative correction factor for a given jet η bin i and fixed p_T^{avg} bin k is obtained by minimizing a matrix of linear equations

$$S(c_{1k}, ..., c_{Nk}) = \sum_{j=1}^{N} \sum_{i=1}^{j-1} \left(\frac{1}{\Delta \langle R_{ijk} \rangle} (c_{ik} < R_{ijk} > -c_{jk}) \right)^2 + X(c_{ik}), \tag{5.6}$$

where N is the number of η-bins, and $\Delta \langle R_{ijk} \rangle$ is the statistical uncertainty of $\langle R_{ijk} \rangle$. The so-called *beta* function

$$X(c_{ik}) = K(N_{bins}^{-1} \sum_{i=1}^{N_{bins}} c_{ik} - 1)^2, \tag{5.7}$$

is used to prevent the trivial solution of $c_{ik} = 0 \ \forall \ i, k \in \{1, .., N\}$, where K is an arbitrary constant much larger than N_{bins}.

5.1.3   Derivation of a residual correction

A final residual correction is evaluated in the kinematics of a probe jet. This involves a transformation from the dijet topology to that of the probe jet.

The in situ double ratio, equivalent to Equation 4.2,

$$\mathcal{C}_{ik} = \frac{c_{ik}^{\text{data}}}{c_{ik}^{\text{MC}}}, \tag{5.8}$$

is used to provide data-driven calibration factor in bins of η_{det}, i, and p_T^{avg}, k of the dijet system. The calibration is applied to individual jets. A given jet with transverse momentum p_T located at η_{det} is mapped to the dijet system with the following relations

$$p_T = \left\langle p_T^{\text{probe}} \right\rangle_{ik} = \frac{2\mathcal{R}_{ik}}{(\mathcal{R}_{ik} + 1)} \langle p_T^{\text{avg}} \rangle_{ik} \tag{5.9}$$

$$\eta_{det} = \left\langle \eta^{\text{probe}} \right\rangle_{ik}. \tag{5.10}$$

A Gaussian smoothing is applied and a smoothly varying residual calibration function, $F^{\text{res}}(p_T, \eta_{\text{det}})$, evaluated where

$$F^{\text{res}}(p_T, \eta_{\text{det}}) = \frac{\sum_{i=1}^{N_{bins}} c_i w_i}{\sum_{j=1}^{N_{bins}} w_j}, \tag{5.11}$$

and

$$w_i = \frac{1}{\Delta C_i} \times \text{Gauss}\left(\frac{\log p_t - \log <p_t^{\text{probe}}>_i}{\sigma_{p_T}} \otimes \frac{\eta_{det} - <\eta_{det}>_i}{\sigma_\eta}\right). \tag{5.12}$$

The index of a given $(\eta_{\text{det}}, p_T^{\text{avg}})$ bin is given by i. The 2D Gaussian smoothing kernel has the width parameters

$$\sigma_\eta = \begin{cases} 0.05 & 2.1 < |\eta| < 2.6 \\ 0.2 & \text{otherwise.} \end{cases} \tag{5.13}$$

and

$$\sigma_{p_T} = 0.2, \tag{5.14}$$

optimised such that the dependence of the residual calibration is captured and the impact of statistical fluctuations are minimised. Here, $\otimes$ denotes addition in quadrature and Gauss(x) denotes a Gaussian function with zero mean and unit width evaluated at point x, ΔC_i is the statistical uncertainty of calibration factor C_i, and $\left\langle p_T^{jet} \right\rangle$ and $\langle \eta_{det} \rangle$ are the average p_T and η of the probe jets in the bin respectively.

5.2 η inter-calibration of 2015 and 2016 data

Physics analyses are performed using calibrations measured with partial datasets as the run progresses, in order to present findings as quickly as possible. As such, η inter-calibration factors are measured over the course of Run 2. This chapter shall primarily discuss the measurement performed with a partial 2016 dataset with a recorded integrated luminosity of $L = 24.3$ fb^{-1}. As shall be shown, the measured η inter-calibration factors were found to be consistent across 2015 and 2016, which have different run conditions. Therefore, the conclusions reached in this chapter should generalise to data recorded throughout Run 2.

5.2.1 Event and data selection

Recorded data were required to satisfy general data quality criteria, such as stable beam conditions and good detector performance. Events were rejected if any jets fail the `LooseBad` jet cleaning working point described in Section 4.4.3. Beyond LO, the p_T-balance of a dijet system is spoilt by the presence of additional radiation. The evaluated response factor c_{ik}^{MC} depends upon the exact subtleties of how additional radiation is handled, how the parton shower is evolved and how the subsequent shower interacts with the complex and varied detector material of ATLAS. To isolate the detector mis-modelling, stringent event selection requirements are enforced to preferentially choose dijet events. The dijet topology was selected for using the event selection requirements:

- At least one HLT jet trigger from the list defined in Table 5.1 must have fired.

- At least one primary vertex with at least two reconstructed tracks.

- At least two reconstructed anti-k_t R=0.4 EM scale jets with a minimum p_T of 25 GeV.

- The angular separation in ϕ between the leading two jets, $\Delta\phi > 2.5$.

- Should an additional radiative jet exist with transverse momentum, p_T^3, its momentum is required to be $p_T^3 < f_{\text{frac}}^{\text{third}} p_T^{\text{avg}}$, where $f_{\text{frac}}^{\text{third}} = 0.4$.

Event Generators

Two MC generators are used to simulate dijet events resulting from pp collisions at the LHC at next-to-leading order accuracy in perturbative QCD. The $2 \to 3$ matrix elements are interfaced with the next-to-next-to leading order (NNLO) CT10 parton distribution functions. The generators used are:

1. POWHEG+PYTHIA8 [112] with the `A14` tune [113]: The Lund string fragmentation framework is used to simulate hadronisation.

2. SHERPA 2.1 [114]: An angular-ordered parton shower was matched to the hard scatter using the CKKW [115, 116] prescription. Hadronisation is simulated using a cluster fragmentation model.

The effects of the ATLAS detector were simulated using GEANTv4 [117]. Further to the event selection described above, Monte Carlo samples had a further *cleaning* applied. The cleaning aims to remove pile-up jets from the event selection in MC. Pile-up jets are overlaid to a hard scatter process, without a truth record. Therefore, the reconstructed leading jet was required to have a transverse momentum within $\pm 40\%$ of the leading *truth* jet.

5.2.2   Trigger and binning considerations

The HLT jet triggers at ATLAS for a given E_T level are separated into a forward ($3.2 < |\eta| \le 4.9$) and a central ($|\eta| < 3.2$) trigger. All jets triggers with a threshold less than $360\,\text{GeV}$ are pre-scaled. This means that for every N events that satisfy the trigger requirements only one is recorded, where N is the pre-scaling factor. For data recorded during 2015 and 2016 data taking periods, the total number of events recorded by the forward and central jet pre-scaled triggers is approximately equal. However, jets are preferentially produced in the central region of the detector. Therefore, the η distributions of measured jets is distorted in the forward region. Before a measurement can be performed, the distortion in jet kinematics due to pre-scaled triggers must be accounted for. Events were classified as forward or central corresponding to which trigger was fired, then scaled to the inverse of the recorded luminosity measured by each trigger. This restores the physical distribution of the η spectrum of dijet

events. Correctly recovering the η spectrum for dijet events acts as validation check for the trigger luminosity weighting procedure. The asymmetry distributions evaluated to perform the η inter-calibration were similarly scaled according to the inverse of the trigger luminosities that entered into them.

Each p_T^{avg} bin was assigned a trigger combination spanning the full detector coverage that is kinematically accessible by the dijet system. Triggers fire based on reconstructed L1 and HLT objects; the kinematics of trigger objects differ from those of the offline physics object for which the calibration is derived. A trigger, or combination of triggers, are required to recover at least 99% of dijet events in a kinematic region of p_T^{avg}. A trigger combination with this property is said to be *fully efficient*.

Every bin of p_T^{avg} required a fully efficient trigger combination. The trigger efficiency for a jet trigger `HLT_jX`, where X is the E_T requirement of the trigger in GeV, is

$$\epsilon_{\texttt{HLT\_jX}}(p_T^{\mathrm{avg}}) = \frac{N_{\texttt{HLT\_jX}}^{\texttt{emulated}}(p_T^{\mathrm{avg}})}{N_{\texttt{HLT\_jY}}^{\mathrm{produced}}(p_T^{\mathrm{avg}})}, \tag{5.15}$$

where $N_{\texttt{HLT\_jY}}$ is the number of events that pass the reference trigger that is fully efficient at the investigated p_T^{avg}, and $N^{\texttt{emulated}}$ are the number of events that pass an emulated version of the trigger with offline objects. The lowest HLT trigger used, `j15`, was found to be fully efficient for $p_T^{\mathrm{avg}} > 25$ GeV in previous performance studies. Performance runs with `HLT_j15` in *pass-through mode*, where an event was recorded even if it fails the trigger selection criteria, were used. The number of events that pass or fail the trigger when it is in pass-through mode is used as the denominator for Equation 5.15, and those that pass are the numerator. The *turn on* point, defined as the 99% efficiency after which triggers are considered fully efficient, can be evaluated from the trigger efficiency curves presented in Figure 5.1. The trigger efficiency plateaus for each trigger combination slightly after the nominal threshold value. The plateau region is fully efficient, and the turn on point in the trigger efficiency curve corresponds to the start of the plateau. The turn on points in terms of p_T^{avg} for all considered trigger combinations used in deriving the dijet η inter-calibration in the years 2015 and 2016 are presented in Table 5.1. There is a 5-40 GeV difference between the turn on point in p_T^{avg} and the threshold of the trigger, depending on the trigger in question. This offset is expected from the difference between trigger and offline physics objects. The p_T^{avg} and η_{det} was optimised such that all p_T^{avg} bins have a fully efficient trigger; furthermore, no η bins spanned a transition between different calorimeter systems.

5.2.3 Validation of the procedure

In order to understand the behaviour of the measured calibration, a suite of validations were performed. These focused on consistency of the derived calibration across method and datasets. Studies of the calibration's performance were also undertaken, whereby calibrated data was examined and compared to uncalibrated data and simulation.
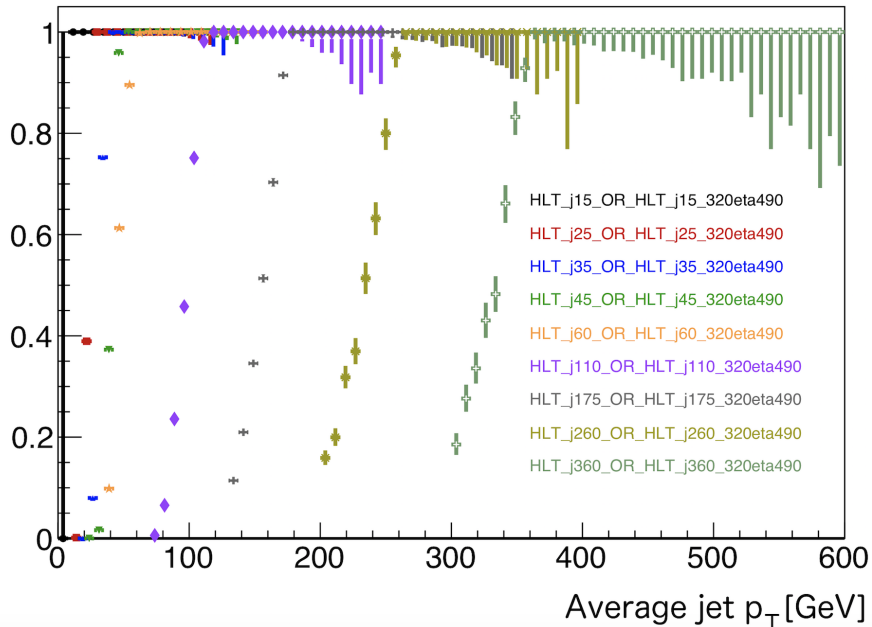
Figure 5.1: The efficiency curves, as defined in the text, for a dijet system with jets calibrated with the EM+JES scheme for the trigger combinations used in the 2015 and 2016 dijet η inter-calibration.

Comparison of methods

The central reference method and matrix method should produce consistent η inter-calibration factors within the statistical uncertainty of each procedure. The inter-calibration factors, c, for both methods in data and simulation were compared over the full region of phase-space covered by the calibration. The methods were found to be consistent within the (correlated) statistical uncertainty. A representative sample of the comparisons is shown in Figure 5.2. The matrix method was used to provide the nominal calibration due to its increased statistical precision.

Comparison of data and simulation

The relative p_T response as a function of η_{det} is shown in Figure 5.3 for data and two MC event generators, POWHEG+PYTHIA8 and SHERPA2.2.1, across a representative range of p_T^{avg}. For $|\eta_{\text{det}}| > 1.2$ there is a consistent disagreement between the relative calorimeter response of data and MC of between 2% and 5%. Previous studies presented in Reference [118] have shown this disagreement in the forward region arises from the energy sampling procedure of the EMEC and HEC. The region $2.0 < |\eta_{\text{det}}| < 3.0$ region has an additional increase in the relative response measured in data compared to simulation. This is larger for $p_T^{\text{avg}} > 55$ GeV, corresponding to poor performance of the HEC relative to the central calorimeter systems for high p_T jets. The η inter-calibration is designed for and intended to correct for features such as these.

Trigger Combination	99% Efficiency point/ p_T^{avg} [GeV]
`HLT_j15_OR_HLT_j15_320eta490`	25
`HLT_j25_OR_HLT_j25_320eta490`	30
`HLT_j35_OR_HLT_j35_320eta490`	40
`HLT_j45_OR_HLT_j45_320eta490`	50
`HLT_j60_OR_HLT_j60_320eta490`	80
`HLT_j110_OR_HLT_j110_320eta490`	175
`HLT_j175_OR_HLT_j175_320eta490`	220
`HLT_j260_OR_HLT_j260_320eta490`	330
`HLT_j360_OR_HLT_j360_320eta490`	400

Table 5.1: The trigger combinations used to evaluate the η inter-calibration factors for 2015 and 2016 data reordered at the ATLAS detector and their corresponding 99% efficiency in terms of p_T^{avg} of the two leading jets of selected dijet events.

Data taking year comparisons

The relative response measured in data recorded throughout 2015 and 2016 is presented in Figure 5.4. The measured calibration factors agree well within their respective statistical uncertainty, indicating that there is little dependence on the differences in run conditions across datasets recorded in 2015 and 2016. The pile-up distribution of recorded events at the LHC is difficult to model and can have a large effect on soft-jets measured by ATLAS. The JVT requirement applied to jets is used to mitigate the effects of pile-up and reject jets likely to originate from pile-up. The JVT is discussed and defined in Section 4.4.4. The pile-up rate increased year-on-year (as discussed in Section 3.1.1), therefore the impact of pile-up upon the inter-calibration is expected to increase between years. Comparing data recorded during different run conditions shows the method is robust to changes in pile-up conditions and run conditions at the LHC.

Closure of the matrix method

The derived residual calibration factors found using the matrix method were applied to the dataset used in their derivation, after which the method was repeated and the η inter-calibration factors, C'_{ik}, were evaluated. This procedure is referred to as a *closure* test, and evaluates how successfully the calibration corrects the detector response. The non-closure of the measured calibration, defined as

$$\sigma_i^{\text{closure}} = 1 - C'_{ik}, \tag{5.16}$$

is shown in Figure 5.5 for two representative bins of p_T^{avg} as a function of η_{det}. The non-closure is found to be significant in the $2 < |\eta_{\text{det}}| < 3$ region for a broad range of p_T^{avg}, where the statistical uncertainty of the measured non-closure is evaluated using
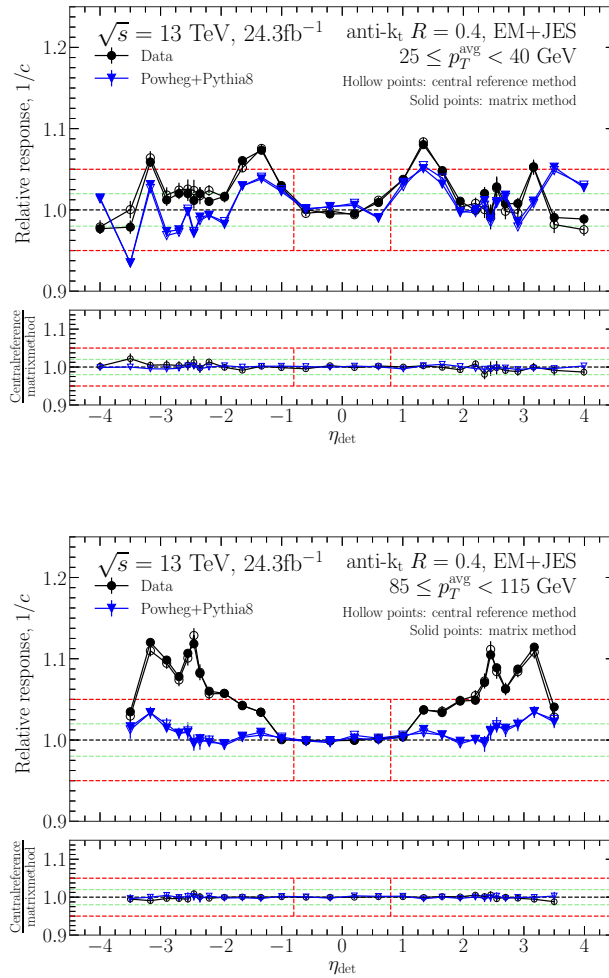
Figure 5.2: The relative p_T-response evaluated by the central reference method (hollow markers) and matrix method (solid markers) for data (black) and simulation (blue) for two representative regions of phase-space. The lower panel of each plot shows the ratio between the relative response evaluated for each method.

the bootstrapping procedure described in Section 5.2.6. The non-closure is largest in the regions with fewest statistics. This is a direct result of the Gaussian smoothing that weights regions by their associated statistical uncertainty. For the high p_T^{avg} region of phase-space the non-closure is largest at $|\eta_{\mathrm{det}}| \sim 2.6$, corresponding exactly to where a sharp increase in the relative response in data compared to that predicted by simulation is observed. For the regions $|\eta_{\mathrm{det}}| < 1.0$ and $|\eta_{\mathrm{det}}| > 3.0$ the non-closure is statistically insignificant, indicating the jets are calibrated to the correct energy scale.

5.2.4   Method bias studies

The observed non-closure seen in Figure 5.5 is most extreme in regions where the measured inter-calibration factors are large or have a large statistical uncertainty. This implies that the method fails to calibrate extreme localised differences between the measured and predicted response. The method was examined by deriving and applying
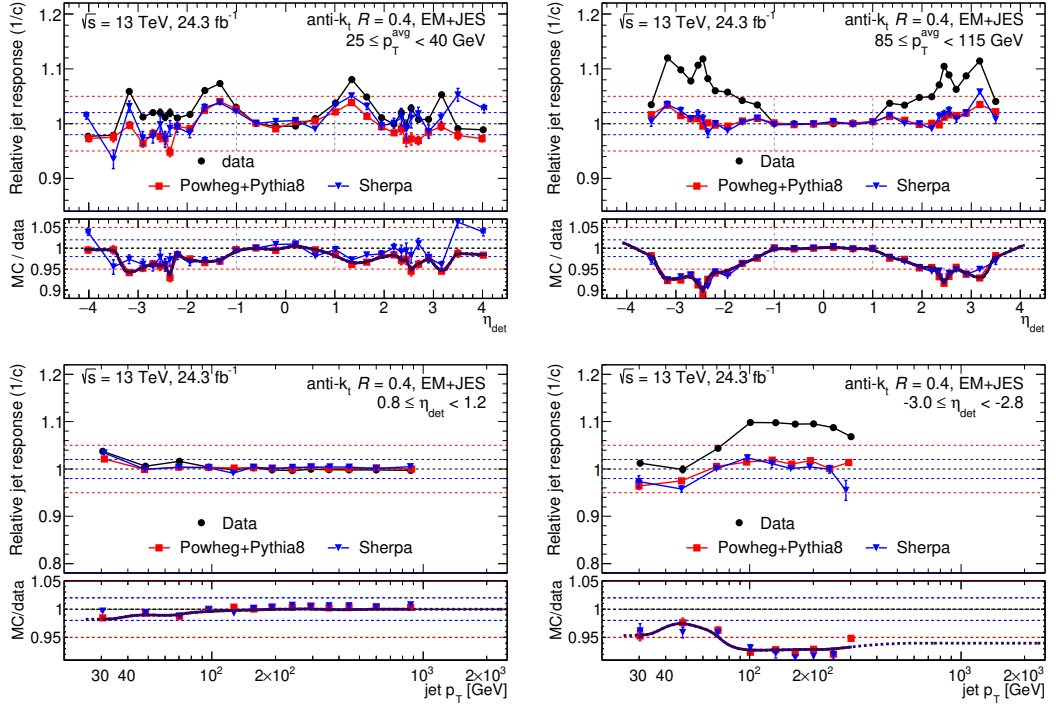
Figure 5.3: The relative p_T-response evaluated by the matrix method for data (black), Powheg+Pythia8 (red) and Sherpa (blue) for four representative regions of phase-space. The lower panel of each plot shows the ratio of the evaluated relative p_T-response for data and simulation.

calibrations using the nominal MC, Powheg+Pythia8, as *pseudo-data*. The pseudo-data were biased in the following two controlled ways:

- **Injected localised bias:** Jet p_T in the region $-1.8 < \eta < -1.5$ were biased by a factor $s_{\mathrm{bias}} = 10\%$, such that $p_T \rightarrow s_{\mathrm{bias}} \cdot p_T$.

- **Stress test:** Jet p_T in the region $|\eta| > 1.0$ were biases by a factor $s_{\mathrm{bias}} = 6\%$, such that $p_T \rightarrow s_{\mathrm{bias}} \cdot p_T$

The biased pseudo-data were calibrated and the closure, as defined above, examined. The stress test corresponds to a constant shift in energy scale, similar to what is observed in the data-simulation comparisons in the forward region. The method captured the bias introduced in the stress test, as shown in Figure 5.6. The ratio between the measured relative response before and after calibration corresponds to $1 + \sigma^{\mathrm{closure}}$. A small residual non-closure compatible with the statistical uncertainty of the method is found after inter-calibration has been applied.

An extreme localised bias of 6% leaves a significant residual non-closure, shown before and after calibration in Figure 5.7. The η_{det} bins adjacent to the biased bin $-1.8 < \eta_{\mathrm{det}} < -1.5$ have a significant non-closure; this originates from the smoothing procedure used to derive the residual calibration. The kernel width is much broader than the biased region. Furthermore each bin has approximately equal statistical uncertainty. The smoothing therefore distributes the increased response to adjacent bins.
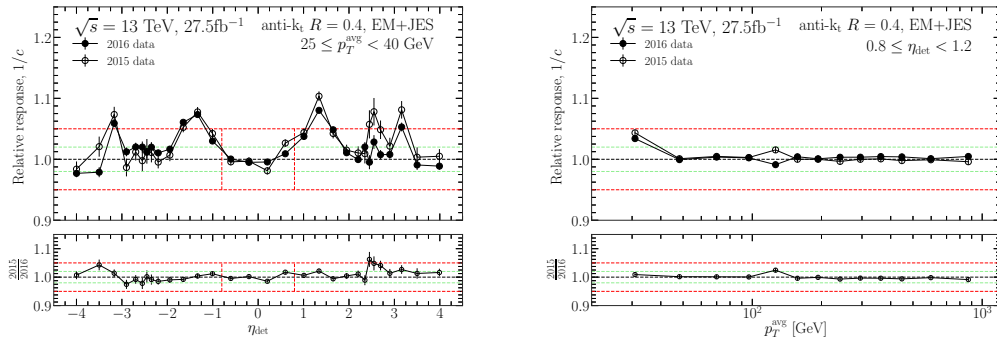
Figure 5.4: The relative response measured using the matrix method for data recorded in 2015 (hollow) and the 2016 (solid) datasets for representative p_T^{avg} (left) and η_{det} (right) bins.
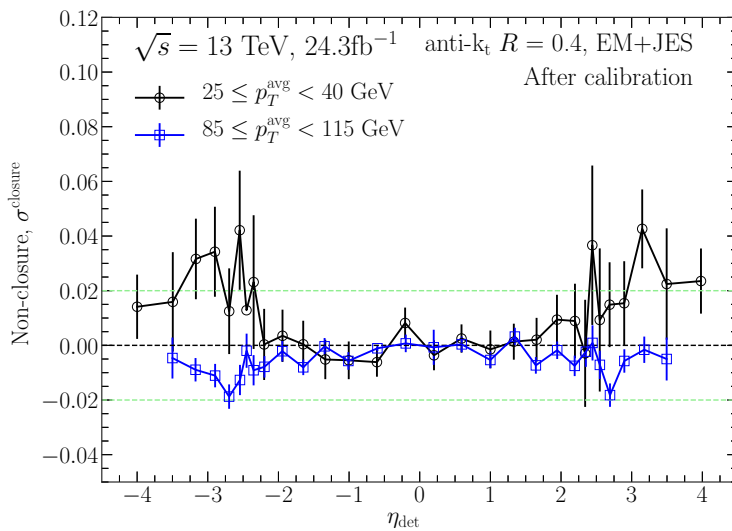
Figure 5.5: The remaining non-closure, defined in Equation 5.16, of the 2016 measured η inter-calibration as a function of η_{det} in two representative p_T^{avg} bins for anti-k_t jets calibrated to the EM+JES scale.

In the un-biased cases this is desired behaviour, and produces an η inter-calibration that smoothly varies as function of η and p_T^{avg} whilst capturing changes in response. However, the smoothing procedure breaks down for localised biases of this size.

5.2.5   Iterative calibration

In order to remove the residual non-closure presented in Figure 5.5, the η inter-calibration procedure was extended to a novel n-step iterative method. An initial set of residual inter-calibration factors, C_0, and corresponding residual calibration F_0^{rel} were found. A secondary set of inter-calibration factors, C_1, and residual calibrations, F_1^{rel}, were derived from data calibrated to EM+JES scale with the F_0^{rel} inter-calibration applied. The inter-calibration procedure can then proceed iteratively, until N calibration factors have been evaluated for each bin. The residual calibrations were derived from
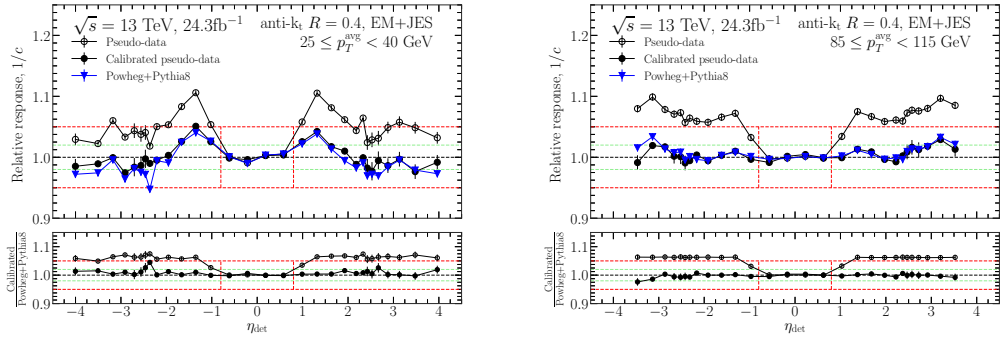
Figure 5.6: The relative response, $1/c$, of pseudo-data before (hollow circles) and after calibration (black) for an injected stress of 6% in the region $|\eta| \geq 1.0$ for the $25 \leq p_T^{\text{avg}} < 40$ GeV (left) and $85 \leq p_T^{\text{avg}} < 115$ GeV (right). The predicted relative response of the POWHEG+PYTHIA8 event generator is shown (blue), as is the ratio of the calibrated and uncalibrated pseudo-data to un-biased simulation (lower panel). This ratio corresponds to $1 + \sigma^{\text{CLOSURE}}$.

calibration factors C_n, where n denotes the iteration step. The total inter-calibration factor in a given bin corresponds to

$$C_{\text{tot}} = C_0 \prod_{i=1}^{N} C_i, \tag{5.17}$$

where N is the total number of steps in the procedure. For an iterative calibration procedure the convergence requirement

$$1 \leq |c_n| < |c_{n+1}| \quad \forall \quad c_n \in C_n, c_{n+1} \in C_{n+1} \tag{5.18}$$

must be satisfied. The closure for step M corresponds to the set of inter-calibration factors for step $M + 1$ of the iterative inter-calibration procedure. Figure 5.8 shows the closure of an iterative inter-calibration procedure with $N = 2$ and $N = 6$ steps in the lowest p_T^{avg} bins accessible to the method. In the region $2 < |\eta_{\text{det}}| < 3$ the inter-calibration diverges and Equation 5.18 is not satisfied. Therefore, repeated applications of the procedure do not resolve the observed non-closure. Secondary to this, each subsequent inter-calibration has decreasing statistical precision as jets migrate outside of the calibration selection. This is visible in the increased statistical uncertainty of the $N = 6$ calibration compared to $N = 2$. An iterative η inter-calibration procedure therefore cannot be used to remove the observed non-closure.

5.2.6 Systematic uncertainties

Three sources of uncertainties affecting the derived η inter-calibration factor were considered:

- **Modelling:** Differences in the predicted relative response by the different MC generators SHERPA and POWHEG+PYTHIA8.
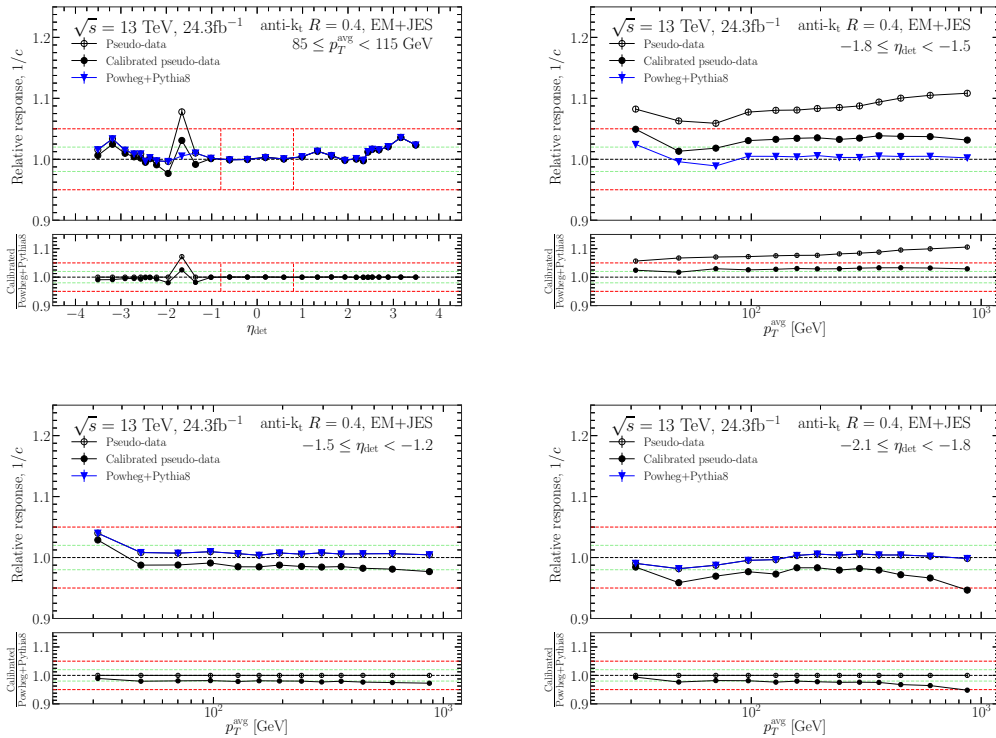
Figure 5.7: The relative response, $1/c$, of pseudo-data before (hollow circles) and after calibration (black) for an injected bias in the region $-1.8 < \eta_{\mathrm{det}} < -1.6$ for the $85 \leq p_T^{\mathrm{avg}} < 115$ GeV bin (top left) and the $-1.8 < \eta_{\mathrm{det}} < -1.5$ (top right), $-1.5 < \eta_{\mathrm{det}} < -1.2$ (bottom left), and $-2.1 < \eta_{\mathrm{det}} < -1.8$ (bottom right) bins. The predicted relative response of the POWHEG+PYTHIA8 event generator is shown (blue), as is the ratio of the calibrated and uncalibrated pseudo-data to un-biased simulation (lower panel). This ratio corresponds to $1 + \sigma^{\mathrm{closure}}$.

- **Dijet topology requirements:** The event selection criteria were changed and the corresponding shift on the measured η inter-calibration evaluated.

- **Closure:** Non-closure, $\sigma^{\mathrm{closure}}$, larger than the statistical uncertainty was evaluated and considered an additional source of uncertainty. Whilst this was found to be related to the smoothing applied, a smoothly varying inter-calibration was deemed more relevant for physics analyses than the observed small residual non-closure.

Uncertainties are smoothed and transformed in the same manner as the residual calibration itself, F^{res}, into a function of individual jet p_T and η_{det}. The smoothed uncertainty on the residual calibration is shown in Figure 5.9 in four representative regions of phase-space.

The following event selection requirements were changed in turn: the JVT requirement was tightened to the calibrated working point JVT > 0.94; The $\Delta\phi(j_1, j_2)$ requirement was varied by ± 0.3 around the nominal value of 2.5; and the requirement on the fractional third jet momentum, $f_{\mathrm{frac}}^{\mathrm{third}}$, was varied by ± 0.1 about its nominal
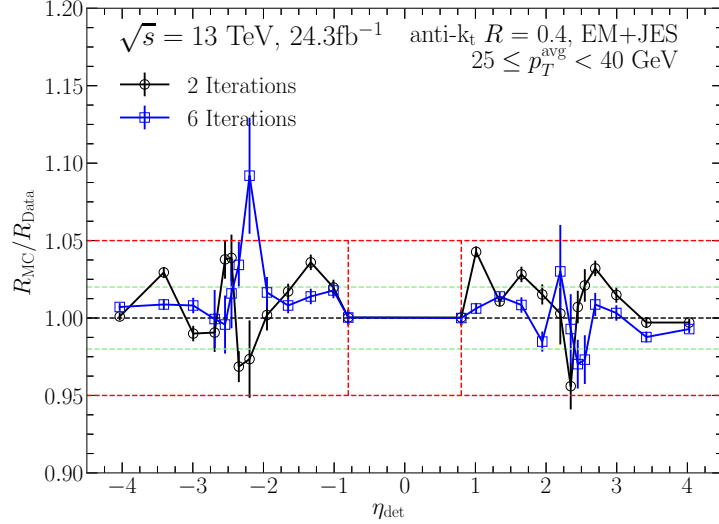
Figure 5.8: The closure of an iterative η inter-calibration procedure as a function of η_{det}, the probe jet η with respect to the geometric centre of the detector, for EM+JES calibrated jets with the derived η inter-calibration factors applied for the $25 \leq p_T^{\mathrm{avg}} < 40$ GeV bin with $N = 2$ (black) and $N = 6$ (green).

value of 0.4. The uncertainty associated with the JVT requirement was symmetrised to provide upward and downward uncertainties.

The statistical significance of the uncertainties related to the dijet topology requirement was evaluated using a *bootstrapping* procedure. Whereby, the original population of simulated and data events are re-sampled to generate pseudo-experiments in the following procedure:

1. For each MC and data event draw a random number from a Poisson distribution with a mean of unity.

2. Evaluate the nominal η inter-calibration factors, $c_i'^{\,\mathrm{nominal}}$ for bin i, with this re-weighting applied to both simulation and data. The re-weighted MC and data samples are considered a pseudo-experiment. The $'$ denotes a pseudo-experiment.

3. Using the *same* event weights defined in step 1, construct the η inter-calibration, $c_i'^{\,\mathrm{syst}}$ for bin i, selected with a systematically varied event selection criteria.

4. Evaluate the size of the systematic uncertainty for this pseudo-experiment, σ, which for bin i is

$$\sigma_i^{\mathrm{syst}} = c_i'^{\,\mathrm{nominal}} - c_i'^{\,\mathrm{syst}} \; . \tag{5.19}$$

5. Repeat Steps 1-4 $N_{\mathrm{toys}} = 900$ times. For each bin i evaluate the mean and root mean square of the evaluated uncertainty for each pseudo-experiment, $\langle \sigma_i \rangle$ and $\mathrm{RMS}(\sigma_i)$ respectively. The evaluated uncertainty for a given systematic is then
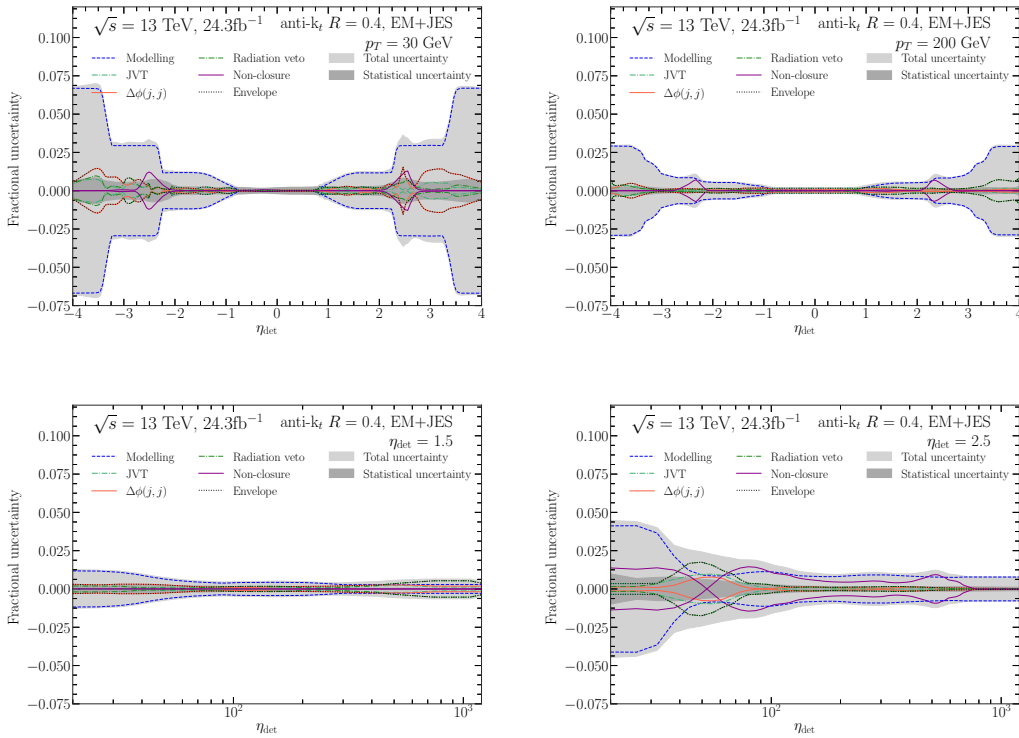
Figure 5.9: The total systematic uncertainty of the residual η inter-calibration as a function of η_{det} (top), the jet η with respect to the geometric centre of the detector, and jet p_T (bottom) for EM+JES calibrated jets in four representative slices of phase-space.

taken as $\langle \sigma_i \rangle \pm \mathrm{RMS}(\sigma_i)$, where $\mathrm{RMS}(\sigma_i)$ is considered the statistical uncertainty of the evaluated systematic uncertainty.

A systematic uncertainty is considered to be statistically significant if $\mathrm{RMS}(\sigma_i) \gtrapprox \langle \sigma_i \rangle$. The five event-selection motivated systematics were evaluated using the boot-strapping procedure outlined above, for the majority of phase-space these were found to be statistically insignificant. A conservative approach of taking the *envelope* of these systematic uncertainties was used, whereby the largest of all statistically insignificant uncertainties was taken for each point in phase-space.

The modelling uncertainty is the dominant source of uncertainty in the method. For the Run 1 η inter-calibration measurement the modelling uncertainty was $\mathcal{O}(10\%)$; advances in event generators since 2012, specifically NLO implementations of a dijet system in *pp* collisions, have resulted in better agreement between predictions and an associated uncertainty. The non-closure of the method is a sub-dominant uncertainty, largest in the studied region of $2.0 < |\eta| < 3.0$.

5.2.7   Residual η inter-calibration

The smoothed residual η inter-calibration factors are shown in Figure 5.10. For the majority of phase-space the inter-calibration corresponds to a lowering of the energy scale of the measured jets in the forward region. The calibration is largest in the forward
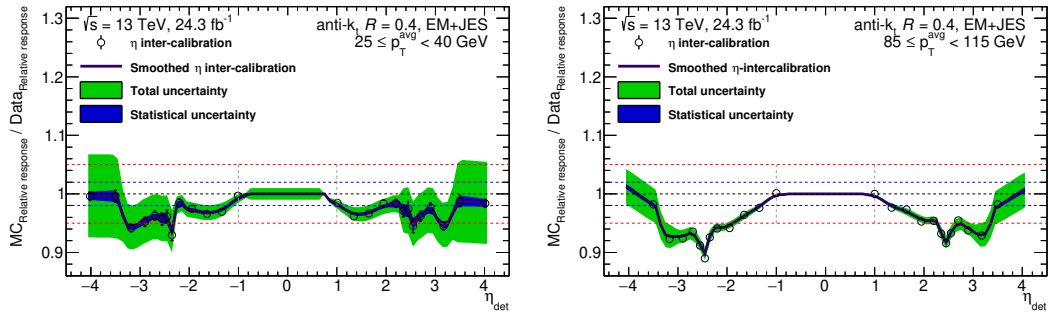
Figure 5.10: Residual η inter-calibration factors as a function of η_{det}, the jet η with respect to the geometric centre of the detector, for EM+JES calibrated jets for two representative p_T^{avg} bins $25 \leq p_T^{\mathrm{avg}} < 40$ GeV (left) and $85 \leq p_T^{\mathrm{avg}} < 115$ GeV (right). The smoothed residual calibration (black) is shown with the smoothed statistical (blue) and systematic (green) uncertainties.

region of the detector, where the dijet system is least well understood, as reflected by the systematic uncertainties. Furthermore, the smoothing is found to capture the large changes in measured calibration across the range $2.0 < |\eta| < 3.0$.

5.3 Conclusion

The calibration of data recorded during 2015 and 2016 has been presented and discussed. This calibration of forward jets is vital to physics efforts within the ATLAS collaboration, as well as the work presented in later sections of this thesis that utilise radius $R = 0.4$ jets. The measured calibration was found to be stable over differing run conditions of the LHC. Future studies can therefore combine the datasets from these periods to achieve higher statistical precision than the measured calibration presented here. New methods and understanding of the behaviour of this calibration have been presented. A bootstrapping procedure was introduced to estimate the statistical significance of systematic uncertainties and ultimately reduce the total uncertainty of the method. The uncertainty due to modelling of the dijet system, whilst lower than in previous measurements, was found to be the dominant source of uncertainty. Non-closure of the method has been identified, reduced and controlled for through modification of the procedure. Furthermore, potential methods of reducing the non-closure through an iterative calibration have been explored.

6. Top tagging

Analytic methods of understanding jet substructure provide an alternative to the extensive Monte Carlo event generator studies typically performed by experimental collaborations [119]. In recent years the analytic understanding of jet substructure has progressed substantially, with a focus on investigating the discrimination power of jet substructure between heavy-particle decays and jets initiated by light QCD partons [120, 121]. Fixed order calculations are limited in the domain of jet substructure. Instead, all-order calculation is required to accurately describe variables sensitive to perturbative QCD in the highly boosted regime. Furthermore, analytic techniques have been used to propose powerful new methods of removing soft contamination from jets, such as the mMDT/Soft-Drop algorithms [121, 122].

The discrimination of hadronically decaying top quarks from a QCD jet background is referred to as *top tagging*. Large-R jets are often used in boosted topologies. A jet is considered to be "large" if its radius parameter $R \gtrsim 0.8$. In the case of a boosted top quark decaying hadronically, large-R jets typically form a 3-prong jet. Experimental collaborations utilise a suite of different top tagging algorithms. So-called simple tagging algorithms utilise requirements on jet kinematics and variables sensitive to the substructure of a jet [123, 124], whereas more complicated algorithms utilise machine learning methods. However, all tagging methods used in physics measurements and searches rely on two ideas: the discrimination power of the jet mass, and identification of multi-prong substructure within a jet.

Two top tagging methods that lend themselves to analytic methods will be discussed in Section 6.1. In Section 6.2 a leading order in α_s calculation of the jet mass after the application of these top taggers is explored, and then generalised to an all-order calculation. Finally the behaviour of top jets is examined in Section 6.3 and a novel understanding of top tagging performance through analytically calculated ROC curves is presented in Section 6.4.

6.1 Top tagging algorithms

Whilst a large range of top tagging algorithms exist and have been studied with Monte Carlo based methods, none have been examined using analytics. As such, an existing experimental algorithm was explored and adapted, along with a new method motivated

by phenomenological studies. The CMS collaboration's historic tagging algorithm, *the CMS tagger*, was studied and understood. It was found to be collinear unsafe at order $\mathcal{O}(\alpha_s^3)$. The collinear unsafety of the tagging algorithm prevented a detailed analytic understanding of the procedure and raises concerns about the general behaviour of the tagger. An IRC safe extension of the CMS tagger, `TopSplitter`, was proposed and studied in detail. Furthermore, the Y-splitter tagger is extended to the Y_m splitter top tagging algorithm. Extending the two prong case of heavy boson tagging to the three prong boosted top tagging.

6.1.1 The Y_m splitter top tagging algorithm

The Y-splitter tagger was introduced as a method of identifying the two-prong structure of a jet for W/Z/Higgs identification [120]. The algorithm reclusters an initial jet using the k_t clustering algorithm, and the k_t clustering history is examined. Subjets are evaluated by decomposing the initial jet according to its k_t clustering history. The k_t splitting distance, $d_{ij}^{p=1} = \min(p_{T,i}^{2p}, p_{T,j}^{2p})\Delta R_{ij}^2$, of the decomposed subjets i and j from the clustering history have a requirement imposed, such that $d_{ij} \sim m_W^2$ for the first declustered set of subjets. The parameter p of the clustering algorithm is unity for the k_t clustering algorithm, as discussed in Section 2.2.6. For Y splitter tagging, the splitting distance is normalised to mass and the y variable is required to meet the condition:

$$y = \frac{d_{ij}}{m_{ij}} > y_{\text{cut}}. \tag{6.1}$$

Extending Y-splitter to the case of three prongs presents the immediate problem of selecting a third prong in an IRC safe manner with high signal to background selection efficiency. Top jets have two characteristic mass scales: that of the electroweak W boson and that of the top quark itself. This implies that the jet mass and pairwise subjet mass is an important property in top tagging. Motivated by this fact, the initial reclustering of a jet was performed with the general k_t clustering algorithm, taking a distance metric that corresponds to the mass of two subjets in the soft and collinear limit. The distance metric d_{ij} in Equation 2.25 was used with $p = 1/2$, instead of the k_t distance metric used in Y-splitter which corresponds to $p = 1$. This algorithm is referred to as Y_m splitter due to this mass based distance metric.

The Y_m splitter top tagging algorithm proceeds as follows:

1. Recluster an initial jet with the general k_t algorithm, $p = 1/2$.

2. **Primary decomposition:** Evaluate two subjets by undoing the last step of clustering. Require each subjets to satisfy the requirement

$$p_T^{\text{subjet}} > \zeta_{\text{cut}} p_T^{\text{jet}} . \tag{6.2}$$

If either subjet fails the ζ_{cut} requirement reject the jet.

71

3. **Secondary decomposition:** Decluster both subjets obtained from primary decomposition. The primary subjet with smallest general k_t ($p = 1/2$) distance between its constituent subjets is retained unaltered. The subjet with the larger distance is decomposed, and the ζ_{cut} imposed on both resultant subjets. After secondary decomposition exactly three subjets are yielded: An unaltered subjet from primary decomposition, and two secondary subjets that pass Equation 6.2.

4. Impose a minimum pairwise mass condition on the three subjets, 1, 2, 3, such that

$$\min(m_{12}, m_{13}, m_{23}) > m_{\text{min}} , \tag{6.3}$$

where $m_{\text{min}} \lesssim m_W$. The minimum pairwise mass is expected to be comparable to the W boson mass, m_W, therefore jets failing this requirement are rejected.

6.1.2   The CMS tagger

The historic CMS tagger is a modification of the John Hopkins Tagger [125], and classifies jets as follows:

1. Recluster the initial anti-k_t jet with the Cambridge/Aachen algorithm.

2. **Primary decomposition:** Evaluate two subjets by undoing the last step of the clustering. Require the declustered subjets to individually satisfy the ζ_{cut} requirement given in Equation 6.2. Should both primary subjets fail, reject the jet. If only one subjet passes the requirement, repeat the declustering upon the subjet that passed the requirement until two subjets that satisfy Equation 6.2 have been declustetred. If no subjets that pass the ζ_{cut} condition can be found, reject the jet.

3. **Secondary decomposition:** Repeat the primary decomposition procedure upon each of the two evaluated subjets from the primary decomposition, with the original jet p_{T} used in Equation 6.2. If the secondary decomposition of a subjet fails, and either one or neither of the jets pass the ζ_{cut} requirement, then the original primary subjet is retained. This results in two, three or four subjets being evaluated. Jets are required to have at least three subjets, otherwise they are rejected. The removal of a subjet at this stage can be considered to be a type of jet grooming, as soft constituents that are likely to be soft radiation are discarded based on their kinematics.

4. The three highest p_{T} subjets are selected, and the minimum pairwise mass of these subjets evaluated. The m_{min} requirement in Equation 6.3 is then imposed. The parameter m_{min} is typically taken as $50\,\text{GeV}$.

5. Two versions of the CMS tagger have been proposed in References [126] and [127]. In the most recent version, an additional requirement was imposed on the decompositions of a subjet into subjets i and j:

$$\Delta R_{ij} > 0.4 - A p_T^{\text{subjet}}, \tag{6.4}$$

where ΔR_{ij} is the angular separation between decomposed subjets i and j. The default value of A is $0.0004\,\text{GeV}$.

The original version of the CMS tagger is *collinear unsafe*. The unsafety arises from the selection of the three hardest out of a possible four subjets, whereby a collinear splitting would change the p_T ordering of these subjets and would render the algorithm unsafe. The introduction of an angular requirement in Equation 6.4 mitigates this unsafety at low-p_T. However for jets with $p_\mathrm{T}/\mathrm{A} > 0.4$ the issue remains.

6.1.3 The `TopSplitter` tagging algorithm

To study the CMS tagger with perturbative QCD calculations, an IRC algorithm is required. The `TopSplitter` algorithm is a modification of the CMS tagger, such that three subjets are chosen after secondary decomposition in an IRC safe manner.

When considering the hadronic decay of a top quark, the splitting with largest mass is the $t \to Wb$. An ideal algorithm would identify this splitting. As the CMS tagger uses the angular ordered CA clustering history, the most massive splitting is not readily identifiable. `TopSplitter` produces a secondary decompositions with the most massive splitting as one subjet, and explores the CA clustering history in order to do this.

How the `TopSplitter` algorithm identifies the most massive splitting can be understood by considering the decomposition of primary subjets A and B. A and B are the result of the primary decomposition. The clustering history of a primary subjet can be thought of as tree, where each recombination constitutes a branch in the tree. The CA tree of a primary subjet is recursed through, choosing the hardest subjet at each recursion step. Any subjets that fail the ζ_{cut} requirement during recursion are removed. The splitting with the largest $p_{T,j}\theta_j$ is identified as A$'$, where j is the index of CA tree recursion, $p_{T,j}$ is the transverse momentum of the softest subjet at splitting j, and θ_j the angular separation of the two branches at splitting j in the CA tree. All of the softer subjets that pass the ζ_{cut} requirement at each splitting are recombined to produce A$''$. Figure 6.1 illustrates the recursion performed at secondary decomposition in the `TopSplitter` tagging algorithm. Finally, the primary subjet with the less massive secondary decomposition is retained and the more massive decomposed using the recursive procedure described above, resulting in exactly three subjets.

The recursion introduces a grooming on each subjet, which has a similar behaviour as previous recursive grooming methods such as SoftDrop/mMDT. Furthermore, the structure of the algorithm lends itself to all order calculation.

(a) Parton ordering: $p_{T,0}\theta_0^3 > p_{T,1}\theta_1^3,\ p_{T,2}\theta_2^2$ **(b)** Parton ordering: $p_{T,2}\theta_2^2 > p_{T,1}\theta_1^2,\ p_{T,0}\theta_0^2$ or $p_{T,1}\theta_1^2 > p_{T,2}\theta_2^2,\ p_{T,0}\theta_0^2$.
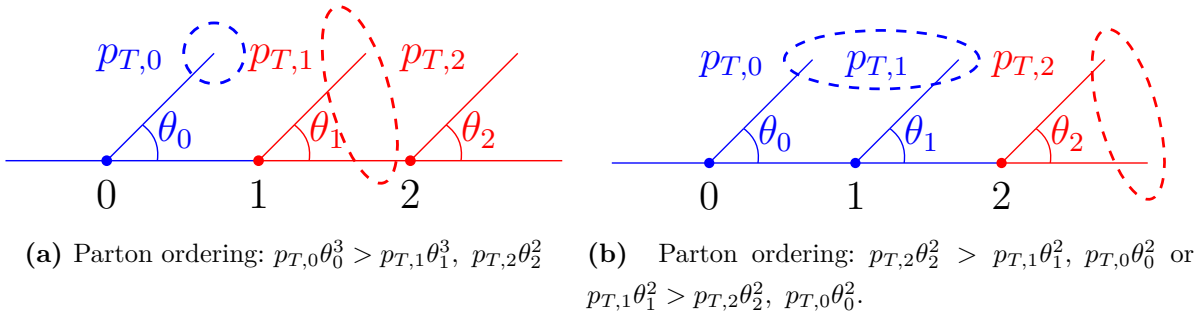
Figure 6.1: An illustration of the results of secondary decomposition of the `TopSplitter` algorithm, in three cases of differing p_{T} orderings of the subjets. The nodes correspond to splittings in the Cambridge Aachen clustering history, ordered such that $\theta_0 > \theta_1 > \theta_2$, and the labelled branches correspond to the softer subjet at each splitting. The red and blue dashed circles correspond to evaluated subjets, where the colour matched lines correspond to the subjet constituents. The CA tree terminates after node 2, and all subjets shown here pass the ζ_{cut} requirement in Equation 6.2.

6.2 The QCD jet background

The action of a tagging algorithm on a background QCD jet can be understood by direct calculation of the jet mass distribution after application of the algorithm. In the boosted limit, the jet mass is small compared to the transverse momentum of a jet, p_{T}. The action of a tagger shall be explored with the boost invariant jet mass, given by

$$\rho = \frac{m^2}{R^2 p_T^2},\tag{6.5}$$

where m is the jet mass and R the radius parameter of the jet clustering algorithm, taken to be $R = 1.0$ for these studies. In the boosted limit $\rho \ll 1$. The m_{min} mass constraint of the top tagging algorithms explored shall be considered as

$$\rho_{\mathrm{min}} = \frac{m_{\mathrm{min}}^2}{R^2 p_T^2},\tag{6.6}$$

in the boosted limit $\rho_{\mathrm{min}} \ll 1$. The ζ_{cut} examined was fixed to $\zeta_{\mathrm{cut}} = 0.05$. This value was chosen based on current usage of ζ_{cut} style requirements in experiment, for example the ATLAS standard trimming configuration.

6.2.1 Leading order calculation of jet mass

The behaviour of a quark-initiated jet can be understood from perturbative QCD calculations performed with the eikonal approximation, where partons are considered massless and radiation is soft and collinear. Two real emissions from the initial hard parton must be considered in order to produce a three-pronged jet. This can be considered simply as repeated emissions from a quark with momentum fractions z_1 and z_2 and angles θ_1, θ_2 with respect to the parent quark p, respectively. Using the approximation of repeated emissions from a quark implies a *strong angular ordering* to the
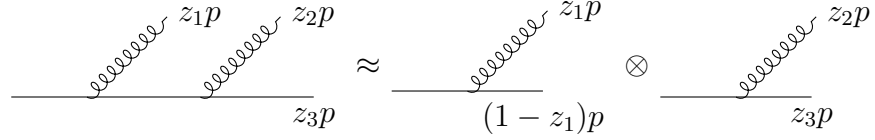
Figure 6.2: An illustration of the eikonal strongly ordered limit for a quark initiated jet. Two emissions from a hard quark with momentum p are produced with fractional momentum z_1 and z_2, where the angles emissions are $\theta_1 \gg \theta_2$ in this limit.

decay, such that $\theta_1 \gg \theta_2$, and the separation between emissions 1 and 2, $\theta_{12} \sim \theta_1$. The strongly ordered approximation is shown schematically in Figure 6.2. In this limit the jet mass is set by the first (larger angle) emission, meaning

$$\rho = \frac{z_1(1-z_2)p_T^2\theta_{12}^2}{R^2 p_T^2} \approx z_1\theta_1^2 . \tag{6.7}$$

Similarly, the minimum pairwise mass requirement is imposed against the mass of the final objects with smallest angular separation, the quark and secondary gluon, $\rho_{23} \approx z_2(1-z_3)\theta_{23}^2 \approx z_2\theta_2^2$. A factor $1/R^2$ has been ignored in both of these approximations, as the radius parameter of all clustering algorithms is taken as $R = 1$.

At leading order, $\mathcal{O}(\alpha_s^2)$ in the context of this calculation, in the soft-collinear strongly ordered limit, the action of the CMS tagger upon a quark initiated jet is

$$\frac{1}{\sigma}\frac{d\sigma}{d\rho} = \left(\frac{C_F\alpha_s}{\pi}\right)^2 \int \frac{dz_1}{z_1}\frac{dz_2}{z_2}\frac{d\theta_1^2}{\theta_1^2}\frac{d\theta_2^2}{\theta_2}\Theta^{\text{tagger}}(z_1, z_2, \theta_1^2, \theta_2^2)$$
$$\Theta^{\text{CA jet}}(z_1, z_2, \theta_1^2, \theta_2^2)\delta(\rho - z_1\theta_1^2), \tag{6.8}$$
$$= \frac{1}{\rho}\left(\frac{C_F\alpha_s}{\pi}\right)^2 \left(\ln^2\frac{1}{\zeta_{\text{cut}}}\ln\frac{\rho}{\rho_{\text{min}}} + \ln^3\zeta_{\text{cut}}\right) \tag{6.9}$$

where the actions of the tagger and CA jet clustering are imposed as a set of restrictions on phase-space in the function

$$\Theta^{\text{tagger}}(z_1, z_2, \theta_1^2, \theta_2^2) = \quad \Theta(\theta_1^2 < \theta_2^2 < 1)\Theta(z_1 > \zeta_{\text{cut}})$$
$$\times\Theta(z_2 > \zeta_{\text{cut}})\Theta(z_2\theta_2^2 > \rho_{\text{min}}), \tag{6.10}$$
$$\Theta^{\text{CA}}(z_1, z_2, \theta_1^2, \theta_2^2) = \quad \Theta(R^2 > \theta_1)\Theta(R^2 > \theta_2)\Theta(R^2 > \theta_{12})$$
$$= \quad \Theta(R^2 > \theta_1). \tag{6.11}$$

The $\Theta(x > a)$ is the Heaviside step function, which is unity for $x > a$ and zero otherwise. As is typical in calculations of this manner, the azimuthal angle for both splittings has been integrated over in Equation 6.8. The jet clustering function, Θ^{CA}, corresponds to the set of limitations on splittings required such that all splittings are clustered into one CA jet. The additional clustering requirements of an anti-k_t (or general-k_T ($p = 1/2$)) jet can be imposed with a similar set of restrictions on phase-space. To clarify the behaviour of the tagging function, these additional jet clustering requirements are not considered.

The restrictions on emissions imposed by the `TopSplitter` tagging algorithm in this limit are described by the tagging function in Equation 6.10. At this order of the perturbative calculation there are no differences between the CMS tagger and `TopSplitter`. Differences such as the collinear divergence in the CMS tagger enter at α_s^3, NLO in this context. The tagging function, Θ^{tagger}, produces large logarithms of the ζ_{cut} and ratio of the mass sale within the jet which are given in Equation 6.9.

In this soft limit the behaviour of a quark and gluon initiated jet differs only by their associated colour factors, C_F and C_A respectively. The soft limit can be lifted to include contributions of hard collinear splittings by taking $\frac{dz_1}{z_1} \to P_{qg}(z_1)dz_1$. However, the utility of this calculation is still limited by the strong angular ordering assumption. As the electroweak scale and the top quark mass are of similar order, the angular ordering assumption does not hold for top jets. The relevant background QCD jets are formed from three hard partons, with no assumption on the parton's angular ordering. To examine the action of taggers on these jets, the $1 \to 2$ AP splitting functions must be extended to the case of three unordered products - the *triple collinear limit.*

6.2.2 The triple collinear limit

Consider a massless parton, a, undergoing a splitting process $a(p) \to a_1(p_1) + a_2(p_2) + a_3(p_3)$. The triple collinear limit is approached when the momentum of the three particles become simultaneously parallel. The momentum of parton a_i can be written in the *light cone* basis such that

$$p_i^\mu = x_i p^\mu + k_{\perp,i}^\mu - \frac{k_{\perp,i}^2}{x_i} \frac{n^\mu}{2p \cdot n}, \tag{6.12}$$

where the collinear direction specified by the parent parton a is denoted by the light-like longitudinal momentum p^μ, x_i is the longitudinal momentum fraction of the daughter parton a_i, $k_{\perp,i}$ is the transverse momentum and n^μ is an auxiliary light-like vector which specifies the direction the collinear limit is approached. Specifically $k_{\perp,i} \cdot n = p^2 = n^2 = 0$.

Note that, in this basis $\sum_i x_i \neq 1.0, \sum_i k_{\perp,i} \neq 0$, therefore it useful to further define the intuitive fractional longitudinal momentum variables z_i that have the property $\sum_i z_i = 1.0$ as well as key Lorentz invariants of the three body system

$$z_i = x_i / \sum_i x_i, \tag{6.13}$$

$$s_{ij} = (p_i + p_j)^2 = 2p_i \cdot p_j = z_i z_j \theta_{ij}, \tag{6.14}$$

$$s_{ijk} = (p_i + p_j + p_k)^2 = s_{ij} + s_{ik} + s_{jk}. \tag{6.15}$$

The invariants s_{ij} and s_{ijk} describe the invariant mass carried by partons i, j and the total three parton system, respectively.

The $1 \to 3$ splitting functions describe the probability of a parton a, undergoing a splitting process $a \to a_1 + a_2 + a_3$ in the triple collinear limit, just as the AP

splitting functions describe the probability of a parton undergoing the splitting process $a \to a_1 + a_2$. The Abelian C_F^2 term for the spin-averaged term of the triple-collinear splitting functions is given by

$$\langle \hat{P}_{g_1 g_2 q_3}^{(\text{ab})} \rangle = C_F^2 \big[\frac{s_{123}^2}{2 s_{13} s_{23}} z_3 \left(\frac{1 + z_3^2}{z_1 z_2} \right) - \frac{s_{23}}{s_{13}} \\ + \frac{s_{123}}{s_{13}} \left(\frac{z_3 (1 - z_1) + (1 - z_2)^3}{z_1 z_2} \right) \big] + (1 \leftrightarrow 2) \,. \tag{6.16}$$

The full set of spin averaged splitting functions, including the remaining $C_F T_R$ and $C_F C_A$ terms for the total quark splitting function $\hat{P}_{q \to xxq}$, can be found in References [128–130]. The details of the functional form of each splitting function is not of interest, therefore it shall not be given or discussed further.

The phase-space in the triple-collinear limit can be written in terms of the angular separation and fractional longitudinal momentum of partons, θ_{ij} and z_i respectively, as

$$d\Phi_3 = \frac{(p_t R)^4}{\pi} (z_1 z_2 z_3) \, dz_2 \, dz_3 \, d\theta_{12}^2 \, d\theta_{23}^2 \, d\theta_{13}^2 \Delta^{-1/2} \Theta (\Delta) \,, \tag{6.17}$$

with the Gram determinant Δ given by [131, 132]

$$\Delta = 4\theta_{13}^2 \theta_{23}^2 - (\theta_{12}^2 - \theta_{13}^2 - \theta_{23}^2)^2. \tag{6.18}$$

Again, the azimuthal degrees of freedom in emissions have been integrated over when defining this phase-space factor.

The leading order calculation of the jet mass in the eikonal strongly ordered limit, given in Equation 6.8, can now be extended as

$$\left(\frac{1}{\sigma} \frac{d\sigma}{d\rho} \right)^{\text{LO,triple-collinear}} = \int d\Phi_3 \frac{\alpha_s(k_{t1}) \alpha_s(k_{t2})}{(2\pi)^2} \frac{\langle \hat{P} \rangle}{s_{123}^2} \Theta^{\text{jet}} \Theta^{\text{tagger}} \\ \cdot \delta \left(\rho - \frac{s_{123}}{R^2 p_t^2} \right), \tag{6.19}$$

where the arguments of the jet and tagger functions, Θ^{jet} and Θ^{tagger}, have been suppressed for clarity. The running of the strong coupling constant has also been accounted for, and each branching is evaluated at the appropriate energy scales of the two leading partons in an event k_{t1} and k_{t2}.

The restrictions on phase-space imposed by the tagging algorithms and jet finding can now be clarified in the triple collinear limit as

$$\Theta^{\text{jet}} (\zeta_{\text{cut}}, \rho_{\text{min}}) = \sum_{i > j \neq k} \Theta \left(d_{ij}^{\text{anti-}k_t} < \min(d_{ik}^{\text{anti-}k_T}, d_{jk}^{\text{anti-}k_t}) \right) \\ \times \Theta(\theta_{ij} < R) \Theta(\theta_{(i+j)k} < R), \tag{6.20}$$

and

$$\Theta^{\text{tagger}} (\zeta_{\text{cut}}, \rho_{\text{min}}) = \sum_{i > j \neq k} \Theta \left(d_{ij}^{(\text{tagger})} < \min(d_{ik}^{(\text{tagger})}, d_{jk}^{(\text{tagger})}) \right) \\ \times \Theta \left(\min(z_k, 1 - z_k) > \zeta_{\text{cut}} \right) \\ \times \Theta \left(\min(z_i, z_j) > \zeta_{\text{cut}} \right) \\ \times \Theta \left(\min(\rho_{ij}, \rho_{jk}, \rho_{ki}) > \rho_{\text{min}} \right), \tag{6.21}$$

where the mass of two emissions i and j is given by $\rho_{ij} = z_i z_j \theta_{ij}$, and the distance metrics, d_{ij}, for the jet function and jet clustering terms in the Y_m splitter and `TopSplitter` tagging functions are

$$d_{ij}^{\text{TopSplitter}} = \theta_{ij}^2, \tag{6.22}$$

$$d_{ij}^{Y_m \text{ splitter}} = \min(z_i, z_j)\theta_{ij}^2, \tag{6.23}$$

$$d_{ij}^{\text{anti-}k_t} = \min(z_i^{-2}, z_j^{-2})\theta_{ij}^2, \tag{6.24}$$

At this order of perturbation theory, the reclustering requirements can be neglected and the action of the tagging function simplified as

$$\Theta^{\text{tagger}}(\zeta_{\text{cut}}, \rho_{\min}) = \Theta\left(\min(z_1, z_2, z_3) > \zeta_{\text{cut}}\right)\Theta\left(\min(\rho_{12}, \rho_{13}, \rho_{23}) > \rho_{\min}\right),$$
$$\tag{6.25}$$

which is the same for the `TopSplitter` and Y_m splitter taggers.

6.2.3 All order calculations

The jet mass distributions described thus far are accurate to fixed order α_s^2. The natural extension to this description is to perform a *resummation* of the many soft emissions from the hard partons described at fixed order. This subsection shall briefly define and discuss the tools needed to perform the resummed calculation, and then discuss the resummed jet mass distribution itself.

It is well known that a fixed order description of a generic variable sensitive to radiative effects, say $\mathcal{J}$, does not capture the small $\mathcal{J}$ behaviour accurately. To describe such an observable, the perturbative series must be re-ordered in terms of $\alpha_s^n \ln^m \frac{1}{\mathcal{J}}$ where $n < m \leq 2n$. A re-ordering of the perturbative series corresponds to consideration of infinitely many real and virtual emissions. Observing a given value of $\mathcal{J}$ imposes restrictions on the phase-space of real emissions, whilst leaving virtual emissions unrestricted. The infinitely many emissions are *resummed* and generate the logarithmic terms, which arise from the inexact cancellations between the real and virtual emissions.

The cumulant (also known as *integrated cross-section*), Σ, for a generic jet shape observable, $\mathcal{J}$, after all order resummation of soft real and virtual contributions corresponds to an exponential Sudakov form factor multiplied by a fixed order cross-section pre-factor. For a generic hard process, this can be expressed as [26, 133]

$$\Sigma(\mathcal{J}) = \int_0^{\mathcal{J}} d\mathcal{J}' \frac{d\sigma}{d\mathcal{J}'} \tag{6.26}$$

$$= \left[\sum_{i=0}^{\infty}\left(\frac{\alpha_s}{2\pi}\right)^i A_i\right] \exp\left[Lg_1(\alpha_s L) + g_2(\alpha_s L) + \alpha_s g_3(\alpha_s L) + ...\right] + B(\alpha, \mathcal{J}), \tag{6.27}$$

where $L = \ln\frac{1}{\mathcal{J}}$. The pre-factor, given as series expansion in α_s^i and A_i coefficients, corresponds to the cross-section of the hard-scatter process at fixed order i in α_s. The

exponential term is known as the *Sudakov form factor*, and can be interpreted as the probability for a decay resulting in the observable taking the value $\mathcal{J}$ *not* occurring. The exponentiated series of terms are ordered by their relative size. The function $Lg_1(\alpha_s L)$ contains all leading logarithmic (LL) contributions of the form $\alpha_s^n L^{n+1}$, where n is the order of the perturbative expansion in α_S required to describe the generic hard process. The so-called B factors vanish in the limit $\mathcal{J} \to 0$, and correspond to a series of power correction terms to the cumulant.

The Sudakov form factor, $\mathcal{S}$, is typically expressed in terms of the exponentiated series as

$$\begin{aligned}
\mathcal{S} &= \exp\left[Lg_1(\alpha_s L) + g_2(\alpha_s L) + \alpha_s g_3(\alpha_s L) + ...\right], \\
&\approx \exp\left[-R(Lg_1(\alpha_S L))\right],
\end{aligned} \tag{6.28}$$

where the truncated series of large logarithmic terms, R, is known as the *radiator*, truncated here to LL accuracy.

The jet mass distribution for the tagging algorithms discussed can now be calculated in the strongly ordered limit at $\mathcal{O}(\alpha_s^2)$ + LL accuracy. Starting at the jet mass distribution in the strongly ordered limit given by Equation 6.8, consider the addition of many soft emissions from the hard parton as

$$\begin{aligned}
\frac{1}{\sigma}\frac{d\sigma}{d\rho} &= \int \left(\frac{C_R \alpha_s}{\pi}\right)^2 \frac{dz_1}{z_1}\frac{d\theta_1^2}{\theta_1^2}\frac{dz_2}{z_2}\frac{d\theta_2^2}{\theta_2^2}\delta(\rho - z_1\theta_1^2)\Theta^{\text{jet}}\Theta^{\text{tagger}} \\
&\qquad \sum_{k'=0}^{\infty} k'! \times \left(\frac{1}{k'}\prod_{i=1}^{k'}\frac{C_R\alpha_s}{\pi}\frac{d\theta_i'^2}{\theta_i'^2}\frac{dz_i^i}{z_i^2}\left[\Theta_i^{\text{real}} - 1\right]\Theta(\theta_i^i > \theta_{i+1}')\right) \quad (6.29)
\end{aligned}$$

$$\begin{aligned}
\frac{1}{\sigma}\frac{d\sigma}{d\rho} &= \int \left(\frac{C_R \alpha_s}{\pi}\right)^2 \frac{dz_1}{z_1}\frac{d\theta_1^2}{\theta_1^2}\frac{dz_2}{z_2}\frac{d\theta_2^2}{\theta_2^2}\delta(\rho - z_1\theta_1^2)\Theta^{\text{jet}}\Theta^{\text{tagger}} \\
&\qquad \times \exp\left[-\int\frac{C_R\alpha_s}{\pi}\frac{dz}{z}\frac{d\theta^2}{\theta^2}\Theta^{\text{vetoes}}\right].
\end{aligned} \tag{6.30}$$

Here, the allowed phase-space for real emissions, i, is given by Θ_i^{real}. The allowed phase-space of real emissions is defined by the tagging algorithm and imposition that the jet mass takes the value $\rho = z\theta_1$. This shall be discussed in more detail in the next section where the radiators are calculated. Angular ordering of emissions is imposed by $\Theta(\theta_i^i > \theta_{i+1}')$. The factor -1 in the $\left[\Theta_i^{\text{real}} - 1\right]$ term corresponds to the cancellation of virtual contributions with real emissions. Virtual emissions are allowed across all of phase space, and therefore contribute as a constant term in the integral $d\theta_i dz_i$. However, the phase-space in which a real emission is allowed is restricted by the tagging algorithm, and by angular ordering. For the exponentiation given in Equation 6.30 to occur, the soft emission dependent terms $\left[\Theta_i^{\text{real}} - 1\right]$ must factorise across all emissions i. Such a factorisation is non-trivial in general. At LL accuracy, this factorisation can be achieved by taking $\left[\Theta_i^{\text{real}} - 1\right] \to \Theta^{\text{vetoes}}$. Here, Θ^{vetoes} describes the restrictions on phase-space imposed by the tagger, as opposed to the allowed regions of phase space described by Θ^{real}. It can be shown very generally that the bottom line of Equation 6.29 corresponds

to the exponential Sudakov form factor at LL accuracy discussed in Equation 6.27 [26, 133]. The second line of Equation 6.30 corresponds to the resummation of all soft radiation from the primary hard parton for a given tagger at LL accuracy, and implicitly defines the radiator as

$$ R = \int \frac{dz}{z} \int \frac{d\theta}{\theta} \frac{\alpha_s(z\theta E)}{\pi} \Theta^{\text{vetoes}}. \tag{6.31} $$

In order to achieve LL accuracy, the running of α_s is calculated to one-loop accuracy for emissions at an energy scale $z\theta E$, where E is the energy of the radiating parton.

As stressed previously, QCD jets formed from three hard partons with no assumptions placed upon their ordering are the subject of study in this Chapter. This is equivalent to treating logarithms of ζ_{cut}, ρ and ρ_{min}/ρ on equal footing, and can be achieved by increasing the accuracy of the pre-factor of the Sudakov in Equation 6.30, moving from the strongly ordered limit to the triple collinear limit as

$$ \frac{1}{\sigma}\frac{d\sigma}{d\rho} = \int \frac{\alpha_s(k_{t,1})\alpha_s(k_{t,2})}{(2\pi)^2} d\Phi_3 \frac{\langle \hat{P}_{1\to3}\rangle}{s_{123}^2} \Theta^{\text{jet}}\Theta^{\text{tagger}} $$
$$ \cdot \delta\left(\rho - \frac{s_{123}}{R^2 p_t^2}\right) \cdot \exp\left[-R_{\text{tagger}}(\rho_1, \rho_2, \theta)\right]. \tag{6.32} $$

The jet mass radiator for a given tagger is $R_{\text{tagger}}(\rho_1, \rho_2, \theta)$, where the parameters shall be defined in detail in the next section. Equation 6.30 introduced radiation from the primary parton, however radiation from the sub-leading hard parton in a QCD jet must also be considered. This corresponds to an additional radiator term in the Sudakov form factor, which shall be evaluated in the next section explicitly.

The triple-collinear calculation that forms the pre-factor of the Sudakov in Equation 6.32 is calculated to higher accuracy than the radiator. A *matching* must be performed so that at order α_s^2 the jet mass distribution uses the full triple-collinear splitting function, while beyond α_s^2 all large LL terms are retained. The parameters of the radiator, ρ_1, ρ_2 and θ, shall be defined separately for each tagging algorithm. It is most convenient to define the parameters at the same time as describing the matching of the Sudakov form factor and the pre-factor, this is detailed in Sections 6.2.4 and 6.2.5. The resummation completes the description of the jet mass under the action of a tagger to the accuracy of $\mathcal{O}(\alpha_s^2)$ + LL.

6.2.4   The Y_m splitter radiator

The Y_m splitter radiator at LL shall first be calculated with a pre-factor in the strongly ordered limit, as described by Equation 6.30, and then matched to the full triple-collinear limit pre-factor. The radiator can be understood by considering two soft emissions k_1 and k_2 from a hard quark. Let x_i and θ_i be the momentum fraction and angle of emission of k_i with respect to the hard parton. The strong angular ordering of this limit means that $\theta_1 \gg \theta_2$ is satisfied by construction. At leading logarithmic accuracy

strong ordering in mass (or equivalently general k_T ($p = 1/2$) distance) can be assumed. The jet mass is set by the first emission meaning $\rho \approx \rho_1$, where $\rho_1 \approx x_1\theta^2 \gg \rho_2 = x_2\theta_2^2$.

By construction, k_1 and k_2 are the emissions obtained by the declustering procedure of the Y_m splitter algorithm. Due to the mass ordering of the emissions, k_1 and k_2 are also the emissions that dominate the pairwise masses entering the $\rho_{\min}$ condition. Therefore, all tagger constraints are fully determined by declustering partons k_1 and k_2 which produce the leading-order pre-factor in Equation 6.30.

To calculate the radiator directly, the form of Θ^{vetoes} must be understood. Consider many soft emissions ordered in mass, or equivalently in the soft limit the general k_T ($p = 1/2$) distance $z\theta^2$. First consider the soft emissions from the *primary* (initial) hard parton, described by momentum fraction z and angle θ with respect to the primary parton. For the pre-factor to match the Sudakov, the many soft emissions must not dominate the mass of the jet or the declustered subjet. Therefore, soft emissions with $z\theta^2 > \rho_2$ are vetoed.

Now consider soft emissions from the *secondary* splitting, k_1, with momentum fraction z and angle θ with respect to the k_1 splitting. Soft emissions must be required to not set the mass of the jet or the decomposed subjets evaluated by the tagging algorithm. The momentum fraction with respect to the primary parton is x_1z. Therefore emissions with $x_1z\theta^2 > \rho_2$ are vetoed. Furthermore, soft emissions are required to be emitted at angle less than θ_1 due to angular ordering. Figures 6.3a and 6.3b show the effect of these vetoes on the allowed kinematics of real emissions in the Lund plane.

The Sudakov form factors calculated at LL accuracy for the Y_m splitter tagging algorithm are given by the exponentiation of the following radiators

$$
\begin{aligned}
R_{\text{Y}_m\text{splitter}}(\rho_1, \rho_2, \theta_1) &= R_{\text{Y}_m\text{splitter}}^{\text{primary}}(\rho_1, \rho_2, \theta_1) + R_{\text{Y}_m\text{splitter}}^{\text{secondary}}(\rho_1, \rho_2, \theta_1) \\
R_{\text{Y}_m\text{splitter}}^{\text{primary}}(\rho_1, \rho_2, \theta_1) &= \int \frac{d\theta^2}{\theta^2} \frac{dz}{z} \frac{\alpha_s(z\theta p_T R)C_R}{\pi} \Theta(z\theta^2 > \rho_2) \\
R_{\text{Y}_m\text{splitter}}^{\text{secondary}}(\rho_1, \rho_2, \theta_1) &= \int \frac{d\theta^2}{\theta^2} \frac{dz}{z} \frac{\alpha_s(z\theta x_1 p_T R)C_R}{\pi} \Theta(zx_1\theta^2 > \rho_2)\Theta(\theta^2 < \theta_1),
\end{aligned}
$$

$$(6.33)$$

where the first term, $R_{\text{Y}_m \text{ splitter}}^{\text{primary}}$, corresponds to restrictions on real emissions from the primary hard parton, and the second term, $R_{\text{Y}_m \text{ splitter}}^{\text{secondary}}$, arises from restrictions on real emissions from the first splitting of this hard parton.

Matching the Sudkaov to the triple-collinear limit

The Sudakov form factors must be matched to the triple-collinear limit at α_s, such that a consistent picture of the jet mass distribution is described. Consider the three final state partons after a $1 \to 3$ splitting process p_1, p_2 and p_3. For the scenario where
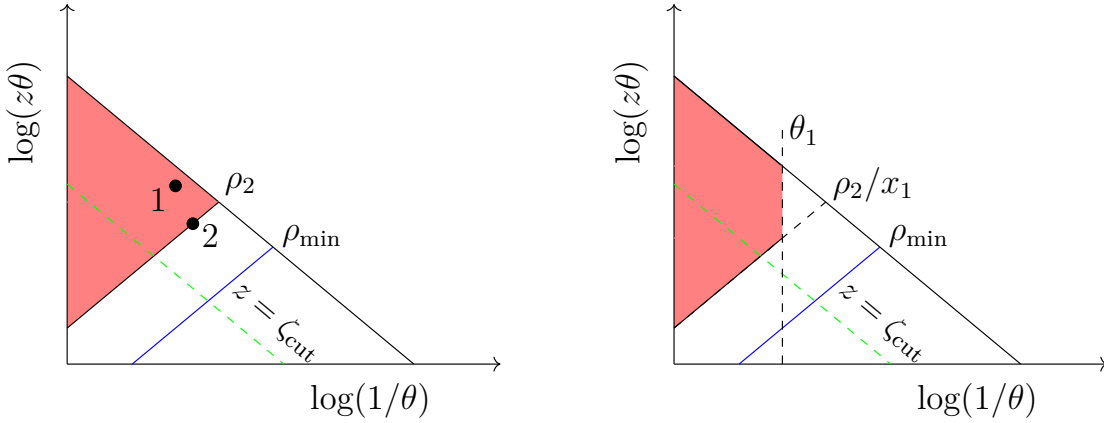
(a) Emissions from primary parton for configuration $\rho \sim \rho_1 \gg \rho_2$.

(b) Emissions from secondary splitting, k_1.

Figure 6.3: The Lund planes for emissions from a primary parton and the first hardest splitting under the action of the Y_m splitter tagging algorithm. The black points in Figure 6.3a illustrate the kinematics of the hardest emissions k_1 and k_2. Both emissions satisfy the ζ_{cut} condition shown in the green dashed line. The blue line represents the boundary of $z\theta^2 = \rho_{\mathrm{min}}$, and the dashed green line depicts $z = \zeta_{\mathrm{cut}}$. The black dashed line in Figure 6.3b represents the boundary for which $\theta < \theta_1$, a requirement imposed on emissions due to angular ordering. The red shaded region corresponds to regions of phase-space which are vetoed by the tagging algorithm.

p_1 is declustered with the prong (p_2, p_3), the matched variables are given by

$$\theta_1 = \theta_{1(2+3)}, \qquad\qquad \theta_2 = \theta_{23}, \qquad\qquad (6.34)$$

$$\rho_1 = \min(z_1, 1 - z_1)\theta_1^2, \qquad\qquad \rho_2 = \min(z_2, z_3)\theta_2^2, \qquad\qquad (6.35)$$

$$k_{t1} = \min(z_1, 1 - z_1)\theta_1 p_t R \qquad\qquad k_{t2} = \min(z_2, z_3)\theta_2 p_t R, \qquad\qquad (6.36)$$

$$x_1 \equiv \rho_1/\theta_1^2 = \min(z_1, 1 - z_1). \qquad\qquad\qquad\qquad (6.37)$$

Note that all permutations of declustering are considered when calculating the jet mass distribution. The above set of definitions defines one of three possible combinations to illustrate the matched variables across regions of different accuracy within the calculation. The matching procedure can be shown to reduce to the correct leading order description of the jet mass distribution, when the pre-factor is calculated in the strongly ordered limit.

6.2.5 The `TopSplitter` radiator

The radiator of the `TopSplitter` tagging algorithm can be evaluated in the same manner. Starting again in soft strongly ordered limit described by Equation 6.30, consider the situation where emission k_1 is declustered first, followed by the declustering of p and k_2 separately. Again, let x_i and θ_i be the fractional longitudinal momentum and angle

of emission k_i with respect to hard parton p. To satisfy `TopSplitter` $x_i > \zeta_{\text{cut}}$, then by definition the k_2 emission dominates the mass of prong such that $\rho \approx rho_2 = x_2 \theta_2^2$.

Now consider many soft emissions off of the primary (initial) hard parton p. To avoid double counting in the radiator and pre-factor, all emissions with a mass larger than $\rho \sim \rho_2$ must be vetoed, i.e $z\theta^2 > \rho_2$. Emissions at angles larger than θ_2 but with $z < \zeta_{\text{cut}}$ are removed by the secondary decomposition stage of the `TopSplitter` algorithm. Emissions at angles smaller than θ_2 by definition cannot dominate the mass of prong, therefore the requirement $z\theta^2 > \rho_2$ is only active when $z > \zeta_{\text{cut}}$. Emissions from the secondary hard prong, k_1, must be angular ordered, such that $\theta < \theta_1$. By the same arguments as above, emissions with a mass larger than ρ_2 and energy fraction with respect to total jet p_T, $x_1 z$, larger than ζ_{cu} are vetoed. These vetoes are shown in Figure 6.4.

The total radiator for the `TopSplitter` algorithm is therefore given by

$$R_{\text{TopSplitter}}(\rho_1, \rho_2, \zeta_{\text{cut}}) = R_{\text{TopSplitter}}^{\text{primary}}(\rho_2, \theta_1) + R_{\text{TopSplitter}}^{\text{primary}}(\rho_2, \theta_1), \tag{6.38}$$

where

$$R_{\text{TopSplitter}}^{\text{primary}}(\rho_1, \rho_2, \zeta_{\text{cut}}) = \int \frac{d\theta^2}{\theta^2} \frac{dz}{z} \frac{\alpha_s(z\theta p_T R) C_R}{\pi} \Theta(z > \zeta_{\text{cut}})$$
$$\times \Theta(z\theta > \rho_2 \text{ or } \theta > \theta_1), \tag{6.39}$$

$$R_{\text{TopSplitter}}^{\text{secondary}}(\rho_1, \rho_2, \zeta_{\text{cut}}) = \int \frac{d\theta^2}{\theta^2} \frac{dz}{z} \frac{\alpha_s(z\theta x_1 p_T R) C_R}{\pi} \Theta(x_1 z > \zeta_{\text{cut}})$$
$$\Theta(z x_1^2 \theta^2 > \rho_2) \Theta(\theta > \theta_1). \tag{6.40}$$

The IRC unsafety of the un-modified CMS tagger prevents an all orders calculation of the jet mass distribution after application of the CMS tagger. Closed form expressions for all discussed radiators discussed are given in Reference [2].

Matching the Sudkaov to the triple-collinear limit

As with the Y_m splitter tagging algorithm, the radiators are defined in terms of ρ_1, ρ_2 and θ_1. As long as the correct jet mass distribution in the strongly ordered limit is recovered, ρ_1, ρ_2 and θ_1 may be defined arbitrarily. As before, consider the three final state partons after a $1 \to 3$ splitting process p_1, p_2 and p_3. For the scenario where p_1 is declustered with the prong (p_2, p_3), the matched variables are given by

$$\theta_1 = \theta_{1(2+3)}, \qquad\qquad\qquad \theta_2 = \theta_{23}, \tag{6.41}$$
$$\rho_1 = z_1(1 - z_1)\theta_1^2, \qquad\qquad \rho_2 = z_2 z_3 \theta_2^2, \tag{6.42}$$
$$k_{t1} = z_1(1 - z_1)\theta_1 p_t R \qquad\qquad k_{t2} = z_2 z_3 \theta_2 p_t R, \tag{6.43}$$
$$x_1 \equiv \rho_1/\theta_1^2 = \min(z_1, 1 - z_1). \tag{6.44}$$

All permutations of declustering are considered when calculating the jet mass distribution.
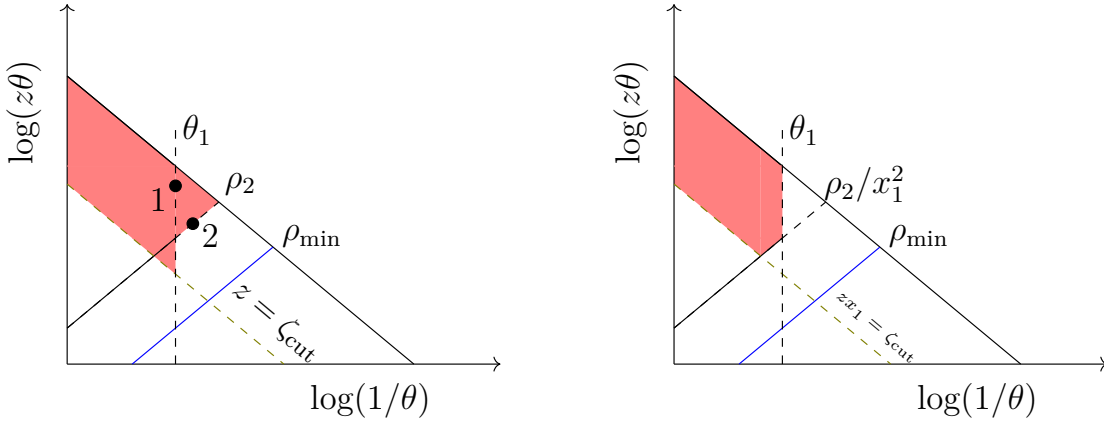
(a) Emissions from primary parton for the configuration $\rho \sim \rho_1 \gg \rho_2$.

(b) Emissions from secondary splitting, k_1.

Figure 6.4: The Lund planes for emissions from a primary parton and the first hardest splitting under the action of the `TopSplitter` tagging algorithm. The black points in Figure 6.4a illustrate the kinematics of the hardest emissions k_1 and k_2. Both emissions satisfy the ζ_{cut} condition shown in the green dashed line. The blue line represents the boundary of $z\theta^2 = \rho_{\text{min}}$, and the dashed green line depicts $z = \zeta_{\text{cut}}$ in Figure 6.4a and $zx_1 = \zeta_{\text{cut}}$ in Figure 6.4b. The vertical black dashed lines represents the boundary for which $\theta < \theta_1$, a requirement imposed on emissions due to angular ordering. The red shaded region corresponds to regions of phase-space which are vetoed by the tagging algorithm.

6.2.6 Results

The master equation for this analysis is Equation 6.30 which cannot be evaluated with a closed form solution. Instead the Monte Carlo based integration algorithm VEGAS was used [134]. An even grid of 350 points in ρ space were evaluated with 10^6 evaluations per value of ρ, and a warm-up number of 10^5 sampling points. VEGAS is most performant across the integration range $[0, 1]$, therefore the variables of integration in Equation 6.30 where transformed to have this numeric range.

Figure 6.5 shows the all order calculation of the jet mass distribution for a quark initiated jet after application of the Y_m splitter or `TopSplitter` taggers. The background selection efficiency, ϵ_b, of a tagger with fixed m_{min} parameter for jets in the mass range $m \in [m_{\text{low}}, m_{\text{high}}]$ is defined as

$$\epsilon_b = \frac{1}{\sigma_0} \int_{m_{\text{low}}}^{m_{\text{high}}} \left(\frac{d\sigma}{d\rho}\right) \left(\frac{2m}{p_{\text{T}}^2}\right) dm \tag{6.45}$$

$$= \frac{1}{\sigma_0} \int_{m_{\text{low}}}^{m_{\text{high}}} \left(\frac{d\sigma}{dm}\right) dm. \tag{6.46}$$

A mass window is placed around the top quark mass when assessing the selection efficiency, as is typical in tagging algorithms used in experiment.

The background selection efficiency was also evaluated using the PYTHIA 8 event generator. Simulated pp collisions with only the $q\bar{q} \to q\bar{q}$ matrix element were consid-
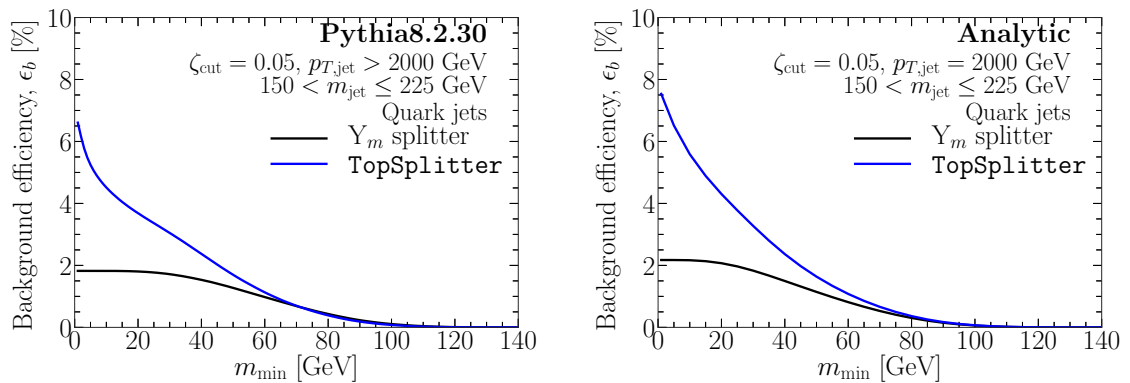
Figure 6.5: The background efficiency, ϵ_b, as a function of $m_{\min}$ cut for various taggers calculated analytically (left) and examined through the Monte Carlo event generator PYTHIA 8 (right).

ered at $\sqrt{s} = 13\,\text{TeV}$. Only jets with $p_T > 2\,\text{TeV}$ were evaluated. No hadronisation or under-lying event activity was considered.

Both the ordering of the tagger performance and approximate background rejection agrees well between PYTHIA 8 and the analytic calculation. The phenomenological region of $m_{\min} > 50$ shows excellent agreement, indicating the strong angular ordering assumption made within the PYTHIA 8 parton shower agrees well with the more precise triple-collinear limit.

6.3 All order calculation of top-tagged jets

The action of a tagging algorithm on the signal jet can be calculated using the same tools described above. However, instead of the splittings of a massless quark described by $\hat{P}_{1\to3}$, the decay products of a top quark must be considered as

$$
\begin{aligned}
\frac{1}{\sigma}\left(\frac{d\sigma}{d\rho}\right)^{\text{LO, signal}} &= \int d\Phi_3 \frac{|\mathcal{M}_{t\to bqq}|^2}{s_{123}^2}\Theta^{\text{jet}}\Theta^{\text{tagger}} \\
&\cdot\delta\left(\rho - \frac{s_{123}}{R^2 p_t^2}\right)\cdot\exp\left[-R_{\text{tagger}}^{\text{signal}}(\rho_1,\rho_2,\theta)\right],
\end{aligned}
\tag{6.47}
$$

where the matrix element for a top quark decay, $\mathcal{M}_{t\to bqq}$, is calculated at fixed electroweak coupling with an additional term in the W boson propagators, $m_t\Gamma_t$, that accounts for in flight on-shell decays [135].

Achieving leading logarithmic accuracy of the signal mass distribution is substantially more complicated than for QCD jets. The ordering of the three prongs found by the taggers' double declustering procedure will in general involve different combinations of the b and W decay products. Therefore, the matching between soft radiation and the hard process described by the matrix element is challenging. The non-trivial combinations of the emission from the W boson and the b quark prevent the systematic matching of a Sudakov factor to an arbitrary secondary emission. Additionally,
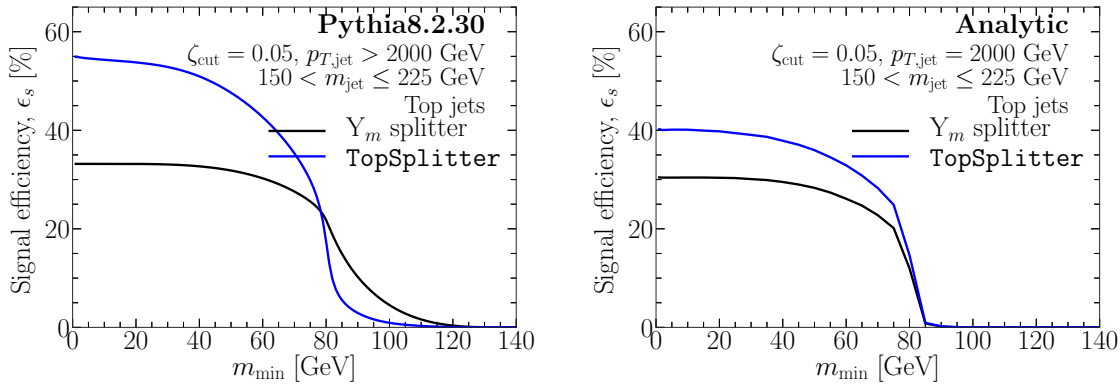
Figure 6.6: The signal efficiency, ϵ_s, as a function of $m_{\min}$ cut for various taggers calculated analytically (left) and examined through the Monte Carlo event generator PYTHIA 8 right).

soft gluon emissions in top productions and decay are well known to complicate the emission pattern for energies near or below the top width. In the extremely boosted regime, the dead-cone effect can be neglected, as the effect is relevant at an angular scale $\theta \ll \rho$. Instead of a general situation, the signal jet shall be considered in the limit where ρ_2 is always set by the W boson decay. At leading logarithmic accuracy in this limit, where only soft and collinear radiation is considered, all of these complications can be neglected.

Radiation of the top quark system can now be considered as originating from a single fast moving colour line in the jet direction. In this approximation the radiators for top jets under the application of `TopSplitter` and Y_m splitter are given by the primary radiators for each tagging algorithm

$$R^{\text{signal}}_{Y_m \text{ splitter}}(\rho_2) = R^{\text{primary}}_{Y_m \text{ splitter}}, \tag{6.48}$$

$$R^{\text{signal}}_{\texttt{TopSplitter}} = R^{\text{primary}}_{\texttt{TopSplitter}}. \tag{6.49}$$

Figure 6.6 compares the calculated signal efficiency for a fixed $m_{\min}$ parameter of the two top tagging algorithms with the PYTHIA 8 predictions for the same system. The signal efficiency is calculated in the same manner as the background efficiency, using Equation 6.46. The agreement between the analytic result and Monte Carlo is substantially poorer than the equivalent result for quark initiated jets. This is unsurprising given the higher accuracy of the quark initiated jet calculation. In particular soft gluon emissions from the top quark have been neglected in the analytics but are accounted for by PYTHIA 8. These emissions are known to have a strong effect on the radiative properties of the top quark.

6.4   Tagging efficiency

The performance of the tagging algorithms can now be understood with a ROC curve, relating the background selection efficiency to a given signal selection efficiency. Cru-
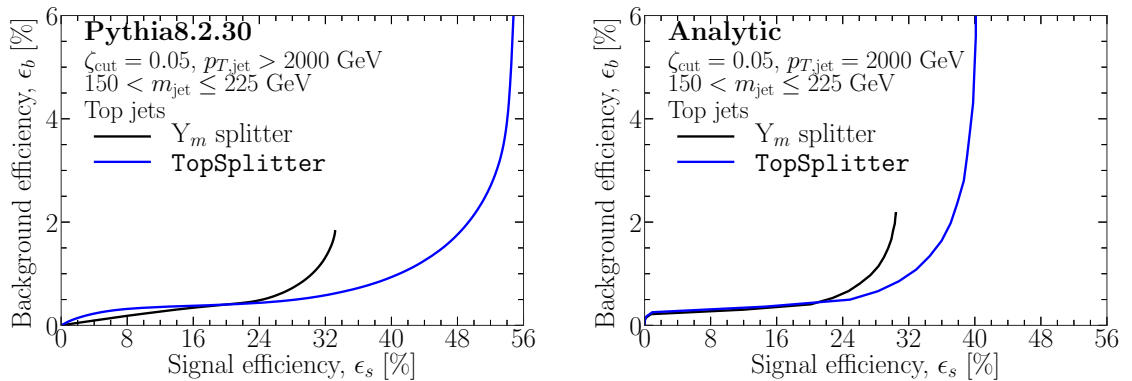
Figure 6.7: The ROC curves from varying the $m_{\min}$ cut for various taggers calculated analytically (right) and examined through the Monte Carlo event generator PYTHIA 8 (left). Figures 6.5 and Figure 6.6 show the input background and signal efficiency curves for the ROC curves presented here.

cially, this can be done using the analytic calculation for the background. The ROC curves for the Y_m splitter and `TopSplitter` algorithms, evaluated by varying $m_{\min}$, are presented in Figure 6.7, calculated with the analytic results discussed previously and PYTHIA 8.

As expected from the poor agreement of the signal efficiency curves in Figure 6.6, the analytics and MC predictions have broad disagreement over a range of signal efficiencies. This is most evident for the `TopSplitter` algorithm at high signal efficiency. The Y_m splitter algorithm also has a high signal efficiency disagreement. The general shape of the ROC curves and relative performance of the algorithms has been captured by the analytic description.

6.5 Conclusion

A novel approach to understanding top tagging algorithms has been presented and discussed. This affords a detailed understanding of the radiation of background and signal jets, which when compared to Monte Carlo highlight the approximations taken within MC that remain valid for phenomenological interesting regions of tagging parameters. An extension of the CMS tagger known as `TopSplitter` has been presented. Furthermore, the Y splitter tagging algorithm was extended for the case of three prong decays and a novel approach to the selection of a third prong presented. Y_m splitter was found to have strong tagging performance, better than the analytically motivated extension to the CMS top tagger, `TopSplitter`. Extending the methods presented here to include jet shape variables, such as energy correlation functions, would be an ideal direction of further study. Furthermore, the discrimination power of gluon initiated jets was not explored in this study, and as such is an important extension to this body of work.

7. Measuring the dead-cone

The radiation pattern of the top quark provides a unique avenue to understand QCD. The mass of the top quark is non-negligible at the energy scale of proton-proton collisions at the LHC. Therefore, the mass dependence of the radiation pattern of the top quark can be examined directly from analysis of LHC data. Radiation produced by a radiator with mass m and momentum p is suppressed for emission angles $\theta_d \lesssim m/|p|$, leading to the dead-cone effect [136]. The dead-cone is a fundamental prediction of QCD and other gauge theories, relying only on the behaviour of radiation from massive particles in the soft and collinear limit.

Recent measurements from the ATLAS collaboration of jet substructure variables [137] and of colour-flow [138] between jets have tested the structure of partonic splitting within and between clustered jets. The former found agreement of $\sim 15\%$ between data and Monte Carlo, while the latter found much stronger disagreement. It is clear that our understanding of partonic splitting in the busy hadronic environment produced in proton-proton collisions at the LHC is incomplete. Further studies of jet multiplicity and behaviour in the $t\bar{t} + 1$ jet environment tested the partonic splitting from heavy quarks in the formation of new jets [139, 140]. The expected jet multiplicity and kinematics of the system from precision NLO+NLL calculations were also found to differ substantially from the data. To understand QCD we must investigate more of its fundamental features, such as the dead-cone.

Rigorous testing of QCD predictions have thus far not yielded a definitive measurement of a dead-cone. Unfortunately, the angular scale of suppression is identical to the scale of the opening angle between decay products of a radiator, typically resulting in the dead-cone being filled by FSR from daughter particles. This has limited the interpretation of direct probes of the dead-cone using bottom and charm quarks that have been attempted, for example in e^+e^- collisions at the LEP collider [141] and proposals made with ep collisions at the HERA collider [142].

This thesis aims to perform a measurement of the dead-cone effect in the $t\bar{t} + 1$ jet system, where one of the top quarks decays leptonically. Previous phenomenological studies have shown that jet substructure techniques allow for a direct measurement of the effect with the data set expected to be recorded at the HL-LHC [51]. This chapter shall show that a simpler and novel measurement is possible with the Run II data currently recorded by the ATLAS detector through the use of an unfolded relative

differential cross-section measurement of the resolved $t\bar{t}$ system with an additional jet.

7.1   Analysis Strategy

To examine the radiative properties of a top quark, a measurement was performed of a newly defined variable

$$A_\theta = \frac{\theta - \theta_d}{\theta + \theta_d}, \tag{7.1}$$

where θ is the angular separation between a top quark and an identified radiative jet, and θ_d is the dead-cone angle. The dead-cone angle is defined as $m/|p|$, which can be approximated to m/E in the boosted limit. In this analysis the approximation was taken across the full kinematic range of measured top quarks and the measured energy and mass of the reconstructed top quarks were used when measured θ. For relatively low p_T top quarks, $p_T \sim 100\,\mathrm{GeV}$, early studies indicated m/E could be measured with better resolution than $m/|p|$. Furthermore, data and simulation are analysed in identical manners. Therefore, θ_d was taken as m/E for the entire measurement discussed in this chapter. By construction, A_θ is bounded to the range $[-1, 1]$. Massive radiators are expected to have a deficit of events in the region $A_\theta < 0$ compared to massless radiators, due to the dead-cone effect. Therefore the A_θ observable is expected to have large shape differences for massive and massless radiators. The relative A_θ differential cross-section, $\frac{1}{\sigma}\frac{d\sigma}{dA_\theta}$, was measured, where σ is the total $t\bar{t}$ production cross-section in the region of phase-space in which the measurement is performed. In effect, the shape of the A_θ distribution was measured. Measuring the shape reduces the total systematic uncertainty, as uncertainties that are uniform as a function of A_θ reduce to zero.

The measurement was structured in the following manner. First, a pre-selection is applied to recorded data to preferentially select $t\bar{t}$ events in the lepton+jets channel. The pre-selection criteria are described in Section 7.3. The kinematics of the $t\bar{t}$ system is then reconstructed in full from measured objects in the detector. The procedure used to perform this reconstruction is discussed in Section 7.4. Signal regions sensitive to the radiative properties of top quarks are then defined with the novel use of a machine learning optimisation procedure detailed in Section 7.5. The effects of the data and background contributions are removed using a statistical procedure known as *unfolding*. The measurement of $\frac{1}{\sigma}\frac{d\sigma}{dA_\theta}$, where $d\sigma$ is the $t\bar{t}$ differential cross-section at particle-level is then performed. The *particle-level* is defined as all detector-stable particles, with $c\tau >$ $10\,\mathrm{cm}$. The unfolding procedure and validation studies of the procedure are presented in Section 7.6. The systematic uncertainties on the measured cross section are evaluated and presented in Section 7.7, including examination of the bin-by-bin correlation of the measured A_θ distributions. Finally, the measurement is presented in Section 7.8. Interpretation of the results is discussed in Section 7.9, where methods of extracting a significance on the strength of angular suppression in the collinear region are proposed and performed.

7.2 Data and simulation

Data collected by the ATLAS detector in the years 2015 to 2018 at a centre of mass energy of $\sqrt{s} = 13\,\text{GeV}$ were used to measure the A_θ observable. The integrated luminosity of the dataset used in the measurement is $138.2\,\text{fb}^{-1}$. Events are only used if they were recorded with all detectors operational and with stable beam conditions.

7.2.1 Simulation

A full description of the physical processes in measured pp collisions facilitates comparison between prediction and data. Monte Carlo event generators using the multi-step procedure outlined in Section 2.3 were used to generate the samples described in Table 7.1. Simulation of pp collisions were crucial for the measurement presented in this chapter. They were used to estimate the number of events originating from background processes that pass the signal selection. The distortion of the A_θ observable induced by the detector was also studied using simulation. Finally, the size and impact of systematic uncertainties from a variety of sources were assessed using simulation.

Signal simulation

A nominal $t\bar{t}$ sample was chosen to model the effect of the detector on the measured A_θ distribution, including modelling the number of events that pass selection, and the size and shape of detector related uncertainties that affect the measurement. This nominal $t\bar{t}$ sample was generated with POWHEG for the NLO matrix element simulation and NNPDF for the parton density function. The hard scatter process was then interfaced with PYTHIA 8 for LO parton shower. The effects of the detector were simulated using GEANT4, discussed in Section 3.3. This sample was chosen as the nominal for consistency with other ATLAS top-quark measurements, and to utilise the extensive validation performed in those measurements.

The h_{damp} parameter controls the energy scale of the first emission beyond the LO configuration in $t\bar{t}$ simulation [143]. In the nominal $t\bar{t}$ sample, h_{damp} was taken to be $1.5m_{\text{top}}$. The choice of the radiation factorisation scale and the h_{damp} parameter were probed using the nominal sample. Historic studies have used alternative signal samples to examine these effects. However, recent advances in POWHEG+PYTHIA 8 have facilitated the use of a weight based procedure to probe the effect of theses choices. The procedure to estimate these uncertainties shall be discussed in more detail in Section 7.7.

It is important to emphasise that the analysis is based on the NLO POWHEG+PYTHIA 8 sample, which implicitly simulates the dead-cone effect within the NLO matrix element. PYTHIA 8 has the ability to switch the dead-cone effect on or off when used as an event generator at LO. However, because the dead-cone effect is an implicit component of the

NLO calculation, it cannot be "switched off" in an NLO calculation. Two LO PYTHIA 8 samples were used: one with the standard model hypothesis where the dead-cone effect is "on", and one with the dead-cone effect "off". The "on" (SM) sample is used to investigate the physics modelling differences between the PYTHIA 8 LO and NLO POWHEG+PYTHIA 8 samples. The "off" sample was used to investigate the effect of top-quark radiation in a scenario where radiation is generated as if the top quarks were massless. These samples are referred to as *dead-cone on* and *dead-cone off* respectively. These two samples were used to assess the size of the dead-cone effect, as measured by the A_θ observable, and their use is described further in Section 7.9.

Alternative signal samples

Additional $t\bar{t}$ samples were generated to study the effects of the modelling of the signal process on the measurement. One sample replaces the NLO ME generation, performed by POWHEG2 in the nominal $t\bar{t}$ sample, with MADGRAPH5_aMC@NLO. Another replaces the LO shower, performed by PYTHIA 8 in the nominal $t\bar{t}$ sample, with HERWIG 7. The effects of the detector were simulated using the AFII detector simulation, discussed in Section 3.3.

Pile-up simulation

To model the effect of pile-up in data events, multiple proton-proton collisions are simulated with the soft QCD processes of PYTHIA 8 [112] using the A2 tune [144], with the detector response simulated using GEANT4 [145]. These pileup events are overlaid on the signal and background processes during the digitisation simulation step, prior to reconstruction. During the analysis, MC events are then re-weighted, based on the simulated pileup profile, in order to match the one observed in data.

The simulated events are split into three different generation campaigns: MC16a, which models the 2015 and 2016 combined dataset; MC16d, which models the 2017 dataset; and MC16e which models the 2018 dataset. Each of these campaigns uses a different profile of pileup interactions which match the relevant running conditions at the time. MC16a events use a pileup profile which matches the distribution in data collected in 2015 and 2016. MC16d and MC16e events use a pileup profile which was based on the distribution of the actual number of interactions per bunch-crossing (rather than the average) in 2017 and 2018 data respectively, with some additional smearing applied.

Background simulation

All processes which produce a similar detector signature to the pair-produced $t\bar{t}$ system are considered sources of background. The lower panel of Table 7.1 gives a detailed description of the background samples used.

Process	Generators	Type	PDF	Tune	Detector simulation
$t\bar{t}$ (nominal)	Powheg2 [146–149]	NLO ME	NNPDF-3.0 [150]	-	
	+Pythia 8	+LO PS	NNPDF-2.3	A14 [151]	FS
	+EvtGen1.6.0	+HF decays	-	-	
$t\bar{t}$	Powheg2	NLO ME	NNPDF-3.0	-	
	+Herwig 7 [152, 153]	+LO PS		MMHT2014 [154]	AFII
	+EvtGen1.6.0	HF decays	-	-	
$t\bar{t}$	MadGraph5_aMC@NLO2.3.3 [155]	NLO ME	NNPDF-3.0	-	
	+Pythia 8	+LO PS		A14	AFII
	+EvtGen1.6.0	HF decays	-	-	
$t\bar{t}$ (dead-cone off)[†]	+Pythia 8	LO ME/PS	NNPDF-2.3	A14	
	+EvtGen1.2.0	HF decays	-	-	-
$t\bar{t}$ (dead-cone on)	+Pythia 8	LO ME/PS	NNPDF-2.3	A14	
	+EvtGen1.20	HF decays	-	-	-
Single top	Powheg2	NLO ME	NNPDF-3.0	-	
	+Pythia 8	+LO PS		A14	FS
	+EvtGen1.6.0	HF decays	-	-	
W/Z +jets	Sherpa 2.2.1	NLO ME	NNPDF-2.3.0	-	
		+LO PS		A14	FS
Diboson	Sherpa 2.2.1	NLO ME	NNPDF-3.0	-	
(WW, WZ, ZZ)		+LO PS		A14	FS
$t\bar{t}+V$	MadGraph5_aMC@NLO2.3.3	NLO ME	NNPDF-2.3.0	-	
($t\bar{t}W, t\bar{t}Z$)	+Pythia 8	+LO PS		A14	FS
	+EvtGen1.6.0	HF decays	-	-	

Table 7.1: A summary of the signal and background MC used in this analysis, shown in the upper and lower half of the table respectively. The effect of the detector was simulated with either Geant4, referred to as FullSim (FS), or with AltFastII (AFII). The MC generator used at each stage of simulation chain is specified using the abbreviations ME for Matrix element, PS for parton shower, and HF for heavy flavour decays. The LO dead-cone off sample denoted by [†] was generated with the setting `TimeShower:recoilDeadCone = off`.

In this analysis, the total estimated background is removed per bin of the observable in order to isolate the signal $t\bar{t}$ process. This procedure is known as background subtraction. To perform background subtraction samples were scaled to match the integrated luminosity of the data. Every MC sample used is normalised to the best-known SM prediction of the cross-section for the respective physics process. This is often referred to as a k-factor correction. The precision of the k-factor correction for each background process is given in Table 7.2. In addition to the pile-up reweighting, additional scale factors for leptons, b-jets and JVT are used to correct the performance of reconstruction algorithms in simulation to match the performance measured in data. The effects of the detector were simulated using Geant4 for all background samples.

Process	Precision	References
Top-pair	NNLO (QCD) + NNLL soft resummation	[42–45, 156–158]
Single-top	NLO (QCD)	[48, 49]
V + jets	NNLO (QCD)	[159]
Top-pair + V	NLO (QCD + EWK)	[160]
Diboson	n/a	n/a

Table 7.2: Summary of higher-order cross-section corrections applied to processes simulated for this analysis.

7.2.2 Fake background estimation

Signatures in the detector that do not originate from a lepton, but *are* reconstructed as one, are considered *fake* leptons. Fake and non-prompt leptons are a poorly modelled non-trivial background. A common source of fake electrons is misidentified jets that shower earlier than typical, and are consequently reconstructed as electrons. Fake muons can originate from particles that pass through the detector completely. These are known as punch-through particles. Punch-through particles can be produced from high energy hadronic showers. Leptons produced in the hard-scatter process are considered *prompt*, all other sources of lepton production are considered *non-prompt*. Non-prompt leptons, usually muons, may originate from heavy-flavour hadron decays within jets that pass isolation requirements, see Sections 4.2 and 4.3 for details on the lepton isolation. Furthermore, non-prompt electrons may occur from the early conversion of photons. The rate of the misidentification and reconstruction of fake and non-prompt leptons, collectively referred to as "fakes", is dependent on the specifics of the reconstruction algorithm and the detector instrumentation used. Therefore, modelling of this background using purely MC based methods is difficult and considered unreliable. A data-driven approach is used to assess the size of these backgrounds.

The *matrix method* [161, 162] is used to estimate the number of fake events occurring within the event selection. Two levels of lepton selection requirements are defined: *tight*, which corresponds to the nominal selection; and *loose*, with less stringent identification and isolation requirements. The tight and loose definitions used in this analysis are presented in Table 7.3. An inclusive data sample, S, is selected, where leptons fulfil either the loose or tight requirements. The set S can be decomposed into events that pass the tight requirements, T, and those that exclusively pass the loose requirements, L. In addition, S can be decomposed into events with real leptons, R, and with fake/non-prompt leptons, F, such that

$$T + L = S,$$
$$R + F = S. \tag{7.2}$$

The matrix method utilises this splitting of the inclusive data set, S, with the
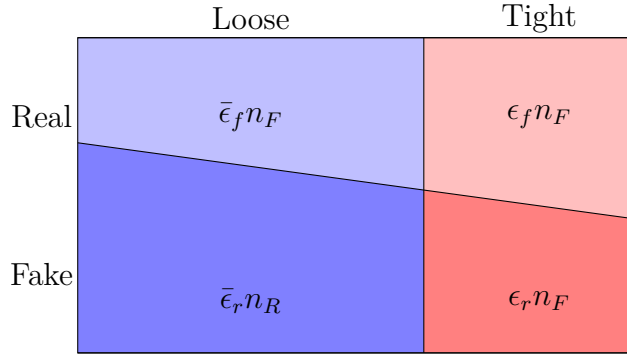
Figure 7.1: An illustration of the matrix method sample definitions.

formula

$$\begin{pmatrix} n_T \\ n_L \end{pmatrix} = \begin{pmatrix} \epsilon_R & \epsilon_F \\ \bar{\epsilon}_R & \bar{\epsilon}_F \end{pmatrix} \begin{pmatrix} n_R \\ n_F \end{pmatrix},$$ (7.3)

where n_T and n_L are the number of events passing the tight and loose selection, respectively. The real and fake efficiency parameters, ϵ_R, and ϵ_F, respectively, quantify the number of real and fake events that pass the tight selection criteria relative to the loose selection criteria. Figure 7.1 illustrates the set of all measured events, and how the real and fake efficiency parameters used in Equation 7.3 are defined.

The real and fake efficiencies are parameterised in variables that capture the likelihood of an event containing a fake lepton, such as the transverse momentum of the leading jet, or the pseudo-rapidity of the lepton. The efficiencies are expected to depend on the topology of an event. Therefore, combining multiple parameterisations can capture analysis-specific event topologies and selections. An arbitrary number, n, of parameterisations, ϵ_k, can be combined multiplicatively as

$$\epsilon_{\text{combined}} = \frac{1}{\epsilon_0^{n-1}} \cdot \prod_{k=1}^{n} \epsilon_k.$$ (7.4)

The combination procedure introduces an order dependence on the parameterisation combination. The first paramaterisation, ϵ_0, is used to average all subsequent parameterisations. This combination procedure was introduced in Reference [162], where it is argued that the combination conserves correlations between parameterisations of continuous and discrete variables. Unfortunately, Equation 7.4 may result in pathological fake estimates as $\epsilon_{\text{combined}}$ is not bounded to the region $[0, 1]$. The choice of parameterisation, or multiple parameterisations, is discussed in Section 7.2.2.

After an appropriate parameterisation of the real and fake efficiencies is chosen and measured, the fake background can be estimated. The expected number of fake events that passes the tight selection, $\hat{n}_{T,F}$, can be estimated by inverting Equation 7.3 to find

$$\hat{n}_{T,F} = \epsilon_F n_F = \frac{\epsilon_f}{\epsilon_r - \epsilon_f}(\epsilon_r(n_T + n_L) - n_T).$$ (7.5)

	Loose Lepton	Tight Lepton
Lepton Isolation	None	GRADIENT
Electron Identification	MEDIUMLH	TIGHTLH
Muon Identification	MEDIUM	MEDIUM

Table 7.3: The tight and loose lepton requirements used within the matrix method for the fake/non-prompt background contribution estimate. See Reference [94] for more details on the definition of these terms.

The fake contribution can be estimated per bin of an arbitrary distribution by using an event-by-event weight

$$w_e = \frac{\epsilon_F}{\epsilon_R - \epsilon_F}(\epsilon_R - \delta_{e \in T}), \tag{7.6}$$

where $\delta_{e \in T} = 1$ if the event, e, satisfies the tight lepton requirements and zero otherwise. The total contribution of the fake lepton background can be calculated by evaluating the sum of w_e over all events passing the loose lepton requirements. Utilising the event-by-event weights the shape of the fake background contribution in the signal region can be evaluated in terms of the variable of interest, A_θ.

Fake parameterisation evaluation

The real efficiency, ϵ_r, was measured using a tag-and-probe method in $Z \to ee$ and $Z \to \mu\mu$ events. Control regions were constructed such that the mass of the lepton pair was close to that of the Z boson. Hence, by construction the overwhelming majority of measured leptonic pairs were composed of two real leptons. One lepton in each event was considered to be the tag, and required to pass the tight lepton requirements. The other lepton in the di-leptonic Z boson event was required to pass the loose lepton requirements. This selection methodology allowed an unbiased sample of loose leptons to be constructed. The tight selection criteria was applied to the real loose leptons, and the efficiency measured as

$$\epsilon_r = \frac{\text{Number of tight probe leptons}}{\text{Number of observed probe leptons}} \tag{7.7}$$

To ensure maximal utility of the measured real efficiency, the event selection criteria for the leptons was chosen to be looser than that of a typical physics analysis.

The fake efficiencies were measured in data samples in control regions (CRs) dominated by non-prompt and fake leptons. The control regions contain at least one loose lepton, and at least one jet. The electron control regions require a low missing transverse energy, whereas the muon control regions require muons with a large track impact parameter, d_0^{sig}. The tight selection criteria was applied to the fake loose lepton, and the fake efficiency was measured as

$$\epsilon_f = \frac{\text{Number of events in fake lepton CR with a tight Lepton}}{\text{Number of events in fake lepton CR}}. \tag{7.8}$$

The full procedure is described in Reference [162].

Fake parameterisation choice

The real and fake efficiencies can be parameterised using one of the following variables: lepton transverse momentum, p_T^{lep}; leading jet transverse momentum, p_T^{jet}; lepton pseudo-rapidity, η^{lep}; the $\Delta\phi$ between the missing transverse energy and the lepton, $\Delta\phi(\ell, \vec{/}E_t)$; and finally, the ΔR between the lepton and leading jet in an event, $\Delta R(\ell, j)$. The parameterisation choice should, in principle, not impact upon the estimation in a substantial manner. The event topology used to measure the efficiencies differs from the event topology of the A_θ measurement. Therefore, parameterisations using variables that have similar behaviour in both topologies are expected to characterise the fake background better than those that do not. Combinations of different efficiency parameterisation is also possible. Only 28 combinations are allowed due to the order dependence of combination in the implementation of the matrix method. However, in practice, not all parameterisations are suitable. A short-list of acceptable parameterisations is evaluated by insisting on the following requirements for a given parameterisation option:

1. All real efficiencies, $\epsilon^{\text{real}} < 1.0$.

2. A positive number of events in all bins of the detector-level A_θ distribution for the pre-selection and signal regions.

Requiring the real efficiency to be within the range $[0, 1]$ is necessary due to the averaging method used to combine different parameterisations, which does not guarantee that $\epsilon^{\text{real}} < 1.0$. These requirements leave a total of six parameterisations. The nominal choice of a fake efficiency parameterisation was chosen as $p_T^{\text{lep}} \otimes p_T^{\text{jet}} \otimes \Delta R(\ell, j)$ for electrons and $\eta^{\text{lep}} \otimes p_T^{\text{jet}}$ for muons. The choice of a single parameterisation is arbitrary, and so a systematic uncertainty that covers the differences between the nominal parameterisation and the parameterisation with the largest difference in yield to the nominal is introduced.

7.3   Event selection

Events are initially required to satisfy general data quality criteria. At least one primary vertex with two associated tracks is required to have been reconstructed. For recorded data, stable-beam conditions and good detector performance criteria were required. Events were rejected if any jets fail the `LooseBad` jet cleaning working point, described in Section 4.4.3.

Further to these generic selection criteria, all events are required to satisfy the requirements summarised in Table 7.4. Events are initially required to have fired one of the lepton triggers described in Table 7.5. The trigger menu was updated year-on-year,

therefore the exact trigger selection used was year dependent. Events are then selected based on reconstructed physics objects, described in Chapter 4. Events are required to have exactly one lepton (electron or muon) with p_T greater than $27\,\text{GeV}$ which is also matched to an appropriate HLT trigger. The $27\,\text{GeV}$ minimum p_T requirement ensured the lepton triggers used were fully efficient across the full dataset examined. Events are also required to have exactly five jets with p_T greater than $25\,\text{GeV}$, of which at least two must be b-tagged using the 85% working point of the MV2c10 b-tagging algorithm. The 85% working point is used over the more commonly used 77% and 70% working points in order to increase the available statistics in the analysis. The double b-tag still effectively suppresses background, even at this highly efficient working point.

Selection Criteria	Reconstruction Level	Particle Level
Number of leptons ($p_T \geq 27\,\text{GeV}$)	$= 1$	$= 1$
Number of jets ($p_T \geq 25\,\text{GeV}$)	$= 5$	$= 5$
Number of b-tagged jets	≥ 2	≥ 2
Missing E_t	$\geq 25\,\text{GeV}$	$\geq 25\,\text{GeV}$

Table 7.4: The basic event selection for all events considered at both particle and reconstruction level.

Year	e+jets channel	μ+jets channel
2015	HLT_e24_lhmedium_L1EM20VH	HLT_mu20_iloose_L1MU15
	HLT_e60_lhmedium	HLT_mu50
	HLT_e120_lhloose	
2016/2017/2018	HLT_e26_lhtight_nod0_ivarloose	HLT_mu26_ivarmedium
	HLT_e60_lhmedium_nod0	HLT_mu50
	HLT_e140_lhloose_nod0	HLT_mu60_0eta105_msonly[†]

Table 7.5: The triggers that are required to have been fired for the years 2015 and 2016/2017 in the e+jets and μ+jets selection channels.
[†] Applies to 2017 and 2018 data only.

The number of events passing selection was measured and compared to the prediction, shown in Table 7.6. The total expectation is in good agreement with the observed number of events within the statistical and systematic uncertainties. The most prominent source of background contamination is from the W+jets and Single top background sources. As the dead-cone effect is a subtle effect, that is expected to be visible in only a small subset of produced $t\bar{t}$ pairs at the LHC, loose pre-selection criteria were chosen. Therefore, a relatively large contribution of background processes is expected.

Figure 7.2 shows the kinematics of a selection of physics objects with the criteria in Table 7.4 applied. In all cases the agreement between data and simulation is well

Process	Yield	Uncertainty
$t\bar{t}$	1525650.9	318579.3
W+jets	108405.1	63553.5
Single top	60796.3	13150.6
Fakes	50508.0	10628.5
Z+jets	19589.3	4177.0
$t\bar{t}$ + V	6368.3	1347.2
Diboson	5618.6	1188.8
Total Prediction	1776936.5	412624.9
Data	1818896.0	-

Table 7.6: Yield table for the inclusive selection defined in Table 7.4 including statistical and systematic uncertainties. The background process cross-section uncertainties and full detector uncertainties are combined in quadrature with the statical uncertainty on the prediction and presented in the rightmost column. These systematic uncertainties are defined in more detail in Section 7.7.

within the statistical and systematic uncertainty. The measured $E_{\mathrm{T}}^{\mathrm{miss}}$ distribution has a slight shape disagreement compared to prediction, at high $E_{\mathrm{T}}^{\mathrm{miss}}$ there is an observed deficit. The deficit is covered by systematic uncertainties arising from modelling of the $t\bar{t}$ system, therefore this level of disagreement is accounted for within the analysis.

(a) e p_T

(b) e η

(c) Missing E_T

(d) μ p_T

(e) μ η

(f) b-jet multiplicity

(g) Leading jet p_T

(h) Leading jet η
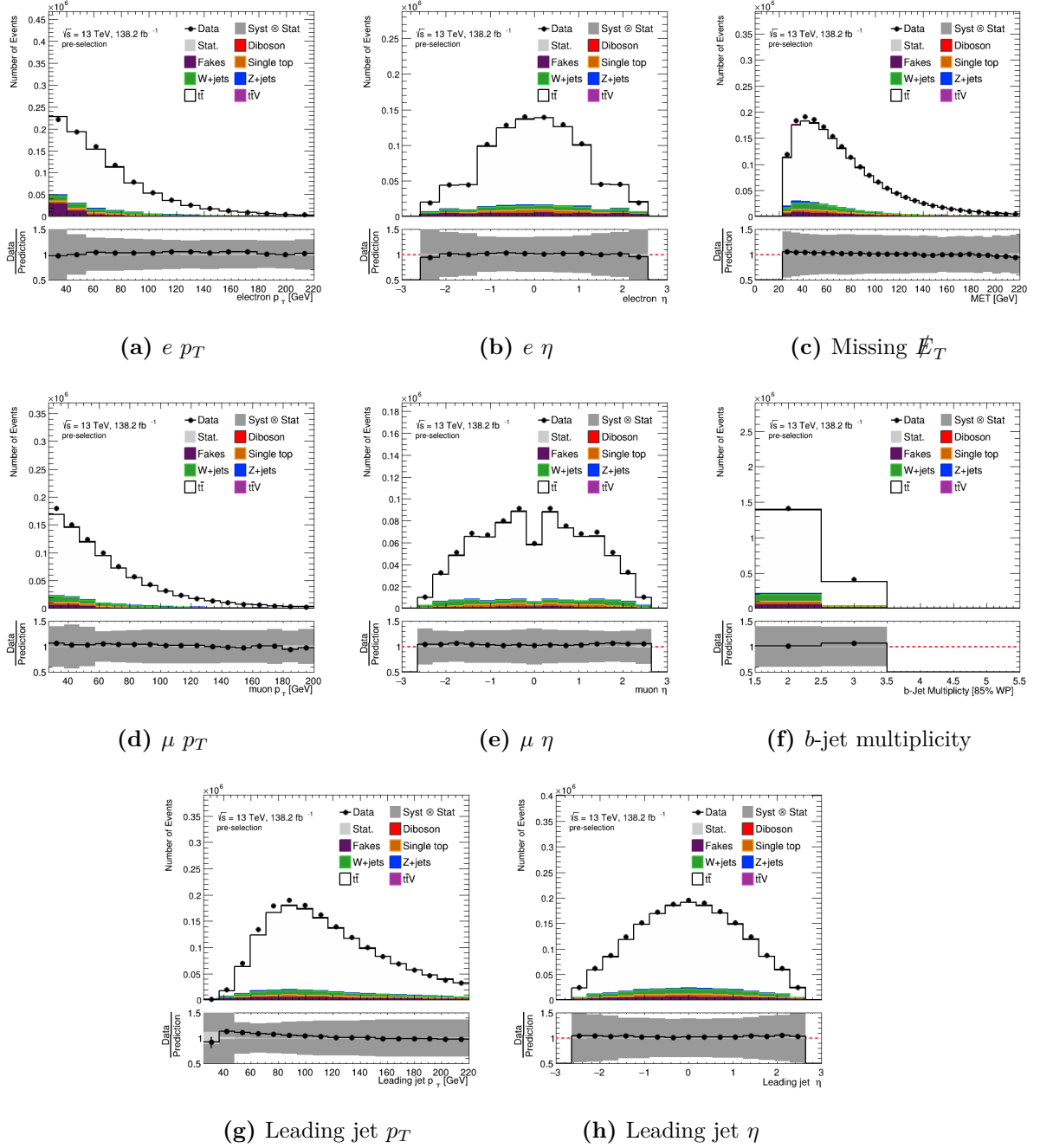
Figure 7.2: Kinematic distributions of physics objects in the pre-selection.

7.4 $t\bar{t}$ reconstruction method

Each event in the desired lepton+jets $t\bar{t}$ topology contains two tops: one hadronically decaying, and one leptonically decaying. Both top quarks can be used to measure the dead-cone, and hence the full four momenta of the tops in the $t\bar{t}$ system are required for this analysis. Events are required to have exactly five jets, of which four will be used to reconstruct the $t\bar{t}$ system. The remaining jet is considered the radiative jet, and assumed to be emitted from a top quark. The angular separation between a reconstructed top and the radiative jet, θ, is used in the construction of the A_θ observable. Two methods of reconstructing the $t\bar{t}$ system in full were explored and compared: the pseudo-top reconstruction algorithm, and the χ^2 method. The optimal method, χ^2, was selected and used in the measurement of A_θ.

7.4.1   Pseudo-top reconstruction

The LHC top working group has defined a general purpose method of reconstructing top quarks in the lepton+jets event topology known as the *pseudo-top* reconstruction algorithm [163]. The pseudo-top reconstruction algorithm applied to events selected with the requirements given in Table 7.4 is executed in the following manner:

- *b*-**jet selection:** Select the two highest *b*-jets as those originating from the decay of the two top quarks in the system.

- **Leptonic** W **boson reconstruction:** The neutrino transverse momentum is assumed to correspond exactly to the missing transverse energy. The on-shell mass constraint of the W boson and negligible mass of the neutrino are used to constrain the neutrino-lepton system and calculate the longitudinal neutrino momentum, p_z^ν. This results in a two-fold ambiguity for real solutions. In such circumstances, the solution with larger $|p_Z^\nu|$ is chosen. For complex solutions of p_Z^ν, the real part of the total solution is used. The leptonically decaying W boson is then reconstructed using the lepton momentum and calculated neutrino momentum.

- **Hadronic** W **boson reconstruction:** Combine the two highest p_T jets in the events, excluding the selected *b*-jets.

- **Top quark reconstruction:** Combine the *b*-jet closest to the lepton with the reconstructed leptonic W boson to form the leptonically decaying top quark. Combine the remaining selected *b*-jet with the hadronic W boson to reconstruct the hadronically decaying top quark.

7.4.2   The χ^2 $t\bar{t}$ reconstruction method

The χ^2-method attempts to reconstruct the $t\bar{t}$ system by evaluating all allowed permutations of jet-to-top matching. From this a χ^2 metric can be constructed and minimised. This is equivalent to the KL Fitter method in the limit where no transfer functions are considered [164]. The method proceeds as follows:

- **Leptonic W boson reconstruction:** The leptonic W boson is reconstructed using the on-shell mass constraint to reconstruct the longitudinal momentum from the missing transverse energy in the same manner as the pseudo-top reconstruction procedure.

- **Jet Assignment:** All possible matchings between jets and top quarks are considered. In a given permutation, 2 b-jets are first selected as those originating from the top quarks. For events with 2 b-jets, there are 2 possible b-jet permutations. For events with 3 b-jets, there are $3! = 6$. There are $3!$ permutations of the remaining three jets. Two of these jets are associated to the hadronically decaying W boson and the third considered as the radiative jet. The four momenta of each top quark is calculated for each permutation. The following χ^2_{reco} variable is evaluated, and the permutation with the minimal χ^2_{reco} selected:

$$\chi^2_{\mathrm{reco}} = \left(\frac{m_{\mathrm{top}} - m_{\mathrm{leptonic\ top}}^{\mathrm{reco}}}{\Gamma_{\mathrm{top}}}\right)^2 + \left(\frac{m_{\mathrm{top}} - m_{\mathrm{hadronic\ top}}^{\mathrm{reco}}}{\Gamma_{\mathrm{top}}}\right)^2 + \left(\frac{m_{\mathrm{W}} - m_{\mathrm{hadronic\ W}}^{\mathrm{reco}}}{\Gamma_{\mathrm{W}}}\right)^2,$$

(7.9)

  where $m_{\mathrm{top}} = 172.44$ GeV, $\Gamma_{\mathrm{top}} = 1.35$ GeV, $m_{\mathrm{W}} = 80.385$ GeV and $\Gamma_{\mathrm{W}} = 2.085$ GeV. With the exception of the top quark mass, these values are all the world averages of these quantities [165, 166]. The top quark mass was taken as the value used in generating the nominal MC. Only the mass is calculated for the hadronically decaying W boson, so swapping the two jets matched to the W will result in the same χ^2_{reco}. As such, the number of permutations required to be evaluated is halved. The remaining jet is taken to be the radiated jet and is paired to the top quark closest in (η, ϕ) space.

- **Top quark reconstruction:** Using the permutation of jets which minimises the χ^2, the decay products of the leptonic and hadronic top quarks are identified. The four-momenta of these objects are then summed to reconstruct the four-momentum of the leptonic and hadronic top-quarks.

7.4.3 $t\bar{t}$ method comparisons

Due to the ambiguity of defining a gluon jet originating from the top-quark before decay at parton-level, the choice of reconstruction method was made based on the resolution of variables defined between parton- and particle-level top quarks. The ratio of partonic
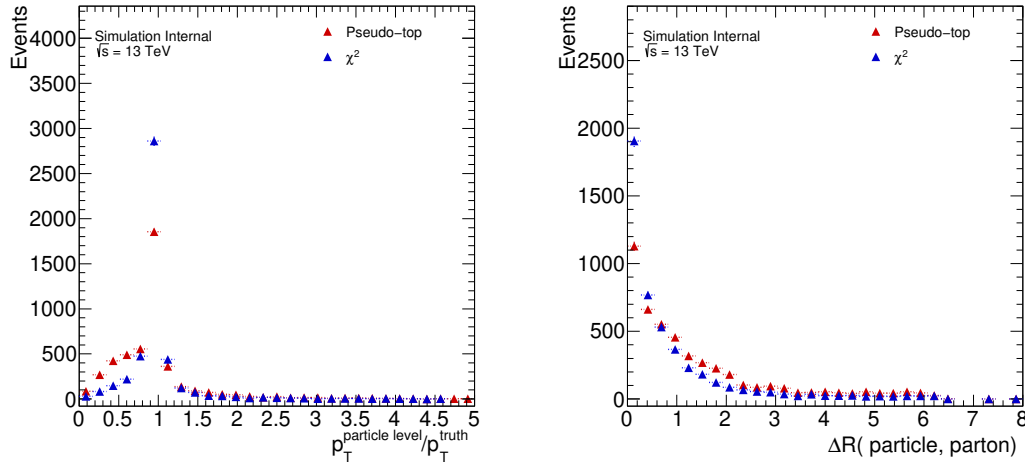
Figure 7.3: The p_T and angular resolution of the reconstructed top at particle-level using the χ^2 method for jet assignment compared to the LHC WG pseudo-top algorithm. The resolution is shown for an inclusive selection of events and measured between the four-momenta of the last top in the decay at parton level and the reconstructed particle-level object.

and particle-level p_T and the angular separation, ΔR, is shown in Figure 7.3 for the χ^2 and pseudo-top algorithms. The χ^2 recovers the partonic top angular position and p_T at a higher rate than the pseudo-top algorithm. Therefore, the χ^2 method was chosen as the reconstruction algorithm used in the measurement of the A_θ variable.

The agreement between data and prediction of the minimum χ^2_{reco} for each reconstructed event is shown in Figure 7.4. A flat normalisation difference is observed, as expected from the difference in data and predicted yields noted previously. However, there are no shape differences as a function of χ^2_{reco}. Therefore, the reconstruction of top quarks across a range of kinematic combinations is described well by prediction compared to the data. Furthermore, the transverse momentum and mass of the leptonic and hadronic top quarks reconstructed using the χ^2 method agrees with data within 10%, shown in Figure 7.4. The relative deficit of data at high top quark p_T is expected from previous measurements of the top quark's differential cross-section measurements [139]. All distributions agree within the systematic uncertainties of the system, discussed in detail in Section 7.7.

(a) leptonic top quark p_T

(b) hadronic top quark p_T

(c) leptonic top quark mass

(d) hadronic top quark mass

(e) χ^2_{reco}
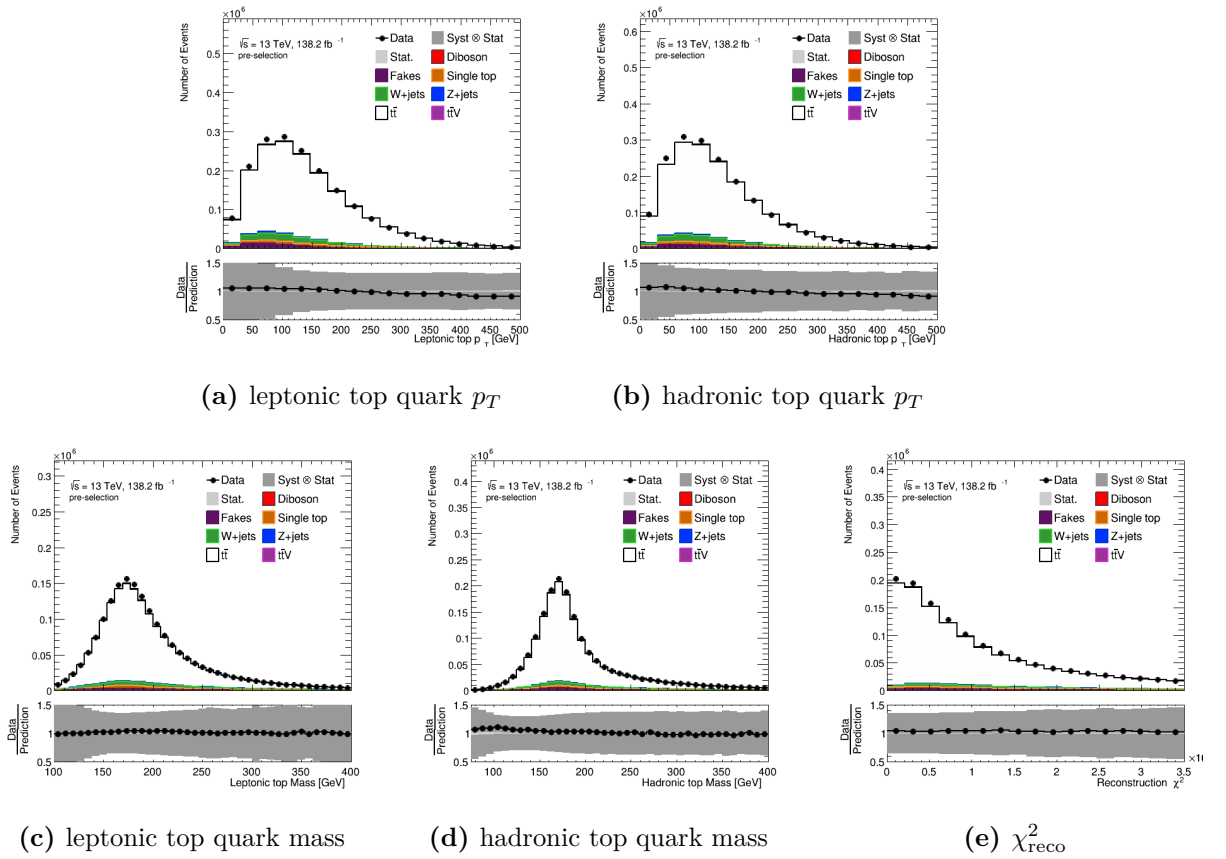
Figure 7.4: Measured kinematic distributions for events reconstructed with the χ^2 method, described in the text, for the reconstructed leptonic top and hadronic top for the transverse momentum and mass

7.5   Optimisation of measurement regions

After the generic event selection detailed in Table 7.4, signal regions were defined that have maximal sensitivity to the dead-cone effect. This sub-section details a generic procedure to optimise the signal region of a physics analysis, and then discuss the specific example of optimising the signal regions used in the measurement of the A_θ observable. Measurements performed at the LHC have, in general, many free parameters that must be decided by the analysers. The region of phase-space for which an analysis is performed is a set of free parameters that must be chosen for each measurement. When performing a measurement, the smallest systematic and statistical uncertainty is desired. The systematic and statistical uncertainty of a measurement often depends on the region of phase-space in which a measurement is performed. Therefore, measurements at the LHC typically chose event selection criteria that define a region of phase space which minimises the combined systematic and statistical uncertainty. Evaluating the region of most sensitivity is challenging; first a metric, p, that quantifies the sensitivity of a measurement must be chosen. The sensitivity metric must then be optimised with respect to phase-space restrictions, $\mathcal{R}$, that define the measurement region for the analysis. A single evaluation of the sensitivity metric corresponds to performing a complete measurement with pseudo-data, including evaluation of all relevant systematic uncertainties. This can be computationally expensive, therefore the number of sampled phase-space restrictions is necessarily small. Optimisation is typically performed using a set of pseudo-data to avoid biasing the measurement.

Whilst a physicist might have an intuition on a sensible choice of $\mathcal{R}$, it is difficult to systematically asses the *optimal* choice. Conventional optimisation methods rely on *gradient descent* based algorithms [167], where free parameters are iteratively updated in a direction in parameter-space that minimises a loss function, L. A loss function characterises the difference between the performance of an algorithm with a set of parameters and the desired performance. In this instance $L \equiv L(p - p^{\mathrm{max}})$, where p^{max} is the unknown maximum sensitivity of an analysis. Due to the computational limitation of evaluating a large number of restrictions $\mathcal{R}$, the gradient of the loss function cannot be estimated for measurement region optimisation.

One could also attempt to apply a maximum likelihood method [168] to estimate the ideal set of phase-space restrictions for an algorithm. However, such methods typically require an analytic expression for the dependence of the sensitivity metric, p, on the restrictions, $\mathcal{R}$, $p(\mathcal{R})$. Due to the complications of a physics analysis - e.g detector simulation, background contamination, or reconstruction efficiencies - $p(\mathcal{R})$ may only be probed through direct evaluation of p for a trial $\mathcal{R}$. Therefore, conventional likelihood maximisation is also not possible.

Gradient-free black box optimisation procedures are a class of optimisation algorithms that specialise in the evaluation of unknown functions (black box), without

evaluation of any derivatives of the optimisation metric. *Bayesian optimisation with Gaussian Processes* (BayesOpt) is one such procedure. It has come to prominence recently as a method of optimising the hyper-parameters of machine learning algorithms [169]. This section shall define BayesOpt, and give a simple one dimensional example. BayesOpt shall be applied to optimise the signal regions used in measuring A_θ. The description of BayesOpt is restricted to what is necessary to perform an optimisation of the measurement region of physics analysis. A more thorough description of the procedure can be found in Reference [170].

Bayesian optimisation with Gaussian processes

BayesOpt shall now be formally defined and used to evaluate the maximum of an unknown function. Consider an input space, $\mathbb{X}$, and a target space, $\mathbb{Y}$. Let $\mathcal{D}$ represent a set of noisy data evaluated at a set of points in the input space, such that $d(x) \in \mathcal{D} \subset \mathcal{Y}$ and $x \in \mathbb{X}$. The maxima of the unknown function that describes the data, $f : x \rightarrow d$, is sought. Bayes' theorem can be used to construct an expression for the most probable function f given the set of observed data

$$p(f|\mathcal{D}) = \frac{p(f)p(\mathcal{D}|f)}{p(\mathcal{D})} \ , \tag{7.10}$$

where the prior, $p(\mathcal{D})$, is a Gaussian Process. The posterior, $p(f|\mathcal{D})$, can be used to estimate the extrema of $f(x)$. BayesOpt is a procedure that evaluates the posterior function given a set of observations, and then uses the posterior to evaluate a point in target space that increases the knowledge of the unknown function maximally.

A Gaussian Process, $\mathcal{GP}$ is a family of random variables, $\{X_\mathbb{X}\}$, all defined in the same probability space, such that for any finite subset, $\mathbb{S} \subset \mathbb{X}$, any random vectors drawn from the Gaussian Process, $\{X_s\} \in \mathbb{S}$, have a joint Gaussian distribution [170]. Gaussian processes can be viewed as infinite dimensional multi-variate Gaussian distributions, and are completely defined by a mean function, μ_o, and covariance function (or kernel), Σ_0. The covariance expresses the dependence of every point in the input space on every other point in the input space, and represents how smoothly the function f varies point-to-point in input space.

Only finite vectors drawn from a Gaussian Process are relevant for an optimisation. Consider the value of f at a finite collection of points $x_1, ..., x_k \in \mathbb{X}$. The value of the function to be estimated at these points is $f(x_1), ..., f(x_l) \in \mathbb{Y}$. Suppose the vector $[f(x_1), ..., f(x_k)]$ is drawn from a random probability distribution. This prior distribution can be constructed with a Gaussian Process. Constructing the prior corresponds to evaluating a multi-variate Gaussian distribution, $\mathcal{N}(\mu_0, \Sigma_0)$, with a mean function evaluated at each point in the input vector, x_i, and a covariance function evaluated for each pair of points x_i, x_j. The prior distribution is therefore [171]

$$p(f(x_{1:k})) \sim \mathcal{N}(\mu_0(x_{1:k})), \Sigma_0(x_{1:k}, x_{1:k}), \tag{7.11}$$
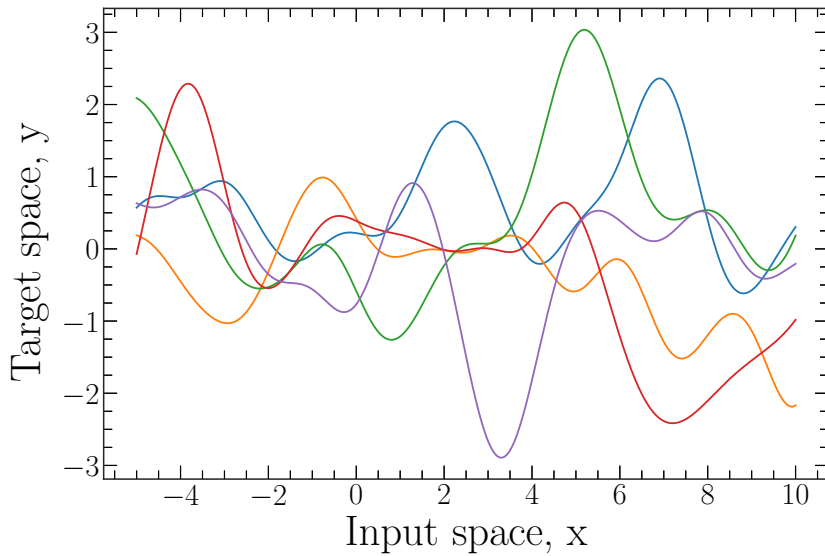
Figure 7.5: Four random vectors drawn from a Gaussian Process with zero mean and a radial basis covariance, defined in Equation 7.18.

where *compact* notation for functions has been used: $x_{1:k}$ indicates the inputs $x_1, ..., x_k$, $f(x_{1:k}) = [f(x_1), ..., f(x_k)]$, $\mu_0(x_{1:k}) = [\mu_0(x_1), ..., \mu_0(x_k)]$, and $\Sigma_0(x_{1:k}, x_{1:k}) = [\Sigma_0(x_1, x_1), ..., \Sigma_0(x_1, x_k); ...; \Sigma_0(x_k, x_1), ..., \sigma_0(x_k, x_k)]$. An example of four such randomly drawn vectors across an arbitrary input space are shown in Figure 7.5 for a Gaussian Process with a mean function of 0 for all $x \in \mathbb{X}$.

Now suppose $f(x_{1:n})$ is observed. For some n, the value of $f(x)$ at some new point x is desired. The posterior probability distribution can be calculated by marginalizing the prior with respect to the observed points $f(x_{1:n})$. Consider $f(x)$ taking an arbitrary value y in target space. The probability that $f(x) = y$ is found to be described by a traditional one-dimensional Gaussian distribution, $N(\mu, \sigma^2)$, with mean and variance set by the underlying Gaussian Process is [170]:

$$p(f(x)|f(x_{1:n})) \sim N(\mu_n(x), \sigma_n^2(x)), \tag{7.12}$$

$$\mu_n(x) = \Sigma_0(x, x_{1:n})\Sigma_0(x_{1:n}, x_{1:n})^{-1}(f(x_{1:n} - \mu_0(x_{1:n})))$$

$$+ \mu_0(x), \tag{7.13}$$

$$\sigma_n^2(x) = \Sigma_0(x, x) - \Sigma_0(x, x_{1:n})\Sigma_0(x_{1:n}, x_{1:n})^{-1}\Sigma_0(x_{1:n}, x). \tag{7.14}$$

For every point x in the input space $\mathbb{X}$ the probability of observing $f(x)$ at a given y in target space $\mathbb{Y}$ is described using Equation 7.12. The posterior mean function $\mu_n(x)$ describes the most probable distribution of the unknown function $f(x)$, given the observed data. The variance function $\sigma_n^2(x)$ can be used to define confidence intervals around this mean function as a function of x.

An iterative procedure to evaluate the maxima of a function using Gaussian Processes and Bayes Theorem can now be established. An *acquisition function* is constructed to effectively select a location in input space that increases the knowledge of

$f(x)$ maximally. The Bayesian description of most probable values of f across all of target space $\mathbb{Y}$ allows an acquisition function to be meaningfully defined. This is the true power of BayesOpt. The form of the acquisition function is a free choice of the method. In this analysis only the *expected improvement* function shall be considered, defined as [171]

$$u_{\text{EI}}(x) = E_n[\max(0, f^{\text{max}} - f(x))|x_{1:n}, f(x_{1:n})] \tag{7.15}$$

$$f^{\text{max}} = \max(f(x_{1:n})). \tag{7.16}$$

The expected improvement acquisition function can be understood as the expected improvement in the maximum observed value of f, given the current observed maximum f^{max}. The expected improvement is largest where the posterior mean is larger than the current largest observation. The expectation taken over probability space at point x in Equation 7.15 has a closed form solution, originally evaluated (to the author's knowledge) in Reference [172] and popularised in Reference [173]. Finally, the next point in input space that the algorithm samples, x^{next}, is that which maximises the acquisition function

$$x^{\text{next}} = \arg\max_{x \in \mathbb{X}}(u_{\text{EI}}(x)). \tag{7.17}$$

The Bayesian optimisation procedure, used to evaluate the maxima of an unknown function f can now be summarised as in Figure 7.6 [171]. A burn-in period of n_0 trial evaluations is performed. The location of the burn-in evaluations can be chosen either randomly or using prior knowledge of the system.

The application of this procedure to an arbitrary target function is shown in Figure 7.7. At all times the posterior mean passes through all observed values of the target function. As the algorithm progresses, points are sampled preferentially in the vicinity regions of local extrema, for example the points sampled in the region $x \in [4, 7]$ and $x \in [1, 2.5]$. Regions of small gradient are sampled less, as can been seen from the lack of sampling in the region $x \in [6, 8]$. The choice of prior sets the length scale of the exploration between evaluated points. After 14 iterations, the BayesOpt algorithm has evaluated the maximal value of the target function. With the chosen prior, further evaluation of the acquisition yields points close to this evaluated maxima at $x = 2.0$. This example therefore can never resolve maxima with a width $\ll 1$. The dependence of the evaluated maximum on the length scale used to probe the input space is a fundamental limitation of any systematic sampling of an unknown function, hence is unavoidable in BayesOpt.

Hyper-parameters of BayesOpt

BayesOpt has found wide-spread usage as a method of optimising the hyper-parameters in machine learning problems. Ironically, the BayesOpt procedure itself has a set of

---

BayesOpt: Evaluating the maximum of unknown function f

Place a Gaussian process prior on f

Observe f at n_0 initial points, some times referred to as *burn-in*. Set $n = n_0$.

while $n \leq N$ **do**

    Update posterior distribution on f using all available data.

    Compute the acquisition function across the input space.

    Evaluate the position input space, x_{n+1}, that maximises the acquisition function.

    Observe $y_n = f(x_n)$

    Increment n

end while

Return either:

    The maximum evaluated $f(x_{1:n})$.

    or The maximum of the posterior mean, $\mu_N(x)$.

Figure 7.6: The BayesOpt procedure for evaluating the maximum of an unknown function. An initial burn-in period of n_0 iterations is considered. The algorithm evaluates the unknown function a total of N times.

(a) After 1 iteration.

(b) After 14 iterations.
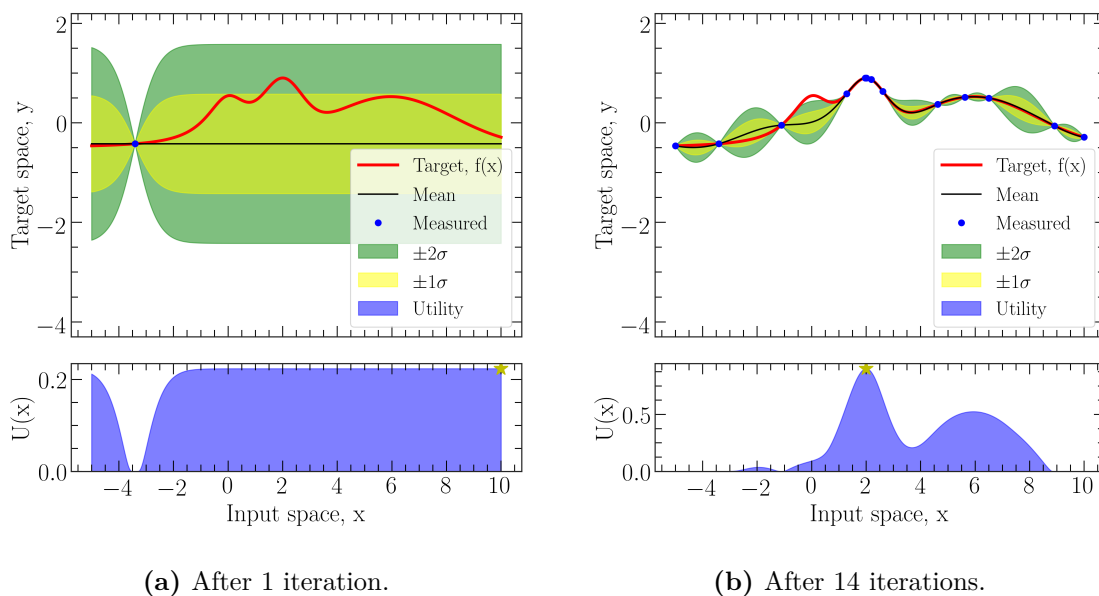
Figure 7.7: Iterations 1 and 14 of the BayesOpt algorithm for evaluating the maximum of the (unknown to algorithm) target function shown in red. The posterior mean, μ_n is shown in black and the mean $\mu_n \pm 1\sigma_n$ and $\mu_n \pm 2\sigma_n$ bands are shown in yellow and green respectively. The posterior mean and standard deviation are evaluated using Equations 7.13 and 7.14. The prior mean function, μ_0 in the text, is taken as $0 \; \forall \; x \; \in \; \mathbb{X}$, and the RBF is chosen as the prior covariance function, Σ_0 in the text. The star in the lower panel shows the maximum of the acquisition function.

hyper-parameters that must be specified. Firstly the choice of covariance must be specified. A common choice is the *radial basis function* (RBF)

$$\Sigma(\mathbf{x}_i, \mathbf{x_j}) = v_0 \exp\left[-\frac{1}{2}\sum_{m=1}^{N}\frac{(x_i^m - x_j^m)^2}{\ell_m}\right] + v_1 d_{ij}, \tag{7.18}$$

where v_0 is an overall vertical scale of variation, ℓ_m are characteristic length scales for each dimension of the input space, and v_1 characterises stochastic noise in the observation and aids numerical inversion. A choice of length scales ℓ_m specifies the rough distance that must be crossed in input space before the function value can change significantly. The kernel choice has a strong effect on the description of probable values of an unknown function f across the input space $\mathbb{X}$. Thus, this choice is not arbitrary. RBF assumes a smoothly varying function f across input space. Despite complications from reconstruction efficiencies and detector effects, the kinematics upon which a physics region of interest are defined are generally smoothly varying functions. Therefore RBF was chosen as the covariance for the BayesOpt applied to optimise the signal regions in this analysis.

Another free choice of the BayesOpt procedure is the acquisition function itself. Many other possible acquisition functions can, and are, defined [170]. The expected improvement is most appropriate for evaluating the extrema of an unknown function, and was therefore used and discussed in this Section.

7.5.1   Signal region definition

The aim of this analysis is to measure a variable sensitive to the dead-cone effect. The differences in the LO PYTHIA 8 dead-cone on/off samples characterise the size of the dead-cone effect for a given signal region. The naive bin-by-bin difference between the predicted distributions is not of primary interest, as a region with large separation might be limited by an associated increase in systematic uncertainties. The BayesOpt procedure was used to evaluate two signal regions (SRs): one for events where the radiative jet was matched to the leptonic top, and one for when the radiative jet was matched to the hadronic top. These SRs are referred to as the leptonic SR and the hadronic SR, respectively. In the leptonic SR, the A_θ variable is constructed using the leptonically decaying top quark. Similarly, in the hadronic SR, the A_θ variable is constructed using the hadronically decaying top quark. The SCI-KIT LEARN python library [174] implementation of Gaussian Processes in conjunction with the open source BAYESOPT library [175] were used to perform the BayesOpt procedure. The covariance function chosen was RBF, the mean function was zero for all regions of the input space, and the expected improvement acquisition function was used. The probability of observing the dead-cone off hypothesis given the dead-cone on hypothesis, or the p-value of this observation, was calculated. The p-value was evaluated using full systematic and statistical uncertainties. A small p-value corresponds to significant separation be-

tween the two dead-cone on/off hypotheses. Therefore, the inverse of this p-value was maximised.

The optimisation procedure was performed in the full analysis chain for a total of three hundred trial signal regions before the algorithm was considered converged. A trial signal region was defined as a list of requirements on the kinematics of reconstructed objects. For each step in the iteration the following was performed:

1. Define a signal region through a set of cuts

2. Optimise the binning of the A_θ distribution within that region. The binning optimisation is discussed in more detail in Section 7.6.2.

3. Predict the the unfolded relative differential A_θ distribution for this region using the nominal MC.

4. Evaluate the systematic and expected statistical uncertainty of the measured data on this pseudo-measurement.

5. Evaluate the expected p-value, $p_0^{\text{dc-off}}$, for observing the dead-cone on hypothesis given the dead-cone off hypothesis using the evaluated systematic and statistical uncertainties.

The procedure described in Figure 7.6 was modified slightly. After an initial burn-in period of $n_0 = 50$, batches of 50 trial regions were evaluated. Should any region in the set have a larger inverse p-value than any evaluated so far, another batch of fifty regions are evaluated. This repeats until the procedure has converged. Convergence occurred after 6 batches of 50, or equivalently 300 trial regions.

The trial signal regions are defined at both particle-level and detector-level using the following event and object-level requirements:

- $p_T^{\text{top,min}} < p_T^{\text{top}}$: A minimum p_T cut on the reconstructed top quark.

- $m^{\text{top,min}} < m^{\text{top}} < m^{\text{top,min}} + m^{\text{top,window}}$: The mass of the reconstructed top quark must be within a window.

- $p_T^{g,\text{min}} < p_T^{g}$: The minimum p_T of the reconstructed radiative jet.

- $\theta_d < \theta_d^{\text{max}}$: Maximum requirement on the reconstructed characteristic dead-cone angle of the reconstructed top quarks.

The five parameters that define a signal region - $p_T^{\text{top}}, m^{\text{top,min}}, m^{\text{top,window}}, p_T^{g,\text{min}}, \theta_d^{\text{max}}$ - are varied using the Bayesian Optimisation procedure separately for the hadronic and leptonic signal regions. The final values of these parameters after optimisation are shown in Table 7.7 and are rounded to the nearest 5 GeV for reconstructed top mass and transverse momentum, and to the nearest 1 GeV for the gluon jet p_t. Although the hadronic and leptonic signal regions were optimised independently, in both cases the

procedure converged on $\theta_d^{\max} = 1.0$, the maximum value allowed for θ_d, and therefore this cut was not applied.

Signal regions were defined for events that satisfy the criteria described above and listed in Table 7.7. The requirement of the $p_T^g/p_T^{\text{top}} > 0.05$ is motivated in section 2.5.1. For an example 25 GeV radiative jet this corresponds to a maximum top-quark p_T of 700 GeV, consequently this cut is typically automatically satisfied due to the minimum requirement on p_T^g.

Selection Criteria	Leptonic SR	Hadronic SR
Dead-cone angle, θ	$\theta^{\text{lep}} < \theta^{\text{had}}$	$\theta^{\text{lep}} > \theta^{\text{had}}$
Ratio of radiative Jet p_T to top quark p_T	> 0.05	
Reconstructed Top quark mass	$\in [150, 300]$ GeV	
Radiative Jet p_T	$> 25\,\text{GeV}$	$> 25\,\text{GeV}$
Reconstructed Top quark p_T	$> 100\,\text{GeV}$	$> 110\,\text{GeV}$

Table 7.7: The selection criteria for the orthogonal hadronic and leptonic signal regions (SRs) of phase-space at detector level. Top quark kinematic properties refer to the reconstructed leptonic or hadronic top quark for the corresponding regions of reconstruction or particle level phase-space.

7.5.2   Signal region kinematics and yields

The total number of events estimated and measured in both SRs is given in Table 7.8. The observed number of events agrees within statistical and systematic uncertainties. The agreement between measured and predicted event yields is closer in the SRs compared to the pre-selection yields given in Table 7.6. In the SRs, the observed reconstructed top quark p_T has a similar fractional deficit of events at high-p_T compared to prediction in the pre-selection region, as shown in Figures 7.8 and 7.9. The number of events falls off steeply with respect to top quark p_T, therefore, this deficit at high-p_T has a small impact on the total observed yield compared to the low p_T regime. A $\sim 1\%$ excess of data is observed at low top quark p_T in the pre-selection region. As each SR requires moderately energetic top quarks, with a $p_T \gtrsim 100\,\text{GeV}$, the excess is removed resulting in closer agreement between prediction and observation. These differences are well below the systematic uncertainty associated with modelling the $t\bar{t}$ system.

The kinematics of the reconstructed top objects and A_θ observables relevant to each SR are presented in Figures 7.8 and 7.9. The previously noted shape difference between the measured and predicted top p_T spectrum is observed in both SRs. The measured top pseudo-rapidity and mass distributions are in good agreement with the prediction. Furthermore, the shape of the measured A_θ distribution agrees well with prediction. The agreement of all measured top quark kinematics is within statistical and systematic

| | Leptonic SR | | Hadronic SR | |
Process	Yield	Uncertainty	Yield	Uncertainty
$t\bar{t}$	293060.9	29156.1	306825.0	34501.2
W+jets	16244.7	8969.0	14146.7	7843.2
Single top	11917.3	1308.2	10806.9	1302.0
Fakes	4342.5	431.1	5128.4	581.1
Z+jets	2585.9	256.5	2143.4	244.7
$t\bar{t}$ +V	1316.3	135.4	1369.3	149.4
Diboson	955.4	94.5	870.6	98.8
Total Prediction	330423.1	40350.8	341290.3	44720.4
Data	333805.0	-	340077.0	-

Table 7.8: Yield table for the leptonic and hadronic SRs defined in Table 7.7 including statistical and systematic uncertainties. The systematic uncertainties are defined in more detail in Section 7.7.

uncertainty. The background processes and NLO $t\bar{t}$ prediction accurately describe the data. In order to probe the radiative properties of the $t\bar{t}$ system to high precision, the signal $t\bar{t}$ process was isolated and the effects of the detector removed with a statistical procedure.
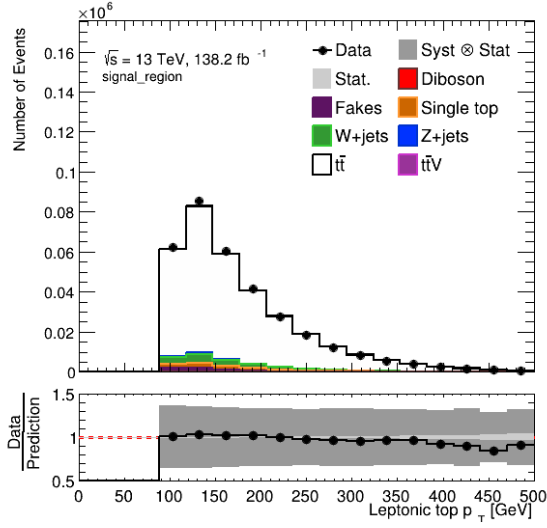
(a) Leptonic top p_T
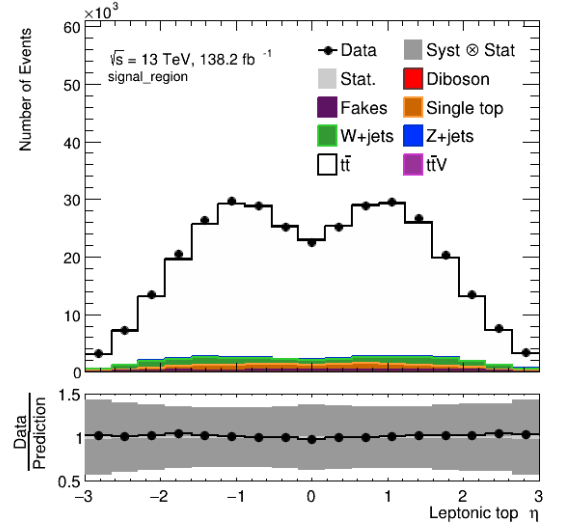
(b) Leptonic top mass
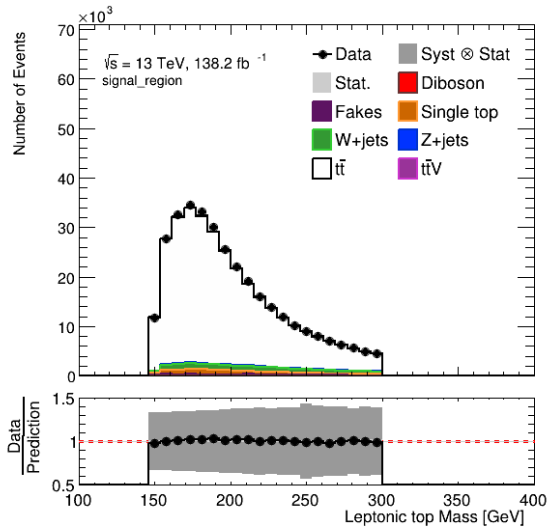
(c) Leptonic top η
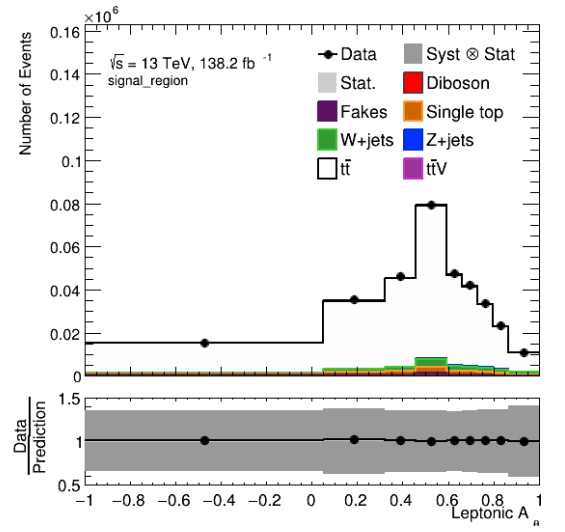
(d) A_θ measured w.r.t the leptonic top quark

Figure 7.8: Measured and predicted kinematic distributions of physics objects in the leptonic signal region defined in Table 7.7.
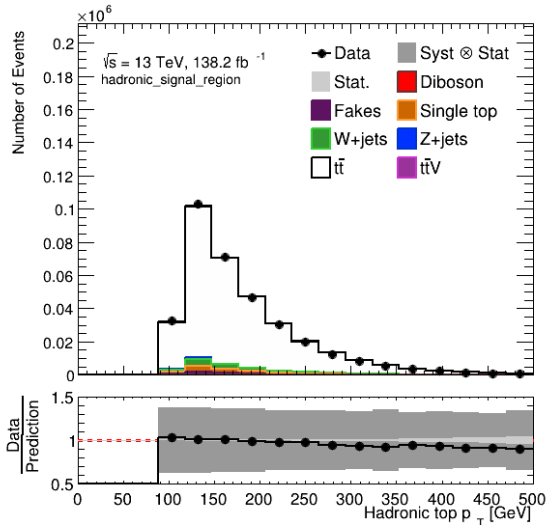
(a) Hadronic top p_T
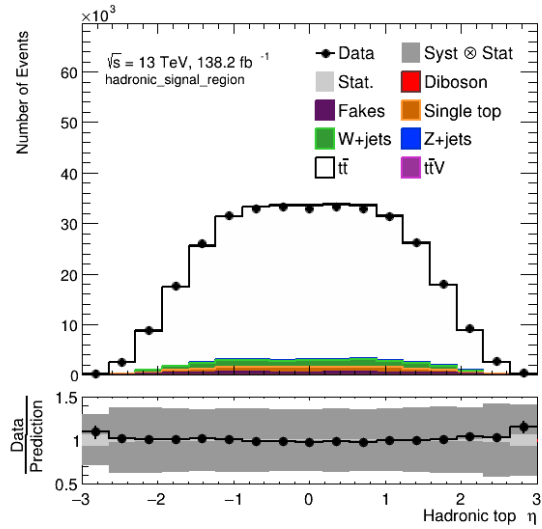
(b) Hadronic top mass
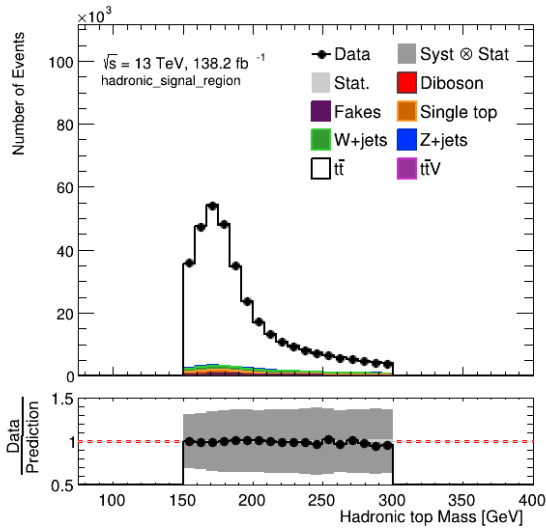
(c) Hadronic top η
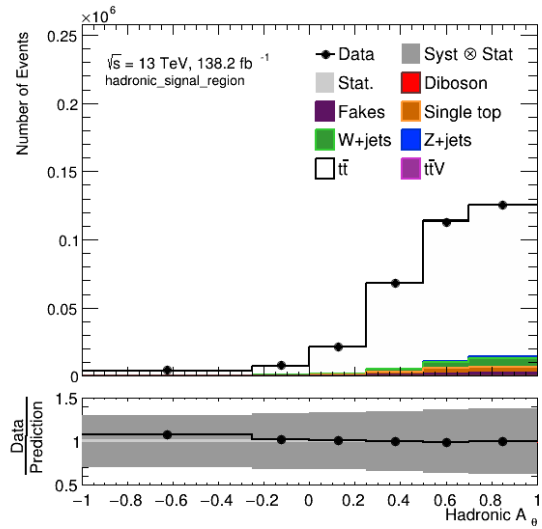
(d) A_θ measured w.r.t the hadronic top quark

Figure 7.9: Measured and predicted kinematic distributions of physics objects in the hadronic signal region defined in Table 7.7.

7.6 Unfolding Procedure

To measure the differential distribution of the A_θ observable at particle-level, the effects of the detector must be removed. Specifically, this analysis aims to evaluate the particle-level equivalent to the measured data. The set of statistical procedures that perform this operation are known as *unfolding* algorithms. To successfully unfold an observable, there must be a strong correspondence between the measured and the particle-level observable, i.e the particle-level information must be encoded in the detector-level distribution.

7.6.1 Iterative bayesian unfolding

The *Iterative Bayesian unfolding* (IBU) procedure [176, 177] is used extensively within top properties measurements performed by the ATLAS and CMS collaborations [138, 139, 178, 179]. IBU shall be used to perform the unfolding of the measured A_θ distribution. The method can be understood initially in the simplest case, with no complications from noise, no background contributions, and identical selection regions between particle-level and detector-level. The estimator, $\hat{h}_{\mathrm{T}}$, of the particle-level distribution that causes an observed detector-level distribution, h_{D}, is given by

$$\hat{h}_{\mathrm{T},i} = \sum_{j=1}^{n} P(h_{\mathrm{t},i}|h_{\mathrm{D},j}) \cdot h_{\mathrm{D},j} \,, \tag{7.19}$$

where the conditional probability that an event originates from bin i of h_{T} given that it is observed in bin j of h_{D} is $P(h_{\mathrm{t},i}|h_{\mathrm{D},j})$. The conditional probability can then be rewritten using Bayes theorem as

$$\hat{h}_{\mathrm{T},i} = \sum_{j=1}^{n} \frac{P(h_{\mathrm{D},j}|h_{\mathrm{T},i}) \cdot P(h_{\mathrm{T},i})}{\sum_{i'} P(h_{\mathrm{D},j}|h_{\mathrm{T},i'}) \cdot P(h_{\mathrm{T},i'})} \cdot h_{\mathrm{D},j}, \tag{7.20}$$

$$\hat{h}_{\mathrm{T}} = U^0 h_{\mathrm{D}}, \tag{7.21}$$

where the matrix U^0 has been implicitly defined in terms of the probability of observing $h_{\mathrm{D},j}$ events in the j-th bin at detector-level, given $h_{\mathrm{T},i}$ events in the i-th bin of the particle-level distribution. This conditional probability, $P(h_{\mathrm{D}}|h_{\mathrm{T}})$, is often referred to as the *response matrix*, R. The response matrix can be evaluated using simulation. The Bayesian prior, $P(h_{\mathrm{T},i})$, describes the initial probability of observing $h_{\mathrm{T},i}$ events in the i-th bin of the particle-level distribution. The response matrix mixes contributions from different bins of the prior and measured data to provide an estimate of the unfolded result.

Strong dependence on the prior of the unfolded distribution is undesirable behaviour. An iterative extension of the above procedure, where the unfolding is repeated and the prior updated using the posterior of the previous iteration, dampens the dependence of the unfolded distribution on the prior. The matrix U is extended as

follows:

$$U^k = \sum_{j=1}^{n} \frac{R_{ji}\tilde{h}_{\mathrm{T},i}^{k-1}}{R_{ji'}\tilde{h}_{\mathrm{T},i'}^{k-1}}, \tag{7.22}$$

$$\hat{h}_{\mathrm{T}}^{k} = \begin{cases} U^{k-1}h_{\mathrm{D}} \ \forall \ k > 0, \\ P(h_{\mathrm{T}}) \ \text{for} \ k = 0, \end{cases} \tag{7.23}$$

where the summation over i' in the denominator of Equation 7.22 is implied. The master equation for the IBU method can now be defined as

$$\hat{h}_T = U^k h_D, \tag{7.24}$$

where the two free parameters of the method are: the number of iterations to perform, k; and the prior of the particle-level distribution, $P(h_{\mathrm{T}})$. The number of iterations acts as a regularisation parameter. In the high k limit the unfolded distribution, $\hat{h}_T$, converges to the input particle-level distribution, h_T, for all priors. However, statistical fluctuations are enhanced in each iteration. The number of iterations must be chosen to balance these two effects, typically done by defining a χ^2 convergence criteria as follows:

$$\chi_k^2/N_{DoF} < 1.0, \tag{7.25}$$

$$\chi_k^2 = \frac{(\hat{h}_T^k - \hat{h}_T^{k-1})^2}{\sigma_{\mathrm{stat}}^2}, \tag{7.26}$$

where k is an index for the number of iterations the estimators are evaluated with, and σ_{stat} is the statistical uncertainty of the unfolding procedure. The prior is typically taken as the appropriately normalised particle-level distribution, as this reflects the a priori knowledge of the system being unfolded. Naturally, the regularisation parameter k depends upon the prior. An appropriate prior reduces the number of iterations required for the procedure to satisfy the convergence criteria.

The IBU method described above has neglected several effects that must be account for. Namely, it was assumed that the measured distribution h_{D} contained no contamination from background sources. Furthermore, there was an unstated assumption that all events pass both detector- and particle-level selection criteria. To account for these sources of complication, the correction factors can be introduced as

$$h_D \rightarrow f_{\mathrm{acc}} \cdot (h_\mathrm{D} - h_\mathrm{B}), \tag{7.27}$$

$$\hat{h}_T \rightarrow \epsilon \hat{h}_T \tag{7.28}$$

where

$$f_{\mathrm{acc}} = \frac{N_{\mathrm{True}\cup\mathrm{Reco}}}{N_{\mathrm{True}}} \qquad \text{and} \qquad \epsilon = \frac{N_{\mathrm{True}\cup\mathrm{Reco}}}{N_{\mathrm{Reco}}}. \tag{7.29}$$

The correction f_{acc} (ϵ) accounts for events that pass particle-level (detector-level) selection, but fail detector-level (particle-level) selection. The distribution h_{B} describes

the number of events that arise from background processes, and are therefore not of interest in the unfolding. These are evaluated in simulation and subtracted from the detector-level distribution.

A generic formula for measuring the differential distribution at particle-level of an observable, X, from a specific process can now be constructed. For a given integrated luminosity $\mathcal{L}$, and for a process measured in a channel with branching ratio, $\mathcal{B}$, the differential cross-section is

$$\frac{d\sigma^t}{dX^t} = \frac{1}{\mathcal{L} \cdot \mathcal{B} \cdot \Delta X^t} \cdot \frac{1}{\epsilon^t} \sum_r U_{rt}^k \cdot f_{\text{acc}} \cdot (N_{\text{Obs}}^r - N_{\text{Bkg}}^r), \tag{7.30}$$

where t indicates a bin index at particle-level of the unfolding, ΔX^t is the width of bin t, and r the bin index at detector-level of the unfolding. The matrix U_{rt}^k is defined in Equation 7.22, and k is the number of iterations performed with the IBU procedure. N_{Obs} and N_{Bkg} are the number of observed events and expected number of background events respectively.

7.6.2 Unfolding A_θ

The response matrix, R_{ij}, convolves the probability of producing an event in bin i of the particle-level distribution, r_i, with the probability that a selected event from bin i of the particle-level distribution is measured in bin j of the detector-level distribution, M_{ij}, known as the *migration matrix*. These two sources of observation probability can be separated as

$$R_{ij} = r_i M_{ij}. \tag{7.31}$$

The migration matrix provides an intuitive understanding of the detector smearing on an observable, separate from the relative production probability between bins. An ideal migration matrix is the diagonal identity matrix.

The IBU procedure used to remove detector effects and evaluate the A_θ differential cross-section distribution in Equation 7.30 is performed by the software package `RooUnfold`, where the migration matrix and correction factors ϵ and f_{acc} are calculated and applied manually. The migration matrices for the A_θ variable in the Leptonic and Hadronic SRs, evaluated using the nominal $t\bar{t}$ MC sample, are presented in Figure 7.10. The binning of the variables is chosen such that the diagonal elements of the migration matrix have a minimum value of 50%. The binning procedure is discussed in more detail in Section 7.6.2. A minimum value of 50% along the diagonal is taken to ensure that each bin of the measured detector-level distribution encodes enough particle-level information for an unfolding procedure to be justified. Furthermore, the more diagonal the migration matrix is the fewer iterations are required before convergence. Therefore, the more diagonal the migration matrix is, the less biased the unfolded result is by the the regularisation inherent in the IBU procedure.
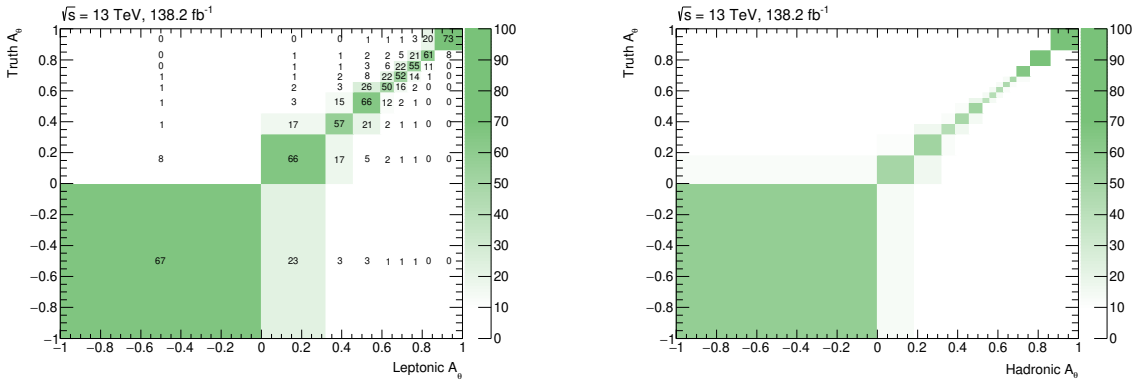
Figure 7.10: Migration matrices for the leptonic (left) and hadronic (right) signal regions relating the detector level angular asymmetry, A_θ, to the particle level angular asymmetry.

Figure 7.11 shows the acceptance and efficiency correction factors. The fiducial acceptance correction in both SRs is $\sim 7\%$, and varies slowly between bins. Therefore, the instrumented region of phase-space is far more restrictive than the corresponding particle-level phase-space for which the unfolding is performed in. The detector acceptance indicates that the event selection between particle-level and detector-level has a correspondence of between 20% and 11% per bin of A_θ. The low correction factors can be understood to arise from multiple sources. Pile-up is not simulated at particle-level, and pile-up jets can mimic low-p_T radiative jets. The b-tagging procedure used at particle-level is the presence of ghost-matched B hadron, which has an efficiency of 100% compared to the 85% used at detector-level. Furthermore, the reconstructed top quark mass at particle-level has better resolution than that of detector-level, due to effects of the jet energy scale and resolution. Finally, a low missing $\not{E}_T$ cut was applied in order to maximise statistics. At particle-level this can only arise from weakly interacting particles, however, at detector-level, terms originating from mis-calibration of other objects can contribute. As the measurement is focused on the shape of the A_θ variable, the absolute size of these correction factors factorises in the normalisation procedure. Therefore, as long as the differences between particle-level and detector-level phase-space are well described, the low efficiency correction factor is unimportant. Before the unfolded procedure can be applied to data, free parameters must be chosen and the method validated.

Binning optimisation

The ability of the unfolding procedure to recover the particle-level spectra from the detector-level spectra depends upon the choice of binning used in the observable. The binning choice has three fundamental constraints: the amount of detector smearing, the available data statistics, and the available Monte-Carlo statistics. For this analysis, the Monte-Carlo statistics is much larger than the available data statistics and therefore is not of concern. As will be shown, the data statistics is also a minor consideration
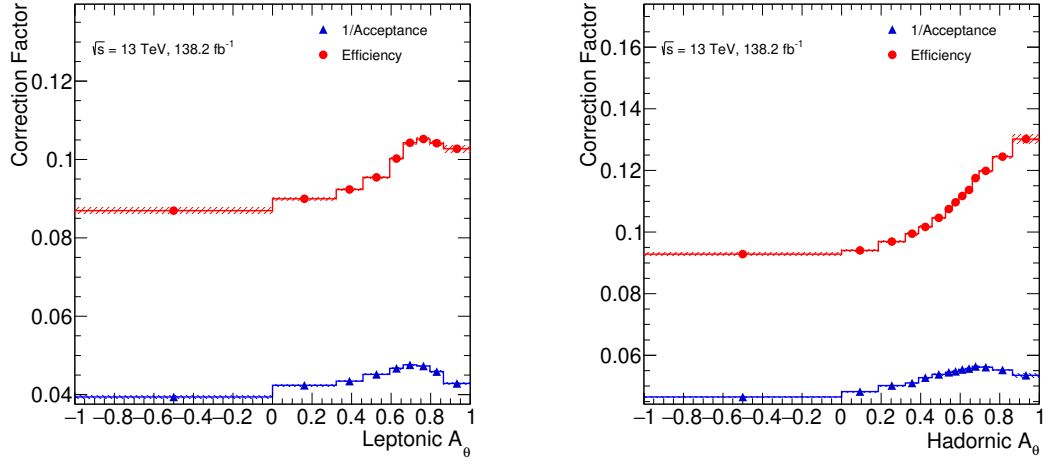
Figure 7.11: Fiducial acceptance (red) and detector efficiency (blue) correction factors, as defined in 7.30, for the leptonic (left) and hadronic (right) signal regions relating the measured angular asymmetry, A_θ to the particle level angular asymmetry.

compared to the resolution of the detector and smearing of the particle-level distribution. In all of the following, the procedures described are performed separately for the Leptonic and Hadronic selections.

The binning was chosen using a simple 3 step procedure. The procedure insists on a maximum statistical uncertainty at detector-level of 8%, and a correspondence between detector- and particle-level distributions of 50% as evaluated by the migration matrix. The algorithm starts with an initial fine-grained binning of $N_{bins} = 80$, where the bin edges are distributed uniformly over the range $[-1, 1]$ and then proceeds as follows:

1. Unfold $N_{\text{toys}} = 300$ with the current binning.

2. Starting at the right-hand-side, merge bin i with its right hand neighbour, j, if either of the following conditions are satisfied:

$$N^i_{\text{yield}} < 150, \tag{7.32}$$

$$M_{ii} < 0.5, \tag{7.33}$$

where N^i_{yield} is the predicted number of events expected in bin i and M_{ii} is the ii element of the normalised migration matrix.

3. Repeat steps 1-3 until no bins were merged in step 2.

A final pass of the algorithm applied starting from the left-hand sized is performed to ensure the right-most bin satisfies the requirements in Equation 7.32 and 7.33. However, these are loose requirements and do not guarantee that the unfolding is unbiased, nor do they provide information on the optimal number of iterations.

(a) Before optimisation

(b) After optimisation
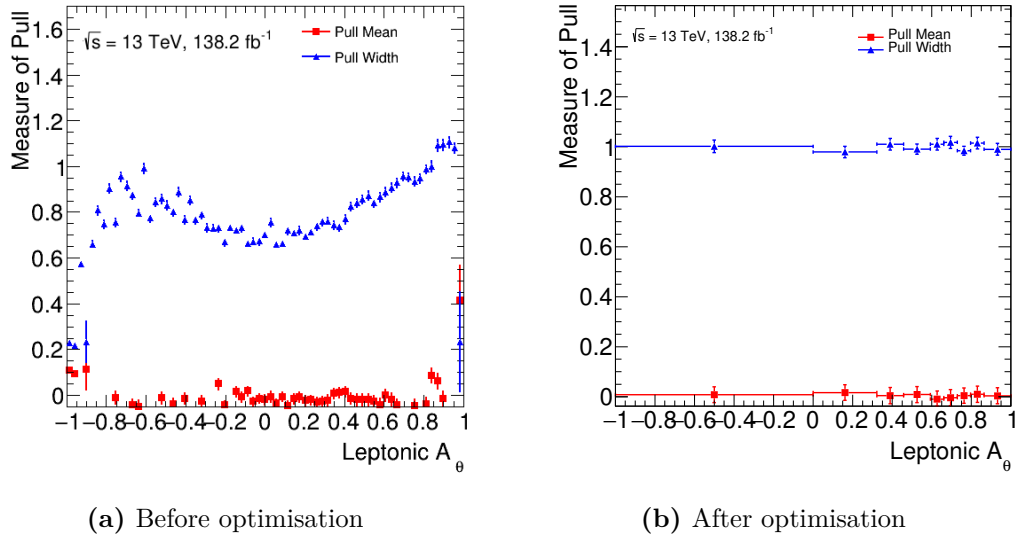
Figure 7.12: The evaluated μ and B values, defined in the text, for the pull tests of binning before (right) and after (left) optimisation evaluated using 300 toys for the Leptonic SR (top) and hadronic SR (bottom).

(a) Before optimisation

(b) After optimisation
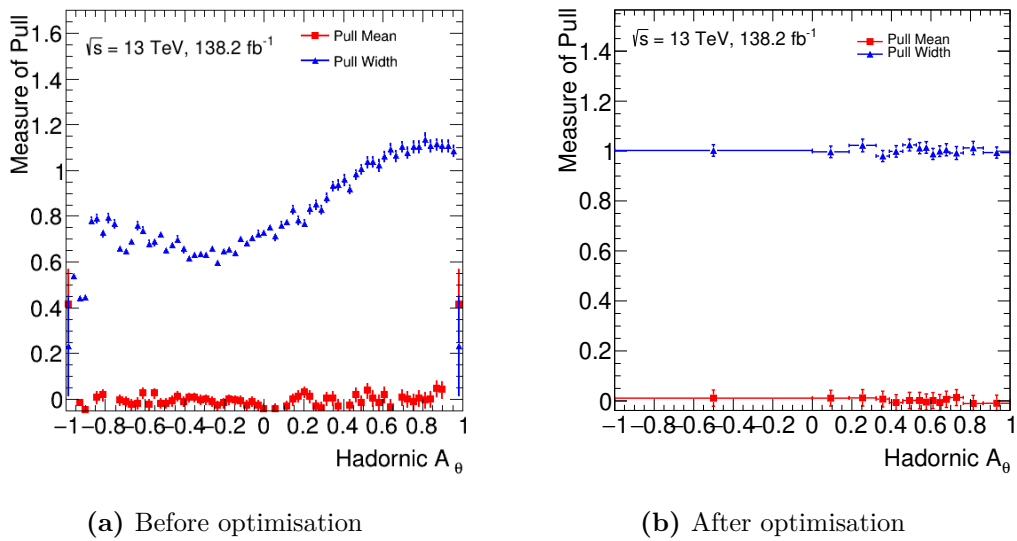
Figure 7.13: The evaluated μ and B values, defined in the text, for the pull tests of binning before and after optimisation evaluated using 300 toys for the hadronic SR before.

Pull tests

One consideration of an unfolding procedure that must be evaluated is the bias it introduces into the unfolded distribution. A method to evaluate this bias is a *pull test*, where the full signal MC is divided into two approximately equal samples *test* and *train*. The test sample is unfolded using the response matrix and efficiency corrections evaluated with the training sample. The pull of the training sample upon the test sample for bin i is defined as

$$P^i = \frac{A_\theta^{i,\text{unfolded, test}} - A_\theta^{i,\text{truth, test}}}{\sigma_{\text{test}}^{i,\text{unfolded}}}, \tag{7.34}$$

where $\sigma_{\text{test}}^{i,\text{unfolded}}$ corresponds to the statistical error on the unfolded test distribution. The pull evaluates how well the differences between the unfolded detector-level spectrum and the particle-level spectrum are explained by the statistical uncertainty.

In this analysis, the full nominal MC signal sample is divided in half $N_{\text{toy}} = 300$ times, where the division is performed by randomly creating N_{toy} separate train and test samples. For a given toy, the train and test samples are mutually exclusive categories, and therefore statistically independent. For each toy the pull distribution is evaluated for every bin i, and a Gaussian is fitted to this distribution. From this fitted Gaussian the variables

$$\mu_P^i = <P^i> \tag{7.35}$$
$$B^i = \text{std}(P^i) \tag{7.36}$$

are extracted. An unbiased unfolding procedure should result in $\mu_P^i, B^i = 0, 1 \; \forall \; i$. Any deviation from these values implies a bias within the procedure. Figures 7.12 and 7.13 show the evaluated μ_P and B distributions for the initial and optimised binnings in the leptonic and hadronic SRs respectively. The initial fine-grain binning biases the unfolded distribution. In both SRs the bias, B, is less than the 1.0 ideal case for a large range of A_θ. The difference between the test MC unfolded and truth level A_θ distribution is less than what is expected from statistical uncertainties in the unfolding. Therefore, the unfolding procedure is biasing the unfolding in the direction of the particle-level A_θ distribution. Such a bias is undesired, and is indicative of a poor choice of binning. After optimisation, the bias and mean of the pull distributions in both SRs agrees (within statistical uncertainties) with the ideal case of 1.0 and 0.0 respectively.

Stress test

In order to make definitive statements on the agreement between data and different Monte Carlo samples, the unfolding procedure must recover variations in prediction. Any deviation between the nominal MC and the measured data at detector-level must
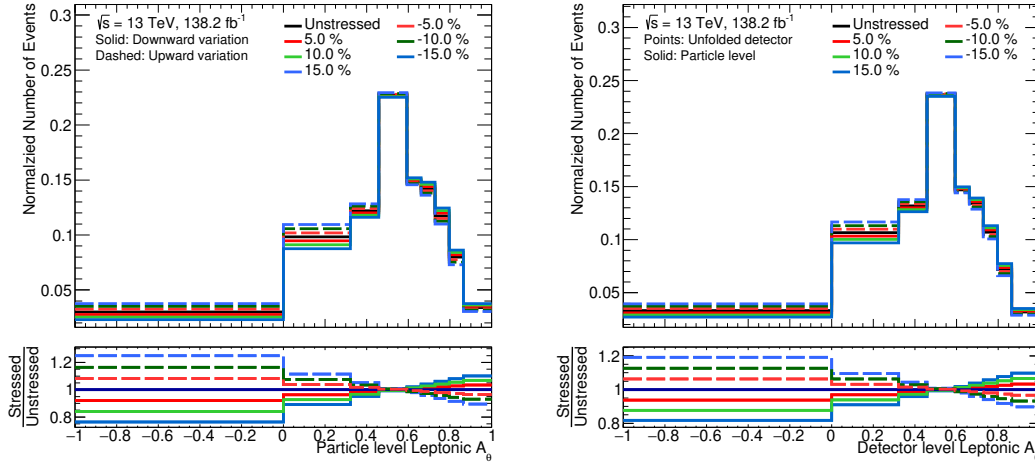
Figure 7.14: Particle level and reconstruction level distribution of the leptonic A_θ observable in the leptonic SR constructed from the nominal POWHEG+PYTHIA 8 $t\bar{t}$ Monte Carlo sample with event-by-event re-weighting given by Equation 7.37, where $s \in \{5\%, 10\%, 15\%\}$.
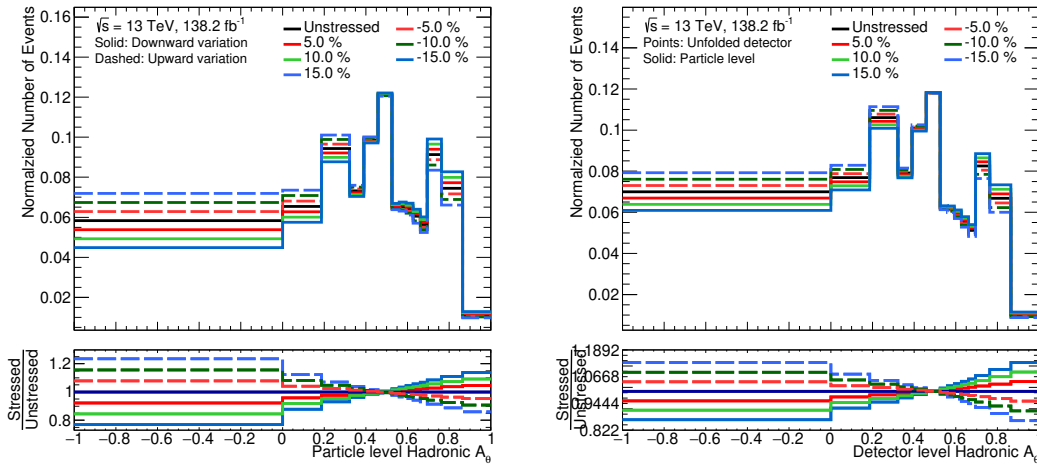
Figure 7.15: Particle level and reconstruction level distribution of the leptonic A_θ observable in the hadronic SR constructed from the nominal POWHEG+PYTHIA 8 $t\bar{t}$ Monte Carlo sample with event-by-event re-weighting given by Equation 7.37, where $s \in \{5\%, 10\%, 15\%\}$.
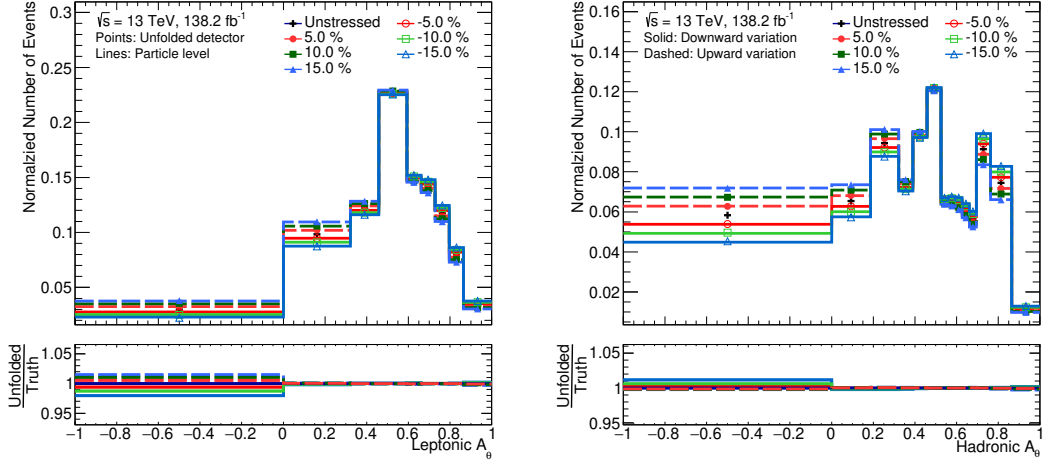
Figure 7.16: Stressed particle level distributions (lines) compared to the stressed reconstruction level unfolded to particle level (points) of the leptonic A_θ variable constructed from the nominal POWHEG+PYTHIA8 $t\bar{t}$ Monte Carlo sample with event-by-event re-weighting given by eq. 7.37 where $s \in \{5\%, 10\%, 15\%\}$ for the leptonic (left) and hadronic (right) signal regions.

be recoverable by the IBU procedure. A *stress test* evaluates the ability of the nominal IBU procedure to unfold variations in measured A_θ distributions. The nominal POWHEG+PYTHIA8 sample was re-weighted event-by-event based upon the particle-level distribution of the $A_\theta^{\text{particle-level}}$ observable, for both leptonic and hadronic measurements using the formula:

$$w(A_\theta^{\text{particle-level}}) = \frac{s}{q_{99}(A_\theta^{\text{particle-level}})} \cdot A_\theta^{\text{particle-level}} + 1, \tag{7.37}$$

where s is the stress applied, typically in the range $s \in [-100\%, 100\%]$, and $q_{99}(A_\theta)$ is the 99th percentile of the particle-level A_θ distribution constructed without any re-weighting. Equation 7.37 was chosen such that the weight, as a function of the stressing variable, is a straight line going from $(-q_{99}(A_\theta), 1 - s)$ to $(q_{99}(A_\theta), 1 + s)$.

Figures 7.14 and 7.15 show the stressed distributions at particle- and detector-level for $s \in \{5\%, 10\%, 15\%\}$ in the signal regions. Stressed distributions are unfolded using the nominal response matrix, i.e without the event re-weighting given in Equation 7.37, and a closure test is performed. Figure 7.16 show that a stress of $s = 0.15$ has a non-closure of less than 1%, well below the statistical and systematic uncertainties of the measurement. A stress of $s = \{\pm 0.15\}$ exceeds the shape variation between data and the nominal MC the unfolding procedure is based upon, as shall become clear in Section 7.8.

Convergence test

Finally, the number of iterations performed in the Iterative Bayesian Unfolding procedure is a free parameter of the method and must be chosen. The number of iterations
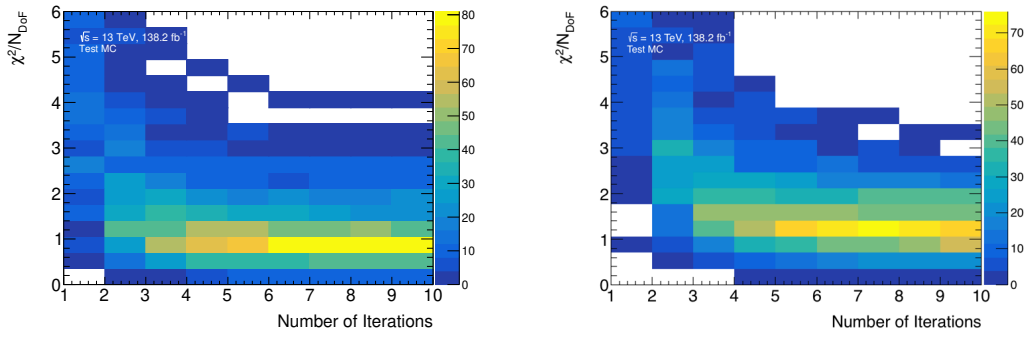
Figure 7.17: Convergence test for leptonic (left) and hadronic (right) signal regions for the angular asymmetry A_θ variable unfolded with the iterative Bayesian unfolding method.

was fixed through the following procedure:

1. Divide MC sample randomly into two roughly equal samples: *test* and *train*.

2. Construct the Migration matrix from the train sample.

3. Unfold the test detector level distribution $n_\text{iteration}$ times.

4. Measure the χ^2/N_{DoF} of the unfolded result for each iteration and toy.

5. Repeat steps 1 to 4 for 250 times.

Figure 7.17 shows the distribution of χ^2/N_{DoF} as a function of $n_\text{iteration}$. For both SRs the χ^2/N_{DoF} converges to unity for iterations $\gtrsim 4$. Therefore, 5 iterations were used for both signal regions.

7.7   Uncertainties

For a typical unfolded measurement, two approaches to assess the impact of systematic uncertainties upon the final measurement can be taken: constructing the response matrix, acceptance, and efficiency corrections with samples varied to account for a systematic uncertainty and then unfolding the nominal MC sample; *or* constructing the response matrix with the nominal sample and varying the predicted detector level distribution in a manner that accounts for the expected size of the systematic uncertainty. The later is generally preferred in all cases since systematic samples may be limited in statistics and, in general, the signal MC sample has the highest statistical power. Both methods should, modulo statistical fluctuations, give the same result, so the choice is more technical than philosophical. The approach of fixing the nominal response matrix and correction factors was taken for this measurement.

The assigned systematic uncertainty for a given bin i can be constructed as

$$\sigma_\text{syst}^i = A_{\theta,\,\text{truth}}^{i,\text{syst}} - A_{\theta,\,\text{unfolded}}^{i,\text{syst}}, \tag{7.38}$$

where $A^{i,\text{syst}}_{\theta,\,\text{unfolded}}$ is the normalized number of events in bin i for the unfolded detector-level distribution of a systematically varied $t\bar{t}$ sample and $A^{i,\text{syst}}_{\theta,\,\text{truth}}$ is the corresponding particle-level distribution. The systematic uncertainty is constructed in this way to account for changes in measured distributions that cannot be recovered by the unfolding procedure. For the majority of systematic uncertainties examined, $A^{i,\text{syst}}_{\theta,\,\text{truth}}$ is degenerate with the nominal particle-level A_θ prediction.

The uncertainties considered in this analysis all arise from one of the following sources:

1. **Detector:** Understanding of the detector and the calibrations of physics objects. These systematics can be evaluated using an additional event weight, known as a scale-factor, that varies the effect of a working point. Furthermore, the extent to which events migrate in and out of the selection based on the uncertainty in calibration was evaluated by independently varying the calibrations of all objects, and repeating event selection with these varied objects.

2. **Modelling:** Understanding of the modelling of the $t\bar{t}$ and radiation in the MC used to construct the unfolding matrix. This category includes uncertainties on the PDF choice, as well as the effect of alternate nominal samples. The latter is used to probe the modelling dependence of the measurement. The modelling uncertainties examined through alternative $t\bar{t}$ samples have correspondingly different particle-level predictions for the relative A_θ differential cross-section. The associated systematic uncertainty is the difference that cannot be recovered by the measurement after unfolding, *not* the difference in prediction.

3. **Background:** All background samples are normalised to the central value of the cross-section prediction to the precision listed in Table 7.2. To assess the uncertainty in background cross-section prediction, the cross-section was varied independently for all background contributions by a fractional amount given in Table 7.9. Due to the poorly understood nature of the fake background, a more conservative approach was taken in estimating the associated systematic uncertainty. The uncertainty due to lack of knowledge of the number of events selected due to fake and non-prompt leptons within the ATLAS detector was estimated by varying the parameterisation used within the matrix method. A conservative approach of taking the largest variation between the nominal and varied parameterisation was used.

4. **Statistical:** The statistical uncertainty due to the finite number of data events is evaluated using pseudo-experiments. The input detector-level A_θ distribution is Poisson fluctuated about the bin content and then unfolded. This process is repeated 1000 times, and the standard deviation of the fluctuated results per-bin is taken as the statistical uncertainty in that bin. This procedure was repeated for

Process	Uncertainty	References
Single-top: t-channel	$^{+4.17\%}_{-3.55\%}$	[48, 180, 181]
Single-top: s-channel	$^{+3.88\%}_{-3.49\%}$	[48, 180, 181]
Single-top: Wt channel	$\pm 5.36\%$	[48, 180, 181]
W/Z + jets	$\pm\sqrt{(5\%)^2 + N_{\text{jets}} \cdot (24\%)^2}$	[182]
$t\bar{t} + W$	$\pm 13\%$	[183]
$t\bar{t} + Z$	$\pm 12\%$	[183]
Diboson	$\pm 6\%$	[159]

Table 7.9: Summary of fractional uncertainties on the production cross-section of each background sample.

the nominal Monte Carlo distribution to evaluate the MC statistical uncertainty. This was found to be negligible compared to all other uncertainties evaluated.

7.7.1   Detector-related uncertainties

There are over 50 sources of detector-related uncertainty. These uncertainties cover the limitation in understanding of the reconstruction of calibrated physics objects from the detector read-out. They are presented grouped together by source.

Luminosity: The uncertainty on the combined 2015-2018 integrated luminosity 1.7%. The total uncertainties on the integrated luminosity for each year range from 2.0-2.4%, and are partially correlated between years. It is derived, following the van derMeer (vDM) methodology, detailed in Reference [184], from calibrations of the luminosity scale using x-y beam-separation scans performed in August 2015, May 2016, July 2017 and June 2018 [185]. As the relative differential cross-section, $\frac{1}{\sigma}\frac{d\sigma}{dA_\theta}$, has no dependence on luminosity this uncertainty was only considered during validation studies of the unfolding and reconstruction procedures, not the final measurement.

Jets: The uncertainty on the jet energy scale (JES) is estimated by varying the jet energies according to uncertainties derived from simulation and *in situ* calibration measurements. A reduced set of 30 orthogonal components were used to assess these uncertainties. The reduction was performed using the *category reduction* scheme. This reduction procedure retains their physical meaning of the sources of JES uncertainty. The reduced JES uncertainties were assumed to be uncorrelated and combined in quadrature.

Mis-modelling in the JVT distribution was accounted for using scale-factor variations of simulation. Scale factors were measured in $Z \to \mu\mu$ events, and capture the difference between simulation and measured JVT distributions. The effect of different MC generators and fragmentation models upon the JVT score are covered by this uncertainty.

The uncertainty due to the jet energy resolution (JER) is determined by smearing the jet p_T in simulation. The smearing is performed in bins of jet p_T and η. As with JES, the total JER uncertainty depends on over one hundred sources. The sources of JER uncertainty are reduced into seven nuisance parameters which correspond to different smearings of the jets in simulation. Unlike the JES uncertainty, the physical meaning of the reduced JER nuisance parameters is not retained with the reduction.

Lepton: The uncertainties due to the MC modelling of the lepton reconstruction, identification, trigger and isolation efficiencies were estimated in bins of p_T and η using scale-factor variations of simulation. The scale factors were measured using the tag-and-probe method in $Z \to ee/\mu\mu$, $J/\psi \to ee/\mu\mu$ and $W \to e\nu$ events.

Flavour tagging: The systematic uncertainties associated with tagging jets originating from b-quarks are separated into three categories. These are the efficiency of the tagging algorithm (b-quark tagging efficiency), the efficiency with which jets originating from c-quarks pass the b-tag requirement (c-quark tagging efficiency) and the rate at which light-flavour jets are tagged (misidentified tagging efficiency). The efficiencies are estimated from data and parametrised as a function of p_T and η. The systematic uncertainties arise from factors used to correct the differences between the simulation and data in each of the categories.

Missing transverse energy (MET): The uncertainty due to shifts in jet and lepton resolution and scale are derived in components parallel and perpendicular to the transverse momentum of the reconstructed hard objects in the event and applied as function of p_T and η [109]. The performance studies used to assess the MET uncertainty are based on $Z \to \ell\ell$, $W \to \ell\nu$ and $t\bar{t}$ Monte Carlo (MC) simulated events and data recorded in 2015, 2016, 2017 and 2018.

Pile-up: The uncertainty on the pileup re-weighting is evaluated by varying the pile-up scale factors by $\pm 1\sigma$ based on the re-weighting of the average interactions per bunch crossing.

7.7.2 Modelling related uncertainties

The nominal simulation choice was taken for consistency with historic top quark property measurements within the ATLAS top working group. However, the choice is somewhat arbitrary. The effect of changing the free parameters of the nominal simulation was estimated using the following set of systematic uncertainties:

Radiation uncertainties: The initial state radiation uncertainty has been evaluated using the A14 var3c down weight variation in conjunction with the hadronisation and factorisation scale re-weighted to $\mu_{\mathrm{F,R}} = 2.0$ [186]. The prescription for var3c up uncertainty (in conjunction with scale and h_{damp} variations) was not evaluated owing to studies which have shown this variation to disagree strongly with data. As such, the var3 down variation was used and symmetrised instead. The A14 var2 eigentune was used to estimate the final state radiation (FSR) uncertainty using a similar re-weighting

prescription.

Hard Scatter Generation and matching: A comparison of NLO subtraction schemes was performed by comparing the nominal Powheg+Pythia 8 with MadGraph5_aMC@NLO+Pythia 8. This systematic will be particularly relevant to the analysis as it can change the description of the first additional jet beyond the leading-order picture of top-pair production.

Fragmentation/Hadronisation model: The nominal Powheg+Pythia 8 $t\bar{t}$ was compared to a $t\bar{t}$ sample generated with Powheg for the same hard matrix element at NLO and alternate fragmentation and hadronisation using Herwig7. It is worth emphasising that, for an unfolded measurement such as this analysis, this uncertainty is a statement on the model dependence of the procedure itself, as opposed to a statement on the expected shape and normalization difference between predictions.

Parton density functions (PDFs): The uncertainty from the limited knowledge of the proton's PDF was assessed following the PDF4LHC15 recommendations [187], which evaluates the differences in three independent PDFs CT14 [188], MMHT2014 [154] and NNPDF3.0 [189]. In addition uncertainties from the PDF choice, PDF4LHC15 also covers the uncertainty in fitted α_s used within the PDF. The nominal prediction of $\frac{1}{\sigma}\frac{d\sigma}{dA_\theta}$ was systematically changed by 20 different event-by-event reweighted variations. These 20 variations were assumed to be independent and combined in quadrature.

7.7.3   Uncertainty on A_θ

The total systematic uncertainty for each bin in the measured A_θ distribution is presented in Figure 7.18, where individual systematic uncertainties covering similar sources of uncertainties have been combined in quadrature to provide an overview. The contributions to each uncertainty are detailed in Sections 7.7.1 and 7.7.2. A complete break-down of all individual systematic uncertainty sources for each bin is given in Appendix A. For both signal regions the dominant source of uncertainty is the modelling of the radiation in the $t\bar{t}$ system. This is by construction of the measurement and analysis design; the goal of the analysis is to measure a variable sensitive to the radiative properties of the top quark, including the dead-cone effect. Therefore, the experiment is expected to be limited by the best description of this radiation.

Tables 7.10 and 7.11 present a more detailed break-down of the uncertainties in the system. The modelling systematic has been decomposed into its leading subcomponents, whereas sub-dominant contributions have been left combined. The fragmentation and hadronisation shower uncertainty was evaluated by examining the ability of the unfolding procedure to recover the systematically shifted detector and particle-level distributions of the $t\bar{t}$ system described by Powheg+Herwig 7. This uncertainty is a fundamental limit on the power of this measurement, and cannot be reduced further. The matrix element uncertainty covers uncertainties in the prediction of the hard

scatter process and matching to the parton shower. The measurement probes radiation from the $t\bar{t}$ system; the matrix element uncertainty covers changes in the description of this radiation directly. Therefore, the large dependence on this uncertainty is expected, and is also a fundamental limitation of this measurement. The uncertainties associated with radiation and PDF choice are small compared to other modelling uncertainties for both SRs.

The jet-related uncertainties presented in Figure 7.18 correspond to the combination of the JES, JER and JVT based uncertainties presented in Tables 7.10 and 7.11. Across the majority of the A_θ bins, the JES and JER contribute a fractional uncertainty of between 0.5% and 1.0%. Uncertainties in the energy scale of reconstructed jets can change both the direction of reconstructed tops and the magnitude of the dead-cone angle of the reconstructed top quark $\theta_d = m/E$ and thus have a large impact on the measurement of A_θ. The A_θ variable is constructed entirely from jet objects in the hadronic SR; in the leptonic SR a significant fraction of the energy is measured by jets. The JES uncertainty is therefore expected to be a large source of uncertainty in the measurement. Each individual JES uncertainty eigenvector contributes $\lesssim 0.35\%$ uncertainty on average for all bins of A_θ, which is relatively small compared to the modelling related uncertainties. For both the hadronic and leptonic SR, the JES modelling uncertainties are significant contributions to the total JES uncertainty, contributing 0.28% and 0.64% respectively in the largest A_θ bin. However, the flavour response and composition uncertainties are the most significant JES uncertainties. These characterise the difference in detector response of quark jets compared to gluon jets. These uncertainties were estimated using a conservative assumption of a 50 : 50 quark-gluon composition of jets within an event. In principle this contribution could be reduced further by estimating the quark-gluon composition of the measured events using the nominal MC. However, as this is a sub-dominant systematic uncertainty compared to Modelling of the $t\bar{t}$ system, this was deemed unnecessary.

The relatively large size of the JER uncertainty in both regions can be understood by the same argument. As discussed above, the JER uncertainty is estimated by using MC smearing of the jet energy scale. Due to the eigenvector decomposition used to combine correlated sources of JER uncertainty, the physical meaning of any individual JER contribution has been lost and cannot be understood further. Leptons are well measured by the ATLAS detector compared to jets, and they contribute $< 0.37\%$ to the uncertainty in any A_θ bin in both SRs. The pile-up uncertainty and JVT uncertainties are sub-percent level for all bins of both SRs.

The uncertainty in measured $E_{\mathrm{T}}^{\mathrm{miss}}$ is small compared to other detector-related uncertainties in the hadronic SR, with a typical size of $< 0.55\%$. In the leptonic SR the uncertainty associated with the $E_{\mathrm{T}}^{\mathrm{miss}}$ is similarly small, typically $\sim 0.55\%$. Leptonic top quark reconstruction uses the $E_{\mathrm{T}}^{\mathrm{miss}}$ directly in calculating the direction and magnitude of the top quark momentum, therefore the $E_{\mathrm{T}}^{\mathrm{miss}}$ is expected to have a non-trivial impact
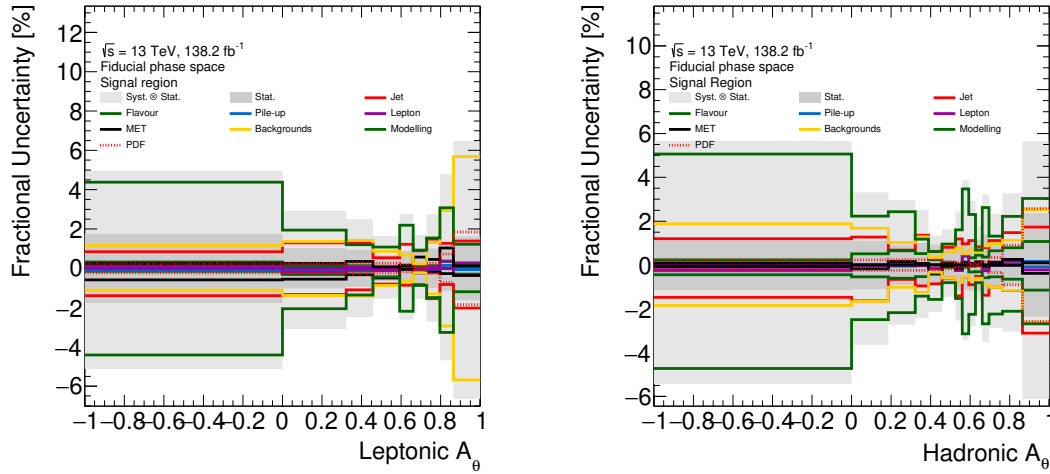
Figure 7.18: The total systematic uncertainty (light grey) and statistical uncertainty (dark grey) for leptonic (left) and hadronic (right) signal regions for the leptonic measurement of the relative differential cross-section of the angular asymmetry in fiducial phase space.

on the measurement in the leptonic SR.

Event selection requires at least 2 b-tagged jets, therefore the flavour tagging uncertainties associated with b-tagging are an important consideration. The uncertainty is $< 0.5\%$ for the leptonic SR and $< 1.1\%$ for the hadronic SR. The largest component of the flavour tagging uncertainty is the mis-identification of charm jets for both SRs. At the cost of reduced statistics, this could be reduced by using a more aggressive b-tagging requirement. As the charm jet mis-identification systematic uncertainty is small this was deemed unnecessary.

The largest contribution to the background uncertainty is the W+jets cross-section variation. The cross-section variation, discussed previously and presented in Table 7.9, is $\pm 54\%$ for W+jets. Furthermore, the yield of the W+jets background is the largest of all background contributions. The large normalisation variation is expected to have a large associated uncertainty. The W+jets background peaks at high A_θ in the leptonic SR. Consequently, the uncertainty associated with variations in the W+jets background is largest in this region. The total uncertainty on the measured A_θ due to this source is $\sim 4.0\%$ in the leptonic SR. The hadronic SR is less sensitive to this background source. The W+jets background uncertainty contributes a roughly 1% uncertainty across A_θ in the Hadronic SR. The analysis aims to examine the low A_θ region, therefore the W+jets background uncertainty has a small impact upon the measurement.

The uncertainty of the fake estimation is $\sim 0.6\%$ for the majority of A_θ bins. The fake background prediction has a large conservative uncertainty in its normalisation and shape. However, the yield of this background is relatively small compared to the total measured data, and therefore contributes a relatively small uncertainty on the measurement.

| | Uncertainty size [%] | | | | | | | | |
| | A_θ bin: | | | | | | | | |
Source	−1.00 - 0.00	0.00 - 0.32	0.32 - 0.46	0.46 - 0.59	0.59 - 0.66	0.66 - 0.73	0.73 - 0.80	0.80 - 0.86	0.86 - 1.00
Frag. and Had.	± 3.984	± 0.703	± 0.861	± 0.323	± 0.678	± 0.671	± 0.677	± 2.913	± 0.199
Matrix Element	± 1.489	± 1.629	± 0.824	± 0.073	± 2.023	± 0.560	± 1.217	± 0.660	± 1.073
Radiation	± 0.397	± 0.794	± 0.117	± 0.222	± 0.442	± 0.010	± 0.111	± 0.216	± 0.125
FSR	±1.044	±0.337	±0.318	±0.582	±0.198	±0.148	±0.571	±1.010	±0.504
PDF	$^{+0.135}_{-0.188}$	$^{+0.141}_{-0.198}$	$^{+0.161}_{-0.223}$	$^{+0.146}_{-0.202}$	$^{+0.094}_{-0.149}$	$^{+0.016}_{-0.047}$	$^{+0.192}_{-0.179}$	$^{+0.590}_{-0.420}$	$^{+1.638}_{-0.856}$
Backgrounds	$^{+1.055}_{-1.001}$	$^{+0.938}_{-0.889}$	$^{+1.052}_{-0.984}$	$^{+0.661}_{-0.636}$	$^{+0.504}_{-0.475}$	$^{+0.129}_{-0.134}$	$^{+0.896}_{-0.948}$	$^{+1.996}_{-2.134}$	$^{+3.882}_{-4.153}$
JVT	$^{+0.041}_{-0.041}$	$^{+0.067}_{-0.067}$	$^{+0.043}_{-0.042}$	$^{+0.034}_{-0.034}$	$^{+0.038}_{-0.038}$	$^{+0.003}_{-0.046}$	$^{+0.049}_{-0.029}$	$^{+0.137}_{-0.137}$	$^{+0.059}_{-0.059}$
Lepton	$^{+0.138}_{-0.013}$	$^{+0.000}_{-0.191}$	$^{+0.038}_{-0.050}$	$^{+0.014}_{-0.102}$	$^{+0.105}_{-0.004}$	$^{+0.006}_{-0.049}$	$^{+0.075}_{-0.029}$	$^{+0.366}_{-0.014}$	$^{+0.279}_{-0.347}$
Pile-up	$^{+0.106}_{-0.114}$	$^{+0.000}_{-0.082}$	$^{+0.094}_{-0.104}$	$^{+0.046}_{-0.081}$	$^{+0.057}_{-0.000}$	$^{+0.008}_{-0.006}$	$^{+0.068}_{-0.098}$	$^{+0.148}_{-0.000}$	$^{+0.016}_{-0.069}$
Flavour	$^{+0.318}_{-0.153}$	$^{+0.112}_{-0.321}$	$^{+0.130}_{-0.137}$	$^{+0.053}_{-0.117}$	$^{+0.161}_{-0.065}$	$^{+0.103}_{-0.160}$	$^{+0.132}_{-0.110}$	$^{+0.348}_{-0.027}$	$^{+0.208}_{-0.292}$
MET	$^{+0.239}_{-0.592}$	$^{+0.249}_{-0.554}$	$^{+0.350}_{-0.332}$	$^{+0.078}_{-0.497}$	$^{+0.129}_{-0.060}$	$^{+0.569}_{-0.232}$	$^{+0.450}_{-0.202}$	$^{+1.029}_{-0.272}$	$^{+0.115}_{-0.365}$
JES	$^{+0.556}_{-1.249}$	$^{+0.983}_{-1.035}$	$^{+0.871}_{-0.554}$	$^{+0.106}_{-0.620}$	$^{+0.895}_{-0.272}$	$^{+0.575}_{-0.478}$	$^{+0.562}_{-0.725}$	$^{+1.054}_{-0.462}$	$^{+1.354}_{-1.998}$
JER	±0.630	±0.841	±0.954	±0.500	±0.820	±0.679	±1.077	±0.681	±0.294

Table 7.10: The total fractional systematic uncertainties for each bin of the the measured relative A_θ differential cross-section in the leptonic SR. The upper panel presents the leading components of the Modelling uncertainty. The lower middle panel presents the upward and downward contribution to all other systematics.

Source	: Uncertainty size [%] A_θ bin:													
	−1.00 - 0.00	0.00 - 0.19	0.19 - 0.32	0.32 - 0.39	0.39 - 0.46	0.46 - 0.53	0.53 - 0.56	0.56 - 0.59	0.59 - 0.63	0.63 - 0.66	0.66 - 0.69	0.69 - 0.76	0.76 - 0.86	0.86 - 1.00
Frag. and Had.	±1.947	±0.038	±0.288	±0.086	±0.401	±0.019	±0.460	±1.074	±0.706	±0.155	±1.247	±0.544	±0.700	±0.230
Matrix Element	±3.646	±1.391	±1.933	±1.037	±0.344	±0.690	±1.244	±2.826	±2.019	±0.443	±2.269	±0.726	±1.937	±2.565
Radiation	±1.627	±1.747	±0.745	±0.442	±0.028	±0.411	±0.751	±0.856	±0.708	±0.490	±0.431	±0.604	±0.461	±0.257
FSR	±2.007	±0.556	±0.915	±0.608	±0.902	±0.291	±0.274	±0.734	±0.252	±0.213	±0.285	±1.347	±0.368	±1.153
PDF	+0.129 / −0.188	+0.139 / −0.194	+0.143 / −0.196	+0.143 / −0.195	+0.124 / −0.170	+0.103 / −0.141	+0.078 / −0.105	+0.055 / −0.081	+0.022 / −0.035	+0.036 / −0.049	+0.093 / −0.099	+0.253 / −0.221	+0.749 / −0.522	+2.302 / −1.166
Backgrounds	+1.462 / −1.386	+1.313 / −1.244	+0.748 / −0.707	+0.999 / −0.947	+0.290 / −0.284	+0.459 / −0.484	+0.609 / −0.641	+0.352 / −0.373	+0.458 / −0.479	+0.410 / −0.434	+0.688 / −0.724	+0.775 / −0.815	+0.859 / −0.905	+2.092 / −2.200
JVT	+0.063 / −0.181	+0.109 / −0.098	+0.091 / −0.058	+0.061 / −0.052	+0.065 / −0.065	+0.025 / −0.021	+0.121 / −0.121	+0.184 / −0.184	+0.061 / −0.064	+0.090 / −0.040	+0.116 / −0.116	+0.095 / −0.040	+0.066 / −0.004	+0.030 / −0.008
Lepton	+0.000 / −0.213	+0.013 / −0.044	+0.071 / −0.000	+0.031 / −0.032	+0.000 / −0.177	+0.023 / −0.014	+0.000 / −0.233	+0.405 / −0.000	+0.026 / −0.004	+0.144 / −0.000	+0.000 / −0.266	+0.134 / −0.004	+0.169 / −0.014	+0.108 / −0.220
Pile-up	+0.093 / −0.262	+0.033 / −0.030	+0.101 / −0.051	+0.038 / −0.000	+0.035 / −0.158	+0.073 / −0.032	+0.000 / −0.101	+0.144 / −0.000	+0.070 / −0.053	+0.052 / −0.000	+0.050 / −0.172	+0.050 / −0.000	+0.052 / −0.011	+0.156 / −0.089
Flavour	+0.235 / −0.441	+0.513 / −0.544	+0.650 / −0.602	+0.518 / −0.525	+0.247 / −0.424	+0.105 / −0.103	+0.032 / −0.254	+0.471 / −0.095	+0.329 / −0.315	+0.452 / −0.302	+0.365 / −0.583	+0.651 / −0.536	+0.785 / −0.651	+1.075 / −1.147
MET	+0.082 / −0.077	+0.000 / −0.175	+0.163 / −0.000	+0.080 / −0.000	+0.000 / −0.369	+0.068 / −0.051	+0.000 / −0.167	+0.103 / −0.013	+0.076 / −0.026	+0.134 / −0.001	+0.000 / −0.068	+0.119 / −0.012	+0.261 / −0.014	+0.097 / −0.384
JES	+1.121 / −1.398	+0.801 / −1.295	+0.648 / −0.623	+1.136 / −0.588	+0.145 / −0.609	+0.550 / −0.156	+0.246 / −0.787	+0.827 / −0.263	+0.967 / −0.700	+0.802 / −0.479	+0.425 / −1.191	+0.777 / −0.617	+1.318 / −0.961	+1.693 / −3.083
JER	±0.376	±0.977	±0.186	±0.752	±0.595	±0.586	±1.162	±0.344	±0.554	±0.158	±0.678	±0.797	±0.653	±0.279

Table 7.11: The total fractional systematic uncertainties for each bin of the the measured relative A_θ differential cross-section in the hadronic SR. The upper panel presents the leading components of the Modelling uncertainty. The lower middle panel presents the upward and downward contribution to all other systematics.

7.7.4 Bootstrapping and correlations

The statistical significance and correlation of each systematic uncertainty was evaluated for all systematics using a bootstrapping procedure with 1000 pseudo-experiments. The bootstrapping procedure is outlined in detail in Section 5.2.6. For systematic uncertainties derived using scale factors there is no statistical uncertainty, as these are evaluated by an event-by-event reweighting of the nominal sample. The statistical significance, σ_{syst}^{stat}, for all other systematics was evaluated as the standard deviation of the distribution of systematic uncertainty sizes evaluated by the pseudo-experiments. Figure 7.19a shows the evaluated uncertainty at particle-level of the first nuisance parameter of the reduced JER uncertainty in the bin $A_{\theta}^{lep} \in [-1, 0.0]$ as evaluated by 1000 pseudo-experiments. As expected from the central limit theory, the distribution is approximately Gaussian, centred on the uncertainty evaluated without the use of the bootstrapping procedure.

The standard deviation of the systematic uncertainty evaluated with pseudo-experiments, $\sigma_{\text{syst},\,i}^{\text{stat}}$, corresponds to the statistical uncertainty on the systematic uncertainty itself. This was evaluated for each bin i of the unfolded A_{θ} distribution. Figure 7.19b shows the standard deviation of the systematic uncertainty compared to the systematic uncertainty as a function of A_{θ} at detector-level. For this example, the systematic uncertainty across multiple-bins was found to be statistically significant and therefore this systematic was retained. Systematics were neglected when the statistical uncertainty was of the same size, according to the criteria

$$\sigma_{syst,i} < 1.5\sigma_{syst,i}^{stat} \qquad \forall \quad i \in \{1, N_{bins}\}. \tag{7.39}$$

The bin-by-bin covariance matrix was evaluated using the bootstrapping procedure. The covariance, K_{ij}, between bin i and j of the unfolded distribution is defined as

$$K_{ij} = E[(A_{\theta}^i - E[A_{\theta}^i])(A_{\theta}^i - E[A_{\theta}^i])], \tag{7.40}$$

where $E[\cdot]$ denotes the expectation value taken over all pseudo-experiments. The Pearson-product-moment correlation coefficients

$$\tilde{K}_{ij} = (K_{ii})^{-\frac{1}{2}} K_{ij} K_{jj}^{-\frac{1}{2}}, \tag{7.41}$$

can be constructed from the covariance matrix. The correlation matrix is normalised such that $\tilde{K}_{ij} \in [-1, 1]$. A large (anti-)correlation corresponds to a value of (-)1.

The covariance matrix for each source of uncertainty, $\mathbf{K}_{\text{syst}}$, describes the effect of the uncertainty on all bins measured simultaneously, and hence characterises the cross-correlation of the measurement. Covariance matrices were calculated using the bootstrap procedure, and combined additively. Figures 7.20 and 7.21 show the total bin-by-bin correlation in fiducial phase space for the leptonic and hadronic asymmetry variables in the signal regions before and after unfolding. Before unfolding the correlation is less than 4% for all off-diagonal elements of the correlation matrix in both SRs.
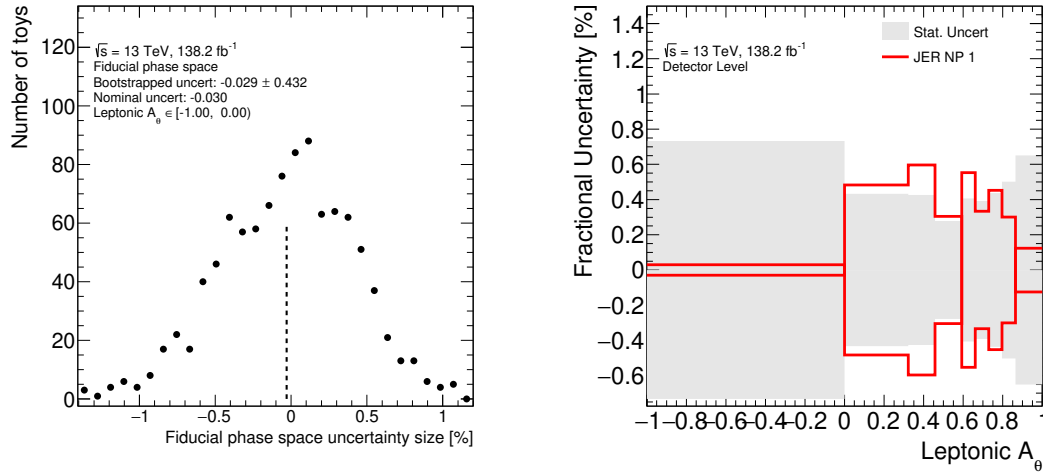
Figure 7.19: The fractional uncertainty of 1000 pseudo-experiments for the jet energy resolution systematic uncertainty at in fiducial phase space for the bin $A_\theta \in [-1, 0.0)$ (left) and the standard deviation of the distribution of systematic uncertainties for each toy compared to size of the systematic uncertainty across the full range of measure A_θ (right). The shape of the spread of the pseudo-experiment uncertainties (left) is representative of the shape of all bootstrapped distributions, however the mean and variance of the distribution vary as function of A_θ.

The observed correlation of the measured relative differential cross-section can be understood to be primarily a result of the unfolding procedure. The unfolding procedure acts probabilistically. At least 50% of events are required to originate from bins with the same A_θ range at detector and particle-level. Therefore, the < 50% of events that originate from bins with different A_θ ranges at detector- and particle-level introduce correlations. As expected, the unfolding has introduced a correlation between bins of between 0% and 35%.
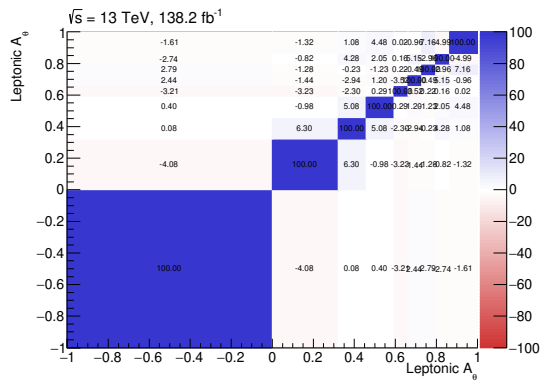
(a) Before unfolding
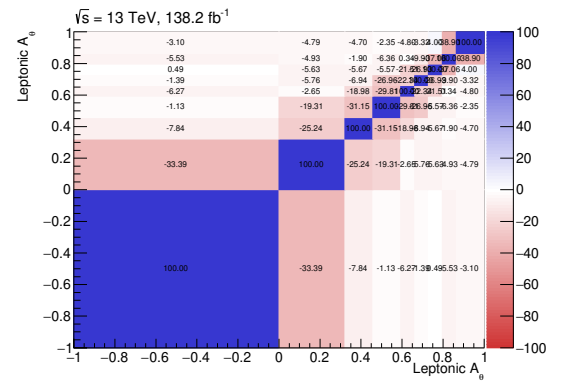
(b) After unfolding

Figure 7.20: The total bin-by-bin correlation between bins of A_θ distribution before and after and the unfolded procedure in the leptonic SR.
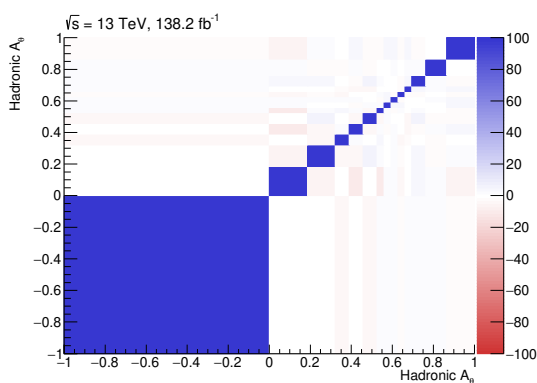
(a) Before unfolding
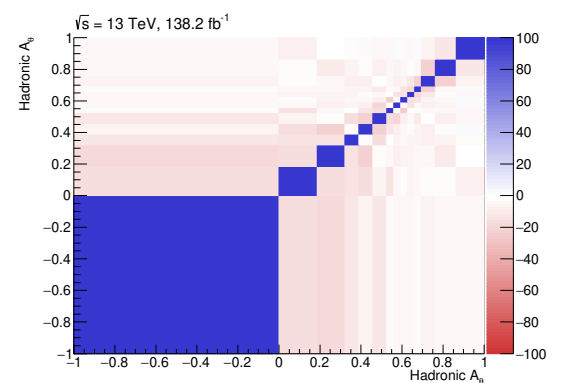
(b) After unfolding

Figure 7.21: The total bin-by-bin correlation between bins of A_θ distribution before and after and the unfolded procedure in the hadronic SR.

7.8   Results

The unfolded measurement of A_θ in the signal regions for the hadronic and leptonic channel is presented in Figure 7.22. The nominal POWHEG+PYTHIA 8 prediction agrees with the data in both SRs, given the systematic and statistical uncertainty of the measurement. The observed data in the Leptonic SR is more compatible with the POWHEG+PYTHIA 8 prediction than the corresponding observation in the Hadronic SR, however this difference is slight and not statistically meaningful. In the Hadronic SR, more data is observed at high A_θ compared to prediction. Moreover, this difference varies smoothly across A_θ. The NLO predictions evaluated using the MAD-GRAPH5_aMC@NLO+PYTHIA 8 and POWHEG+HERWIG 7 samples both agree with the data within the statistical and systematic uncertainties of the measurement. In particular, the disagreement between the three predictions is largest in the low A_θ region, indicating the A_θ variable is sensitive to both how the parton shower is evolved, and the matching procedure used between the parton shower and matrix element. The sensitivity of the A_θ variable to these effects is by design, since the measurement aims to examine the radiation of the $t\bar{t}$ system as well as the subsequent evolution of that radiation. The POWHEG+PYTHIA 8 prediction has been used extensively within the ATLAS collaboration to model the $t\bar{t}$ system, including radiative properties. Free parameters, such as factorisation scales, have been tuned prior to this measurement. Therefore, the POWHEG+PYTHIA 8 sample has less predictive power than the other NLO samples and it is not unexpected to find good agreement between the data and this sample.

To quantify the agreement between prediction and data, a Pearson χ^2 goodness-of-fit test was performed [168]. The χ^2 test statistic for simultaneous measurements with non-zero correlation is

$$\chi^2 = (\mathbf{D} - \mathbf{M})_{N-1}^T \cdot \mathbf{\Sigma}^{-1} \cdot (\mathbf{D} - \mathbf{M})_{N-1}, \tag{7.42}$$

where $\mathbf{\Sigma}$ is the total covariance matrix, combining additively the covariance due to statistical and systematic uncertainties. The measured distribution is normalised, hence a degree of freedom has been removed from the system. The χ^2 test statistic is calculated with one bin removed. As the analysis has been designed for maximum sensitivity to the extrema of the A_θ distribution, the modal bin was chosen for blinding. This amounts to measuring the differential cross-section relative to the yield in this region of phase-space.

From the χ^2 test statistic, the p-value and z-scores can be evaluated. The p-value, in this context, is defined as

$$P(\chi^2 > \chi^2_{\text{measured}}) = 1.0 - \int_0^{\chi^2_{\text{measured}}} p(\chi^2) d\chi^2 \tag{7.43}$$

where $p(\chi^2)$ is the probability distribution of the χ^2 statistic [168]. The p-value corresponds to the probability of observing the data given the hypothesis being tested is true.

Therefore, low p-values correspond to poor agreement between observation and prediction. The z-score, or σ-significance, is often used within the field of particle-physics to provide an intuitive understanding of agreement between data and prediction. The z-score represents how many standard deviations an observation is from the mean expectation. Assuming Gaussian distributed uncertainties, an assumption made implicitly throughout this analysis and the wider particle-physics community, the p-value can be used to evaluate the z-score from the inverse cumulative probability of the Gaussian distribution [168].

Table 7.12 presents z-score, p-value and χ^2 for the three discussed NLO generators. The global value of these test statistics has also been calculated for all the predictions by combining the measurement in both SRs. The z-score between data and POWHEG+PYTHIA 8 is $< 10^{-2}$. Furthermore, the global z-score between POWHEG+HERWIG 7 and data is < 0.02 meaning no deviation is systematically or statistically significant. The observed p values between data and both the POWHEG+HERWIG 7 and POWHEG+PYTHIA 8 predictions are > 0.95. This level of agreement between data and these predictions is unlikely given the uncertainties associated with this measurement. As previously discussed, mis-modelling of radiation in the system is a dominant systematic uncertainty in this analysis, referred to in Section 7.7 as the modelling uncertainty. The modelling uncertainties characterise the affect of mis-modelling on the measurement, and are fundamentally different from experimental uncertainties which are Gaussian noise associated with an observation. As MC modelling of the top quark system was used extensively in performing this measurement, a conservative approach of treating modelling systematic uncertainties as Gaussian uncertainties was used. The uncertainty describing the measured data is typically larger than observed residual between prediction and data, because of the large modelling uncertainty. Therefore, the modelling uncertainties contribute to the strength of the observed agreement between data and POWHEG+HERWIG 7 and POWHEG+PYTHIA 8. Of the NLO predictions, the MADGRAPH5_aMC@NLO+PYTHIA 8 has the most significant deviation from data, with an observed z-score of 1.38. From the difference between the POWHEG+HERWIG 7 and MADGRAPH5_aMC@NLO+PYTHIA 8 agreement, it can be concluded that the A_θ variable has increased sensitivity to the matching scale between the ME and PS compared to the PS evolution procedure. As previously discussed, this is by construction of the variable.

The dead-cone effect has been implicitly included within all NLO predictions thus-far discussed. The observed compatibility between data and NLO therefore strongly implies the effect. However, without a prediction that explicitly factorises out the dead-cone effect, the significance of this agreement cannot be stated.
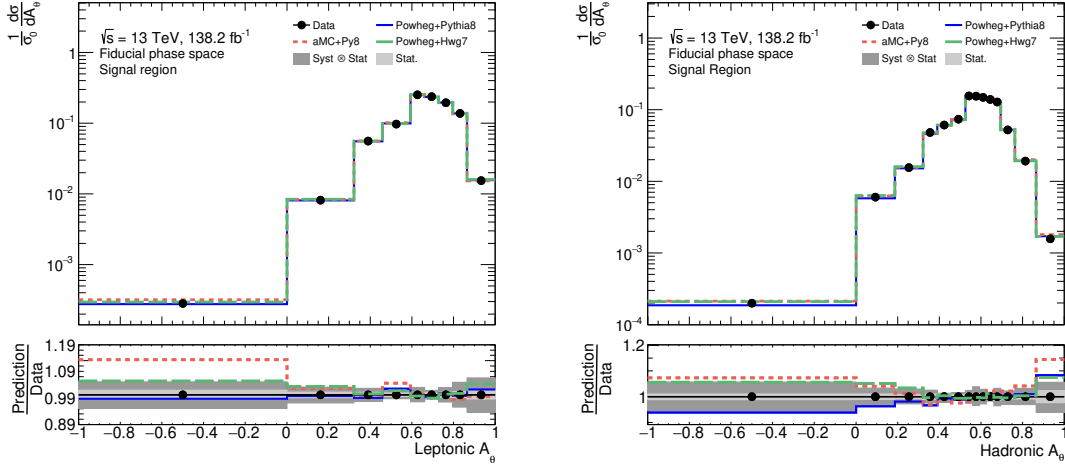
Figure 7.22: The relative differential cross-section of the angular asymmetry in fiducial phase space for the leptonic (left) and hadronic (right) signal regions using data recorded over the years 2015-2018 with the ATLAS detector.

	Leptonic SR			Hadronic SR			Global		
	χ^2/N_{DoF}	p-value	z-score	χ^2/N_{DoF}	p-values	z-score	χ^2/N_{DoF}	p-values	z-score
Powheg+Pythia 8 (Nominal)	2.43/8	0.965	0.044	5.77/13	0.954	0.058	8.2/21	0.994	0.007
Powheg+Herwig 7	3.41/8	0.906	0.118	5.81/13	0.953	0.059	9.22/21	0.987	0.016
MadGraph5_aMC@NLO+Pythia 8	11.8/8	0.161	1.402	15.3/13	0.29	1.057	27.1/21	0.168	1.380
Pythia 8 DC on	18.4/8	0.0187	2.351	59.8/13	5.7×10^{-8}	5.428	78.2/21	1.61×10^{-8}	5.649
Pythia 8 DC off	31.3/8	1.22×10^{-4}	3.841	73.9/13	1.5×10^{-10}	6.405	105/21	3.43×10^{-13}	7.276

Table 7.12: The χ^2, calculated as defined in the text, evaluated between the nominal and dead-cone on/off Monte Carlo samples and the corresponding p-value and z-scores.

7.9   Interpretation

The dead-cone effect is factorisable from the matrix element to LO accuracy. Figure 7.23 shows the PYTHIA 8 prediction of the relative A_θ differential cross-section, with and without the dead-cone effect. Unlike the NLO predictions, at LO the description of radiation in the $t\bar{t}$ system does not agree with data for both SRs. In both SRs, the SM-like dead-cone on prediction lies closer to data than the dead-cone off hypothesis. The agreement between the two LO predictions has been quantified with the previously discussed test statistics, and is presented in the lower half of Table 7.12. The Leptonic SR has greater power at observing the difference between the two LO hypotheses, as shown by a difference in z-scores of 1.49. This indicates the dead-cone effect is a very weak effect, even in the LO picture. However, the A_θ variable is still sensitive to the dead-cone effect. The hadronic SR has far weaker separation between the LO templates, and correspondingly a smaller difference in z-score. However, data and both LO predictions have a more significant separation in this region of phase-space compared to the Leptonic SR. This is primarily driven by the increased resolution, and therefore increased binning, in the region $A_\theta \sim 0.5$. The increased resolution of A_θ in the hadronic SR compared to the leptonic SR is in the region where the dead-cone effect is not present, i.e $A_\theta > 0.0$. Therefore, strong rejection of both LO templates was observed but poor rejection of one template compared to the other was also found. A method to examine the significance of the observed LO dead-cone effect prediction was sought.

Reweighting

To isolate the size of the dead-cone effect from differences between LO and NLO predictions an event-level re-weighting procedure was used. The A_θ distribution of the LO particle-level dead-cone on hypothesis was constructed in fine bins of A_θ, as was the same distribution for the nominal MC at particle-level. These distributions are shown for both SRs in Figure 7.24. The re-weighting factors, w_i, for an arbitrary event with A_θ in bin i is

$$w_i = \frac{A_\theta^{\text{nom},i}}{A_\theta^{\text{DC on},i}}. \tag{7.44}$$

The `353QH` smoothing procedure[1] is applied to reduce the impact of statistical fluctuation in the derived weights [190]. Due to the smoothing, there is a small non-closure at low A_θ. Assuming the LO and NLO effects factorise from the dead-cone on and off predictions, this procedure can be used to examine the observed magnitude of the dead-cone effect. This re-weighting procedure can be considered to be a multiplicative method of matching LO to NLO predictions. An alternative additive method was also

---

[1]Implemented in using the scientific software toolkit `ROOT`, with the TH1::Smooth method.
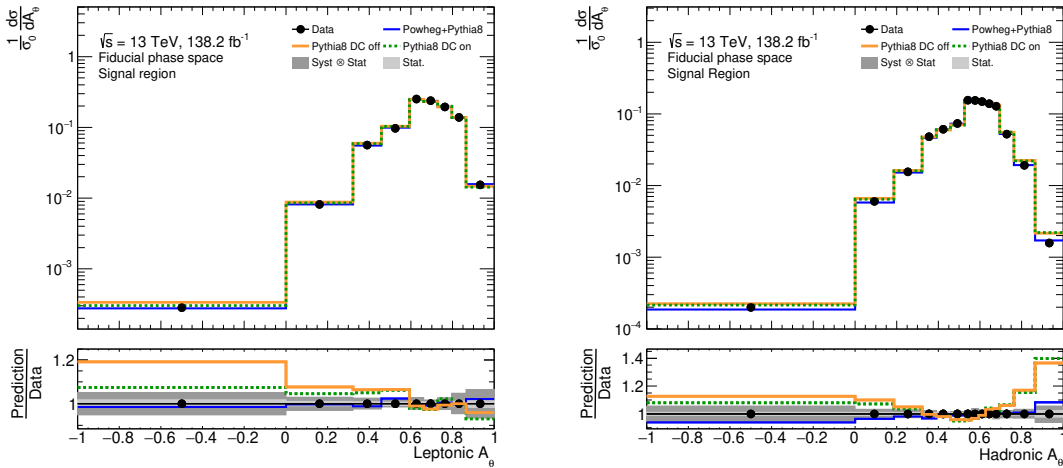
Figure 7.23: The relative differential cross-section of the angular asymmetry in fiducial phase space for the leptonic (left) and hadronic (right) signal regions using data recorded over the years 2015, 2016 and 2017 with the ATLAS detector.

considered, in which the an additive correction factor defined as

$$\Delta_i = A_\theta^{\text{nom},i} - A_\theta^{\text{DC on},i}. \tag{7.45}$$

Both procedures produced identical results, and the multiplicative re-weighting method will be discussed exclusively herein. Figure 7.25 shows the A_θ distributions before and after re-weighting for the dead-cone on and off samples in both SRs. The ratio between each sample before and after re-weighting agrees well within the statistical uncertainty of the samples. Therefore the re-weighting procedure affects both LO samples in the same manner, whilst maintaining the differences in description of the dead-cone effect.

7.9.1   Template fit

A maximum likelihood fit was performed that aims to fit a parameter characterising the best fractional combination of two predictions, or templates, to data. Two templates are used to perform a maximum likelihood fit; T which corresponds to the SM dead-cone on hypothesis and t which corresponds to the alternate hypothesis. The likelihood function maximised is

$$L = \prod_i \frac{(f_{\text{DC}}T_i + (1 - f_{\text{DC}})t_i)^{d_i}}{d_i!} \exp\left(-(f_{\text{DC}}T_i + (1 - f_{\text{DC}})t_i\right), \tag{7.46}$$

where i is a binning index; d_i, T_i and t_i are the number of entries in bin i for data, template T and template t respectively, f_{DC} is the fitted parameter of interest representing the strength of suppression of the dead-cone effect. By construction, f_{DC} is expected to be in the range $[0, 1]$. The likelihood L was maximised by minimising its negative logarithm through the use of the L-BFGS-B algorithm, implemented in SKLEARN python package [191], where the bounded constraints used on f_{DC} ($[-20, 20]$) are much larger than the expectation of $f_{\text{DC}} \in [0, 1]$.

(a) Leptonic SR

(b) Hadronic SR
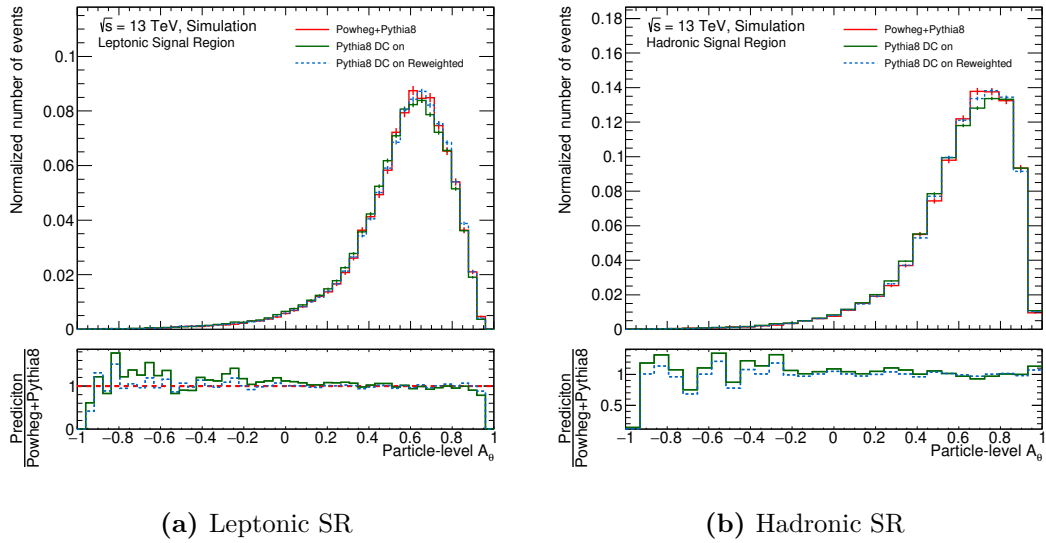
Figure 7.24: The LO PYTHIA 8 dead-cone on samples before and after the reweighting procedure in the fine-grained binning used to define the weights with Equation 7.45. The nominal $t\bar{t}$ sample used in the re-weighting procedure is also shown.

(a) Leptonic SR

(b) Hadronic SR
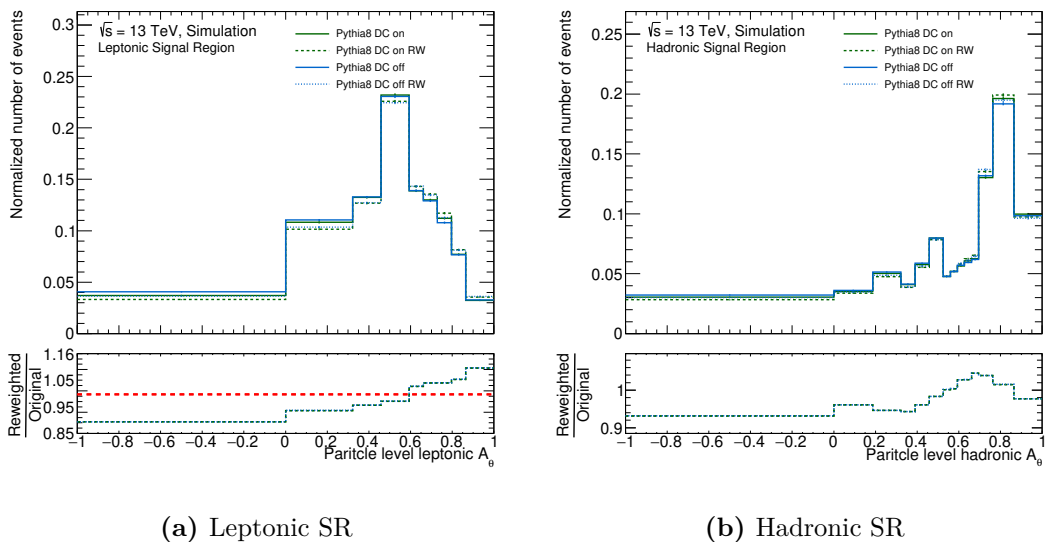
Figure 7.25: The LO PYTHIA 8 dead-cone on and off samples before and after the reweighting procedure in bins optimised during the unfolding procedure detailed in Section 7.6.2. The ratio shown in the lower panel is taken between the sample before and after the re-weighting has been applied.

The likelihood shown in Eq. 7.46 has a very low computational cost to evaluate, therefore in addition to the use of the L-BFGS-B algorithm to evaluate the minimum of L with respect to f_{DC}, a fine scan of 10^5 points around the evaluated minimum was performed to validate the smoothness of the likelihood.

The LO PYTHIA 8 templates were re-weighted to match the NLO POWHEG+PYTHIA 8 sample using the A_θ variable at particle-level. The re-weighting was assumed to affect both LO distributions in the same manner, resulting in a pseudo-NLO description of a $t\bar{t}$ system where top quarks radiate as if they were massless.

Figure 7.26 shows the measured values for f_{DC} with the standard model template T corresponding to the nominal POWHEG+PYTHIA8 sample, or equivalently the re-weighted LO PYTHIA 8 dead-cone on sample. The radiatively suppressed template, t in Eq. 7.46, corresponds to the re-weighted dead-cone off sample. The statistical uncertainty on f_{DC} was evaluated through the use of pseudo-experiments. The measured A_θ distribution was smeared bin-by-bin by a random number drawn from a Gaussian of mean 1.0 and width equal to the size of the statistical uncertainty in that bin. 1000 pseudo-experiments were performed to evaluate the statistical uncertainty of the measurement. The systematic uncertainty of f_{DC} was taken to be the difference in fitted f_{DC} between the nominal and systematically shifted MC distributions.

A joint fit across the leptonic and hadronic signal regions was performed and the measured dead-cone suppression strength was found to be

$$f_{\mathrm{DC}} = 0.527 \pm 0.041 \pm 0.295. \tag{7.47}$$

The data measured in the Hadronic SR favours the re-weighted LO prediction, unlike the data measured in the Leptonic SR which favours the NLO prediction. As a result of this disagreement, the combination yields an ambiguous result. The uncertainty on the measured value of f_{DC} in the Hadronic SR is 0.50, much larger than the 0.30 uncertainty in the leptonic SR. As discussed previously, this indicates the dead-cone effect is resolved less precisely in the Hadronic SR than the Leptonic SR. The disagreement between the two regions indicate the FSR pattern of a top quark that subsequently decays via the hadronic or leptonic top is measurably different, implying the interference diagrams present in the hadronic decay of a top quark contribute substantially. The combination benefits from the enhanced statistics available from both measurement regions, as is clear from the reduced statistical uncertainty compared to the individual channels. However, the constraint one region imposes on another during the fitting procedure causes an increase in systematic uncertainty in the global measurement compared to the leptonic SR. This arises due to the large difference in measured value of f_{DC}. The novel method proposed in this thesis has the potential to reject the dead-cone off hypothesis with a sensitivity of 3σ. However, due to the different measured values in the two observation regions, this sensitivity is not observed. The measurement is compatible with both LO hypotheses, and lies 1.77σ away from the dead-cone off hypothesis and 1.59σ away from the dead-cone on hypotheses.
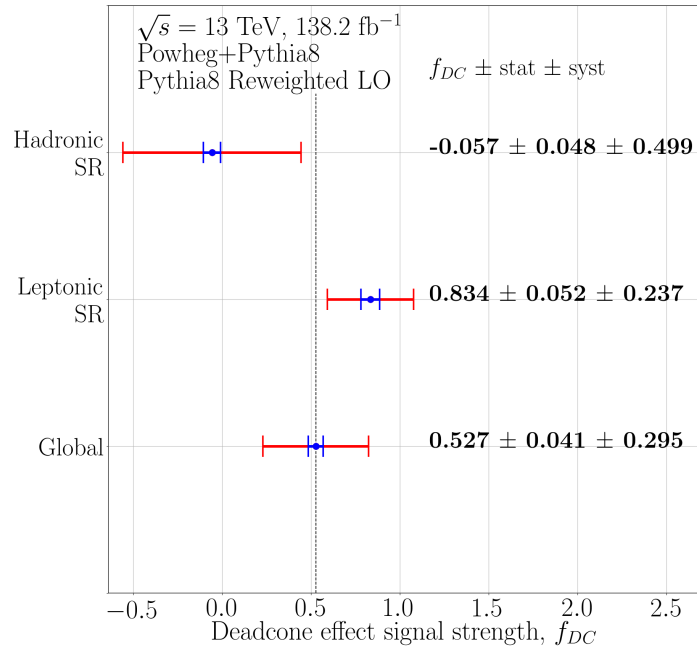
Figure 7.26: The fitted value of f_{DC} in the leptonic and hadronic regions, as defined in the text, as well as the global fit. The total statistical uncertainty of the fitted parameter, f_{DC}, is shown in blue and the total systematic uncertainty is shown in red.

Figure 7.27 shows how the sources and size of the systematic uncertainties affect f_{DC} when fitted globally. The relative importance of each systematic is consistent between the template fit and the relative differential distribution as described in Tables 7.10 and 7.11. The background uncertainty due to the W+jets background process remains a prominent source of uncertainty in the procedure. However, the uncertainty due to the fake background estimation is larger in the global fit. The W+jet uncertainty has a different shape in both SRs, therefore the global fit constrains and reduces this uncertainty. Uncertainties arising from modelling and jets remain the largest combined contributions.
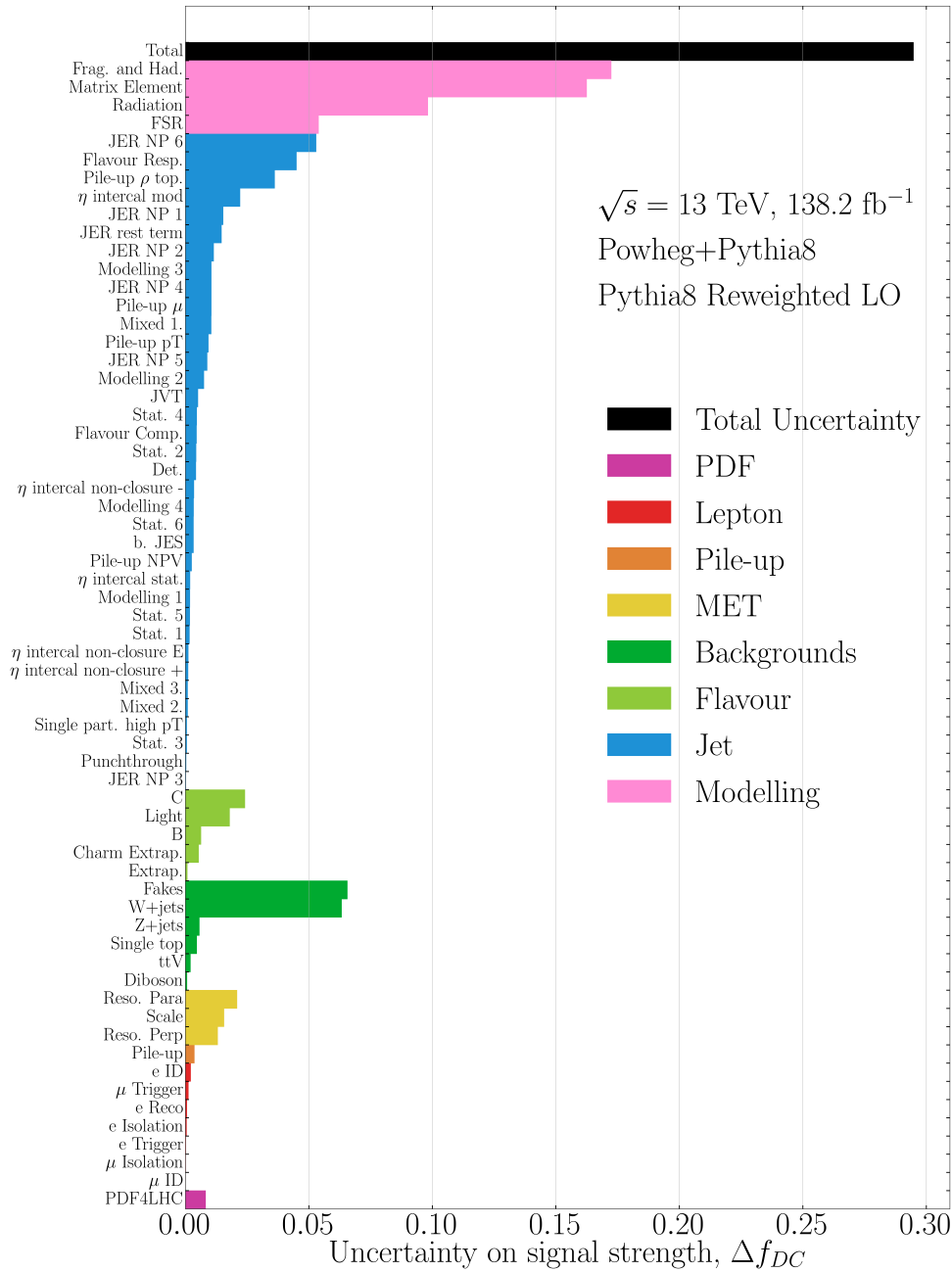
Figure 7.27: The sources of systematic uncertainty for the f_{DC} evaluated in the global template fit, grouped together by source. The quadrature sum of the 20 PDF4LHC nuisance parameters is shown as the PDF uncertainty.

7.10   Conclusion

The relative differential distributions of the newly proposed A_θ variable, that has large sensitivity to the dead-cone effect, have been measured and compared to a set of MC predictions. The NLO description of the radiation in the $t\bar{t}$ sample was compatible with measured data within systematic uncertainties. The differences in NLO prediction compared to data are understood to arise from free parameters within the matching and showering procedures used. Therefore, this measurement provides useful information that can be used to further improve the description of radiation from the $t\bar{t}$ system.

The leading order predictions with the dead-cone on and off scenarios of PYTHIA8 were rejected with a significance of 5.65σ and 7.28σ respectively, as measured by a conservative χ^2 comparison. To isolate the description of the dead-cone, a binned maximum log-likelihood fit of the fractional contribution of the dead-cone off hypothesis, f_{DC}, needed to describe the measured data was performed. For the fit, the dead-cone off hypothesis was re-weighted to remove differences between LO and NLO predictions of the $t\bar{t}$ system. The dead-cone strength parameter was measured to be $f_{\mathrm{DC}} = 0.527 \pm 0.041 \pm 0.295$, which is compatible with both the dead-cone on or off hypotheses.

8.   Conclusion

In this thesis several novel approaches to probing QCD at the LHC have been presented. Firstly, the radiation of the top quark system was explored using an analytic approach. Top tagging algorithms were examined using analytic-based substructure techniques. The CMS Top Tagger algorithm was explored and found to be IRC unsafe at order α_s^3 in QCD. The `TopSplitter` extension to this algorithm was proposed as an IRC safe extensions. `TopSplitter` was found to have strong tagging performance, in part due to the implicit jet grooming that was introduced in the procedure. Furthermore, the analytically motivated Y_m splitter algorithm was proposed. The application of the top tagging algorithms on top jets was examined with an all order calculation and compared to MC prediction. The analytic jet mass distributions of top jets were found to have large quantitative and qualitative differences with the MC prediction. These arise ultimately from the neglected effect of soft gluon emissions in the analytic calculation compared to MC. Furthermore, the description of quark-initiated jets with a three-prong structure after the application of a top tagging algorithm was examined with an all order calculation, and compared to MC based predictions. The MC prediction was found to agree with the all order calculation in the relevant phenomenological region. Therefore, the assumption often made across the particle physics community, that the mass ordering of radiative prongs in a parton shower accurately captures all-order effects, has been shown to be valid.

Furthermore, the calibration of jets in the forward region of the ATLAS detector was studied. The dijet η inter-calibration was performed for data collected in the years 2015 and 2016. The presence of an under-correction in the dijet η inter-calibration procedure was identified. A potential iterative extension to the method was explored, and found to be ultimately unsuccessful in removing the under-correction. A new systematic uncertainty was introduced to account for this issue. This uncertainty was found to be sub-dominant in comparison to the uncertainties associated with modelling. Furthermore, the bootstrapping procedure was introduced to the η inter-calibration procedure for the first time, which led to a greater understanding and ultimate reduction of the systematic uncertainties within the method. The statistical significance of systematic uncertainties associated with the choice of cuts selecting a dijet event topology was evaluated. These topology-related uncertainties were found to be statistically insignificant. The conservative approach of taking an envelope of these statistically insignificant

uncertainties was taken, which ultimately resulted in a reduction of the total uncertainty from this source compared to previous implementations of the method that did not bootstrap the systematic uncertainties of the measurement.

As a central part of this thesis, the dead-cone effect was studied in detail. A new analysis procedure was designed and implemented. In this novel analysis, a new variable, A_θ, was constructed to have sensitivity to the dead-cone effect and the radiation pattern from the $t\bar{t}$ system. The new approach allowed for a measurement potentially sensitive to the radiation pattern, and therefore dead-cone effect, of top quarks at the LHC to be performed with the recorded Run 2 data-set of the ATLAS experiment. This is a large improvement compared to the current expectation from literature, where proposals require a minimum of $L = 300\,\mathrm{fb}^{-1}$ for a measurement. A novel application of the machine learning tool BayesOpt was introduced as a general method to define a signal region. The relative A_θ differential cross-section distribution was measured in regions of phase-space determined by this procedure. Detector effects were removed using an unfolding procedure. The procedure was extensively validated to ensure no bias was introduced. The measured A_θ distribution was found to have excellent agreement with NLO predictions of radiation from the $t\bar{t}$ system across a range of three different NLO predictions. The A_θ observable was found to provide information on the matching and factorisation scale in $t\bar{t}$ simulation, as examined by comparison with different NLO predictions. All NLO predictions implicitly contain the prediction of a dead-cone. However, without a suitably high precision alternative hypothesis a definitive observation of the effect cannot be claimed. To isolate the dead-cone effect explicitly, two leading order samples with the dead-cone effect turned on and off were compared to data. Differences between the LO and NLO sample were assumed to factorise with the dead-cone effect. A re-weighting procedure was then used to produce a dead-cone off sample, corrected for NLO effects. The strength of the dead-cone effect was parameterised using a new observable, f_{DC}, which characterises the amount of dead-cone like radiation suppression in the $t\bar{t}$ system. The method had the potential for a 3σ sensitivity, provided that f_{DC} was measured to be the standard model expectation of 1.0. The strength of the dead-cone effect was measured to be $f_{\mathrm{DC}} = 0.527 \pm 0.041 \pm 0.295$. which is compatible ith both dead-cone on and off hypothesis.

Appendices

A. Full uncertainties of the A_θ differential cross-section measurement

The Tables A.1 and A.2 show a complete break-down of the systematic uncertainties in the measurement of the $\frac{1}{\sigma}\frac{d\sigma}{dA_\theta}$ for the leptonic and hadronic SRs respectively.

Uncertainty size [%]

Source	A_θ bin:								
	−1.00 - 0.00	0.00 - 0.32	0.32 - 0.46	0.46 - 0.59	0.59 - 0.66	0.66 - 0.73	0.73 - 0.80	0.80 - 0.86	0.86 - 1.00
PDF4LHC_121	±0.000	±0.002	±0.003	±0.002	±0.002	±0.002	±0.008	±0.005	±0.006
PDF4LHC_122	±0.083	±0.086	±0.099	±0.090	±0.062	±0.001	±0.101	±0.266	±0.580
PDF4LHC_123	±0.023	±0.022	±0.035	±0.024	±0.007	±0.014	±0.033	±0.054	±0.111
PDF4LHC_124	±0.055	±0.053	±0.056	±0.055	±0.037	±0.002	±0.066	±0.166	±0.319
PDF4LHC_125	±0.045	±0.051	±0.067	±0.055	±0.025	±0.019	±0.070	±0.137	±0.282
PDF4LHC_126	±0.061	±0.066	±0.076	±0.068	±0.036	±0.019	±0.088	±0.183	±0.346
PDF4LHC_127	±0.010	±0.008	±0.012	±0.007	±0.005	±0.001	±0.005	±0.022	±0.078
PDF4LHC_128	±0.028	±0.025	±0.029	±0.022	±0.009	±0.009	±0.039	±0.072	±0.065
PDF4LHC_129	±0.041	±0.038	±0.041	±0.036	±0.020	±0.007	±0.056	±0.120	±0.136
PDF4LHC_130	±0.041	±0.044	±0.045	±0.043	±0.034	±0.001	±0.062	±0.147	±0.212
PDF4LHC_131	±0.028	±0.030	±0.018	±0.026	±0.023	±0.003	±0.047	±0.093	±0.074
PDF4LHC_132	±0.031	±0.034	±0.038	±0.031	±0.015	±0.005	±0.031	±0.077	±0.231
PDF4LHC_134	±0.015	±0.021	±0.023	±0.030	±0.034	±0.017	±0.025	±0.102	±0.244
PDF4LHC_135	±0.003	±0.009	±0.009	±0.008	±0.008	±0.000	±0.003	±0.014	±0.101
PDF4LHC_136	±0.173	±0.183	±0.207	±0.188	±0.138	±0.032	±0.163	±0.538	±1.580
PDF4LHC_137	±0.003	±0.005	±0.007	±0.005	±0.000	±0.007	±0.012	±0.008	±0.007
PDF4LHC_138	±0.001	±0.000	±0.000	±0.002	±0.001	±0.004	±0.008	±0.005	±0.041
PDF4LHC_139	±0.007	±0.005	±0.007	±0.004	±0.004	±0.000	±0.006	±0.018	±0.034
PDF4LHC_140	±0.035	±0.035	±0.032	±0.036	±0.033	±0.007	±0.037	±0.119	±0.257

Fakes var 0	−0.977	0.305	−0.259	0.305	0.145	−0.036	−0.276	−0.238	−0.034
Fakes var 1	1.030	−0.321	0.274	−0.322	−0.153	0.038	0.291	0.251	0.036
Frag. and Had.	±3.984	±0.703	±0.861	±0.323	±0.678	±0.671	±0.677	±2.913	±0.199
Matrix Element	±1.489	±1.629	±0.824	±0.073	±2.023	±0.560	±1.217	±0.660	±1.073
FSR Up	0.973	−0.356	−0.253	1.000	−0.207	0.122	−0.504	−1.314	−0.482
FSR Down	−1.116	−0.572	−0.583	−0.164	0.188	0.270	0.638	0.705	0.525
Var3Down	±0.397	±0.794	±0.117	±0.222	±0.442	±0.010	±0.111	±0.216	±0.125
ttV σ upward var	±0.030	±0.018	±0.013	±0.002	±0.010	±0.010	±0.008	±0.004	±0.004
ttV σ downward var	±0.030	±0.018	±0.013	±0.002	±0.010	±0.010	±0.008	±0.004	±0.004
Diboson σ upward var	±0.004	±0.004	±0.004	±0.001	±0.002	±0.000	±0.002	±0.007	±0.012
Diboson σ downward var	±0.004	±0.004	±0.004	±0.001	±0.002	±0.000	±0.002	±0.007	±0.012
W+jets σ upward var	±0.189	±0.825	±0.943	±0.545	±0.449	±0.103	±0.843	±1.971	±3.835
W+jets σ downward var	±0.203	±0.883	±1.010	±0.583	±0.482	±0.111	±0.903	±2.112	±4.108
Z+jets σ upward var	±0.085	±0.063	±0.095	±0.064	±0.005	±0.055	±0.074	±0.185	±0.602
Z+jets σ downward var	±0.086	±0.063	±0.096	±0.065	±0.005	±0.056	±0.075	±0.187	±0.609
Single top σ upward var	±0.052	±0.054	±0.045	±0.017	±0.019	±0.036	±0.037	±0.043	±0.051

A. Full uncertainties of the A_θ differential cross-section measurement

	±0.052	±0.054	±0.045	±0.017	±0.019	±0.036	±0.037	±0.043	±0.051
Single top σ downward var	0.003	−0.028	0.043	−0.001	0.034	−0.046	−0.029	0.053	−0.058
JVT Up	0.041	−0.061	−0.042	−0.034	0.018	0.003	0.049	0.126	−0.009
JVT Down	0.018	−0.050	0.009	−0.049	0.005	0.006	0.014	0.115	0.065
e Trigger Up	0.039	−0.039	0.002	−0.011	0.030	−0.011	0.005	0.058	−0.086
e Trigger Down	0.029	−0.050	−0.005	−0.021	0.025	−0.012	0.013	0.086	−0.015
e Reco Up	0.035	−0.046	−0.006	−0.017	0.025	−0.013	0.011	0.080	−0.032
e Reco Down	−0.013	−0.078	−0.029	−0.060	−0.004	−0.011	0.039	0.183	0.262
e ID Up	0.074	−0.012	0.031	0.011	0.046	−0.004	−0.017	−0.014	−0.299
e ID Down	0.027	−0.052	−0.010	−0.019	0.027	−0.014	0.016	0.088	−0.010
e Isolation Up	0.037	−0.047	−0.006	−0.014	0.028	−0.015	0.010	0.076	−0.043
e Isolation Down	0.011	−0.076	−0.034	−0.043	0.014	−0.010	0.052	0.159	0.070
μ Trigger Up	0.052	−0.025	0.019	0.008	0.042	−0.020	−0.024	0.006	−0.123
μ Trigger Down	0.030	−0.049	−0.008	−0.017	0.026	−0.018	0.012	0.086	−0.014
μ ID Up	0.040	−0.056	−0.004	−0.018	0.030	−0.008	0.000	0.097	−0.048
μ ID Down	0.029	−0.054	−0.015	−0.022	0.025	−0.015	0.021	0.099	−0.005
μ Isolation Up	0.039	−0.044	−0.007	−0.008	0.032	−0.016	0.003	0.066	−0.052
μ Isolation Down	−0.114	−0.082	0.094	0.046	0.001	−0.006	−0.098	0.053	−0.069
Pile-up Up	0.106	−0.004	−0.104	−0.081	0.057	0.008	0.068	0.138	0.016
Pile-up Down	0.012	−0.166	−0.094	−0.038	0.082	0.043	0.056	0.114	0.128
B Up	0.059	0.068	0.077	0.005	−0.029	−0.072	−0.031	0.051	−0.184
B Down	−0.091	−0.204	−0.074	−0.086	0.094	0.075	0.102	0.219	0.031
C Up	0.247	0.070	0.083	0.053	−0.041	−0.119	−0.102	−0.027	−0.080
C Down									

Light Up	-0.123	-0.155	0.042	-0.013	0.088	0.046	0.049	0.014	-0.208
Light Down	0.174	0.055	-0.043	-0.031	-0.041	-0.066	-0.020	0.152	0.161
Extrap. Up	0.034	-0.038	0.002	-0.030	0.014	-0.005	0.007	0.094	-0.004
Extrap. Down	0.027	-0.044	0.000	-0.024	0.020	-0.003	0.009	0.081	-0.022
Charm Extrap. Up	0.065	-0.005	0.048	-0.004	-0.006	-0.045	-0.018	0.041	-0.032
Charm Extrap. Down	-0.001	-0.080	-0.050	-0.046	0.045	0.032	0.037	0.132	-0.000
Reso. Para	-0.227	-0.414	-0.071	-0.356	0.036	0.421	0.295	0.636	-0.105
Reso. Perp	-0.536	-0.215	-0.152	-0.254	0.038	0.318	0.215	0.558	0.051
Scale Up	-0.109	-0.299	-0.286	-0.236	0.118	0.214	0.263	0.585	0.103
Scale Down	0.239	0.249	0.350	0.078	-0.060	-0.232	-0.202	-0.272	-0.350
JER_NP_1	±0.030	±0.483	±0.596	±0.304	±0.553	±0.334	±0.453	±0.300	±0.124
JER_NP_2	±0.187	±0.385	±0.465	±0.330	±0.517	±0.209	±0.490	±0.335	±0.080
JER_NP_3	±0.155	±0.069	±0.525	±0.178	±0.257	±0.273	±0.265	±0.284	±0.168
JER_NP_4	±0.200	±0.415	±0.057	±0.042	±0.064	±0.117	±0.156	±0.055	±0.037
JER_NP_5	±0.516	±0.147	±0.118	±0.100	±0.013	±0.229	±0.250	±0.108	±0.045
JER_NP_6	±0.176	±0.016	±0.005	±0.128	±0.125	±0.399	±1.077	±0.247	±0.115
JER_rest_term	±0.020	±0.357	±0.213	±0.083	±0.119	±0.075	±0.341	±0.325	±0.191
Flavour Comp. down	0.256	0.468	0.266	-0.184	0.388	-0.013	-0.351	-0.311	-1.118
Flavour Comp. up	-0.682	-0.589	0.111	-0.186	-0.170	0.299	0.300	0.387	0.937

Flavour Resp. down	−0.411	−0.660	−0.229	−0.094	−0.020	0.391	0.288	0.427	0.506
Flavour Resp. up	0.255	0.536	0.309	−0.096	0.301	−0.232	−0.395	−0.255	−0.841
b. JES down	0.070	0.081	−0.233	−0.156	0.187	−0.012	0.044	0.333	−0.068
b. JES up	−0.034	0.024	0.199	−0.000	0.039	−0.095	−0.074	−0.047	−0.199
Det. down	0.085	0.058	−0.062	−0.027	0.061	−0.071	0.043	0.042	−0.069
Det. up	−0.049	−0.045	−0.023	−0.011	0.089	−0.078	0.052	0.064	−0.041
Modelling 1 down	−0.045	0.310	−0.148	−0.217	0.418	0.052	−0.088	−0.131	−0.281
Modelling 1 up	−0.308	−0.300	0.315	0.023	−0.200	0.066	0.056	0.064	0.156
Modelling 2 down	0.069	0.001	0.001	0.021	0.084	−0.066	−0.007	−0.041	−0.188
Modelling 2 up	−0.131	0.035	−0.081	−0.059	0.032	−0.042	0.052	0.239	0.029
Modelling 3 down	−0.100	−0.006	−0.018	−0.028	0.023	−0.071	0.065	0.149	−0.001
Modelling 3 up	0.046	0.037	−0.023	−0.032	0.069	−0.026	−0.006	0.053	−0.144
Modelling 4 down	−0.005	0.021	−0.038	−0.033	0.089	−0.056	0.022	0.052	−0.043
Modelling 4 up	−0.026	−0.012	−0.055	−0.023	0.103	−0.073	0.035	0.076	−0.016
η intercal mod down	0.352	0.488	0.291	0.064	0.085	−0.260	−0.358	−0.143	−1.128
η intercal mod up	−0.623	−0.348	−0.218	−0.238	0.102	0.254	0.261	0.424	0.784
η intercal non-closure E down	0.017	−0.021	−0.038	−0.030	0.059	−0.013	0.012	0.072	−0.012
η intercal non-closure E up	−0.049	0.020	−0.002	−0.043	0.028	0.000	0.001	0.068	0.003

η intercal non-closure - down	0.088	−0.027	−0.011	−0.021	0.075	−0.064	0.003	0.057	−0.027
η intercal non-closure - up	−0.018	−0.028	−0.036	−0.037	0.054	−0.010	0.017	0.106	−0.007
η intercal non-closure + down	0.034	−0.006	−0.028	−0.014	0.052	−0.042	0.018	0.082	−0.111
η intercal non-closure + up	0.046	−0.035	−0.036	−0.031	0.053	−0.030	0.029	0.072	0.034
η intercal stat. down	0.026	0.120	−0.122	−0.013	0.071	−0.048	−0.024	0.094	−0.095
η intercal stat. up	−0.021	−0.112	0.019	−0.005	0.017	−0.049	0.046	0.101	0.058
Pile-up μ down	0.042	0.227	0.183	−0.083	0.111	−0.081	−0.182	0.020	−0.438
Pile-up μ up	−0.365	−0.169	0.028	−0.014	0.050	−0.003	0.067	0.177	0.046
Pile-up NPV down	−0.066	0.090	0.029	−0.200	0.200	0.062	−0.094	0.046	0.118
Pile-up NPV up	−0.392	−0.105	0.350	0.003	0.023	−0.039	−0.132	0.051	−0.217
Pile-up pT down	0.052	−0.011	0.012	0.035	0.057	−0.031	−0.040	0.012	−0.295
Pile-up pT up	−0.080	−0.019	−0.067	−0.072	−0.005	0.006	0.089	0.202	0.106
Pile-up ρ top. down	−0.261	0.102	−0.158	−0.277	0.339	0.111	−0.038	0.248	0.068
Pile-up ρ top. up	−0.119	−0.109	0.444	0.069	−0.069	−0.060	−0.177	−0.097	−0.309

A. Full uncertainties of the A_θ differential cross-section measurement

Punchthrough down	−0.038	0.015	0.019	−0.040	0.011	0.002	−0.007	0.068	−0.008
Punchthrough up	0.049	−0.029	−0.020	−0.022	0.033	−0.033	0.028	0.078	−0.014
Single part. high pT down	0.043	−0.028	−0.007	−0.027	0.029	−0.019	0.007	0.082	−0.009
Single part. high pT up	0.042	−0.026	−0.004	−0.030	0.026	−0.016	0.007	0.083	−0.006
Mixed 1. down	0.070	0.126	0.014	−0.004	0.105	−0.052	−0.100	−0.030	−0.308
Mixed 1. up	−0.081	−0.016	−0.110	−0.084	0.025	−0.049	0.140	0.251	0.144
Mixed 2. down	−0.043	−0.050	−0.006	−0.019	−0.009	−0.034	0.068	0.129	−0.001
Mixed 2. up	−0.013	0.027	−0.036	−0.039	0.067	−0.034	−0.006	0.106	−0.044
Mixed 3. down	0.004	0.047	−0.042	−0.043	0.065	−0.031	0.023	0.034	−0.009
Mixed 3. up	−0.013	0.025	−0.038	−0.036	0.069	−0.037	−0.005	0.104	−0.048
Stat. 1 down	0.050	0.031	−0.061	−0.009	0.073	−0.062	0.026	0.032	−0.081
Stat. 1 up	−0.089	0.028	−0.080	−0.042	0.102	−0.036	0.027	0.102	−0.025
Stat. 2 down	0.053	−0.056	0.021	0.014	0.031	−0.082	0.037	0.035	−0.059
Stat. 2 up	0.009	0.051	−0.135	−0.010	0.050	−0.058	0.046	0.111	0.014
Stat. 3 down	−0.042	0.000	−0.059	−0.039	0.059	−0.034	0.054	0.081	0.038
Stat. 3 up	−0.007	0.026	−0.030	−0.021	0.097	−0.074	0.010	0.064	−0.106
Stat. 4 down	0.034	0.028	−0.070	−0.034	0.088	−0.051	0.018	0.091	−0.068
Stat. 4 up	−0.070	−0.018	−0.025	−0.011	0.065	−0.054	0.055	0.027	−0.013
Stat. 5 down	−0.025	0.010	−0.034	−0.040	0.079	−0.028	0.006	0.089	−0.055
Stat. 5 up	0.017	0.009	−0.066	−0.031	0.042	−0.006	0.031	0.062	0.007
Stat. 6 down	0.038	0.034	−0.049	−0.046	0.072	−0.036	0.042	0.044	−0.052

Stat. 6 up							
-0.020	0.004	-0.048	-0.043	0.071	-0.031	0.033	0.094	-0.027

Table A.1: The total fractional systematic uncertainties for each bin of the the measured relative A_θ differential cross-section in the leptonic SR.

Uncertainty size [%]

Source	A_θ bin:													
	−1.00 - -0.00	0.00 - 0.19	0.19 - 0.32	0.32 - 0.39	0.39 - 0.46	0.46 - 0.53	0.53 - 0.56	0.56 - 0.59	0.59 - 0.63	0.63 - 0.66	0.66 - 0.69	0.69 - 0.76	0.76 - 0.86	0.86 - 1.00
PDF4LHC_121	±0.003	±0.003	±0.002	±0.001	±0.002	±0.001	±0.002	±0.003	±0.003	±0.001	±0.003	±0.003	±0.013	±0.016
PDF4LHC_122	±0.080	±0.086	±0.087	±0.087	±0.076	±0.062	±0.047	±0.035	±0.006	±0.015	±0.050	±0.128	±0.329	±0.803
PDF4LHC_123	±0.023	±0.022	±0.026	±0.030	±0.026	±0.017	±0.007	±0.002	±0.011	±0.021	±0.028	±0.042	±0.060	±0.133
PDF4LHC_124	±0.052	±0.057	±0.054	±0.050	±0.042	±0.037	±0.031	±0.022	±0.005	±0.007	±0.031	±0.081	±0.207	±0.434
PDF4LHC_125	±0.043	±0.043	±0.056	±0.061	±0.055	±0.041	±0.024	±0.011	±0.014	±0.029	±0.048	±0.086	±0.165	±0.385
PDF4LHC_126	±0.055	±0.062	±0.065	±0.069	±0.059	±0.050	±0.037	±0.023	±0.002	±0.025	±0.053	±0.111	±0.229	±0.446
PDF4LHC_127	±0.010	±0.009	±0.009	±0.011	±0.007	±0.006	±0.003	±0.001	±0.001	±0.005	±0.006	±0.010	±0.027	±0.110
PDF4LHC_128	±0.028	±0.028	±0.025	±0.022	±0.018	±0.014	±0.011	±0.005	±0.003	±0.012	±0.022	±0.043	±0.081	±0.074
PDF4LHC_129	±0.043	±0.039	±0.037	±0.033	±0.030	±0.026	±0.021	±0.009	±0.001	±0.013	±0.033	±0.066	±0.134	±0.178
PDF4LHC_130	±0.044	±0.048	±0.044	±0.038	±0.033	±0.029	±0.025	±0.020	±0.007	±0.004	±0.026	±0.070	±0.179	±0.279
PDF4LHC_131	±0.033	±0.035	±0.023	±0.012	±0.008	±0.015	±0.022	±0.017	±0.014	±0.008	±0.016	±0.049	±0.119	±0.064
PDF4LHC_132	±0.036	±0.031	±0.031	±0.032	±0.028	±0.023	±0.013	±0.007	±0.004	±0.016	±0.021	±0.046	±0.100	±0.321
PDF4LHC_134	±0.013	±0.019	±0.023	±0.023	±0.024	±0.022	±0.023	±0.021	±0.018	±0.013	±0.002	±0.028	±0.133	±0.342
PDF4LHC_135	±0.002	±0.002	±0.007	±0.008	±0.007	±0.006	±0.007	±0.007	±0.002	±0.002	±0.001	±0.006	±0.022	±0.149
PDF4LHC_136	±0.171	±0.178	±0.181	±0.182	±0.159	±0.131	±0.095	±0.074	±0.022	±0.022	±0.076	±0.223	±0.690	±2.225
PDF4LHC_137	±0.005	±0.003	±0.006	±0.006	±0.006	±0.003	±0.001	±0.001	±0.003	±0.008	±0.009	±0.012	±0.008	±0.021
PDF4LHC_138	±0.001	±0.002	±0.000	±0.001	±0.001	±0.001	±0.003	±0.002	±0.001	±0.001	±0.005	±0.006	±0.002	±0.047
PDF4LHC_139	±0.008	±0.007	±0.005	±0.004	±0.004	±0.003	±0.001	±0.000	±0.001	±0.002	±0.002	±0.007	±0.021	±0.032
PDF4LHC_140	±0.033	±0.036	±0.036	±0.030	±0.025	±0.024	±0.020	±0.018	±0.014	±0.010	±0.010	±0.045	±0.154	±0.364

Fakes var 0	1.937	0.700	0.697	0.498	0.018	-0.147	0.001	0.478	0.349	-0.242	-0.788	-0.150	-0.828	-0.946
Fakes var 1	-2.035	-0.736	-0.732	-0.523	-0.020	0.155	-0.002	-0.501	-0.367	0.254	0.830	0.157	0.870	0.995
Frag. and Had.	±0.230	±0.700	±0.544	±1.247	±0.155	±0.706	±1.074	±0.460	±0.019	±0.401	±0.086	±0.288	±0.038	±1.947
Matrix Element	±2.565	±1.937	±0.726	±2.269	±0.443	±2.019	±2.826	±1.244	±0.690	±0.344	±1.037	±1.933	±1.391	±3.646
FSR Up	1.581	-0.045	-1.952	-0.568	-0.334	0.298	1.343	0.516	0.523	-1.480	-0.869	1.240	-0.979	2.423
FSR Down	-0.724	0.691	0.743	-0.057	-0.266	0.406	0.594	-0.031	-0.059	0.325	0.347	-0.590	-0.526	-1.591
Var3Down	±0.257	±0.461	±0.604	±0.431	±0.490	±0.708	±0.856	±0.751	±0.411	±0.028	±0.442	±0.745	±1.747	±1.627
ttV σ upward var	±0.011	±0.002	±0.001	±0.000	±0.000	±0.002	±0.003	±0.002	±0.004	±0.004	±0.003	±0.000	±0.004	±0.010
ttV σ downward var	±0.011	±0.002	±0.001	±0.000	±0.000	±0.002	±0.003	±0.002	±0.004	±0.004	±0.003	±0.000	±0.004	±0.010
Diboson σ upward var	±0.017	±0.005	±0.005	±0.001	±0.001	±0.004	±0.003	±0.006	±0.002	±0.002	±0.004	±0.007	±0.004	±0.009
Diboson σ downward var	±0.017	±0.005	±0.005	±0.001	±0.001	±0.004	±0.003	±0.006	±0.002	±0.002	±0.004	±0.007	±0.004	±0.009
W+jets σ upward var	±0.790	±0.497	±0.338	±0.474	±0.409	±0.430	±0.351	±0.377	±0.297	±0.140	±0.525	±0.690	±0.927	±1.011
W+jets σ downward var	±0.836	±0.526	±0.358	±0.501	±0.433	±0.455	±0.372	±0.399	±0.314	±0.149	±0.555	±0.731	±0.982	±1.070
Z+jets σ upward var	±0.016	±0.006	±0.006	±0.003	±0.004	±0.004	±0.004	±0.010	±0.004	±0.008	±0.003	±0.006	±0.011	±0.011
Z+jets σ downward var	±0.016	±0.006	±0.006	±0.003	±0.004	±0.004	±0.004	±0.010	±0.004	±0.008	±0.003	±0.006	±0.011	±0.011
Single top σ upward var	±0.009	±0.008	±0.019	±0.008	±0.013	±0.025	±0.019	±0.015	±0.026	±0.005	±0.020	±0.029	±0.041	±0.049

Single top σ downward var	±0.049	±0.041	±0.029	±0.020	±0.005	±0.027	±0.015	±0.019	±0.025	±0.013	±0.008	±0.019	±0.008	±0.009
JVT Up	0.063	0.109	0.091	0.061	−0.026	−0.021	−0.121	0.043	−0.064	−0.040	−0.115	−0.040	−0.004	0.030
JVT Down	−0.181	−0.098	−0.058	−0.052	−0.060	0.025	−0.005	0.179	0.061	0.090	−0.015	0.095	0.066	−0.008
e Trigger Up	−0.070	−0.012	0.013	−0.001	−0.033	0.001	−0.080	0.100	0.011	0.029	−0.061	0.035	0.051	0.043
e Trigger Down	−0.050	0.005	0.017	0.008	−0.039	0.001	−0.056	0.112	−0.001	0.027	−0.079	0.028	0.019	−0.020
e Reco Up	−0.054	0.001	0.011	0.004	−0.043	−0.003	−0.056	0.113	0.000	0.028	−0.077	0.037	0.032	0.010
e Reco Down	−0.055	−0.000	0.013	0.005	−0.041	−0.001	−0.057	0.111	0.001	0.029	−0.076	0.034	0.030	−0.001
e ID Up	−0.065	−0.034	0.005	−0.032	−0.084	−0.011	−0.077	0.096	0.021	0.068	−0.044	0.064	0.111	0.081
e ID Down	−0.049	0.001	0.046	0.024	−0.037	0.022	−0.063	0.104	−0.003	0.049	−0.071	−0.004	−0.014	−0.204
e Isolation Up	−0.055	−0.000	0.011	0.002	−0.044	−0.003	−0.058	0.111	0.001	0.030	−0.074	0.037	0.036	0.015
e Isolation Down	−0.055	0.001	0.014	0.006	−0.040	0.000	−0.056	0.112	0.000	0.029	−0.077	0.032	0.026	−0.006
μ Trigger Up	−0.067	−0.011	0.007	−0.001	−0.048	−0.007	−0.060	0.110	0.001	0.035	−0.067	0.047	0.056	0.050
μ Trigger Down	−0.044	0.012	0.018	0.012	−0.036	0.002	−0.052	0.116	−0.001	0.020	−0.086	0.024	0.005	−0.039
μ ID Up	−0.055	0.003	0.011	0.003	−0.045	−0.003	−0.056	0.114	−0.002	0.030	−0.077	0.037	0.033	0.020
μ ID Down	−0.054	0.001	0.011	0.009	−0.039	−0.002	−0.052	0.113	−0.000	0.025	−0.077	0.034	0.026	−0.008
μ Isolation Up	−0.062	−0.020	0.024	−0.004	−0.060	0.004	−0.071	0.100	0.009	0.059	−0.056	0.032	0.054	−0.051
μ Isolation Down	−0.055	−0.010	0.024	0.000	−0.051	0.003	−0.069	0.102	0.007	0.047	−0.062	0.027	0.040	−0.048
Pile-up Up	−0.262	0.033	−0.051	0.028	0.035	0.073	−0.098	0.101	0.070	0.014	−0.172	0.048	0.052	0.156
Pile-up Down	0.093	−0.030	0.101	0.025	−0.158	−0.032	−0.026	0.103	−0.053	0.050	−0.013	0.015	−0.011	−0.089
B Up	0.152	0.094	0.068	0.066	−0.029	−0.003	−0.067	0.059	−0.057	−0.033	−0.158	−0.037	−0.087	−0.153
B Down	−0.257	−0.087	−0.051	−0.056	−0.057	−0.005	−0.029	0.174	0.051	0.086	−0.001	0.113	0.143	0.174
C Up	−0.238	−0.450	−0.527	−0.441	−0.315	−0.099	0.027	0.312	0.280	0.359	0.303	0.531	0.646	0.897
C Down	0.129	0.431	0.558	0.438	0.207	0.098	−0.144	−0.095	−0.273	−0.270	−0.437	−0.456	−0.562	−0.944

Light Up	-0.240	-0.289	-0.286	-0.277	-0.249	-0.026	0.018	0.215	0.160	0.232	0.204	0.349	0.407	0.566
Light Down	0.125	0.262	0.321	0.268	0.135	0.032	-0.144	-0.000	-0.146	-0.132	-0.324	-0.280	-0.317	-0.627
Extrap. Up	-0.046	0.005	0.012	0.005	-0.043	-0.003	-0.056	0.111	-0.001	0.027	-0.079	0.034	0.028	0.001
Extrap. Down	-0.068	-0.013	0.019	0.001	-0.044	0.003	-0.069	0.105	0.007	0.041	-0.062	0.032	0.043	-0.013
Charm Extrap. Up	-0.041	0.017	0.057	0.028	-0.020	0.018	-0.066	0.079	-0.019	0.007	-0.092	-0.009	-0.002	-0.069
Charm Extrap. Down	-0.074	-0.051	-0.006	-0.034	-0.100	-0.009	-0.074	0.121	0.037	0.109	-0.023	0.069	0.099	-0.050
Reso. Para	-0.030	-0.083	0.080	0.054	-0.210	0.031	-0.093	-0.013	0.065	-0.001	-0.028	0.066	0.153	0.060
Reso. Perp	0.071	-0.132	0.103	0.017	-0.245	-0.021	-0.016	0.046	-0.026	0.129	-0.027	0.080	0.140	-0.281
Scale Up	0.041	-0.043	0.067	0.046	-0.173	-0.047	-0.129	0.039	0.040	0.035	-0.055	0.058	0.158	0.076
Scale Down	-0.071	-0.068	0.071	0.032	-0.046	0.060	-0.048	0.083	0.003	0.009	-0.008	-0.012	-0.014	-0.262
JER_NP_1	±0.175	±0.373	±0.067	±0.362	±0.275	±0.399	±0.323	±0.197	±0.216	±0.002	±0.042	±0.423	±0.341	±0.132
JER_NP_2	±0.075	±0.532	±0.019	±0.339	±0.264	±0.368	±0.554	±0.192	±0.045	±0.035	±0.281	±0.528	±0.405	±0.111
JER_NP_3	±0.208	±0.609	±0.158	±0.345	±0.237	±0.120	±0.647	±0.118	±0.114	±0.121	±0.408	±0.373	±0.336	±0.260
JER_NP_4	±0.191	±0.241	±0.097	±0.249	±0.203	±0.108	±0.363	±0.133	±0.271	±0.025	±0.235	±0.022	±0.088	±0.092
JER_NP_5	±0.262	±0.058	±0.040	±0.186	±0.222	±0.065	±0.159	±0.196	±0.120	±0.140	±0.159	±0.077	±0.069	±0.110
JER_NP_6	±0.063	±0.101	±0.017	±0.257	±0.157	±0.050	±0.221	±0.190	±0.269	±0.063	±0.360	±0.080	±0.064	±0.043
JER_rest_term	±0.043	±0.323	±0.028	±0.194	±0.193	±0.128	±0.561	±0.209	±0.295	±0.027	±0.050	±0.178	±0.130	±0.035
Flavour Comp. down	-0.517	-0.347	0.040	-0.192	-0.213	0.341	0.092	0.093	0.383	0.531	0.068	0.085	-0.075	-1.887
Flavour Comp. up	0.252	-0.192	-0.195	0.367	0.014	-0.038	-0.331	0.029	-0.312	-0.017	-0.177	-0.024	0.490	0.667

Source														
Flavour Resp. down	−0.434	−0.719	−0.314	0.202	−0.203	0.072	0.178	0.201	0.002	0.280	0.033	0.187	0.581	0.749
Flavour Resp. up	0.383	0.412	0.212	0.120	0.027	0.182	−0.316	−0.191	0.195	−0.202	−0.282	−0.229	−0.428	−1.126
b. JES down	0.065	−0.079	0.076	−0.127	−0.155	0.053	−0.041	0.151	0.134	−0.056	−0.219	0.081	0.068	0.037
b. JES up	−0.152	−0.067	−0.052	0.187	0.070	0.072	−0.136	0.176	−0.057	0.093	−0.139	0.007	−0.074	−0.172
Det. down	0.070	−0.038	0.046	0.026	−0.093	0.003	−0.051	0.120	0.047	0.002	−0.139	−0.009	0.037	−0.133
Det. up	−0.091	−0.040	−0.040	0.025	−0.060	0.053	−0.052	0.126	0.041	0.051	−0.112	0.023	0.082	−0.129
Modelling 1 down	−0.003	−0.146	0.174	−0.225	−0.122	0.096	−0.066	−0.000	0.424	−0.166	−0.009	0.095	−0.023	−0.649
Modelling 1 up	0.129	−0.234	−0.123	0.523	0.039	−0.015	−0.073	0.145	−0.361	0.082	−0.295	−0.100	0.196	0.163
Modelling 2 down	0.254	0.096	0.125	0.162	−0.100	−0.024	−0.100	0.058	0.009	−0.071	−0.284	−0.069	−0.069	−0.325
Modelling 2 up	−0.308	−0.149	−0.108	−0.093	−0.054	0.091	0.044	0.137	0.107	0.115	−0.050	0.124	0.139	0.088
Modelling 3 down	−0.198	−0.100	−0.096	−0.043	−0.021	0.054	−0.001	0.136	0.054	0.092	−0.056	0.085	0.106	−0.029
Modelling 3 up	0.177	0.074	0.089	0.065	−0.109	0.016	−0.050	0.088	0.014	−0.064	−0.222	−0.055	−0.038	−0.217
Modelling 4 down	−0.007	−0.039	0.020	0.027	−0.047	0.022	−0.051	0.126	0.024	0.033	−0.123	−0.015	0.026	−0.070
Modelling 4 up	−0.069	−0.037	−0.006	−0.003	−0.048	0.037	−0.066	0.124	0.036	0.054	−0.116	0.013	0.068	−0.025
η intercal mod down	0.554	0.415	0.270	0.305	0.097	0.060	−0.013	−0.089	0.079	−0.301	−0.334	−0.294	−0.758	−1.540
η intercal mod up	−0.524	−0.549	−0.306	−0.174	−0.177	−0.004	−0.119	0.096	0.165	0.283	0.175	0.366	0.782	1.298
η intercal non-closure E down	−0.072	−0.030	0.007	−0.013	−0.041	0.032	−0.072	0.121	0.040	0.064	−0.088	−0.006	0.052	−0.030
η intercal non-closure E up	−0.072	−0.030	0.014	−0.009	−0.037	0.029	−0.064	0.117	0.029	0.059	−0.096	−0.004	0.049	−0.007

Source														
η intercal non-closure - down	-0.047	-0.015	0.030	0.008	-0.016	0.032	-0.077	0.103	0.024	0.054	-0.115	-0.006	-0.009	-0.054
η intercal non-closure - up	-0.081	-0.042	-0.007	-0.008	-0.060	0.023	-0.054	0.119	0.027	0.100	-0.100	-0.004	0.083	0.102
η intercal non-closure + down	-0.064	-0.028	0.023	-0.011	-0.048	0.048	-0.067	0.094	0.021	0.083	-0.101	0.001	0.040	-0.130
η intercal non-closure + up	-0.076	-0.027	0.010	-0.019	-0.059	0.036	-0.055	0.109	0.011	0.081	-0.088	-0.001	0.061	0.067
η intercal stat. down	-0.054	-0.047	0.040	-0.094	-0.023	0.061	-0.008	0.093	0.090	-0.019	-0.039	-0.021	0.016	-0.162
η intercal stat. up	0.028	-0.060	0.026	0.056	-0.055	0.033	-0.124	0.057	0.026	0.033	-0.166	0.023	0.074	-0.053
Pile-up μ down	0.242	0.053	0.230	0.121	-0.053	0.047	-0.127	-0.011	-0.028	-0.111	-0.069	-0.052	-0.250	-0.855
Pile-up μ up	-0.236	-0.270	-0.165	0.008	-0.077	0.048	-0.118	0.047	0.133	0.205	-0.090	0.210	0.292	0.293
Pile-up NPV down	-0.122	-0.219	0.051	-0.155	-0.060	0.097	-0.155	0.142	0.183	0.143	0.124	0.112	-0.041	-0.627
Pile-up NPV up	-0.081	-0.056	0.045	0.331	0.060	0.040	-0.207	-0.115	0.046	0.049	-0.112	-0.158	0.042	0.028
Pile-up pT down	0.124	0.124	0.096	0.006	-0.081	0.078	-0.128	0.032	0.025	0.001	-0.167	-0.053	-0.099	-0.301
Pile-up pT up	-0.226	-0.091	-0.067	-0.023	-0.102	0.039	-0.167	0.097	0.130	0.112	-0.123	0.158	0.238	0.132
Pile-up ρ top. down	-0.830	-0.626	-0.246	-0.381	-0.216	0.213	0.136	0.108	0.618	0.053	0.359	0.513	0.428	-0.043
Pile-up ρ top. up	0.691	0.509	0.354	0.707	0.024	-0.149	-0.268	-0.108	-0.506	-0.195	-0.584	-0.425	-0.251	-0.398

Punchthrough down	−0.063	0.006	0.027	−0.009	−0.038	0.019	−0.093	0.097	0.007	0.017	−0.064	0.015	0.062	−0.064
Punchthrough up	−0.072	−0.006	0.023	−0.006	−0.042	0.018	−0.086	0.100	0.003	0.037	−0.064	0.024	0.056	−0.050
Single part. high pT down	−0.067	−0.008	0.025	−0.004	−0.041	0.016	−0.083	0.095	0.006	0.027	−0.059	0.021	0.058	−0.050
Single part. high pT up	−0.067	−0.008	0.025	−0.004	−0.041	0.016	−0.083	0.095	0.006	0.027	−0.059	0.021	0.058	−0.050
Mixed 1. down	0.215	0.056	0.170	0.163	−0.079	0.006	−0.079	0.069	−0.035	−0.078	−0.261	−0.096	−0.104	−0.333
Mixed 1. up	−0.268	−0.142	−0.131	−0.105	−0.056	0.067	−0.009	0.156	0.068	0.078	−0.007	0.150	0.202	0.143
Mixed 2. down	−0.174	−0.061	−0.060	−0.036	−0.059	0.052	−0.040	0.104	0.040	0.052	−0.049	0.112	0.113	−0.027
Mixed 2. up	−0.039	−0.031	0.002	0.020	−0.061	0.034	−0.060	0.117	0.024	0.042	−0.125	0.002	0.068	−0.063
Mixed 3. down	−0.041	−0.059	0.011	0.025	−0.041	0.020	−0.051	0.107	0.025	0.055	−0.097	0.009	0.033	−0.053
Mixed 3. up	−0.039	−0.031	0.002	0.020	−0.061	0.034	−0.060	0.117	0.024	0.042	−0.125	0.002	0.068	−0.063
Stat. 1 down	−0.048	−0.021	0.018	−0.003	−0.071	0.026	−0.032	0.143	0.050	0.033	−0.126	0.005	0.039	−0.124
Stat. 1 up	−0.034	0.013	−0.003	0.048	−0.085	0.023	−0.047	0.116	0.027	0.022	−0.139	−0.009	0.076	−0.083
Stat. 2 down	0.070	0.055	0.053	0.080	−0.050	0.006	−0.140	0.144	−0.023	−0.010	−0.216	−0.020	0.021	−0.202
Stat. 2 up	−0.097	−0.049	−0.006	−0.086	−0.079	0.069	−0.004	0.128	0.117	0.020	−0.120	0.059	0.031	−0.044
Stat. 3 down	−0.133	−0.044	−0.041	−0.018	−0.058	0.047	−0.017	0.123	0.030	0.065	−0.060	0.034	0.076	0.021
Stat. 3 up	0.029	−0.012	0.048	0.029	−0.066	0.037	−0.052	0.116	0.012	0.019	−0.177	−0.018	0.009	−0.131
Stat. 4 down	0.121	0.033	0.055	0.005	−0.103	0.034	−0.043	0.126	−0.001	−0.026	−0.182	−0.034	−0.002	−0.097
Stat. 4 up	−0.184	−0.064	−0.046	−0.024	−0.027	0.062	−0.023	0.126	0.044	0.068	−0.068	0.040	0.082	−0.017
Stat. 5 down	−0.062	−0.022	−0.015	0.029	−0.039	0.020	−0.057	0.127	0.016	0.082	−0.124	−0.006	0.055	−0.043
Stat. 5 up	−0.047	−0.034	0.033	−0.032	−0.065	0.042	−0.037	0.120	0.044	−0.002	−0.119	0.030	0.041	−0.069
Stat. 6 down	−0.004	−0.009	0.024	−0.012	−0.055	0.027	−0.044	0.117	0.025	0.048	−0.128	−0.012	0.020	−0.068

| Stat. 6 up | -0.104 | -0.046 | -0.031 | 0.020 | -0.055 | 0.045 | -0.069 | 0.136 | 0.034 | 0.070 | -0.085 | 0.003 | 0.085 | -0.020 |

Table A.2: The total fractional systematic uncertainties for each bin of the the measured relative A_θ differential cross-section in the hadronic SR.

References

[1]   ATLAS Collaboration. *Jet energy scale measurements and their systematic un-certainties in proton-proton collisions at $\sqrt{s} = 13$ TeV with the ATLAS detector.* In: (2017). arXiv: `1703.09665 [hep-ex]`.

[2]   Dasgupta, M. et al. *Top tagging : an analytical perspective.* In: *JHEP* 09 (2018), p. 170. arXiv: `1807.04767 [hep-ph]`.

[3]   Dirac, P. A. M. *The Quantum Theory of the Electron.* In: *Proceedings of the Royal Society of London Series A* 117 (Feb. 1928), pp. 610–624.

[4]   NobelPrize.org. *The Nobel Prize in Physics 1933.* `https://www.nobelprize.org/prizes/physics/1933/summary/`. accessed: 2018-11-29.

[5]   Odom, B. et al. *New Measurement of the Electron Magnetic Moment Using a One-Electron Quantum Cyclotron.* In: *Phys. Rev. Lett.* 97 (3 July 2006), p. 030801. URL: `https://link.aps.org/doi/10.1103/PhysRevLett.97.030801`.

[6]   Glashow, S. L. *Partial Symmetries of Weak Interactions.* In: *Nucl. Phys.* 22 (1961), pp. 579–588.

[7]   Salam, A. "Weak and Electromagnetic Interactions". In: *Elementary Particle Theory.* Ed. by N. Svartholm. Stockholm: Almqvist and Wiksell, 1968, p. 367.

[8]   Weinberg, S. *A Model of Leptons.* In: *Phys. Rev. Lett.* 19 (1967), pp. 1264–1266.

[9]   Gell-Mann, M. *The Eightfold Way: A Theory of strong interaction symmetry.* In: (1961).

[10] Tanabashi, M. et al. *Review of Particle Physics.* In: *Phys. Rev. D* 98 (3 Aug. 2018), p. 030001. URL: `https://link.aps.org/doi/10.1103/PhysRevD.98.030001`.

[11] *Standard Model — Wikipedia, The Free Encyclopedia.* Accessed 25/02/19. 2019. URL: `https://en.wikipedia.org/wiki/Standard_Model`.

[12] Kajita, T., Kearns, E., and Shiozawa, M. *Establishing atmospheric neutrino oscillations with Super-Kamiokande.* In: *Nuclear Physics B* 908 (2016), pp. 14–29. ISSN: 0550-3213. URL: `http://www.sciencedirect.com/science/article/pii/S0550321316300554`.

[13]   Ahmad, Q. R. et al. *Measurement of the rate of $\nu_e + d \to p + p + e^-$ interactions produced by ^8B solar neutrinos at the Sudbury Neutrino Observatory.* In: *Phys. Rev. Lett.* 87 (2001), p. 071301. arXiv: `nucl-ex/0106015 [nucl-ex]`.

[14]   NobelPrize.org. *The Nobel Prize in Physics 1965.* `https://www.nobelprize.org/prizes/physics/1965/summary/`. accessed: 2018-11-29.

[15]   Peskin, M. E. and Schroeder, D. V. *An Introduction to quantum field theory.* Reading, USA: Addison-Wesley, 1995. ISBN: 9780201503975, 0201503972. URL: `http://www.slac.stanford.edu/~mpeskin/QFT.html`.

[16]   Glashow, S. L. *Partial-symmetries of weak interactions.* In: *Nuclear Physics* 22.4 (1961), pp. 579–588. ISSN: 0029-5582. URL: `http://www.sciencedirect.com/science/article/pii/0029558261904692`.

[17]   Salam, A. *Weak and Electromagnetic Interactions.* In: *Conf. Proc.* C680519 (1968), pp. 367–377.

[18]   Weinberg, S. *A Model of Leptons.* In: *Phys. Rev. Lett.* 19 (21 Nov. 1967), pp. 1264–1266. URL: `https://link.aps.org/doi/10.1103/PhysRevLett.19.1264`.

[19]   Higgs, P. W. *Broken Symmetries and the Masses of Gauge Bosons.* In: *Phys. Rev. Lett.* 13 (16 Oct. 1964), pp. 508–509. URL: `https://link.aps.org/doi/10.1103/PhysRevLett.13.508`.

[20]   Englert, F. and Brout, R. *Broken Symmetry and the Mass of Gauge Vector Mesons.* In: *Phys. Rev. Lett.* 13 (9 Aug. 1964), pp. 321–323. URL: `https://link.aps.org/doi/10.1103/PhysRevLett.13.321`.

[21]   Aad, G. et al. *Observation of a new particle in the search for the Standard Model Higgs boson with the ATLAS detector at the LHC.* In: *Phys. Lett.* B716 (2012), pp. 1–29. arXiv: `1207.7214 [hep-ex]`.

[22]   Chatrchyan, S. et al. *Observation of a new boson at a mass of 125 GeV with the CMS experiment at the LHC.* In: *Phys. Lett.* B716 (2012), pp. 30–61. arXiv: `1207.7235 [hep-ex]`.

[23]   Kobayashi, M. and Maskawa, T. *CP Violation in the Renormalizable Theory of Weak Interaction.* In: *Prog. Theor. Phys.* 49 (1973), pp. 652–657.

[24]   NobelPrize.org. *The Nobel Prize in Physics 1969.* `https://www.nobelprize.org/prizes/physics/1969/summary/`. accessed: 2019-1-17.

[25]   Zweig, G. *An SU_3 model for strong interaction symmetry and its breaking; Version 1.* Tech. rep. CERN-TH-401. Geneva: CERN, Jan. 1964. URL: `http://cds.cern.ch/record/352337`.

[26]   Ellis, R. K., Stirling, W. J., and Webber, B. R. *QCD and collider physics.* In: *Camb. Monogr. Part. Phys. Nucl. Phys. Cosmol.* 8 (1996), pp. 1–435.

[27] Georgi, H. *Lie algebras in particle physics.* In: *Front. Phys.* 54 (1999), pp. 1–320.

[28] Wissenschaften zu Berlin, D. A. der. *Sitzungsberichte der Königlich Preussischen Akademie der Wissenschaften zu Berlin.* pt. 1. The Academy, 1905. URL: `https://books.google.co.uk/books?id=KwUoAAAAYAAJ`.

[29] Gross, D. J. and Wilczek, F. *ASYMPTOTICALLY FREE GAUGE THEORIES. 2.* In: *Phys. Rev.* D9 (1974), pp. 980–993.

[30] Wilson, K. G. *Confinement of Quarks.* In: *Phys. Rev.* D10 (1974). [,319(1974)], pp. 2445–2459.

[31] Bjorken, J. D. and Paschos, E. A. *Inelastic Electron Proton and gamma Proton Scattering, and the Structure of the Nucleon.* In: *Phys. Rev.* 185 (1969), pp. 1975–1982.

[32] Feynman, R. P. *Very high-energy collisions of hadrons.* In: *Phys. Rev. Lett.* 23 (1969). [,494(1969)], pp. 1415–1417.

[33] Ellis, S. D. and Soper, D. E. *Successive combination jet algorithm for hadron collisions.* In: *Phys. Rev.* D48 (1993), pp. 3160–3166. arXiv: `hep-ph/9305266 [hep-ph]`.

[34] Salam, G. P. and Soyez, G. *A Practical Seedless Infrared-Safe Cone jet algorithm.* In: *JHEP* 05 (2007), p. 086. arXiv: `0704.0292 [hep-ph]`.

[35] The ATLAS Collaboration. *Jet energy resolution in proton-proton collisions at $\sqrt{s} = 7$ TeV recorded in 2010 with the ATLAS detector.* In: *The European Physical Journal C* 73.3 (Mar. 2013), p. 2306. ISSN: 1434-6052. URL: `https://doi.org/10.1140/epjc/s10052-013-2306-0`.

[36] Salam, G. P. *Towards Jetography.* In: *Eur. Phys. J.* C67 (2010), pp. 637–686. arXiv: `0906.1833 [hep-ph]`.

[37] Höche, S. *Introduction to parton-shower event generators.* In: *Proceedings, Theoretical Advanced Study Institute in Elementary Particle Physics: Journeys Through the Precision Frontier: Amplitudes for Colliders (TASI 2014): Boulder, Colorado, June 2-27, 2014.* 2015, pp. 235–295. arXiv: `1411.4085 [hep-ph]`.

[38] Abachi, S. et al. *Observation of the top quark.* In: *Phys. Rev. Lett.* 74 (1995), pp. 2632–2637. arXiv: `hep-ex/9503003 [hep-ex]`.

[39] Abe, F. et al. *Observation of top quark production in $\bar{p}p$ collisions.* In: *Phys. Rev. Lett.* 74 (1995), pp. 2626–2631. arXiv: `hep-ex/9503002 [hep-ex]`.

[40] Bigi, I. et al. *Production and decay properties of ultra-heavy quarks.* In: *Physics Letters B* 181.1 (1986), pp. 157–163. ISSN: 0370-2693.

[41] Group, L. T. W. *NNLO+NNLL top-quark-pair cross sections.* `https://twiki.cern.ch/twiki/bin/view/LHCPhysics/TtbarNNLO`. accessed: 2019-01-20.

[42] Czakon, M., Fiedler, P., and Mitov, A. *Total Top-Quark Pair-Production Cross Section at Hadron Colliders Through $O(\alpha \frac{4}{S})$*. In: *Phys. Rev. Lett.* 110 (2013), p. 252004. arXiv: `1303.6254 [hep-ph]`.

[43] Czakon, M. and Mitov, A. *NNLO corrections to top pair production at hadron colliders: the quark-gluon reaction*. In: *JHEP* 01 (2013), p. 080. arXiv: `1210.6832 [hep-ph]`.

[44] Czakon, M. and Mitov, A. *NNLO corrections to top-pair production at hadron colliders: the all-fermionic scattering channels*. In: *JHEP* 12 (2012), p. 054. arXiv: `1207.0236 [hep-ph]`.

[45] Bärnreuther, P., Czakon, M., and Mitov, A. *Percent Level Precision Physics at the Tevatron: First Genuine NNLO QCD Corrections to $q\bar{q} \to t\bar{t} + X$*. In: *Phys. Rev. Lett.* 109 (2012), p. 132001. arXiv: `1204.5201 [hep-ph]`.

[46] Beneke, M. et al. *Hadronic top-quark pair production with NNLL threshold resummation*. In: *Nucl. Phys.* B855 (2012), pp. 695–741. arXiv: `1109.1536 [hep-ph]`.

[47] Group, L. T. W. *NLO single-top channel cross sections*. `https://twiki.cern.ch/twiki/bin/view/LHCPhysics/SingleTopRefXsec`. accessed: 2019-01-20.

[48] Aliev, M. et al. *HATHOR: HAdronic Top and Heavy quarks crOss section calculatoR*. In: *Comput. Phys. Commun.* 182 (2011), pp. 1034–1046. arXiv: `1007.1327 [hep-ph]`.

[49] Kant, P. et al. *HatHor for single top-quark production: Updated predictions and uncertainty estimates for single top-quark production in hadronic collisions*. In: *Comput. Phys. Commun.* 191 (2015), pp. 74–89. arXiv: `1406.4403 [hep-ph]`.

[50] Group, L. T. W. *LHCTopWG Summary Plots*. `https://twiki.cern.ch/twiki/bin/view/LHCPhysics/LHCTopWGSummaryPlots`. accessed: 2019-01-20.

[51] Maltoni, F., Selvaggi, M., and Thaler, J. *Exposing the dead cone effect with jet substructure techniques*. In: *Phys. Rev.* D94.5 (2016), p. 054015. arXiv: `1606.03449 [hep-ph]`.

[52] Benedikt, M. et al. *LHC Design Report*. Tech. rep. Geneva, 2004. URL: `https://cds.cern.ch/record/823808`.

[53] ATLAS Collaboration. *The ATLAS Experiment at the CERN Large Hadron Collider*. In: *JINST* 3 (2008), S08003.

[54] The LHCf Collaboration. *The LHCf detector at the CERN Large Hadron Collider*. In: *Journal of Instrumentation* 3.08 (2008), S08006. URL: `http://stacks.iop.org/1748-0221/3/i=08/a=S08006`.

[55] The ALICE Collaboration. *The ALICE experiment at the CERN LHC*. In: *Journal of Instrumentation* 3.08 (2008), S08002. URL: http://stacks.iop.org/1748-0221/3/i=08/a=S08002.

[56] The CMS Collaboration. *The CMS experiment at the CERN LHC*. In: *Journal of Instrumentation* 3.08 (2008), S08004. URL: http://stacks.iop.org/1748-0221/3/i=08/a=S08004.

[57] The TOTEM Collaboration. *The TOTEM Experiment at the CERN Large Hadron Collider*. In: *Journal of Instrumentation* 3.08 (2008), S08007. URL: http://stacks.iop.org/1748-0221/3/i=08/a=S08007.

[58] The LHCb Collaboration. *The LHCb Detector at the LHC*. In: *Journal of Instrumentation* 3.08 (2008), S08005. URL: http://stacks.iop.org/1748-0221/3/i=08/a=S08005.

[59] The MoEDAL Collaboration. *Technical Design Report of the MoEDAL Experiment*. Tech. rep. CERN-LHCC-2009-006. MoEDAL-TDR-001. June 2009. URL: https://cds.cern.ch/record/1181486.

[60] Schindl, K. *The Injector Chain for the LHC; rev. version*. In: CERN-PS-99-018-DI (Mar. 1999), 7 p. URL: https://cds.cern.ch/record/384396.

[61] Aad, G. et al. *Luminosity Determination in pp Collisions at $\sqrt{s} = 7$ TeV Using the ATLAS Detector at the LHC*. In: *Eur. Phys. J.* C71 (2011), p. 1630. arXiv: 1101.2185 [hep-ex].

[62] Mobs, E. *The CERN accelerator complex. Complexe des accélérateurs du CERN*. General Photo. July 2016. URL: https://cds.cern.ch/record/2197559.

[63] The ATLAS Collaboration. *LuminosityPublicResultsRun2*. https://twiki.cern.ch/twiki/bin/view/AtlasPublic/LuminosityPublicResultsRun2#Publications%20and%20Conference%20Resu. accesed: 2018-11-23.

[64] The ATLAS Collaboration. *The ATLAS Experiment at the CERN Large Hadron Collider*. In: *JINST* 3 (2008), S08003.

[65] The ATLAS Collaboration. *ATLAS inner detector: Technical Design Report, 1*. Technical Design Report ATLAS. Geneva: CERN, 1997. URL: http://cds.cern.ch/record/331063.

[66] ATLAS Collaboration. *Technical Design Report for the ATLAS Inner Tracker Strip Detector*. CERN-LHCC-2017-005, ATLAS-TDR-025. 2017.

[67] Vogel, A. *ATLAS Transition Radiation Tracker (TRT): Straw Tube Gaseous Detectors at High Rates*. Tech. rep. ATL-INDET-PROC-2013-005. Geneva: CERN, Apr. 2013. URL: https://cds.cern.ch/record/1537991.

[68] ATLAS Collaboration. *ATLAS Insertable B-Layer Technical Design Report.* ATLAS-TDR-19. 2010. URL: https://cds.cern.ch/record/1291633. *ATLAS Insertable B-Layer Technical Design Report Addendum*, ATLAS-TDR-19-ADD-1, 2012, URL: https://cds.cern.ch/record/1451888.

[69] Griffiths, D. *Introduction to Elementary Particles.* 2nd edition. Wiley-VCH, 2008.

[70] Martin, B. R. and Shaw, G. *Particle Physics.* 3rd edition. Manchester Physics Series. Wiley-Blackwell, 2013.

[71] The ATLAS Collaboration. *ATLAS liquid-argon calorimeter: Technical Design Report.* Technical Design Report ATLAS. Geneva: CERN, 1996. URL: https://cds.cern.ch/record/331061.

[72] The ATLAS Collaboration. *ATLAS tile calorimeter: Technical Design Report.* Technical Design Report ATLAS. Geneva: CERN, 1996. URL: https://cds.cern.ch/record/331062.

[73] Artamonov, A. et al. *The ATLAS Forward Calorimeter.* In: *Journal of Instrumentation* 3.02 (2008), P02010. URL: http://stacks.iop.org/1748-0221/3/i=02/a=P02010.

[74] Gillberg, D. *Performance of the ATLAS Forward Calorimeters in First LHC Data.* Tech. rep. ATL-LARG-PROC-2010-006. Geneva: CERN, Aug. 2010. URL: http://cds.cern.ch/record/1284260.

[75] The ATLAS Collaboration. *ATLAS magnet system: Technical Design Report, 1.* Technical Design Report ATLAS. Geneva: CERN, 1997. URL: https://cds.cern.ch/record/338080.

[76] The ATLAS Collaboration. *ATLAS central solenoid: Technical Design Report.* Technical Design Report ATLAS. Electronic version not available. Geneva: CERN, 1997. URL: https://cds.cern.ch/record/331067.

[77] Badiou, J. P. et al. *ATLAS barrel toroid: Technical Design Report.* Technical Design Report ATLAS. Electronic version not available. Geneva: CERN, 1997. URL: https://cds.cern.ch/record/331065.

[78] *ATLAS end-cap toroids: Technical Design Report.* Technical Design Report ATLAS. Electronic version not available. Geneva: CERN, 1997. URL: https://cds.cern.ch/record/331066.

[79] The ATLAS Collaboration. *ATLAS detector and physics performance: Technical Design Report, 1.* Technical Design Report ATLAS. Geneva: CERN, 1999. URL: https://cds.cern.ch/record/391176.

[80] Hauser, R. *The ATLAS trigger system.* In: *The European Physical Journal C - Particles and Fields* 34.1 (July 2004), s173–s183. ISSN: 1434-6052. URL: https://doi.org/10.1140/epjcd/s2004-04-018-6.

[81] Nedden, M. zur. *The Run-2 ATLAS Trigger System: Design, Performance and Plan.* Tech. rep. ATL-DAQ-PROC-2016-039. Geneva: CERN, Dec. 2016. URL: `https://cds.cern.ch/record/2238679`.

[82] Duckeck, G. et al. *ATLAS computing: Technical design report.* In: (2005).

[83] Collaboration, A. *Technical Design Report for the Phase-II Upgrade of the ATLAS TDAQ System.* Tech. rep. CERN-LHCC-2017-020. ATLAS-TDR-029. Geneva: CERN, Sept. 2017. URL: `https://cds.cern.ch/record/2285584`.

[84] The ATLAS Collaboration. *ATLAS level-1 trigger: Technical Design Report.* Technical Design Report ATLAS. Geneva: CERN, 1998. URL: `http://cds.cern.ch/record/381429`.

[85] Jenni, P. et al. *ATLAS high-level trigger, data-acquisition and controls: Technical Design Report.* Technical Design Report ATLAS. Geneva: CERN, 2003. URL: `http://cds.cern.ch/record/616089`.

[86] *The ATLAS Simulation Infrastructure. The ATLAS Simulation Infrastructure.* In: *Eur. Phys. J. C* 70.arXiv:1005.4568. CERN-PH-EP-2010-044 (May 2010). Submitted to Eur. Phys. J. C, 823–874. 53 p. URL: `https://cds.cern.ch/record/1267853`.

[87] *Performance of the Fast ATLAS Tracking Simulation (FATRAS) and the ATLAS Fast Calorimeter Simulation (FastCaloSim) with single particles.* Tech. rep. ATL-SOFT-PUB-2014-001. Geneva: CERN, Mar. 2014. URL: `http://cds.cern.ch/record/1669341`.

[88] ATLAS Collaboration. *The simulation principle and performance of the ATLAS fast calorimeter simulation FastCaloSim.* 2010. URL: `https://cds.cern.ch/record/1300517`.

[89] Edmonds, K. et al. *The Fast ATLAS Track Simulation (FATRAS).* Tech. rep. ATL-SOFT-PUB-2008-001. ATL-COM-SOFT-2008-002. Geneva: CERN, Mar. 2008. URL: `http://cds.cern.ch/record/1091969`.

[90] Aaboud, M. et al. *Electron efficiency measurements with the ATLAS detector using 2012 LHC protonproton collision data.* In: *Eur. Phys. J.* C77.3 (2017), p. 195. arXiv: `1612.01456` [`hep-ex`].

[91] ATLAS Collaboration. *Vertex Reconstruction Performance of the ATLAS Detector at $\sqrt{s} = 13$ TeV.* ATL-PHYS-PUB-2015-026. 2015. URL: `https://cds.cern.ch/record/2037717`.

[92] Meloni, F. *Primary vertex reconstruction with the ATLAS detector.* Tech. rep. ATL-PHYS-PROC-2016-163. 12. Geneva: CERN, Oct. 2016. URL: `https://cds.cern.ch/record/2222390`.

[93] Lampl, W. et al. *Calorimeter Clustering Algorithms: Description and Performance*. ATL-LARG-PUB-2008-002. 2008. URL: https://cds.cern.ch/record/1099735.

[94] *Electron efficiency measurements with the ATLAS detector using the 2015 LHC proton-proton collision data*. Tech. rep. ATLAS-CONF-2016-024. Geneva: CERN, June 2016. URL: https://cds.cern.ch/record/2157687.

[95] ATLAS Collaboration. *Electron and photon energy calibration with the ATLAS detector using data collected in 2015 at $\sqrt{s} = 13$ TeV*. ATL-PHYS-PUB-2016-015. 2016. URL: https://cds.cern.ch/record/2203514.

[96] Aad, G. et al. *Muon reconstruction performance of the ATLAS detector in protonproton collision data at $\sqrt{s} = 13$ TeV*. In: *Eur. Phys. J.* C76.5 (2016), p. 292. arXiv: 1603.05598 [hep-ex].

[97] Aad, G. et al. *Topological cell clustering in the ATLAS calorimeters and its performance in LHC Run 1*. In: *Eur. Phys. J.* C77 (2017), p. 490. arXiv: 1603.02934 [hep-ex].

[98] Topological cell clustering in the ATLAS calorimeters and its performance in the LHC Run 1. *ATLAS Collaboration*. In: *Eur. Phys. J* C 77 (2017), p. 490.

[99] Strizenec, P., Minaenko, A., and Atlas Lar Endcap group), the. *Performance of the ATLAS liquid argon endcap calorimeter in beam tests*. In: *Journal of Physics: Conference Series* 160.1 (2009), p. 012078. URL: http://stacks.iop.org/1742-6596/160/i=1/a=012078.

[100] The ATLAS Collaboration. *Response Uniformity of the ATLAS Liquid Argon Electromagnetic Calorimeter*. In: *Nuclear Instruments and Methods in Physics Research Section A Accelerators Spectrometers Detectors and Associated Equipment* 582 (Oct. 2007).

[101] The ATLAS Collaboration. *Testbeam studies of production modules of the ATLAS Tile Calorimeter*. In: *Nuclear Instruments and Methods in Physics Research Section A: Accelerators, Spectrometers, Detectors and Associated Equipment* 606.3 (2009), pp. 362–394. ISSN: 0168-9002. URL: http://www.sciencedirect.com/science/article/pii/S016890020900792X.

[102] The ATLAS Collaboration. *Performance of the ATLAS hadronic end-cap calorimeter in beam tests*. In: *Nucl. Instrum. Meth.* A482 (2002), pp. 94–124.

[103] The ATLAS Collaboration. *Jet energy measurement with the ATLAS detector in proton-proton collisions at $\sqrt{s} = 7$ TeV. Jet energy measurement with the ATLAS detector in proton-proton collisions at $\sqrt{s} = 7$ TeV*. In: *Eur. Phys. J. C* 73.CERN-PH-EP-2011-191. CERN-PH-EP-2011-191 (Dec. 2011). Comments: 100 pages plus author list (111 pages total), 93 figures, 17 tables, submitted

to European Physical Journal C, 2304. 100 p. URL: https://cds.cern.ch/record/1409965.

[104] Aaboud, M. et al. *Jet energy scale measurements and their systematic uncertainties in proton-proton collisions at $\sqrt{s} = 13$ TeV with the ATLAS detector.* In: *Phys. Rev.* D96.7 (2017), p. 072002. arXiv: 1703.09665 [hep-ex].

[105] ATLAS Collaboration. *Performance of b-Jet Identification in the ATLAS Experiment.* In: *JINST* 11 (2016), P04008. arXiv: 1512.01094 [hep-ex].

[106] *Optimisation and performance studies of the ATLAS b-tagging algorithms for the 2017-18 LHC run.* Tech. rep. ATL-PHYS-PUB-2017-013. Geneva: CERN, July 2017. URL: http://cds.cern.ch/record/2273281.

[107] ATLAS Collaboration. *Selection of jets produced in* 13 *TeV proton–proton collisions with the ATLAS detector.* ATLAS-CONF-2015-029. 2015. URL: https://cds.cern.ch/record/2037702.

[108] Aad, G. et al. *Performance of pile-up mitigation techniques for jets in pp collisions at $\sqrt{s} = 8$ TeV using the ATLAS detector.* In: *Eur. Phys. J.* C76.11 (2016), p. 581. arXiv: 1510.03823 [hep-ex].

[109] ATLAS Collaboration. *Expected performance of missing transverse momentum reconstruction for the ATLAS detector at $\sqrt{s} = 13$ TeV.* ATL-PHYS-PUB-2015-023. 2015. URL: https://cds.cern.ch/record/2037700.

[110] ATLAS Collaboration. *Performance of missing transverse momentum reconstruction with the ATLAS detector in the first proton–proton collisions at $\sqrt{s} = $ 13 *TeV.* ATL-PHYS-PUB-2015-027. 2015. URL: https://cds.cern.ch/record/2037904.

[111] James, F. *MINUIT Function Minimization and Error Analysis: Reference Manual Version 94.1.* In: (1994).

[112] Sjöstrand, T., Mrenna, S., and Skands, P. Z. *A Brief Introduction to PYTHIA 8.1.* In: *Comput. Phys. Commun.* 178 (2008), p. 852. arXiv: 0710.3820 [hep-ph].

[113] ATLAS Collaboration. *ATLAS Run 1 Pythia8 tunes.* In: ATL-PHYS-PUB-2014-021 (Nov. 2014). URL: https://cds.cern.ch/record/1966419.

[114] Gleisberg, T. et al. *Event generation with SHERPA 1.1.* In: *JHEP* 02 (2009), p. 007. arXiv: 0811.4622 [hep-ph].

[115] Krauss, F. *Matrix elements and parton showers in hadronic interactions.* In: *JHEP* 08 (2002), p. 015. arXiv: hep-ph/0205283 [hep-ph].

[116] Catani, S. et al. *QCD matrix elements + parton showers.* In: *JHEP* 11 (2001), p. 063. arXiv: hep-ph/0109231 [hep-ph].

[117] Agostinelli, S. et al. *GEANT4: A Simulation toolkit.* In: *Nucl. Instrum. Meth.* A506 (2003), pp. 250–303.

[118] Queitsch-maitland, M. "Measurements of cross sections for Higgs boson production and forward jet calibration with the ATLAS detector". PhD thesis. University of Manchester, 2016.

[119] *Impact of Alternative Inputs and Grooming Methods on Large-R Jet Reconstruction in ATLAS.* Tech. rep. ATL-PHYS-PUB-2017-020. Geneva: CERN, Dec. 2017. URL: http://cds.cern.ch/record/2297485.

[120] Butterworth, J. M. et al. *Jet substructure as a new Higgs search channel at the LHC.* In: *Phys. Rev. Lett.* 100 (2008), p. 242001. arXiv: 0802.2470 [hep-ph].

[121] Dasgupta, M. et al. *Towards an understanding of jet substructure.* In: *JHEP* 09 (2013), p. 029. arXiv: 1307.0007 [hep-ph].

[122] Larkoski, A. J. et al. *Soft Drop.* In: *JHEP* 05 (2014), p. 146. arXiv: 1402.2657 [hep-ph].

[123] *W and top tagging scale factors.* In: (July 2017). URL: http://cds.cern.ch/record/2275225.

[124] *Search for dark matter in final states with a top quark and missing transverse momentum using new hadronic top quark tagging techniques.* Tech. rep. CMS-PAS-EXO-16-051. Geneva: CERN, 2017. URL: https://cds.cern.ch/record/2273454.

[125] Kaplan, D. E. et al. *Top Tagging: A Method for Identifying Boosted Hadronically Decaying Top Quarks.* In: *Phys. Rev. Lett.* 101 (2008), p. 142001. arXiv: 0806.0848 [hep-ph].

[126] *A Cambridge-Aachen (C-A) based Jet Algorithm for boosted top-jet tagging, CMS-PAS-JME-09-001.* In: (2009).

[127] *Boosted Top Jet Tagging at CMS, CMS-PAS-JME-13-007.* In: (2014).

[128] Campbell, J. M. and Glover, E. W. N. *Double unresolved approximations to multiparton scattering amplitudes.* In: *Nucl. Phys.* B527 (1998), pp. 264–288. arXiv: hep-ph/9710255 [hep-ph].

[129] Catani, S. and Grazzini, M. *Collinear factorization and splitting functions for next-to-next-to-leading order QCD calculations.* In: *Phys. Lett.* B446 (1999), pp. 143–152. arXiv: hep-ph/9810389 [hep-ph].

[130] Catani, S. and Grazzini, M. *Infrared factorization of tree level QCD amplitudes at the next-to-next-to-leading order and beyond.* In: *Nucl. Phys.* B570 (2000), pp. 287–325. arXiv: hep-ph/9908523 [hep-ph].

[131] Gehrmann-De Ridder, A. and Glover, E. W. N. *A Complete O (alpha alpha-s) calculation of the photon + 1 jet rate in e+ e- annihilation.* In: *Nucl. Phys.* B517 (1998), pp. 269–323. arXiv: hep-ph/9707224 [hep-ph].

[132] Bertolini, D., Thaler, J., and Walsh, J. R. *The First Calculation of Fractional Jets*. In: *JHEP* 05 (2015), p. 008. arXiv: `1501.01965 [hep-ph]`.

[133] Banfi, A., Salam, G. P., and Zanderighi, G. *Principles of general final-state resummation and automated implementation*. In: *JHEP* 03 (2005), p. 073. arXiv: `hep-ph/0407286 [hep-ph]`.

[134] Lepage, G. P. *VEGAS: AN ADAPTIVE MULTIDIMENSIONAL INTEGRATION PROGRAM*. In: (1980).

[135] Fuchs, E. and Weiglein, G. *Breit-Wigner approximation for propagators of mixed unstable states*. In: *JHEP* 09 (2017), p. 079. arXiv: `1610.06193 [hep-ph]`.

[136] Dokshitzer, Y. L., Khoze, V. A., and Troian, S. I. *On specific QCD properties of heavy quark fragmentation ('dead cone')*. In: *J. Phys.* G17 (1991), pp. 1602–1604.

[137] ATLAS Collaboration. *Performance of shower deconstruction in ATLAS*. ATLAS-CONF-2014-003. 2014. URL: `https://cds.cern.ch/record/1648661`.

[138] ATLAS Collaboration. *Measurement of colour flow using jet-pull observables in $t\bar{t}$ events with the ATLAS experiment at $\sqrt{s} = 13$ TeV*. In: (2018). arXiv: `1805.02935 [hep-ex]`.

[139] Aaboud, M. et al. *Measurements of differential cross sections of top quark pair production in association with jets in pp collisions at $\sqrt{s} = 13$ TeV using the ATLAS detector*. In: *JHEP* 10 (2018), p. 159. arXiv: `1802.06572 [hep-ex]`.

[140] CMS Collaboration. *Measurement of differential cross sections for the production of top quark pairs and of additional jets in lepton+jets events from pp collisions at $\sqrt{s} = 13$ TeV*. In: (2018). arXiv: `1803.08856 [hep-ex]`.

[141] Battaglia, M., Orava, R., and Salmi, L. *A Study of depletion of fragmentation particles at small angles in b-jets with the DELPHI detector at LEP*. Tech. rep. DELPHI-2004-037-CONF-712. CERN-DELPHI-2004-037-CONF-712. Geneva: CERN, July 2004. URL: `http://cds.cern.ch/record/989441`.

[142] Chekanov, S. V. *Soft gluon angular screening in heavy quark fragmentation*. In: *Phys. Lett.* B484 (2000), pp. 51–57. arXiv: `hep-ph/0005119 [hep-ph]`.

[143] ATLAS Collaboration. *Measurements of the $t\bar{t}$ production cross-section in the dilepton and lepton-plus-jets channels and of the ratio of the $t\bar{t}$ and Z boson cross-sections in pp collisions at $\sqrt{s} = 13$ TeV with the ATLAS detector*. ATLAS-CONF-2015-049. 2015. URL: `https://cds.cern.ch/record/2052605`.

[144] ATLAS Collaboration. *Summary of ATLAS Pythia 8 tunes*. ATL-PHYS-PUB-2012-003. 2012. URL: `https://cds.cern.ch/record/1474107`.

[145] Agostinelli, S. et al. *GEANT4: A Simulation toolkit*. In: *Nucl. Instrum. Meth.* A 506 (2003), p. 250.

[146] Nason, P. *A New method for combining NLO QCD with shower Monte Carlo algorithms*. In: *JHEP* 11 (2004), p. 040. arXiv: `hep-ph/0409146` `[hep-ph]`.

[147] Frixione, S., Nason, P., and Oleari, C. *Matching NLO QCD computations with Parton Shower simulations: the POWHEG method*. In: *JHEP* 11 (2007), p. 070. arXiv: `0709.2092` `[hep-ph]`.

[148] Alioli, S. et al. *A general framework for implementing NLO calculations in shower Monte Carlo programs: the POWHEG BOX*. In: *JHEP* 06 (2010), p. 043. arXiv: `1002.2581` `[hep-ph]`.

[149] Frixione, S., Nason, P., and Ridolfi, G. *A Positive-weight next-to-leading-order Monte Carlo for heavy flavour hadroproduction*. In: *JHEP* 09 (2007), p. 126. arXiv: `0707.3088` `[hep-ph]`.

[150] Ball, R. D. et al. *Parton distributions with LHC data*. In: *Nucl. Phys.* B867 (2013), pp. 244–289. arXiv: `1207.1303` `[hep-ph]`.

[151] *ATLAS Run 1 Pythia8 tunes*. Tech. rep. ATL-PHYS-PUB-2014-021. Geneva: CERN, Nov. 2014. URL: `https://cds.cern.ch/record/1966419`.

[152] Bahr, M. et al. *Herwig++ Physics and Manual*. In: *Eur. Phys. J.* C58 (2008), pp. 639–707. arXiv: `0803.0883` `[hep-ph]`.

[153] Bellm, J. et al. *Herwig 7.0/Herwig++ 3.0 release note*. In: *Eur. Phys. J.* C76.4 (2016), p. 196. arXiv: `1512.01178` `[hep-ph]`.

[154] Harland-Lang, L. A. et al. *Parton distributions in the LHC era: MMHT 2014 PDFs*. In: *Eur. Phys. J.* C75.5 (2015), p. 204. arXiv: `1412.3989` `[hep-ph]`.

[155] Alwall, J. et al. *The automated computation of tree-level and next-to-leading order differential cross sections, and their matching to parton shower simulations*. In: *JHEP* 07 (2014), p. 079. arXiv: `1405.0301` `[hep-ph]`.

[156] Beneke, M. et al. *Hadronic top-quark pair production with NNLL threshold resummation*. In: *Nuclear Physics B* 855.3 (2012), pp. 695–741. ISSN: 0550-3213. URL: `http://www.sciencedirect.com/science/article/pii/S0550321311005803`.

[157] Cacciari, M. et al. *Top-pair production at hadron colliders with next-to-next-to-leading logarithmic soft-gluon resummation*. In: *Phys. Lett.* B710 (2012), pp. 612–622. arXiv: `1111.5869` `[hep-ph]`.

[158] Czakon, M. and Mitov, A. *Top++: A Program for the Calculation of the Top-Pair Cross-Section at Hadron Colliders*. In: *Comput. Phys. Commun.* 185 (2014), p. 2930. arXiv: `1112.5675` `[hep-ph]`.

[159] Butterworth, J. et al. *Single Boson and Diboson Production Cross Sections in pp Collisions at sqrts=7 TeV*. Tech. rep. ATL-COM-PHYS-2010-695. Geneva: CERN, Aug. 2010. URL: `https://cds.cern.ch/record/1287902`.

[160] Florian, D. de et al. *Handbook of LHC Higgs Cross Sections: 4. Deciphering the Nature of the Higgs Sector*. In: (2016). arXiv: `1610.07922` `[hep-ph]`.

[161] Abbott, B. et al. *Extraction of the width of the W boson from measurements of $\sigma(p\bar{p} \to W + X) \times B(W \to e\nu)$ and $\sigma(p\bar{p} \to Z + X) \times B(Z \to ee)$ and their ratio*. In: *Phys. Rev.* D61 (2000), p. 072001. arXiv: `hep-ex/9906025` (hep-ex).

[162] ATLAS Collaboration. *Estimation of non-prompt and fake lepton backgrounds in final states with top quarks produced in proton–proton collisions at $\sqrt{s} = 8$ TeV with the ATLAS Detector*. ATLAS-CONF-2014-058. 2014. URL: `https://cds.cern.ch/record/1951336`.

[163] Aad, G. et al. *Differential top-antitop cross-section measurements as a function of observables constructed from final-state particles using pp collisions at $\sqrt{s} = 7$ TeV in the ATLAS detector*. In: *JHEP* 06 (2015), p. 100. arXiv: `1502.05923` `[hep-ex]`.

[164] Erdmann, J. et al. *A likelihood-based reconstruction algorithm for top-quark pairs and the KLFitter framework*. In: *Nucl. Instrum. Meth.* A748 (2014), pp. 18–25. arXiv: `1312.5595` `[hep-ex]`.

[165] M.W Gruenewald, A. G. *The Mass and Width of the W Boson*. In: (2017). eprint: `http://pdg.lbl.gov/2017/reviews/rpp2017-rev-w-mass.pdf`.

[166] T.M. Liss, F. M. *The Top quark*. In: (). eprint: `http://pdg.lbl.gov/2017/reviews/rpp2017-rev-top-quark.pdf`.

[167] Bishop, C. M. *Pattern recognition and machine learning, 5th Edition*. Information science and statistics. Springer, 2007. ISBN: 9780387310732. URL: `http://www.worldcat.org/oclc/71008143`.

[168] Cowan, G. *Statistical Data Analysis*. Oxford: Clarendon (Oxford), 1998 (ISBN: 0-19-850156-0 or 0-19-850155-2 in paperback).

[169] Snoek, J., Larochelle, H., and Adams, R. P. *Practical Bayesian Optimization of Machine Learning Algorithms*. In: *arXiv e-prints*, arXiv:1206.2944 (June 2012), arXiv:1206.2944. arXiv: `1206.2944` `[stat.ML]`.

[170] Rasmussen, C. and Williams, C. *Gaussian Processes for Machine Learning*. Adaptive Computation and Machine Learning. Cambridge, MA, USA: MIT Press, Jan. 2006, p. 248.

[171] Frazier, P. I. *A Tutorial on Bayesian Optimization*. In: *CoRR* abs/1807.02811 (2018). arXiv: `1807.02811`. URL: `http://arxiv.org/abs/1807.02811`.

[172] Clark, C. E. *The Greatest of a Finite Set of Random Variables*. In: *Operations Research* 9.2 (Apr. 1961), pp. 145–162. URL: `https://ideas.repec.org/a/inm/oropre/v9y1961i2p145-162.html`.

[173] Jones, D. R., Schonlau, M., and Welch, W. J. *Efficient Global Optimization of Expensive Black-Box Functions*. In: *J. of Global Optimization* 13.4 (Dec. 1998), pp. 455–492. ISSN: 0925-5001. URL: `https://doi.org/10.1023/A:1008306431147`.

[174] Pedregosa, F. et al. *Scikit-learn: Machine Learning in Python*. In: *Journal of Machine Learning Research* 12 (2011), pp. 2825–2830.

[175] Martinez-Cantin, R. *BayesOpt: A Bayesian Optimization Library for Nonlinear Optimization, Experimental Design and Bandits*. In: *Journal of Machine Learning Research* 15 (2014), pp. 3915–3919. URL: `http://jmlr.org/papers/v15/martinezcantin14a.html`.

[176] D'Agostini, G. *A multidimensional unfolding method based on Bayes' theorem*. In: *Nuclear Inst. and Methods in Physics Research, A* 362.2-3 (1995), pp. 487–498. ISSN: 01689002.

[177] Adye, T. *Unfolding algorithms and tests using RooUnfold*. 2011. arXiv: `1105.1160 [physics.data-an]`.

[178] Aad, G. et al. *Measurement of the correlations between the polar angles of leptons from top quark decays in the helicity basis at $\sqrt{s} = 7\,TeV$ using the ATLAS detector*. In: *Phys. Rev.* D93.1 (2016), p. 012002. arXiv: `1510.07478 [hep-ex]`.

[179] Sirunyan, A. M. et al. *Measurement of normalized differential $t\bar{t}$ cross sections in the dilepton channel from pp collisions at $\sqrt{s} = 13\ TeV$*. In: *JHEP* 04 (2018), p. 060. arXiv: `1708.07638 [hep-ex]`.

[180] Kidonakis, N. *Top Quark Production*. In: *Proceedings, Helmholtz International Summer School on Physics of Heavy Quarks and Hadrons (HQ 2013): JINR, Dubna, Russia, July 15-28, 2013*. 2014, pp. 139–168. arXiv: `1311.0283 [hep-ph]`.

[181] Kidonakis, N. *Two-loop soft anomalous dimensions for single top quark associated production with a W- or H-*. In: *Phys. Rev.* D82 (2010), p. 054018. arXiv: `1005.4451 [hep-ph]`.

[182] ATLAS Collaboration. *Measurement of $W^{\pm}$ and Z Boson Production Cross Sections in pp Collisions at $\sqrt{s} = 13\ TeV$ with the ATLAS Detector*. ATLAS-CONF-2015-039. 2015. URL: `https://cds.cern.ch/record/2045487`.

[183] *Modelling of the $t\bar{t}H$ and $t\bar{t}V$ ($V = W, Z$) processes for $\sqrt{s} = 13\ TeV$ ATLAS analyses*. Tech. rep. ATL-PHYS-PUB-2016-005. Geneva: CERN, Jan. 2016. URL: `http://cds.cern.ch/record/2120826`.

[184] ATLAS Collaboration. *Luminosity determination in pp collisions at $\sqrt{s} = 8\ TeV$ using the ATLAS detector at the LHC*. In: (2016). arXiv: `1608.03953 [hep-ex]`.

[185] *Luminosity determination in pp collisions at $\sqrt{s} = 13\ TeV$ using the ATLAS detector at the LHC*. Tech. rep. ATLAS-CONF-2019-021. Geneva: CERN, June 2019. URL: `https://cds.cern.ch/record/2677054`.

[186] *TopFocusGroup: How to get the radiation uncertainties using the shower weights.* Tech. rep. CERN, 2018. URL: https://twiki.cern.ch/twiki/bin/viewauth/ AtlasProtected/TopFocusGroup#How_to_get_the_radiation_uncerta.

[187] Butterworth, J. et al. *PDF4LHC recommendations for LHC Run II.* In: *J. Phys.* G43 (2016), p. 023001. arXiv: 1510.03865 [hep-ph].

[188] Dulat, S. et al. *New parton distribution functions from a global analysis of quantum chromodynamics.* In: *Phys. Rev.* D93.3 (2016), p. 033006. arXiv: 1506. 07443 [hep-ph].

[189] Ball, R. D. et al. *Parton distributions for the LHC Run II.* In: *JHEP* 04 (2015), p. 040. arXiv: 1410.8849 [hep-ph].

[190] *1974 CERN School of Computing, Godoysund, Norway, 11-24 Aug 1974: Proceedings.* 1974. URL: http://www.slac.stanford.edu/spires/find/books/ www?cl=QA76:C2:1974.

[191] Byrd, R. H., Lu, P., and Nocedal., J. *A Limited Memory Algorithm for Bound Constrained Optimization.* In: *SIAM Journal on Scientific and Statistical Computing* 16 (1995), pp. 1190–1208.